Experimental and Numerical Investigation of Graphite-Steam Oxidation for HTGRs

by

Chengqi Wang

A dissertation submitted in partial fulfillment
of the requirements for the degree of
Doctor of Philosophy
(Nuclear Engineering and Radiological Sciences)
in the University of Michigan
2021

Doctoral Committee:

Professor Xiaodong Sun, Chair
Professor Richard N. Christensen, University of Idaho
Professor Ronald Larson
Associate Research Scientist Victor Petrov
Senior Research Scientist Piyush Sabharwall, Idaho National Laboratory
Professor Lumin Wang

Chengqi Wang
nukewang@umich.edu
ORCID ID: 0000-0003-4607-3726

This dissertation is dedicated to my family,
for their endless love, patience, and support.

ACKNOWLEDGEMENTS

First and foremost, I would like to express my greatest gratitude to my advisor Professor Xiaodong Sun for his guidance, support, and continuous encouragement. This work could not be completed without Professor Sun's support. His humility, hardworking and rigorous attitude always inspire me in my future career.

In addition, I would like to thank my committee members, Professor Ronald Larson, Professor Lumin Wang, and Dr. Victor Petrov from University of Michigan, Dr. Piyush Sabharwall from Idaho National Laboratory, and Professor Richard Christensen from University of Idaho. Their comments and suggestions kept me on the right track. I also thank Dr. Cristian Contescu from Oak Ridge National Laboratory for offering selfless help in the whole progress.

The Ph.D. study was an exciting adventure in which I met so many amazing people. Dr. Nanjun Chen always gave me the best support whenever I encounter a challenge. Professors Minghui Chen and Wentao Zhou, and Dr. Adam Burak were always willing to help and gave me advice. Dr. Sheng Zhang and Dr. Qingqing Liu saved me many times when I was locked out the laboratory, sometimes at piercing cold midnight. Besides, Drs. Yafei Wang, Chenyang Lu, Miao Song, David Arcilesi, Yalan Qian, Yang Liu, Xiao Wu, and so on, also made this journey enjoyable. I also thank my cat Ergo who helped nothing at all, except creating a couple of beautiful scars on my arms.

I cannot wait to express my deepest gratitude to my parents. Living in a small village of east China, they struggled to raise me and my sister up. In the past decades, hey had to work overload

every day in harsh environment no matter if it was hot, cold, windy, rainy, or snowy. Nevertheless, they never thought about giving up. I did not know how much they had given to me until someday I suddenly found gray hair has replaced their original black one. It turns out that they have been pushing me high on their own shoulders so I can obtain a better view of this world. It was them who taught me tenacity and integrity. It was also them who gave me endless encouragement and love in my darkest days. It is my biggest honor to be the son of such great parents. I also want to express my deepest gratitude to my sister, who always put herself in my shoes. During the past years, she has taken all responsibilities of taking care of my parents so I can focus on my studies.

Last but not least, I would like to thank U.S. Department of Energy (DOE) Office of Nuclear Energy, Nuclear Energy University Program (NEUP) for supporting this research.

TABLE OF CONTENTS

LIST OF FIGURES

LIST OF TABLES

Abstract

Nuclear graphite is proposed for use in High-temperature Gas-cooled Reactor (HTGR) designs as the neutron moderator, reflector, and core structural material. During the normal operation of an HTGR, a small amount of moisture can exist in the primary helium circuit even with a helium purification system included to remove any impurities present in the primary coolant. In addition, a large amount of moisture can quickly enter the primary side during a steam ingress accident for those HTGRs that feature a steam Rankine cycle as the power conversion unit. The moisture can react with nuclear graphite in high-temperature environments, which degrades mechanical strength of graphite. Therefore, it is necessary to investigate the graphite-steam oxidation phenomena in detail to facilitate future HTGR licensing and deployment.

In this research, the oxidation behavior of nuclear graphite IG-110 by steam was investigated under various temperature, moisture concentration, and hydrogen partial pressure conditions. A graphite-steam oxidation test facility was constructed to obtain high-resolution experimental data. The reaction environment was jointly controlled by a tube furnace, a peristaltic pump, and gas mass controllers. The concentrations of production gases CO and CO_2 were measured online by a gas chromatography, which were then used to derive the oxidation rates. A total of 141qualified data points of the kinetic oxidation rates were collected at temperatures 850 to 1100 °C with steam partial pressure up to 20 kPa and hydrogen partial pressure varied from 0 to 3 kPa. Boltzmann-enhanced Langmuir-Hinshelwood (BLH) reaction rate equation was obtained through

multivariable optimization. The overall mean relative difference between the predicted oxidation rate and the experimental data is 24%, with the maximum difference being 55%.

In addition, experiments were performed to investigate the effect of mass loss on graphite oxidation rate. It was believed the graphite-moisture reaction expands the existing micro pores in graphite and opens those originally isolated pores, both resulting in an increase of active surface area. In the experiment, the graphite mass loss fraction was found to have a more prominent effect on increasing the oxidation rate at lower temperatures.

Furthermore, a multiphysics model was developed for graphite-steam oxidation. The numerical model couples all important physical processes, including the kinetic chemical reaction, multi-species transport, free and porous flow, heat transfer, and microporous structure evolution. The multiphysics model was validated against our experimental data. Our comparisons show that the numerical model can well simulate the apparent oxidation rate and accurately predict the post-oxidation density distribution.

The validated model was then applied to the prototypic MHTGR design for normal operating conditions. The chronic graphite-moisture oxidation during a full MHTGR service period of 36-months was simulated. The simulation indicates that at the end of the 36-month operation, the maximum local graphite mass loss can reach to about 85%. However, the oxidation is well confined within a thin layer of about 0.5 mm thickness into the graphite surface. Therefore, chronic graphite-moisture oxidation will not significantly decrease the mechanical strength of graphite, nor jeopardize the integrity of graphite fuel blocks in MHTGR during its normal operation.

Chapter 1 Introduction

1.1 Research Background

High-temperature Gas-cooled Reactors (HTGRs) exhibit advantages in improving the efficiency of thermal-to-electric energy conversion and providing high-temperature process heat in addition to their inherent safety features [1], [2]. Therefore, it has been selected by U.S. Department of Energy (DOE) as one of the candidates in the Next Generation Nuclear Plant (NGNP) project to demonstrate the technical and licensing viability as a CO_2-free source of energy [3]. Several HTGR concepts have been proposed by different institutions. In general, the HGTR designs adopt either a pebble bed type [4] or prismatic type active core [5].

To lower the engineering risks of helium turbine fabrication, a conventional steam Rankine cycle (SRC) is coupled to the primary helium circuit via a steam generator (SG) for power conversion in the Modular High Temperature Gas-cooled Reactor (MHTGR) design, as shown in Figure 1-1. Similarly, the SRC is also adopted by the pebble type gas-cooled reactor HTR-PM [6]. A common feature of the current HTGR designs is that graphite is widely used as the neutron moderators, reflectors, and core structural material. For example, the MHTGR design has three layers of active graphite fuel columns which are then surrounded by the inner and side graphite reflectors. The layout of reactor pressure vessel (RPV) system in the MHTGR design is depicted in Figure 1-2. In addition, the weight of the fuel columns and those replaceable graphite reflectors are mounted to the graphite cylinder posts in the hot plenum. A similar prismatic HTGR design was proposed by AREVA that has two SRC power conversion units [7].

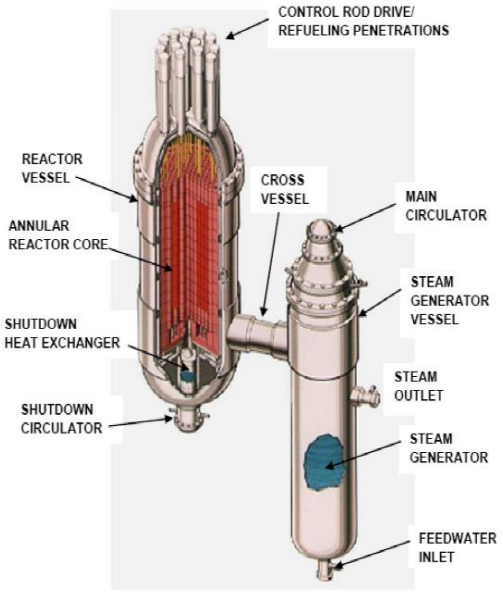

Figure 1-1 Schematic of MHTGR system layout

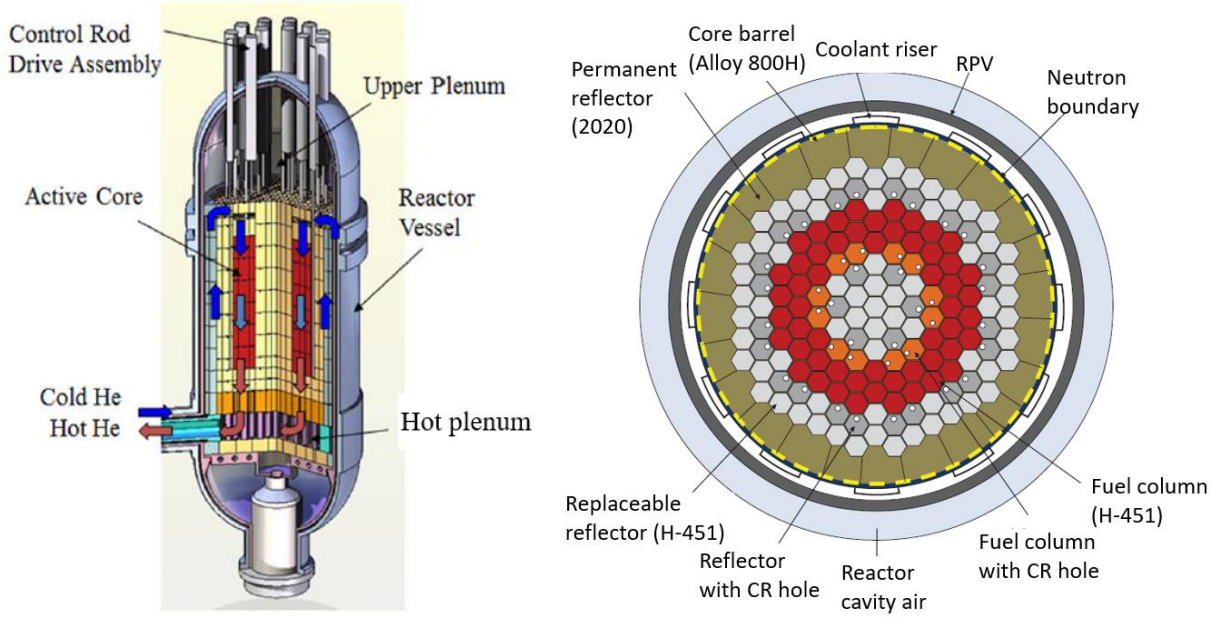

(a) (b)

Figure 1-2 Schematic layout of MHTGR: (a) cut-away view of RPV system, and (b) cross sectional view of active core [5]

Although nuclear graphite exhibits excellent neutron irradiation and high temperature properties, the graphite oxidation under specific conditions has to be carefully investigated to support HTGR design, licensing, and deployment activities. For different HTGR designs, a small amount of moisture, with most practical values grouped around 1.1-1.4 Pa at a total pressures of 7-9 MPa, could exist in the primary helium even with helium purification systems included to remove the impurities [8]. Although the graphite-moisture oxidation rate is very small, it can chronically and continuously corrode the graphite materials. In order to ensure the safety of an HTGR, the graphite in reactor core has to survive through its full service period. For example, the replaceable graphite fuel blocks and reflectors should maintain their integrity during the 36-months refueling period, and the permanent reflectors and structural graphite should maintain enough mechanical strength for a full service time of 40 years. In addition to the small concentration of moisture during reactor normal operation, a relatively larger amount of moisture could enter the primary side from the water-lubricated bearings of the helium circulator. For example, the Fort St. Vrain HTGR power plant recorded moisture level of 4 to 240 ppm (equivalent to moisture partial pressure of 20 to 1,152 Pa) at a total helium pressure of 4.8 MPa during the first 16 weeks after reactor start up [9].

Another concern of graphite oxidation comes from the postulated steam ingress accident. In order to improve the system thermal efficiency, the pressure of the secondary steam/water loop (~20 MPa) is typically much higher than the primary helium pressure (~7 MPa). As a consequence, a large amount of moisture will quickly enter the primary side once a generator tube rupture (SGTR) accident occurs [10]–[12]. The nuclear graphite in the core region will, thereafter, be oxidized at a higher rate within a short period due to the larger steam concentration.

It has been shown that the mechanical strength of nuclear grade graphite IG-110 decreased by about 50% at a mass loss fraction of 8-10% [13], [14]. The experiments using matrix graphite, which is more vulnerable to oxidation, showed 77.3% and 12.5% of compressive strength have been lost with 10% mass loss fraction at 550 °C and 900 °C, respectively [15]. The severer strength degradation at lower temperature is attributed to more uniform reaction over the graphite sample volume. The chemical reaction between steam and graphite not only weakens the mechanical strength, but also produces combustible gases, such as H_2 and CO. Therefore, the graphite-steam oxidation has to be carefully investigated to facilitate the future HTGR licensing and deployment.

When the MHTGR concept was first introduced, nuclear grade graphite H-451 was chosen as the candidate material for the fuel matrix, fuel blocks, and replaceable reflectors [16], [17]. Later, more grades of nuclear graphite were developed while the commercial production of H-451 was ceased. Some of these latest nuclear grade graphite and their applications are listed in Table 1-1. The U.S. Nuclear Regulatory Commission (NRC) requires the safety analyses be performed based on the actual material that will be used in the reactor. Therefore, certain tests must be conducted to verify that the properties of these new developed graphite meet the HTGR operation requirements. One of these tests is to study their resistance to steam oxidation during both reactor normal operation and under accidental conditions.

Table 1-1 Summary of new developed nuclear grade graphite [18]

Graphite	Manufacture/Country	Proposed application
IG-110	Toyo Tanso/Japan	Prismatic fuel element, replaceable reflector, support posts
IG-430	Toyo Tanso/Japan	Prismatic fuel element, replaceable reflector, support posts
PCEA	Graftech/USA	Fuel and replaceable block, pebble reflector
NBG-17	SGL Carbon/Germany	Fuel and replaceable block, pebble reflector, insulation block
NBG-18	SGL Carbon/Germany	Fuel and replaceable block, pebble reflector, insulation block
2114	Mersen/USA	Fuel and replaceable block, pebble reflector, insulation block

1.2 Literature Review of Nuclear Graphite Oxidation

1.2.1 Classical theory of graphite oxidation

Experimental studies on graphite oxidation can be dated back to 1960s when Gulbransen et al. performed an oxygen-graphite reaction study at vacuum conditions [19], which proposed the oxidation rate is governed by three factors, (i) the primary chemical reaction, (ii) the diffusion-controlled reaction, and (iii) the theoretical rate based on collision theory. This theory is also suitable for graphite-steam/moisture reaction except the kinetic reaction rate is much lower. The chemical reaction during the graphite oxidation process is a complex phenomenon that has multiple possible reaction routes, on which no consensus has been reached in the community over the past decades [20]. Different assumptions have been proposed regarding the elementary reaction sequences in graphite-moisture/steam reaction [21]–[23]. Fortunately, the exact sequences of the

elementary reaction routes at atomic scale do not affect the format of the kinetic reaction rate equation [24]. For graphite-oxygen oxidation, an Arrhenius equation (Eq. (1-1)) was used to fit the experimental data when the inhibition effect of the production gases (CO and CO_2) on the reaction rate could be ignored [25]–[27].

$$Rate = k \exp(\frac{E}{RT}) p_{O_2}, \tag{1-1}$$

where k, E, R, T and p_{O_2} are the reaction frequency, activation energy, ideal gas constant, temperature, and oxygen partial pressure, respectively.

The graphite-steam oxidation is more complicated because the heterogeneous chemical reaction (Eq. (1-2)) produces H_2:

$$C_{graphite} + H_2O_{vapor} = CO_{gas} + H_{2\ gas}. \tag{1-2}$$

The production gas H_2 can compete with water molecules to occupy the active graphite sites, which then slows down the chemical reaction. Therefore, the Langmuir-Hinshelwood (LH) expression (Eq. 1-3) is used to consider this effect [17], [22]:

$$Rate = \frac{k_1 \exp(\frac{E_1}{RT}) p_{H_2O}}{1 + k_2 \exp(\frac{E_2}{RT}) p_{H_2}^n + k_3 \exp(\frac{E_3}{RT}) p_{H_2O}}, \tag{1-3}$$

which contains three reaction frequency coefficients k_i and their corresponding activation energy E_i. The reaction order of hydrogen, n, was usually assumed to be 0.5-1.0 [17], [22]. Take the elementary reaction schemes proposed by Gadsby and Hinshelwood [23] as an example, the theoretical basis for the LH equation is that the chemical reaction between graphite and steam

depends on three distinct processes: (i) sorption of water molecules on active graphite sites, (ii) chemical reaction of the absorbed water to form H_2 and CO, and (iii) inhibition of water sorption by competitive sorption of H_2 molecules. These three processes can be described respectively by Eqs. (1-4) to (1-6). It should be noted only Eq. (1-5) is irreversible.

$$H_2O_{vapor} + C \underset{j_1}{\overset{i_1}{\rightleftharpoons}} C(H_2O) \tag{1-4}$$

$$C(H_2O) \xrightarrow{j_3} CO + H_2 \tag{1-5}$$

$$H_2 + C \underset{j_2}{\overset{i_2}{\rightleftharpoons}} C(H_2) \tag{1-6}$$

The combination of Eqs. (1-4) to (1-6) generates Eq. (1-7):

$$Rate = \frac{\frac{i_1 j_3}{j_1 + j_3} p_{H_2O}}{1 + \frac{i_2}{j_2} p_{H_2}^n + \frac{i_1}{j_1 + j_3} p_{H_2O}}, \tag{1-7}$$

which forms the basis for the LH kinetic reaction rate equation.

It was later found the LH model tends to underestimate the kinetic reaction rate, especially in high temperature and high steam pressures environment. In addition, the reaction order for steam/moisture has a sigmoid-type variation with temperature [20]. Correspondingly, an integral Boltzmann distribution function was added as the reaction order for steam/moisture, which forms the Boltzmann-enhanced Langmuir-Hinshelwood (BLH) model [20]:

$$R_{spe} = \frac{k_1 \exp(-\frac{E_1}{RT}) p_{H_2O}{}^{m(T)}}{1 + k_2 \exp(-\frac{E_2}{RT}) p_{H_2}^n + k_1 \exp(-\frac{E_3}{RT}) p_{H_2O}{}^{m(T)}} \quad (a)$$

$$m(T) = m_{max} + \frac{m_{min} - m_{max}}{1 + \exp\left(\frac{T - T_0}{\theta}\right)} \quad (b) \qquad , \qquad (1\text{-}8)$$

where m_{min} and m_{max} specify the lower and upper limits of the apparent kinetic order. The constants T_0 and θ are a characteristic temperature and scaling parameter, respectively. All these constants along with the reaction frequencies k_i and activation energies E_i should be determined by experiment.

1.2.2 Graphite oxidation experiments

Velasquez first obtained the constants in the LH equation by fitting observed oxidation rate of H-451 to the LH equation [17]. Having difficulty in fitting all experimental data into one LH equation, the experimental data were divided into two groups that covers steam partial pressure from 0 to 300 pa, and 300 to 3500 Pa individually, and two sets of constants were therefore proposed. Since that time, this model has been widely used to estimate the moisture-graphite oxidation, even for other grades of nuclear graphite [28]–[32]. However, different grades of nuclear graphite can exhibit very different chemical reaction properties due of the distinct manufacturing processes, impurity levels, raw materials, grain sizes, and internal pore structures, etc. As mentioned above, the NRC requires that nuclear reactor safety analysis be based on the exact materials used in the reactor design.

In recent studies, Contescu et al. conducted graphite-moisture oxidation tests using four different grades of nuclear graphite, namely IG-110, 2114, PCEA, and NBG-17, and obtained the

reaction constants in the LH and BLH equations for each graphite [4], [8], [20], [25], [33], [34]. In Contescu's work, the moisture partial pressure mainly varies between 10 to about 1,000 Pa. Cho et al. conducted graphite-steam oxidation experiments using nuclear graphite IG-110 in Ar-steam mixture at temperature up to 1400 °C [35]. It was found the reaction activation energy decreased from 318.6 to 148.9 kJ/mol with temperature. Although the steam volume ratio in Cho's work reached 20%, the carrier gas Ar might lead to different mass transfer phenomenon as He. In addition, the Arrhenius expression was used to interpret the measured oxidation rate, which is not accurate enough.

1.2.3 Numerical modeling techniques for graphite oxidation

The experimental works in existing literature are mainly aimed to investigate the kinetic reaction phenomena between nuclear graphite and oxidants, e.g., to derive the reaction frequencies and activation energies. In addition to the kinetic oxidation experiments, numerical modeling is expected to predict the graphite oxidation depth, mass loss, and post-oxidation under a specified condition. In order to estimate the graphite oxidation and mass loss during an air ingress accident of pebble-type reactor HTR-10, the kinetic reaction rate equation for graphite-oxygen oxidation [36] is adopted by a computational fluid dynamic (CFD) simulation, in which the pebble core is regarded as a homogenous porous media [37]. The same approach was also used to study the graphite-steam oxidation during a steam ingress accident [38]. Since the porous flow approach does not distinguish the solid and fluid domains separately, it cannot predict the oxidation depth, which is critical to graphite mechanical strength loss.

A more reasonable modeling technique is to consider the graphite itself as a porous media and solves the gas diffusion reaction equation for it. Based on this strategy, the water penetration depth

was obtained by solving the one-dimensional (1-D) gas diffusion reaction equation [29]. Similarly, a quasi-steady state analytical method was proposed for the chronic graphite-moisture oxidation under HTGR normal operation conditions, which adopts Fick's law to calculate the gas diffusion in nuclear graphite and neglects the Knudsen and surface diffusion [39], [40]. In addition, the density distribution of oxidized graphite samples was measured by image analysis, which was then used to validate the analytical model. The oxidant diffusion through fluid boundary layer was also included in later works [41]–[43]. Although these 1-D analyses show promising results, their applications are limited due to the simplifications, e.g., steady-state assumption.

The latest development of Multiphyisc COMSOL allows the easy coupling of multiple physical fields [44]. Taking the advantages of COMSOL, the porous gas diffusion reaction equation can be coupled to other governing equations such as flow and heat transfer in both porous media and free flow regions. In addition, the accommodation of ordinary differential equations (ODEs) brings flexibility to model user-defined physical process. For example, the ODEs can be used to describe the micro pore expansion in graphite oxidation process. Using this methodology, the graphite-moisture oxidation during reactor normal operations has been simulated [32], [45], [46]. Nevertheless, this modeling technique has not been validated. In these simulations, it was assumed the size of the micro pores is uniform. Therefore, the mean pore diameter can be used to solve the mass transfer and flow equations. This assumption simplifies the problem and reduces computational load significantly. However, the sizes of the micro pores in nuclear graphite span four orders of magnitude [47]. For example, the mercury intrusion measurement indicates the pore size of graphite IG-110 cover a few nanometers to a few hundred micrometers [48]. To consider the effect of pore size spectrum on the gas diffusion reaction in nuclear graphite, pore network modeling methods [47], [49]–[51] are recommended.

1.3 Research Objectives

Although numerous research activities have been carried out in literature, the available data is still far from enough to support HTGR licensing and deployment. For example, the existing experiments of graphite-steam oxidation were usually performed with moisture partial pressure of 100 to 3000 Pa which is too large to reflect the moisture level during reactor normal operations. On the other hand, it is too small to cover the steam/water ingress accident. For example, the highest moisture/steam partial pressure in the primary side can reach up to about 50 kPa depending on the SGTR size, location, and accident mitigation strategy [52]. Therefore, it is necessary to extend the graphite-steam reaction experiments cover a wider moisture concentration range.

In addition, there is a lack of validated model to simulate the integral graphite oxidation phenomena. As so far, the experimental works are mainly focused on kinetic oxidation rate equation. The total oxidation rate of a graphite component under a specified oxidizing condition is dependent not only on the kinetic oxidation rate but also on mass transfer. In order to build a model that can accurately simulate the graphite oxidation behavior regardless graphite sizes, surface-to-volume ratio, and oxidizing condition, it is desired to couple the chemical reaction with other related physical processes together.

This research is aimed to address the above challenges. The final objective of this research is to establish a validated model that can be used to simulate the graphite oxidation phenomenon in more details. More specifically, the tasks and objectives of this research can be summarized as follows:

(a) to experimentally investigate the kinetic graphite-steam oxidation under different conditions, e.g., various steam and hydrogen partial pressures, and reaction temperature;

(b) to provide a kinetic reaction rate equation using the experimental data from task (a);

(c) to measure the reaction rate at different graphite mass loss fractions;

(d) to establish a multiphysics model that include all related physical processes;

(e) to validate the multiphysics model against experimental data; and finally

(f) to conduct numerical simulations using the validated model for prototypic reactor operation conditions.

1.4 Dissertation Organization

In Chapter 1, a literature review describes the state-of-art of graphite oxidation studies, based on which the knowledge gap and research objectives are defined. Chapter 2 provides an introduction to the experiment methodology and the construction of a test facility for graphite oxidation. The experimental results are presented in Chapter 3 using four sections that focus on different objectives individually. In Chapter 4, the experimental data is used to derive the kinetic oxidation rate equations via multivariable optimization. Chapter 5 describes the development of a multiphysics model for graphite-steam oxidation, including the mathematics and its validation. Using this validated model, the graphite-moisture oxidation under prototypic MHTGR operation conditions is simulated, which is presented in Chapter 6. Finally, the major conclusions are summarized and a few research topics are suggested in Chapter 7.

Chapter 2 Design and Construction of Graphite-Steam Oxidation Test Facility

2.1 ASTM Standard Method for Graphite Oxidation Experiments

In order to investigate the nuclear graphite-air oxidation, a standard testing method has been proposed in literature [53]. In this method, a tube furnace is used to control the reaction temperature. A mass balance scale is installed onto the top of the tube furnace, which measures the mass of the graphite sample during the oxidation process. A lot metal elements, especially the alkaline earths, are known to catalyze the graphite oxidation [54]. Therefore, alumina or quartz tube are recommended to avoid the catalyzing effects from possible metal particles. In addition, the graphite sample should be hold by a platinum (Pt) basket. A schematic of the ASTM test facility is depicted in Figure 2-1.

This ASTM facility was modified to accommodate graphite-moisture reaction experiments by adding a water bath & bubbler, as shown in Figure 2-2. Using this method, the maximum moisture partial pressure can reach to about 2 kPa. One of the objectives in this research is to investigate the graphite-steam oxidation rate at higher steam concentrations that are comparable to a steam/water ingress accident. Therefore, an alternative method is needed to introduce a larger steam flows, which will be described in the next section.

In the ASTM-7542 facility, the graphite mass loss is monitored by a thermal gravimetric analysis (TGA). In this method, the mass loss rate (in unit g/s) directly indicates the oxidation rate. However, the graphite oxidation has to run long enough to accumulate a mass loss value that

overwhelms the uncertainty associated with TGA. In addition, the gas flow fluctuation can also disturb the measurement. An alternative measuring method is monitor the concentrations of productions gases [55]. In this research, gas chromatograph (GC) was used to measure the oxidation rate.

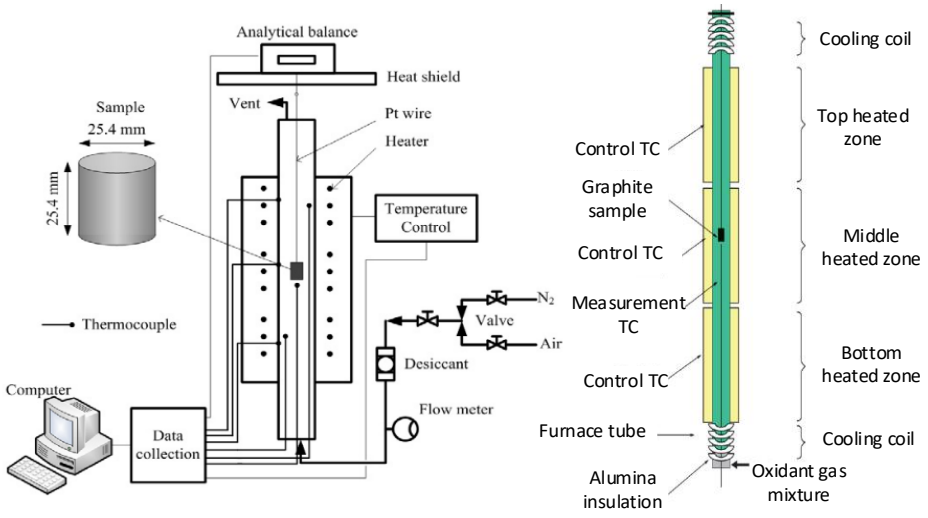

Figure 2-1 Schematic of ASTM graphite air test facility [53]

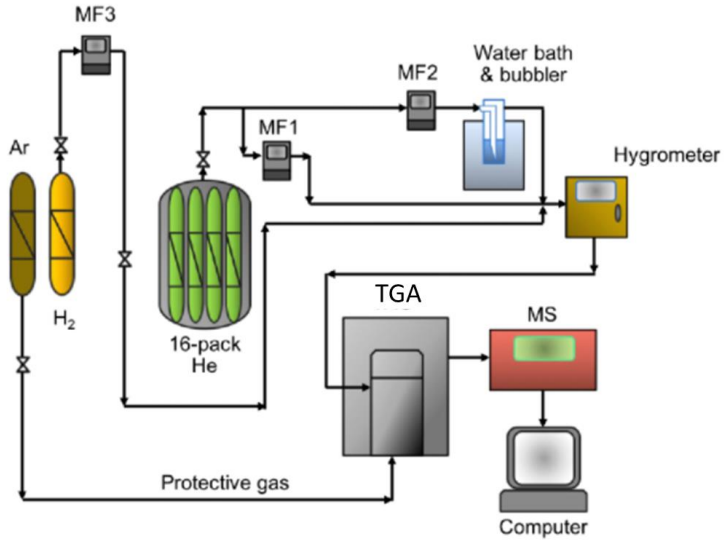

Figure 2-2 Schematic of graphite-moisture/steam oxidaton test facility at Oak Ridge National Laboratory (ORNL) [8]

2.2 Construction of a High-resolution Test Facility for Graphite Oxidation

2.2.1 Measurement of graphite oxidation rate using GC

The GC deployed in this research is customized by Agilent Technologies, which has a resolution of 0.1 ppm by mole for CO, CO_2, and CH_4 in scientific grade helium (99.9999%). It has one thermal conductive detector (TCD) and one flame ionization detector (FID). The FID shows better linearity and resolution than the TCD in the test. Furthermore, the calibration of FID is much easier and straightforward. Therefore, only FID signals were adopted for data analysis in this research.

The mechanism of FID detection is demonstrated by Figure 2-3. In each measurement, the sampling gas mixture, containing CO, CO_2, and CH_4, is introduced into two micro capillary glass HP-PLOT columns that are arranged in serial. As the gas mixture flows through the two glass columns, they will be separated into a sequence via interaction with the coating materials. Then, the gas mixture will flow through a nickel catalyzer, in which CO and CO_2, are converted into CH_4. Finally, the gas stream flow through the FID, where CH_4 are burned in the H_2 flame. The pulses of CH_4 leads to an increase of flame ions, which generates an electric current signal. Since the flux of flame ions is linear to the concentration of carbon atoms, the FID detector signal is always linear to the quantity of CO, CH_4, and CO_2.

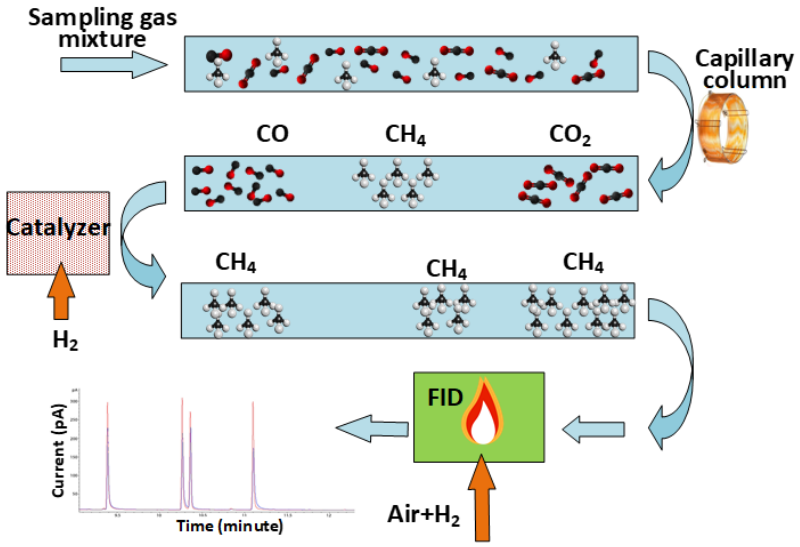

Figure 2-3 Schematic of molecule separation and detection by GC FID

The GC was calibrated at installation using a standard gas sample that is made by mixing CO, CO_2, and CH_4 in ultra-high purity (UHP) helium (99.999%). The concentration of each components by mole in this standard gas sample is listed in Table 2-1. The signal peaks are shown in Figure 2-4 and Table 2-2. Three peaks appear in a time sequence, which represent CO, CH_4, and CO_2 in order, respectively. The sequence of these three peaks are determined by referring to the user manual of the HP-PLOT column. A validation of this sequence is provided in the following section.

Table 2-1 Concentration of different gas species in standard gas sample

Component	Concentration [ppm]	Analytical uncertainty [%]	Concentration ratio [--]
CO	9.65	±5	0.831
CH_4	10.09	±5	0.869
CO_2	11.61	±2	1
He	balance		N/A

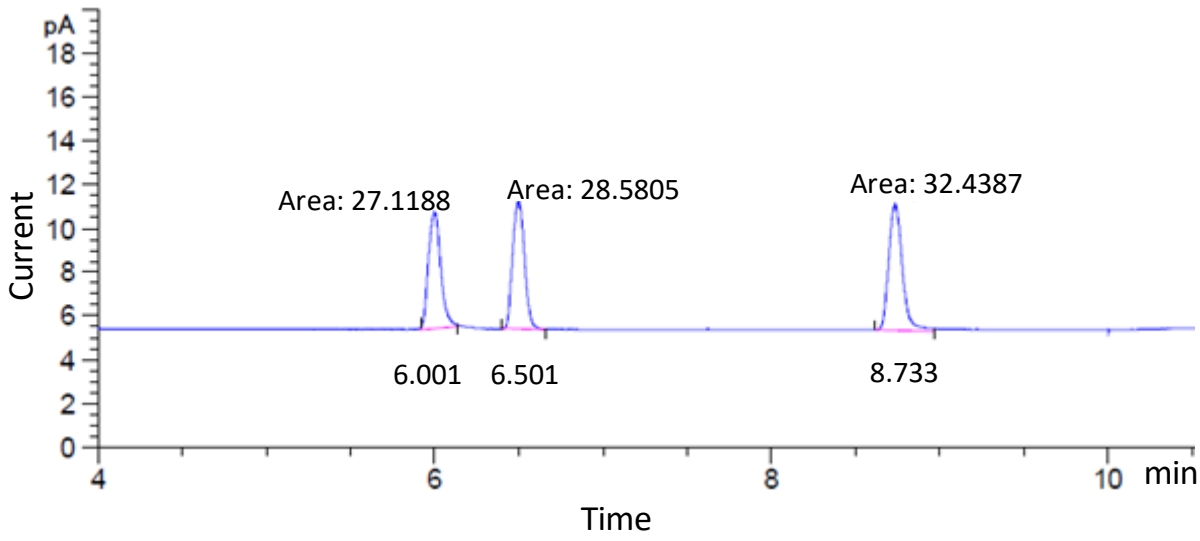

Figure 2-4 Signal peaks of CO, CH_4, and CO_2 obtained using standard gas sample

The accuracy of the measurement can be confirmed by comparing the area ratio of the peaks in Table 2-2 with the actual concentration ratio in Table 2-1. For example, if CO_2 is used as the base reference, the error of this measurement is less than 1.5%, which is well covered by the uncertainty of the standard gas sample. In the shakedown tests, it was found the sample injection rate can affect the absolute value of the peak area if it drops below a certain threshold about 0.1 standard liter per minute (SLPM). Therefore, the sampling gas flow rate was always maintained at 0.2 SLPM in the experiments.

Table 2-2 GC measurement using standard gas sample

Component	**Peak time [min]**	**Width [min]**	**Peak area [pA·s]**	**Area fraction [%]**	**Area ratio [--]**
CO	6.001	0.0842	27.1188	30.77	0.836
CH_4	6.501	0.0795	28.5805	32.53	0.881
CO_2	8.733	0.0873	32.4387	36.80	1

2.2.2 Design and construction of graphite oxidation test facility

As aforementioned, the highest steam partial pressure that can be generated by water bath & bubbler method is about 2 kPa. Therefore, an online steam generation method was applied in this research. In this method, a stream of liquid water at constant flow rate is mixed with helium which comes from upstream. The mixture then flows through an electric heating tube, where the liquid water is converted into single phase steam. Given the system pressure, temperature and inlet gas mixture flow rate, the steam partial pressure can be calculated. The schematic of the graphite oxidation test facility is depicted in Figure 2-5. The test facility mainly consists of a gas supplying system, a tube furnace, moisture condenser and trap, and the customized GC.

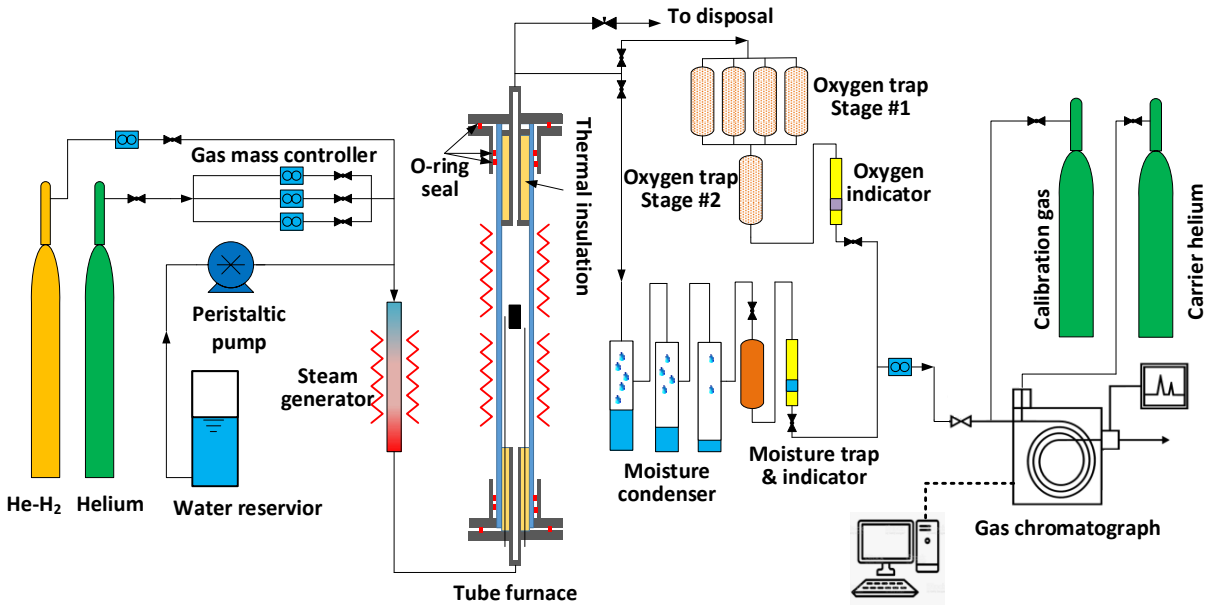

Figure 2-5 Schematic of graphite oxidation test facility

Figure 2-6 BT100-2J peristaltic pump for liquid water injection

In the graphite-steam oxidation test facility, a peristaltic pump as shown in Figure 2-6, is used to inject liquid water into the heating tube which serves as a steam generator. At the same time, a stream of helium-hydrogen mixture is injected into the system by two Alicat mass controllers at upstream, as shown in Figure 2-7. The liquid water, carried by the upstream helium-hydrogen mixture, and under the function of gravity, flows through the heating tube. Six tape heaters, which are controlled by three PID controllers, are installed to the heating tube until to the inlet of reaction tube.

Figure 2-7 Gas mass controllers used for flow control

In addition, three thermal couples are inserted into the heating tube to ensure the gas mixture temperature is above 250 °C at the reaction tube inlet, which means all liquid water has been heated into single phase steam. In this way, a constant gas mixture flow rate was achieved with steam concentrations already known. In order to ensure the steam is mixed well in the gas mixture, the heating tube is constructed with multiple V-type and 90° bends, which is shown in Figure 2-8.

Figure 2-8 Structure of the heating tube

A two heating zone tube furnace is used to control the reaction temperature. To avoid any catalytic elements, a quartz tube with I.D. 75 mm was used. In addition, a basket made by Pt wire is used as the graphite sample holder. An example of a cylindrical graphite sample loaded into the quartz tube is shown in Figure 2-9. Three K-type thermocouples are applied to measure the temperature around the graphite sample.

In order to prevent steam from condensing, tape heaters with PID controllers are applied to the top and bottom of the quartz tube, as shown in Figure 2-10. The quartz tube is sealed by three

silicon rubber O-rings at each end. The temperature limit of these O-rings is 232 °C. Therefore, these O-rings have to be thermally insulated from the high temperature gas mixture. To prevent the rubber O-rings from being overheated, a three-quarter inch tube, welded on the flange cap, is inserted into the quartz tube at the bottom and top end as the inlet and outlet flow channel. The annular region between the intrusion tube and the quartz tube is then filled with ceramic fibers as thermal insulation. Figure 2-11 shows the structure of the outlet channel surrounded by ceramic fiber thermal insulation. The length of the intrusion inlet and outlet tubes is 250, and 500 mm respectively. In the experiments, the outer surface temperature at the two ends of the quartz tube is controlled at about 200 °C, which ensures the steam does not condense and the integrities of the seal O-rings are also maintained.

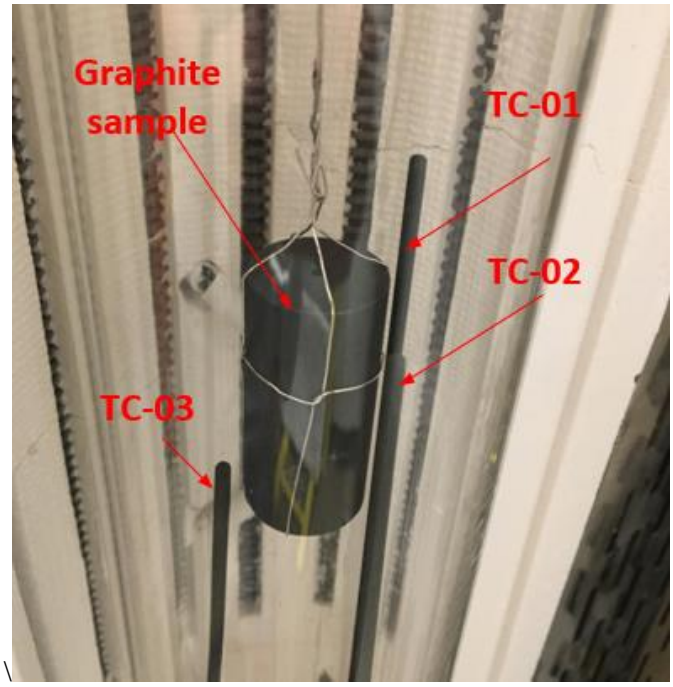

Figure 2-9 Cylindrical graphite sample loaded into quartz tube

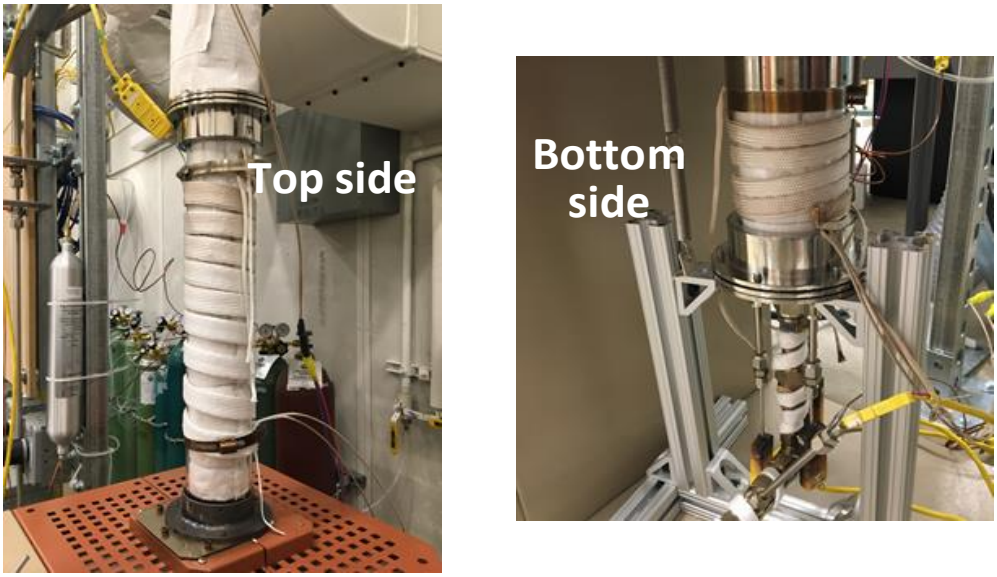

Figure 2-10 Tape heaters at top and bottom of quart tube (outer thermal insulation is removed for better view)

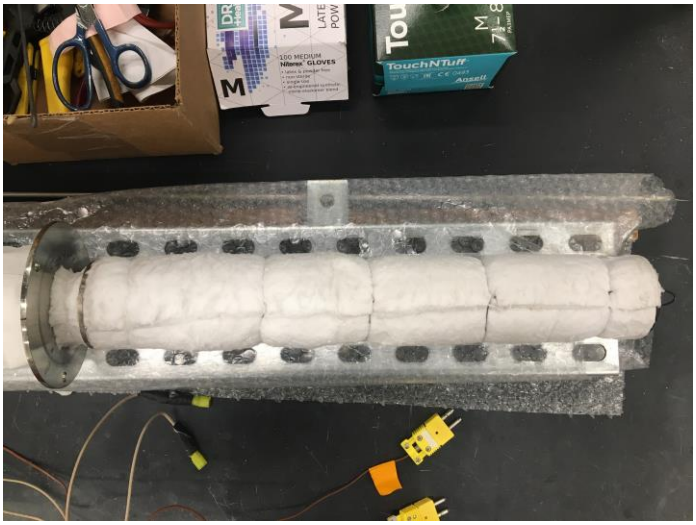

Figure 2-11 Outlet intrusion tube and thermal insulation

After the outlet of the quartz tube, a stream of gas mixture is introduced into the purification system to remove the remaining moisture. Otherwise the accumulation of moisture will damage the GC capillary glass columns. A three-stage moisture condenser first removes the bulk water

droplets. Then a moisture trap purifies the sampling gas further. Last, a moisture indicator ensures the moisture concentration is less than 50 ppb. In this way, the sampling entering the GC will be a mixture of helium and production gases CO and H_2. The gas purification system has a high pressure drop coefficient due to its small fillers. Therefore, the system pressure is lifted slightly to provide driving force for the sampling gas. The layout of graphite-steam oxidation test facility is shown in Figure 2-12.

Figure 2-12 Overall layout of graphite-steam oxidation test facility

2.2.3 Reaction temperature control and measurement

A computational fluid dynamics (CFD) simulation was performed to determine the best position for the graphite sample in the quartz tube. Figure 2-13 shows the setup of the CFD simulation. The highest reaction temperature in this research is 1100 °C, which is mainly limited by the operation limit of the furnace (1200 °C). Two extreme cases were simulated with 0 and 20% steam by mole mixed in helium, respectively. The inlet flow rates of the two cases are 15 SLPM. The pressure outlet is set as 0.124 MPa. Isothermal 1150 and 200 °C are applied to the surface of the heating section and the two thermal insulation sections, respectively. In the actual experiments, the gas mixture always consists of helium and steam, and sometimes contains a small fraction of hydrogen that does not obviously alter the thermal physical properties of gas mixture. Therefore, the thermal physical properties of the gas mixture can be calculated by regarding the gas mixture as a binary species mixture.

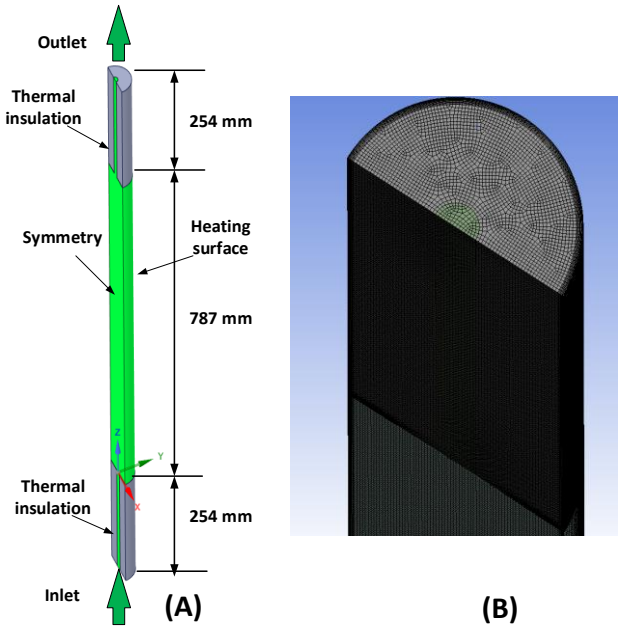

Figure 2-13 CFD simulation setup for tube furnace heating: (A) simulation domain and boundary conditions, and (B) mesh generation

In this simulation, the thermal physical properties of pure helium and steam are based on KTA correlations [56] and NIST data base [57], respectively. The dynamic viscosity and thermal conductivity of helium-steam mixture are calculated using Wilke formulas [58]:

$$\mu_{\text{mix}} = \sum_{i}^{n} \frac{x_i \mu_i}{\sum_{j=1}^{n} x_j \Phi_{i,j}}, \tag{2-1}$$

$$k_{\text{mix}} = \sum_{i}^{n} \frac{x_i k_i}{\sum_{j=1}^{n} x_j \Phi_{i,j}}, \tag{2-2}$$

$$\Phi_{i,j} = \frac{1}{\sqrt{8}} \left(1 + \frac{M_i}{M_j}\right)^{-\frac{1}{2}} \left(1 + \left(\frac{\mu_i}{\mu_j}\right)^{\frac{1}{2}} \left(\frac{M_j}{M_i}\right)^{\frac{1}{4}}\right)^2, \tag{2-3}$$

where:

n	number of chemical species
x_i, x_j	mole fraction of species i, j
μ_i, μ_j	dynamic viscosity of species i, j
k_i, k_j	thermal conductivity of species i, j
M_i, M_i	molar mas of species i, j.

The specific heat capacity at constant pressure is calculated by:

$$c_{p\text{mix}} = \sum_{i=1}^{n} \frac{x_i M_i}{\sum_{i=1}^{n} x_i M_i} c_{pi} \tag{2-4}$$

The simulated temperature distribution on the symmetric plane is depicted in Figure 2-14 for the two scenarios, which shows the temperature is not fully developed until to the upper half region of the quartz tube. Figure 2-15 depicts the simulated temperature of the gas mixture along the central axial line, which indicates the graphite specimen should be placed at height between 0.5 to 0.78 m. A radial temperature is then extracted from the two simulations, as shown in Figure 2-16. As can be seen, the partitioning of steam leads to non-uniform radial temperatures. However, the temperature difference along the radial direction can be negligible if the specimen is placed higher than 0.7 m, which is adopted in the experimental practice.

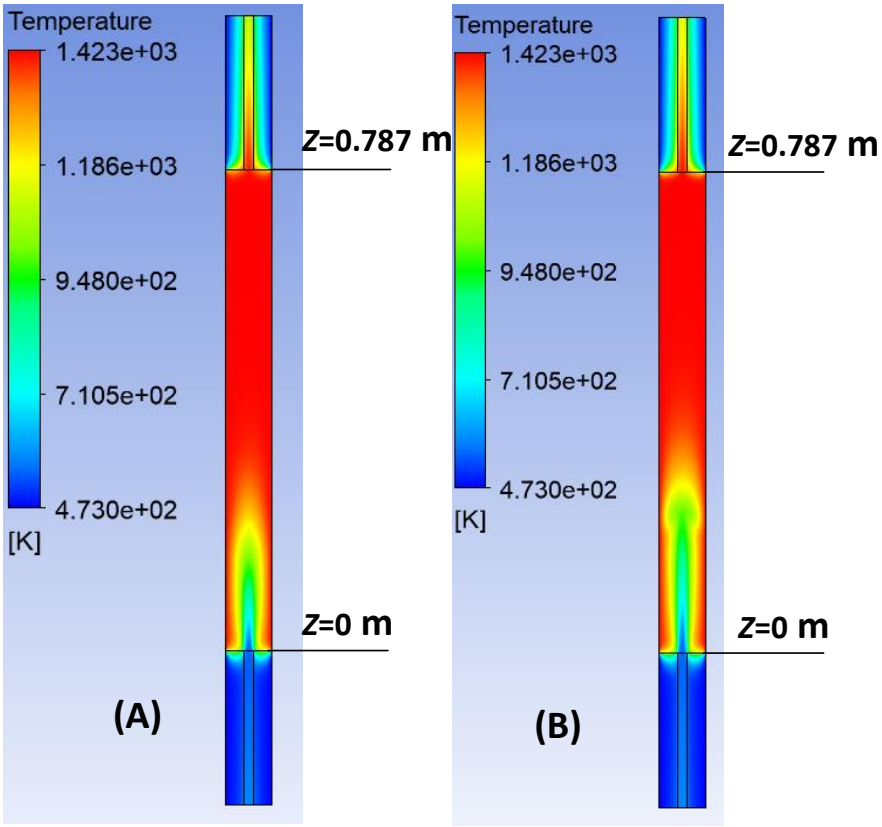

Figure 2-14 Simulated temperature distribution in quartz tube for: (A) pure helium, and (B) helium-steam mixture

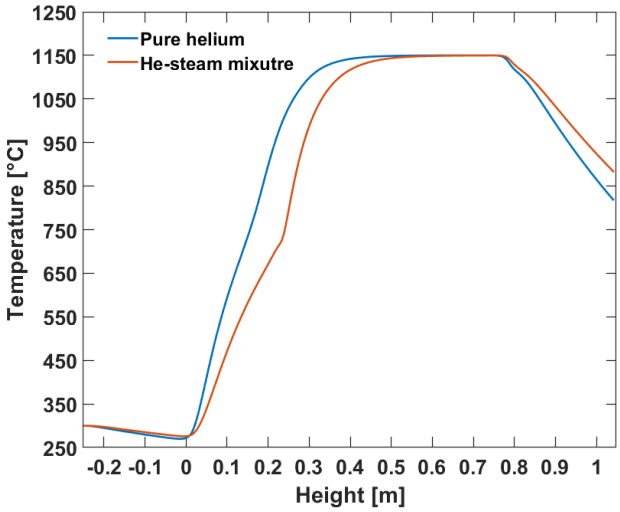

Figure 2-15 Simulated temperature along the central axil of the quartz tube

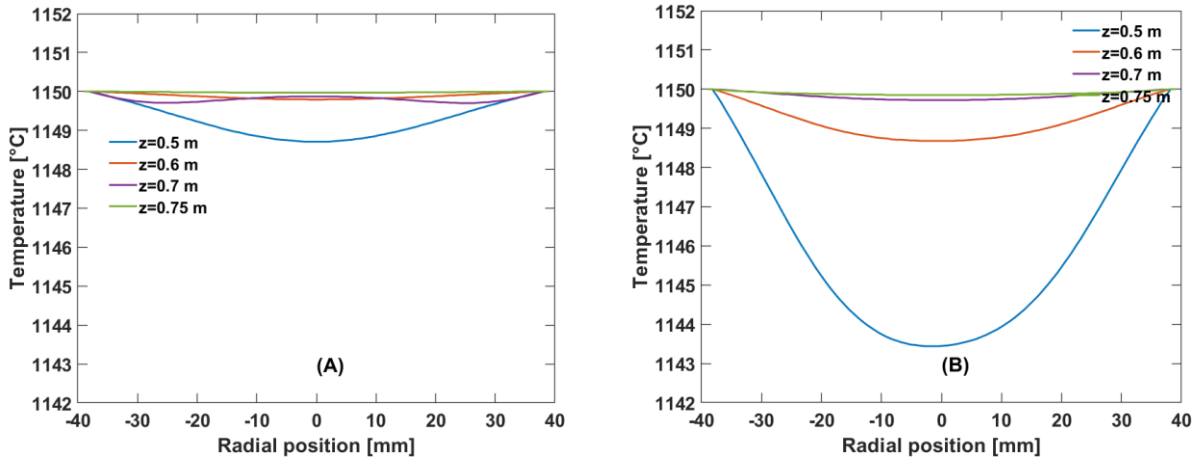

Figure 2-16 Simulated radial temperature distribution at different height for: (A) pure helium, and (B) helium-steam mixture

In the experiment, the reaction temperature is monitored by averaging the values from three K-type thermocouples surrounding the graphite sample. All three thermocouples were calibrated against resistive temperature detector (RTD) before they were installed into the system. The

comparison of TCs' value with RTD is depicted in Figure 2-17. The calibration equations for the three thermocouples are:

$$y = 0.9988x - 2.1183,\ R^2 = 1, \tag{2-5}$$

$$y = 0.9997x - 0.9317,\ R^2 = 1, \tag{2-6}$$

and

$$y = 1.0014x - 2.9058,\ R^2 = 1, \tag{2-7}$$

respectively. The calibration indicates negligible difference between the TCs and RTD results. The largest difference is less than 2.5 °C within a temperature range 100 to 950 °C.

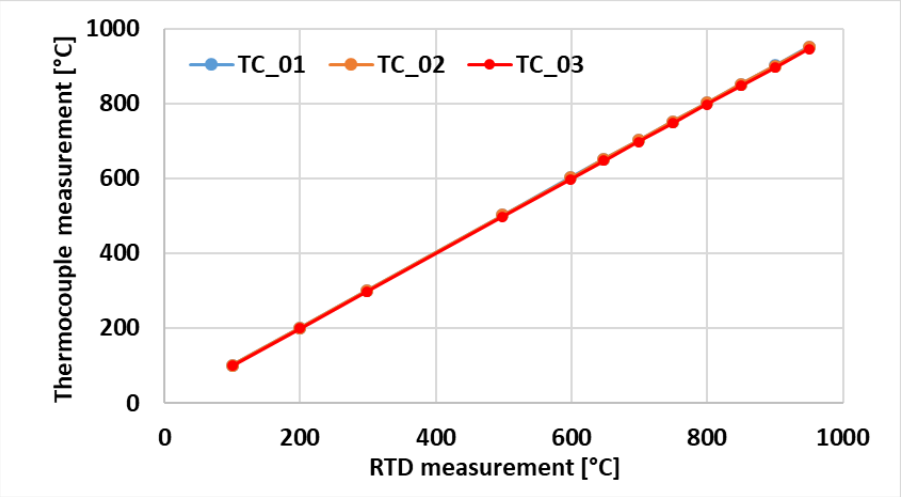

Figure 2-17 Calibration of thermocouple measurement against RTD

At high temperatures, thermal radiation plays an important role in heat transfer. The emissivity of graphite and TC sheath material may not be the same. As a consequence, the TC measurement might not represent the actual graphite temperature. However, it is know that the chemical reaction

rate behaves exponentially as a function of temperature. Therefore, it is necessary to quantify the difference between TC values and the actual graphite temperature.

A test was thereafter conducted using a cylindrical graphite sample. A 3/16 inch hole was drilled into the center of the sample from its bottom surface. This graphite sample is then anchored to the 1/8 inch thermocouple (TC-02) using the central hole. The setup of this test is shown in Figure 2-18. In this way, the thermal radiation between TC-02 and furnace heating elements is eliminated. In addition, the tip of TC-02 directly touches the graphite. Since the graphite-steam oxidation rate is very small, the endothermic reaction will not form an obvious heat sink, which means the temperature distribution in the graphite will be fairly uniform. Therefore, the temperature obtained by TC-02 can be regarded as the actual graphite temperature, which is compared with the other two TC measurement values.

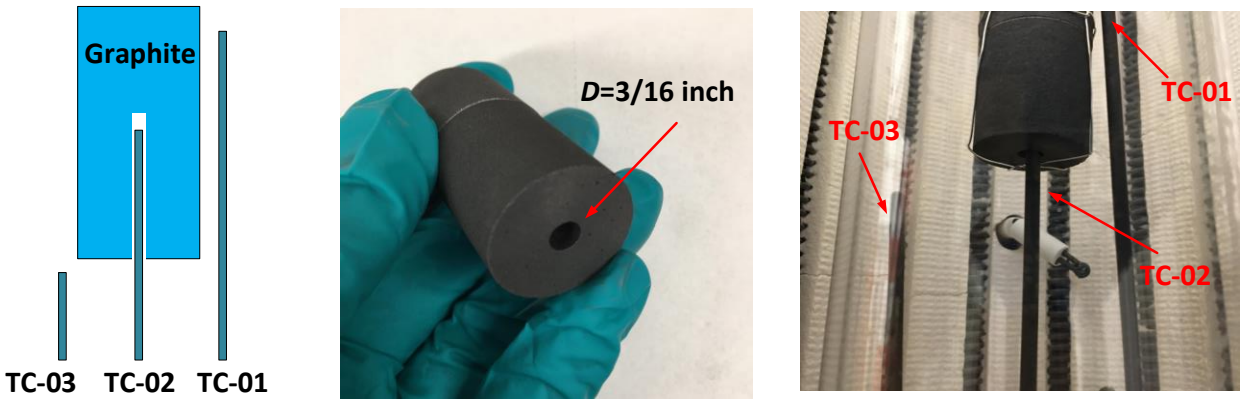

Figure 2-18 Experiment setup for verification of reaction temperature measurement

The measured temperature of the three TCs is shown in Figure 2-19 at different temperature levels. As shown in Figure 2-19, TC-03 shows the lowest temperature among the three measurements, which can be attributed to its lower position. The above CFD simulation indicates the temperature should be uniform at the sample location. In the numerical simulation, isothermal

condition was adopted for the tube surface, which is an ideal assumption. In reality, the furnace heating power is controlled by PID controllers and thereafter is not constant, which can affect the tube surface temperature slightly and periodically. However, the largest difference between the three TC measurements is less than 5 °C. Therefore, the temperature measured outside of graphite sample can be regarded as the actual graphite temperature.

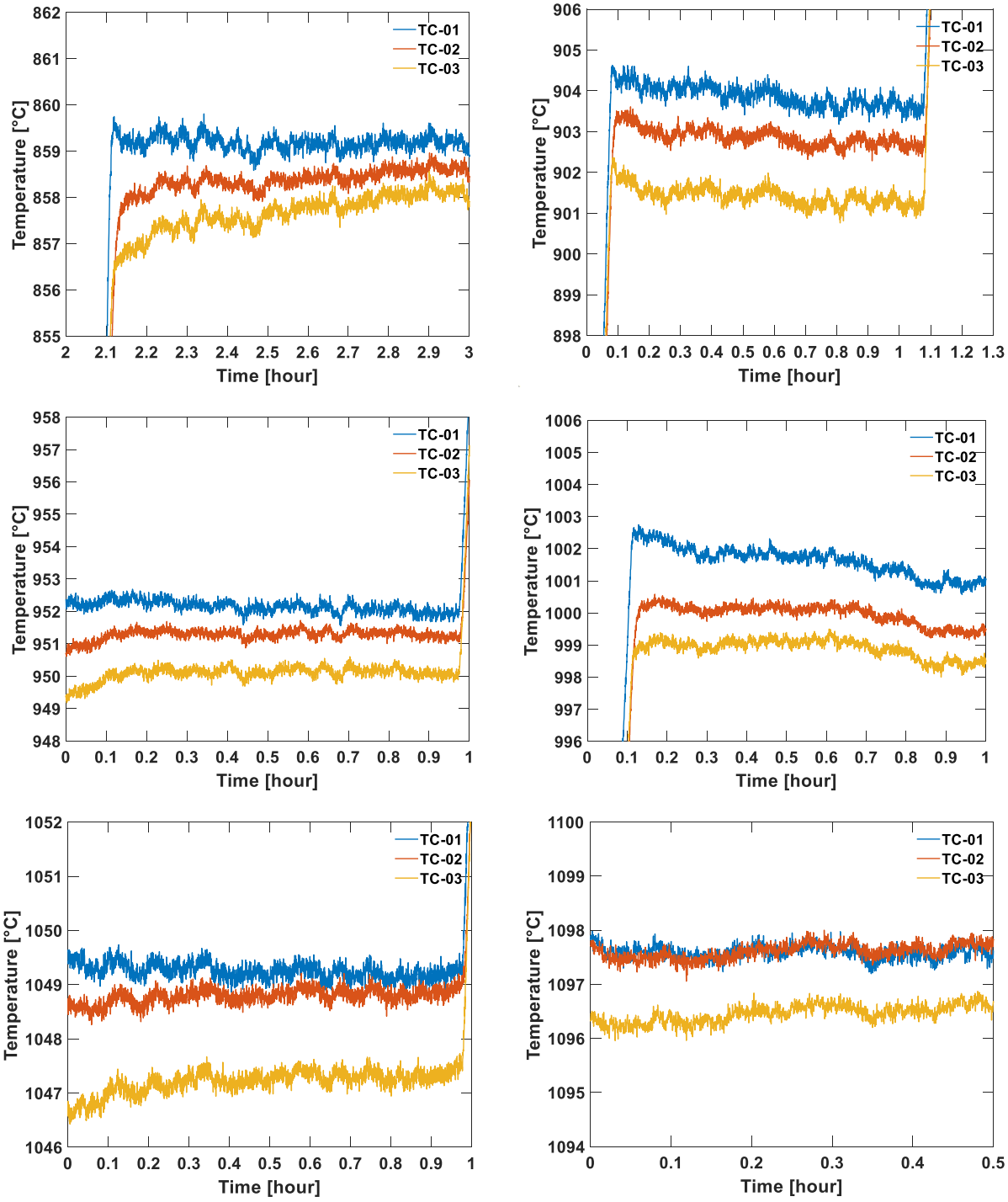

Figure 2-19 Temperature measurement inside and outside of graphite sample

2.3 Operation Procedure of Experiments

2.3.1 Experiment preparation

A standard operation procedure was programed to ensure the consistency of the experiments. The mass and dimension of the pristine graphite sample are first measured and recorded before loading into the tube furnace. Vinyl gloves are wearied whenever the sample is handled to avoid any contamination. After loading the graphite sample into the quartz tube, a leakage test is then performed to ensure no obvious leakage.

Next, the test facility is isolated by closing the valves at the inlet and outlet. A vacuum pump is started to withdraw the air in the test facility until a vacuum level about 30 Torr is reached. The vacuum is maintained for about 30 minutes to let the air trapped in the graphite sample to diffuse out. The test facility is then pressurized to about 1.24 bar (abs) using UHP helium. To minimize the quantity of remaining air, the vacuum and recharging process is repeated at least three times.

2.3.2 Measurement of graphite-steam oxidation rate

After the above preparation works, a stream of UHP helium is introduced into the test facility at flow rate of 3.0 SLPM. The needle valve at the disposal line is adjusted at the same time to stable the pressure in the test facility. Then the power of the furnace is turned on to increase the temperature at a rate of 8 °C/min, and the tape heaters on the heating tube are also turned on. A stream of sampling gases is then introduced into GC at flow rate of 0.2 SLPM. When the temperature in the quartz tube stabilizes at the target temperature, the flow rate of helium-hydrogen mixture is adjusted according to the test matrix. The needle valve at the outlet is adjusted to prevent the system from being over pressurized. At least three measurements are taken at the target temperature as background signal before injecting any deionized water. The background signal is

then deducted from the following measurements. The background signal mainly comes from the impurities of the UHP helium. Depending on the different helium batches, the background signal is slightly different.

Next, the peristaltic pump is turned on to inject liquid water. The rotation speed of the pump is determined according to its calibration. The sudden water participation will increase the system pressure. Therefore, the needle value is adjusted again to keep the system pressure at desired value. During the experiment, the water flow rate is recorded, as well as the system pressure and temperature. The GC can complete one analysis every about 12.5 minutes. The injection time of each sampling is automatically recorded, which is assumed to be the reaction time.

2.3.3 Experiment stopping procedure

The water injection was stopped first when the measurement is completed. The power of tube furnace and heating tube are maintained for about ten minutes to avoid any water accumulation in the facility, and then they are turned off. At the same time, the helium-hydrogen flow is stopped, and the flow rate of UHP helium is decreased to 3.0 SLPM. The needle valve on the disposal line is adjusted to keep a slightly pressurized condition. The UHP helium flow is maintained until the temperature in the quartz tube drops below 200 °C to avoid any graphite-oxygen reaction. The graphite sample is taken out after the facility is cooled down to environmental temperature. The post-oxidation mass and dimension of the sample are measured again.

Chapter 3 Experiments on Graphite-Steam Oxidation

3.1 Verification of Experimental Strategy

The graphite oxidation rate is measured using GC rather than mass balance scale, which means the reaction rate is not directly measured. In order to achieve a higher steam concentration, liquid water is heated into single-phase steam that mixes with helium. The instability of two phase flow might distort the system pressure if it is not well controlled. All these concerns should be addressed before starting the formal measurement.

3.1.1 Derivation of oxidation rate using GC signal

The principle of GC analysis has been discussed in Section 2.2.1. A calibration was performed at installation to ensure the GC works as expected. Before or after each experiment, the GC is calibrated again using another standard He-CO-CO_2 mixture to derive the oxidation rate and to ensure the GC works normally.

The concentrations of CO and CO_2 in this standard He-CO-CO_2 mixture are labeled as 24.87 (±5%) ppm and 53.57 (±2%) ppm by mole, respectively. One example of the calibration measurements is depicted in Figure 3-1. In this example the CO and CO_2 peaks appear at time of 6.089 and 8.856 minutes with areas of 70.66 and 149.91 pA·min, respectively. The ratio of the two peak area in the measurement is 2.12 while the label value is 2.15. Considering the uncertainty of the species concentration in the standard gas sample, it is safe to claim the accuracy of GC measurement is validated.

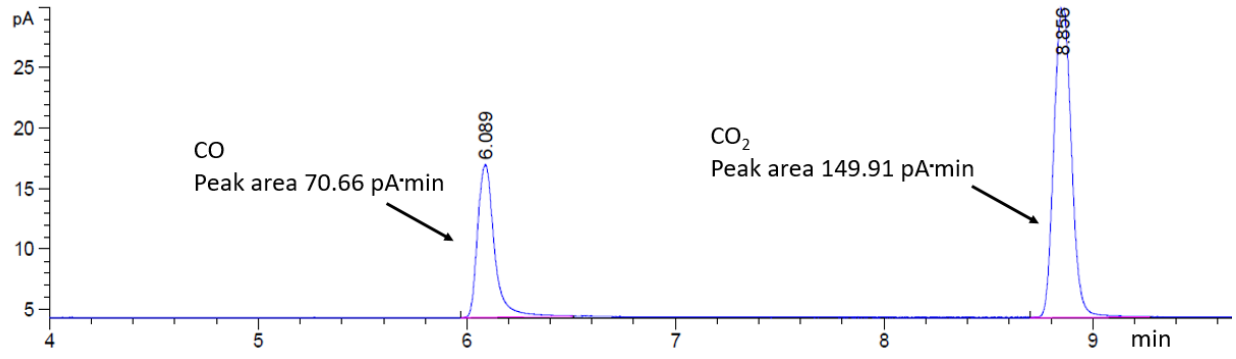

Figure 3-1 CO and CO_2 peaks obtained by GC using 0.2 SLPM standard gas sample

Next, the concentration of the production gases in the sampling mixture can be calculated using equation:

$$c_i = \frac{A_i}{A_{\text{st}}} \times c_{i,\text{st}}\,, \tag{3-1}$$

where subscript i represents a production gas species, such as CO or CO_2. Symbol c_i and $c_{i,\text{st}}$ indicate concentration of interested gas species by mole in the sampling gas and standard gas, respectively. A_i and $A_{i,\text{st}}$ are the corresponding peak areas. Theoretically, the CO_2 can also be used to calibrate CO because both molecules have only one carbon atom. Since the uncertainty of CO_2 in the standard gas sample is smaller, CO_2 is used as the reference in all of the following analyses.

Two oxidation rates are defined in this research. The first one is the apparent reaction rate, which is the observed total oxidation rate regardless the mass and dimension of the graphite specimen. The other one is named as specific oxidation rate, which is defined as the apparent oxidation rate divided by the pristine mass of the graphite sample. The specific oxidation rate is only valid when the graphite sample has a large surface-to-volume ratio. The two oxidation rates can be derived using the GC signal by:

$$Rate_{app}\,[\mathrm{g/s}]=1\times10^{-6}\,\frac{A_{sum}}{A_{sum,\,st}}\,c_{st}\,\frac{\left(V_{He}+V_{H_2}\right)P}{RT}\,M\ , \tag{3-2}$$

and

$$Rate_{spe}\,[1/s]=1\times10^{-6}\,\frac{A_{sum}}{A_{sum,st}}\,c_{st}\,\frac{\left(V_{He}+V_{H_2}\right)P}{RT}\,\frac{M}{m_0} \tag{3-3}$$

respectively, where:

A_{sum}	sum of peak areas for sampling gas,	pA·min
$A_{sum,\,st}$	sum of peak areas for standard gas ,	pA·min
$A_{s,\,CO_2}$	peak area of CO_2 for standard gas,	pA·min
c_{st}	mole concentration of CO_2 in standard gas sample,	ppm
V_{He}	volumetric flow rate of helium under SPT condition,	SLPM
V_{H_2}	volumetric flow rate of hydrogen under SPT condition,	SLPM
P	system pressure in quartz tube,	Pa
R	specific ideal gas constant,	J/K/mol
T	temperature,	K
M	mole mass of carbon,	g/mol
m_0	mass of graphite sample before oxidation,	g.

It should be note the underlying assumption behind Eqs. (3-2) and (3-3) is the generation rate of CO and CO_2 is negligible compared with the inlet gas flow rate. This assumption is later

confirmed in the experiments, which demonstrate the CO and CO_2 concentrations at the furnace outlet are only a few hundred ppm at maximum.

The data collection frequency of the GC is about 5/ hour, which is determined by the length of the HP-PLOT columns and the allowed maximum flow velocity in it. Therefore, the obtained graphite oxidation rates are a series of separate points. The total graphite mass loss in the oxidizing experiment can be calculated by Eq. (3-5):

$$\triangle m_{\mathrm{GC}} \approx \sum_{1}^{N}\left(\frac{Rate_{\mathrm{app}}(j-1)+Rate_{\mathrm{app}}(j)}{2}\right)\Delta t_{j-1,j} \tag{3-5}$$

where:

$\triangle m_{\mathrm{GC}}$	mass loss based on GC signal	g
N	total number of measurements	--
$\Delta t_{j-1,j}$	time interval between j-1 and j th measurement	s

The mass of graphite sample is measured using a mass balance scale before and after each experiment, which gives another mass loss value $\triangle m_{\mathrm{MB}}$. Ideally, the value of $\triangle m_{\mathrm{GC}}$ should be equal, or close to $\triangle m_{\mathrm{MB}}$.

3.1.2 Verification of GC measurement

A name convention is defined to present the experimental condition for each test, which is also adopted in the following chapters. The experiments are named as Tα-PWβ-PHγ-Heδ, in which T, PW, PH, and He represent reaction temperature in °C, partial pressure of steam in Pa, partial pressure of hydrogen in Pa, and volumetric flow rate of carrier helium in SLPM, respectively. The Greek letters represent their associated values.

Four experiments were first conducted to verify the theory in Section 3.1.1. The experimental conditions of these four tests are summarized in Table 3-1. It should be noted $V_{H_2O,\,l}$ in Table 3-1 indicates flow rate of liquid water. Thin graphite disks, as received from Toyo Tanso, are used in these experiments. The dimeter and thickness of these specimen are 30 and 2 mm, respectively. A small hole of 3 mm is left at the specimen center for Pt wire holder. A comparison of these four oxidized specimen with a pristine graphite sample is shown in Figure 3-9.

Table 3-1. Summary of test conditions

Test No.	**Test name**	**Temperature [°C]**	**Pressure [bar]**	V_{He} **[SLPM]**	$V_{H_2O,\,l}$ **[ml/min]**
A	T1002-PW15796-PH0-He15	1001.7	1.337±0.055	15±0.37	1.36±0.04
B	T1002-PW16000-PH0-He10	1002.2	1.335±0.055	10±0.18	0.92±0.02
C	T1002-PW16214-PH0-He5	1001.5	1.338±0.055	5±0.06	0.47±0.13
D	T1000-PW17213-PH0-He5	999.9	1.348±0.055	5±0.06	0.50±0.03

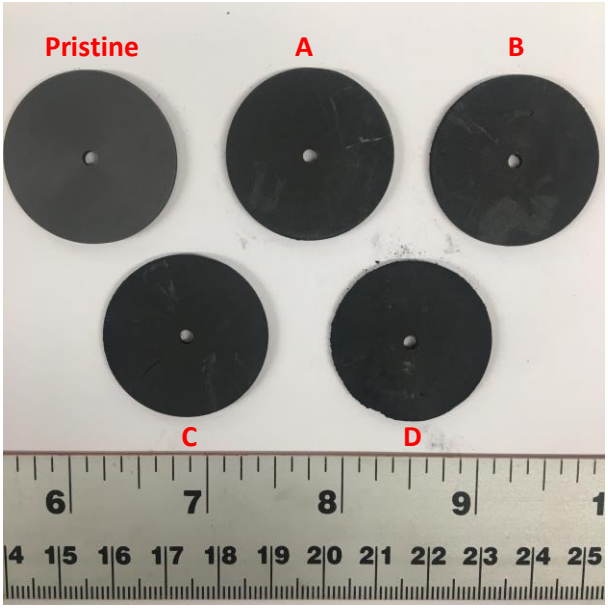

Figure 3-2 Comparison of oxidized and pristine graphite specimen

The system pressure and reaction temperature are depicted in Figure 3-3 to Figure 3-6 for the four experiments. It can be seen that the reaction temperature (mean value of the three TCs measurements) in the whole experimental process is controlled fairly stable, which fluctuates within about 1 °C. However, the system pressure can fluctuates by over 4000 Pa. In test T1002-PW15796-PH0-He15 and T1002-PW16000-PH0-He10, low frequency and high frequency pressure fluctuations are observed. The high frequency fluctuation, which has smaller magnitude, is believed to be induced by the instability of two phase flow in the heating tube, which can be challenging to be eliminated totally. The reason for the low frequency fluctuation remains unclear. A possible reason is the periodic blockage of condensed water at the outlet needle valve.

In test T1000-PW16000-PH0-He5, the frequency of pressure fluctuation is obvious different from the other three experiments, in which magnitude of high frequency fluctuation is larger. The sudden pressure drop at about 6.8 hours was caused by adjusting the outlet needle valve manually. After trouble shooting, it was found a section of heating tube near the quartz tube is not well insulated. The heat loss there might induce steam condensation. After replacing the thermal insulation, and increasing heating power of the tape heaters, the system pressure stability was improved significantly, which can be seen from test T1000-PW17213-PH0-He5. In general, the system pressure is controlled well, with fluctuations less than 4% although occasional pressure shock can occur.

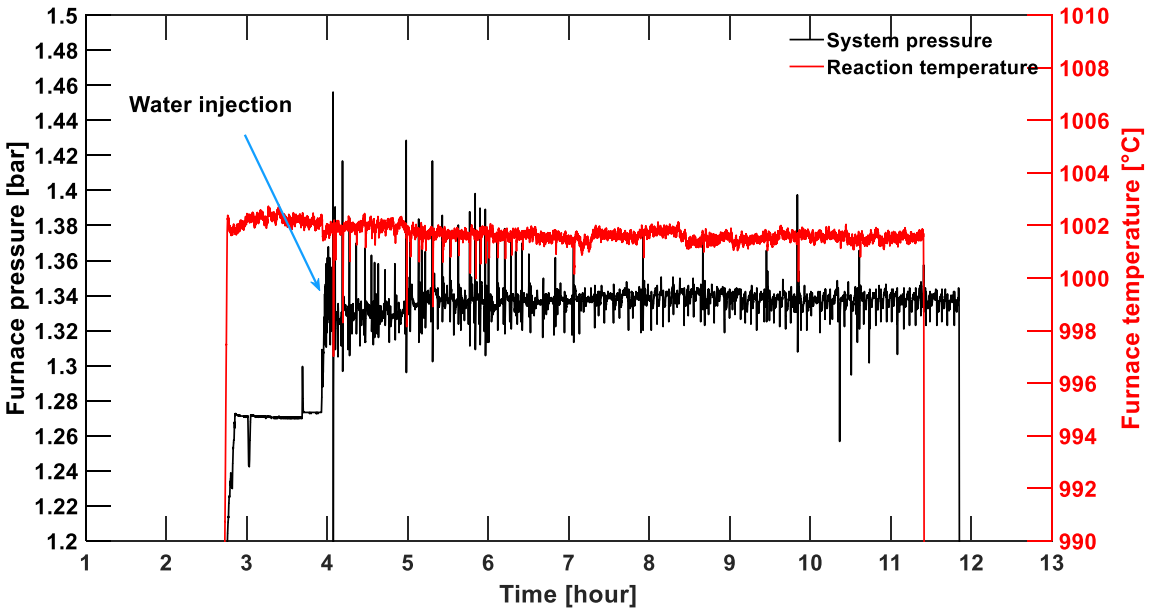

Figure 3-3 System pressure and temperature for test T1002-PW15796-PH0-He15

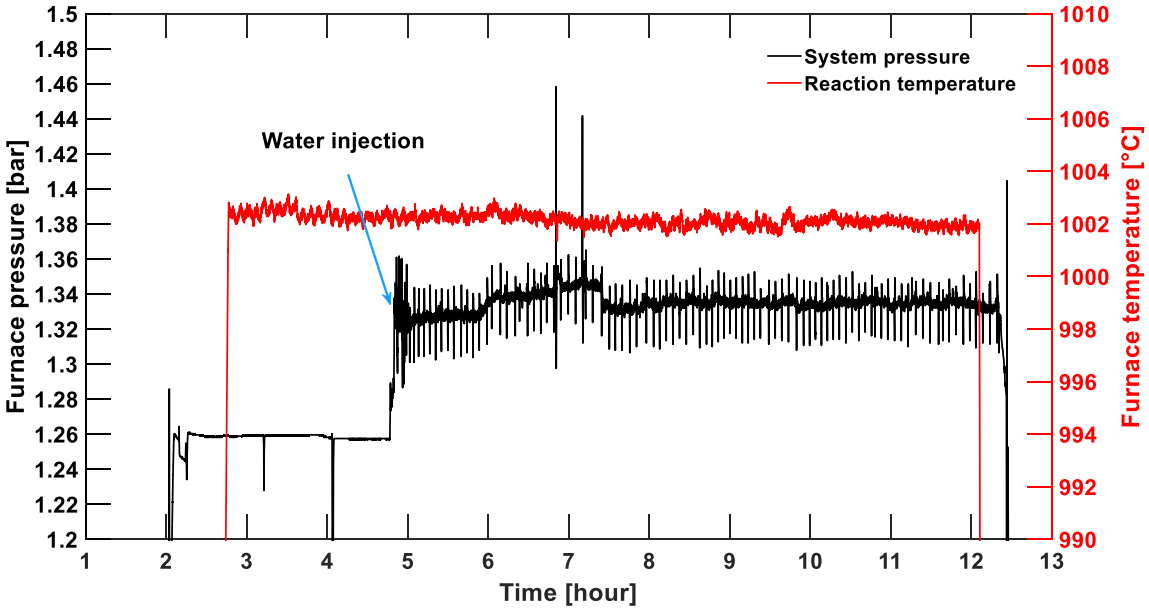

Figure 3-4 System pressure and temperature for test T1002-PW16000-PH0-He10

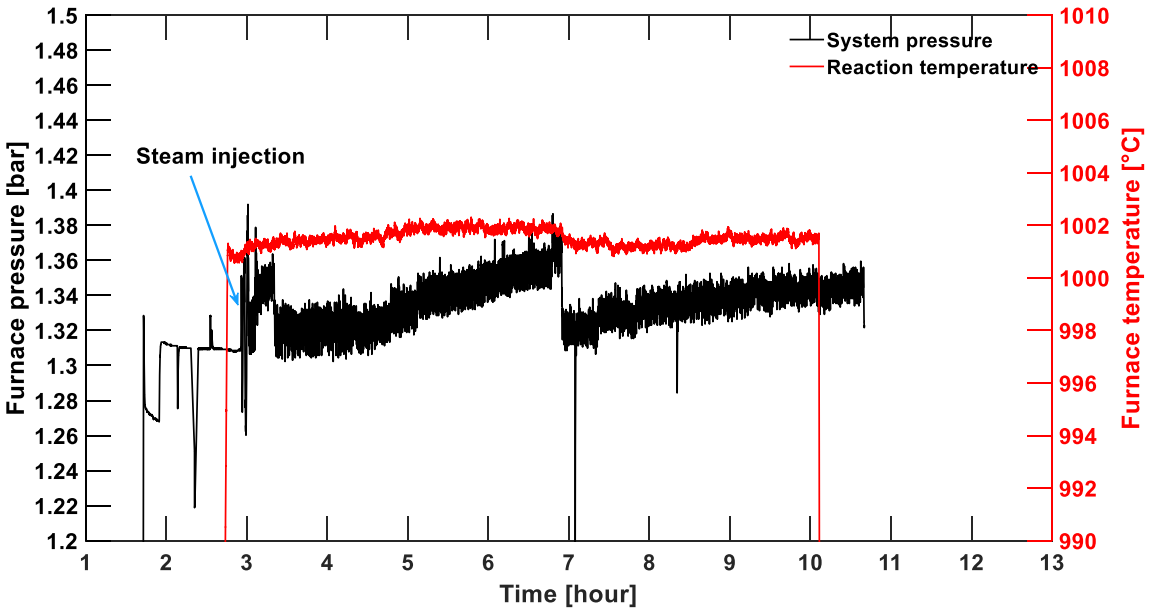

Figure 3-5 System pressure and temperature for test T1002-PW16214-PH0-He5

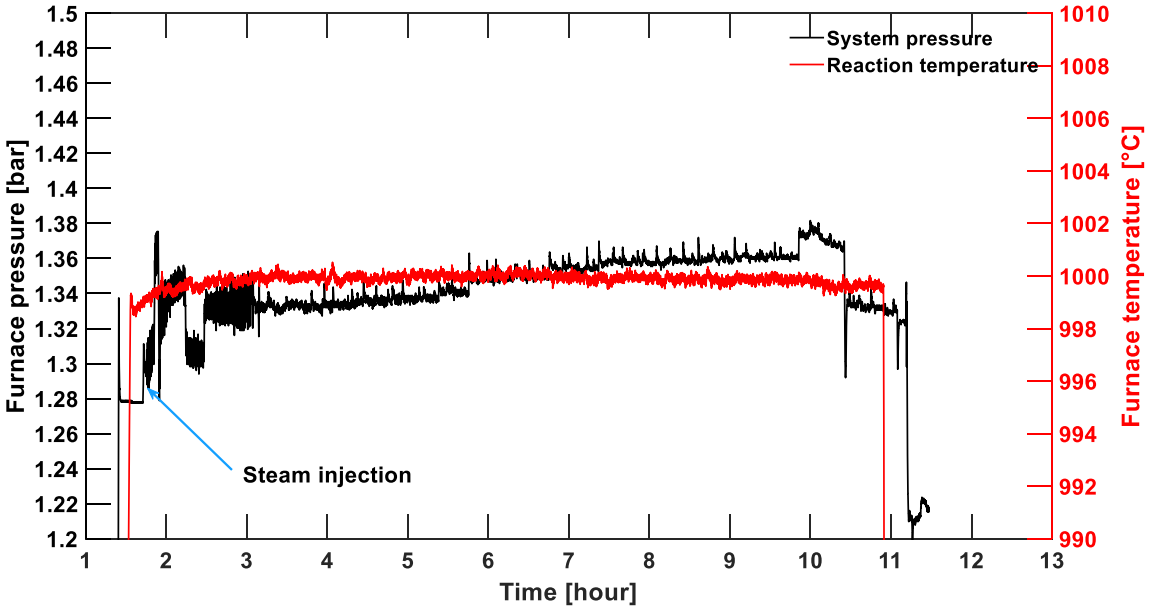

Figure 3-6 System pressure and temperature for test T1000-PW17213-PH0-He5

The apparent reaction rate of these four experiments are depicted in Figure 3-7. The oxidation rate of the first two experiments almost overlaps for the first four hours, which confirms the

oxidation rate is independent to the carrier gas flow rate within helium flow rate 10 to 15 SLPM. However, they tends to divert slight after five hours oxidation. The oxidation rate of test C fluctuates over a wide range, which can be attributed to the instability of the system pressure which has been shown in Figure 3-5. This phenomenon indicates the future experimental data should be carefully reviewed if flow instability is observed. Due to the higher steam partial pressure in test T1000-PW17213-PH0-He5, its oxidation rate is obviously higher than the other three cases.

Applying Eq. (3-5) to Figure 3-7, the graphite mass loss can be calculated, which is listed in Table 3-2. Among the four tests, Case A shows the largest difference when compared with mass balance scale measurement. The mass loss obtained by GC is slightly smaller than that of mass balance scale measurement for test A and D. In these two tests, the GC was stopped once water injection was ceased. However, the graphite oxidation could continue for a few seconds due to the remaining moisture in the test facility. These extra oxidation information was lost in these two tests. In general, the difference is acceptable, which confirms the oxidation rate measured by GC is reliable.

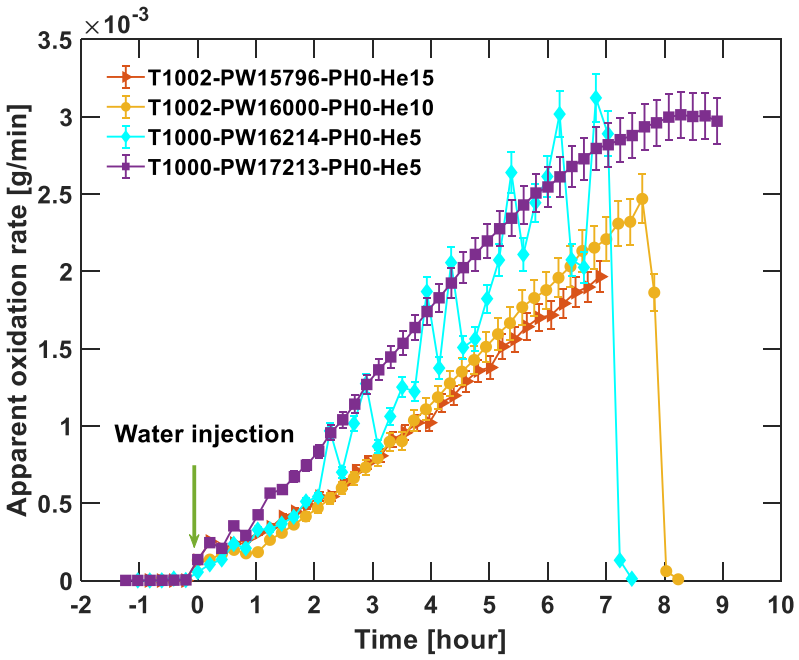

Figure 3-7 Evolution of apparent oxidation rates

Table 3-2. Comparison of mass loss measurement by mass balance and GC signal

Test No.	**Pristine mass [g]**	**Δm_{MB} [g]**	**Δm_{GC} [g]**	**Difference [--]**
A	2.510±0.002	0.424	0.396	-6.6%
B	2.514±0.002	0.543	0.557	+2.6%
C	2.521±0.002	0.568	0.583	+2.6%
D	2.518±0.002	0.970	0.934	-3.7%

One obvious trend observed from Figure 3-7 is the oxidation rate increases as the reaction proceeds. This phenomenon is induced by the expansion of micro pores and the opening of original isolated pores. An investigation of oxidation rate evolution is discussed in Section 3.3.

3.1.3 Uncertainty analysis for graphite-steam oxidation rate measurement

According to Eqs. (3-2) and (3-3), the systematic uncertainty source of apparent oxidation rate measurement comes from the integration of GC signal peaks, the uncertainty of CO_2 in standard

gas sample, the volumetric flow rate of helium, hydrogen, the measurement of reaction temperature, and system pressure. The specific reaction rate has another uncertainty source coming from the measurement of pristine graphite sample mass.

The uncertainty in GC peak integration can be automatically canceled if the same integration method, e.g., slope sensitivity, signal trial trim, and height rejection, is applied to both calibration and experimental measurements. As discussed in Section 3.1.1, CO_2-is used as a reference due to its lower uncertainty value (±2%).

The two mass controllers have different uncertainty values. A mass controller with full range of 50.00 SLPM is primarily used to control the carrier helium flow, while a stream of helium-hydrogen mixture is controlled by another 10 SLPM controller. The two mass controllers were calibrated at the factory, which proves their uncertainties are within ±0.8% reading plus ±0.2% full scale. The uncertainty of pressure transducer is ±0.5% of its full scale 1.1 MPa. The mass of graphite sample is measured by an Intelligent PM300 milligram balance scale with accuracy of ±0.002 g.

According to the thermocouple calibration results, the uncertainties of the three thermocouples are 0.33%, 0.12%, and 0.15%, respectively. The reaction temperature is calculated by averaging the values of these three thermocouples. Therefore, the variance in temperature measurement can be calculated by Eq. (3-6):

$$\left(\frac{\sigma}{T}\right)^2 = \frac{1}{9}\left[\left(\frac{\sigma_{T_1}}{T_1}\right)^2 + \left(\frac{\sigma_{T_2}}{T_3}\right)^2 + \left(\frac{\sigma_{T_3}}{T_3}\right)^2\right] + ... \\ \frac{2}{9}\left[\left(\frac{\sigma_{T_1}}{T_1}\right)\left(\frac{\sigma_{T_2}}{T_3}\right) + \left(\frac{\sigma_{T_2}}{T_3}\right)\left(\frac{\sigma_{T_3}}{T_3}\right) + \left(\frac{\sigma_{T_1}}{T_1}\right)\left(\frac{\sigma_{T_3}}{T_3}\right)\right], \tag{3-6}$$

which is 0.2%. Therefore, the systematic uncertainty associated with apparent and specific reaction rates measurement are:

$$\left(\frac{\sigma}{Rate_{\text{abs}}}\right)^2=\left(\frac{\sigma_{\text{CO}_2}}{c_{\text{CO}_2}}\right)^2+\left(\frac{\sigma_V}{V}\right)^2+\left(\frac{\sigma_T}{T}\right)^2+\left(\frac{\sigma_P}{P}\right)^2, \tag{3-7}$$

and

$$\left(\frac{\sigma}{Rate_{\text{spe}}}\right)^2=\left(\frac{\sigma_{\text{CO}_2}}{c_{\text{CO}_2}}\right)^2+\left(\frac{\sigma_V}{V}\right)^2+\left(\frac{\sigma_T}{T}\right)^2+\left(\frac{\sigma_P}{P}\right)^2+\left(\frac{\sigma_m}{m_0}\right)^2, \tag{3-8}$$

respectively.

Another uncertainty that is not stated above comes from gas mixture leakage. Depending on the position of the leakages, its effect on oxidation rate measurement can be different. The leakage will not affect oxidation rate measurement if the ratio of absolute leakage rate of each gas species is the same as the ratio of species concentration. But it is believed that helium has a higher leakage rate due to its smaller molecule size and larger diffusion coefficient. Under this circumstance, the gas leakage will affect the measured reaction rate differently depending on the leakage positions. Five most possible leakage scenarios are summarized, and Figure 3-8 is used to distinguish the different scenarios:

(A) The leakage appears before the graphite sample (before point A): It does not affect the oxidation rate measurement. But the actual partial pressure of moisture/hydrogen will be higher than the pre-setting values.

(B) The leakage occurs after passing the sample and before entering the sampling line (between B and C): the production gas concentrations entering the GC are higher than actual values, which leads to overestimated oxidation rate.

(C) The leakage occurs in the sampling line (between C and GC): the production gas concentrations entering the GC are higher than actual values, which leads to overestimated oxidation rate. Compared with case (B), it can induce a higher distortion.

(D) The leakage occurs on disposal line (between C and disposal): the leakage does not affect the oxidation rate measurement.

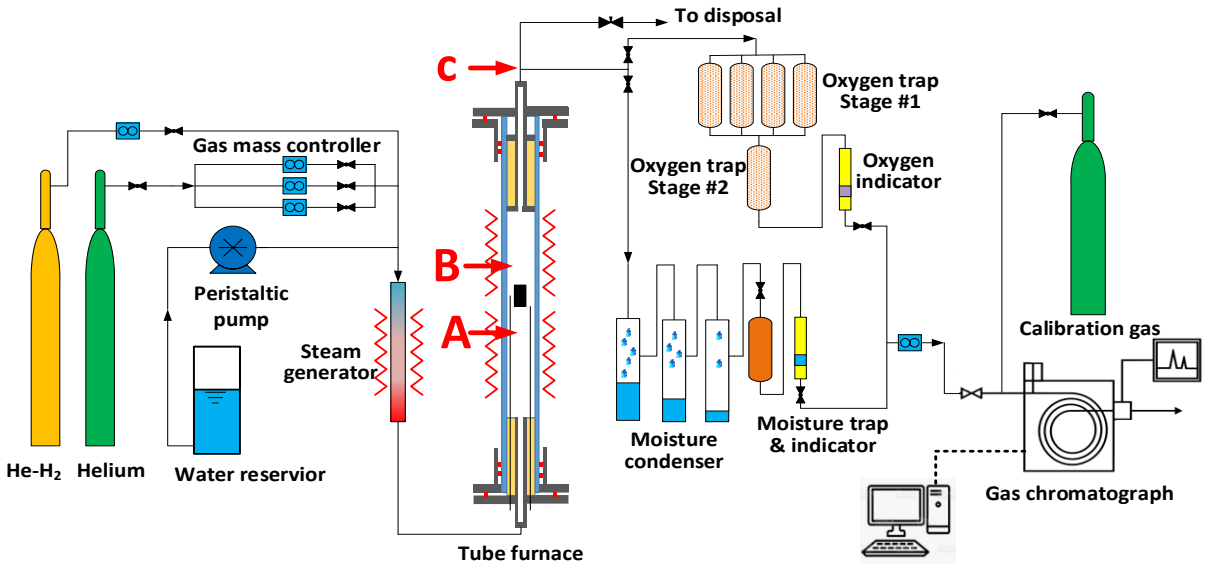

Figure 3-8 Schematic of test facility to show possible helium leakage positions

Before each experiment, a leakage test at cold state is run to ensure that the test facility is well sealed. An example of cold leakage test is depicted in Figure 3-9(A). The absolute pressure drops from 19 to 17 psia within about 177.7 min. The total volume of the test facility is about 7.01 L. Accordingly, the leakage rate is about 0.0027 SLPM. At lifted temperature, the leakage rate is

increased because the gas diffusion coefficient is proportional to $T^{3/2}$. Figure 3-9(B) shows a leakage test at furnace temperature of 1000 °C, which has leakage rate about 0.033 SLPM. A helium detector is used to find the dominant leakage positions, which shows helium mainly leaks from the rubber O-ring sealings. However, it is very challenging, if not infeasible, to monitor the leakage rate of each gas species at each position during the experiment. In generaly, the leakage rate is only about 0.22% to 0.5% of total inlet helium flow. Therefore, the uncertianty caused by gas leakage is not considered.

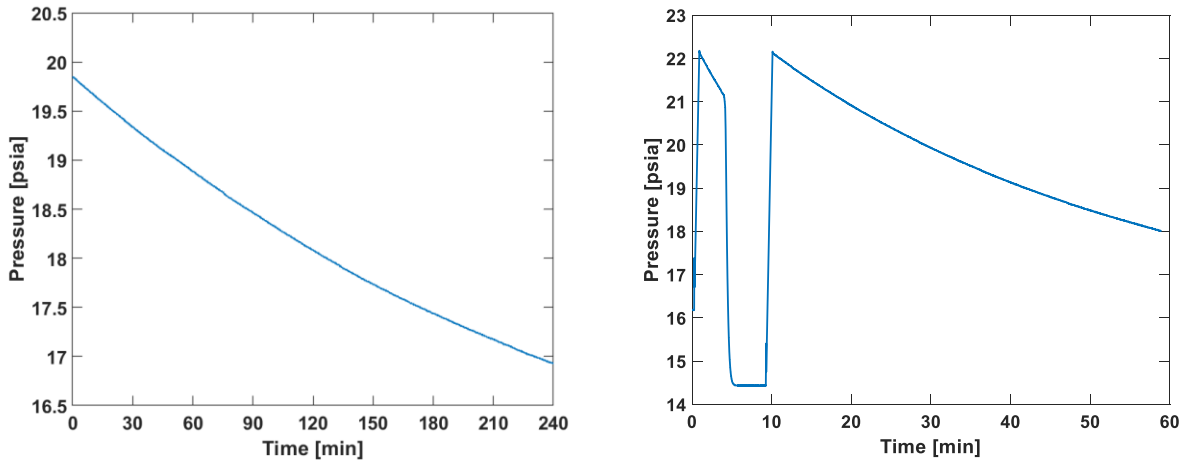

(A) (B)

Figure 3-9 Leakage test of graphite oxidation test facility at: (A) environmental temperature, and (B) furnace temerature of 1000 °C and heating tube surface temperature of about 350°C

3.2 Experiments of Kinetic Graphite-Steam Oxidation

3.2.1 Summary of experimental conditions

The objective of this section is to experimentally investigate the kinetic graphite-steam oxidation rate under various conditions. In existing literature, the partial pressure of moisture in the gas mixture flow is about 100 to 2,000 Pa. However, this moisture partial pressure is not large

enough to cover a steam ingress accident. Therefore, the experimental work here will mainly focus on higher steam concentrations. In addition, the effect of hydrogen on suppressing the graphite-steam oxidation will also be studied. The reaction temperature in this section varies from about 850 to 1100 °C with 50 °C intervals. The system pressure is controlled at about 1.24 bar. In order to achieve different steam and hydrogen partial pressures, the flow rate of UHP helium and hydrogen, and the rotation speed of the peristaltic pump were set at different values. In actual practice, the partial pressure of steam varies between 0.5 to 20 kPa, while the hydrogen partial pressure mainly varies from 0 to 2,000 Pa.

It is desired to eliminate the effects of mass transfer in these kinetic reaction experiments. Therefore, a large surface-to-volume ratio is preferred for graphite samples. For most experiments conducted in this section, round shape IG-110 disks as received from Toyo Tanso were used. These graphite samples have been shown in Figure 3-2. In addition, a few samples were cut from a larger IG-110 rod. The small graphite pieces were then polished using grade 1500 sand film and cleaned in deionized water using an ultrasonic cleaner. Then, they were baked at temperature of 200 °C for 12 hours to remove the absorbed water. Figure 3-10 shows two of the lab-cut samples. These samples were only used for experiments with reaction temperature about 850 and 1100 °C.

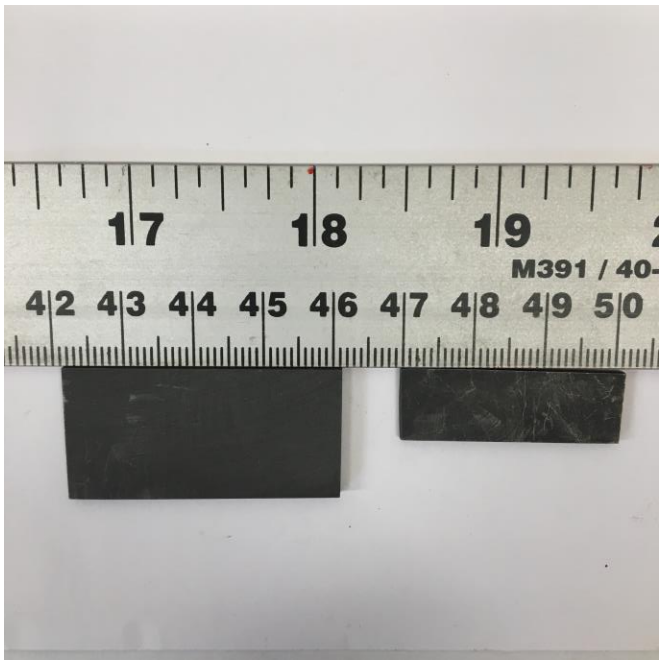

Figure 3-10 Lab-cut IG-110 graphite specimen

These lab-cut specimen are in rectangular shape with different dimensions. The thickness of these specimen varies from about 1 to 4 mm with mass varying from about 0.5 to 15 g. For reaction temperature lower than 900 °C, the oxidation rate is so small that a larger graphite sample (thickness of about 4 mm) is used to generate enough CO and CO_2 to be detectable. Under low reaction temperature, the apparent oxidation is limited by kinetic reaction rate. Therefore, the reaction can be regarded as uniform over the whole sample volume. For reaction temperature of 1100 °C, lab-cut thin specimen (thickness about 1 mm) were used so that the effect of mass transfer can be minimized. In addition, taking the advantage of small sample mass, the total amount of CO and CO_2 in the sampling line can be reduced, which helps to mitigate the GC signal tail.

3.2.2 Data reduction due to local accelerated oxidation sites

In some of the experiments, abnormal high oxidation rates were observed after water injection. In these experiments, local accelerated oxidation spots were found on the graphite sample surface, as shown in Figure 3-11 and Figure 3-12. Whenever this phenomenon occurred, the measured oxidation rate does not reflect the kinetic oxidation rate anymore. Therefore, the data were rejected. However, it is worth to examine the reason behind this phenomenon as it might also happen to a nuclear reactor. After reviewing these experiments, it was found these abnormal phenomenon only happens to tests with low steam concentration, i.e, less than 2 kPa.

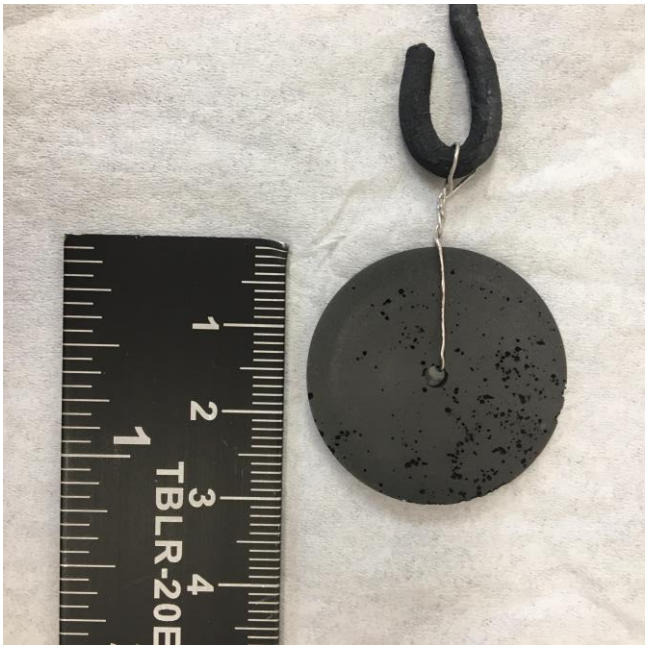

Figure 3-11 Graphite sample with lcoal oxidization spots

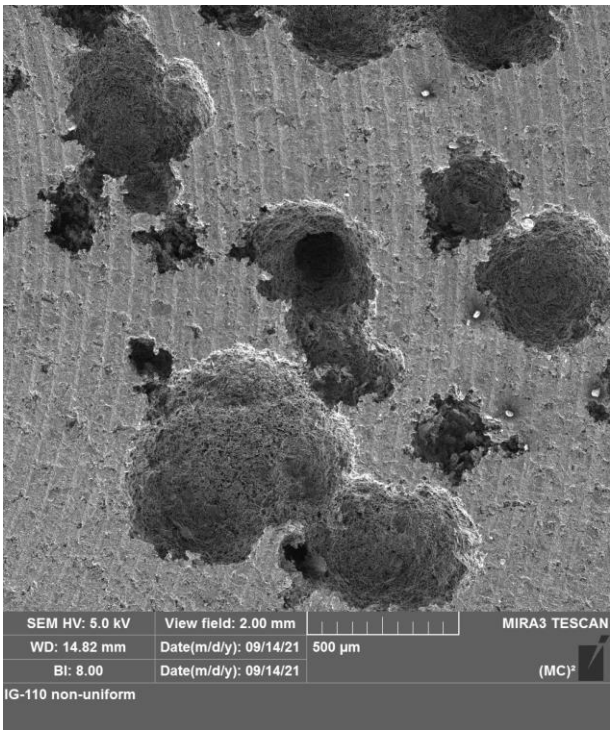

Figure 3-12 SEM image of local oxidation spots

Two assumptions are proposed to explain this phenomenon. First, these heavy oxidized sites are caused by metal particles. Although only Pt wire directly touches the graphite sample during an experiment, there are stainless steel 316 (SS316) components in the quartz tube, i.e., the upper and lower thermal insulation holder. As shown in Figure 3-13, the high temperature environment has turned the holder surface into black color after a few experiments. In addition, the Pt wire is connected to a SS316 hook that is then connected to the upper thermal insulation holder. The SS316 hook can also be oxidized in high temperature environment. The oxidized metal particles might peel off and land on the graphite surface, which then catalyzes the graphite-steam oxidation. The SS316 component at the lower side of quartz tube was not obviously oxidized due to its lower temperature. In order to minimize this consequence, the SS316 hook was later replaced by a Pt

wire. However, the abnormal high oxidation rate still exists for low steam partial pressure experiments.

Figure 3-13 Thermal insulation holder on the oulet intrusion tube

In order to verify if these spots were induced by stainless steel particles, an experiment was performed by loading a specimen horizontally into the quartz tube. In this way, the metal particles, if any, drop on the upper face of the sample, it will stay there and keep catalyzing the reaction. On the contrary, the lower face of the sample cannot hold those particles. Figure 3-14 shows the upper and lower faces of the graphite sample after oxidation. The sample shows local oxidized spots on its both faces. Therefore, it cannot be concluded if these spots are caused by metal catalyzers. An energy disperse spectroscopy (EDS) analysis is suggested to analyze the chemical elements of these spots in the future.

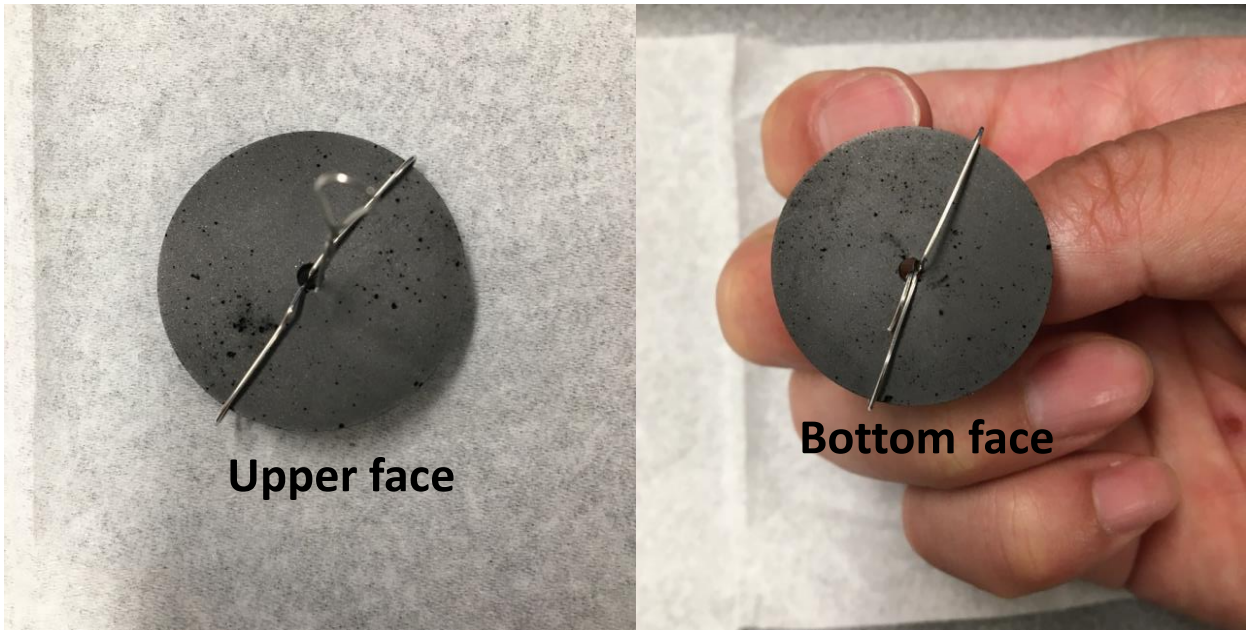

Figure 3-14 Comparision of upper and bottom face of an ununiformly oxidized sample

A second assumption is these accelerated oxidization sites are related to the two-phase flow in the heating tube. In the experiment, the liquid water is injected through a 1/16 inch tube into the heating tube horizontally, as shown in Figure 3-15. A small gap between the injection tube and the main tube inner surface is desired in order to prevent the liquid water forming droplets at the injection point. On the other hand, the gap cannot be too small. Otherwise, the injection channel will be blocked when tightening the compression fitting. Therefore, a gap less than 1 mm is left there.

For experiments with low steam concentrations, e.g., steam partial pressure of 500 Pa at 950 °C, the liquid water flow rate should be about 0.045 ml/min if the flow rate of carrier helium is set as 15 SLPM. Under this circumstance, the liquid water might still form droplets at the tip of the injection tube due to its small flow rate. The water droplet grows up gradually until the surface tension cannot hold up its own gravity and the helium flow shear stress. After that, the water

droplet will be carried away by helium and break up into smaller droplets. If these small droplets are not converted into steam thoroughly, they might hit the high temperature graphite sample directly, and be quickly heated up into steam at the graphite surface. As a result, a local high steam concentration spot appears, which then leads to higher oxidation rate.

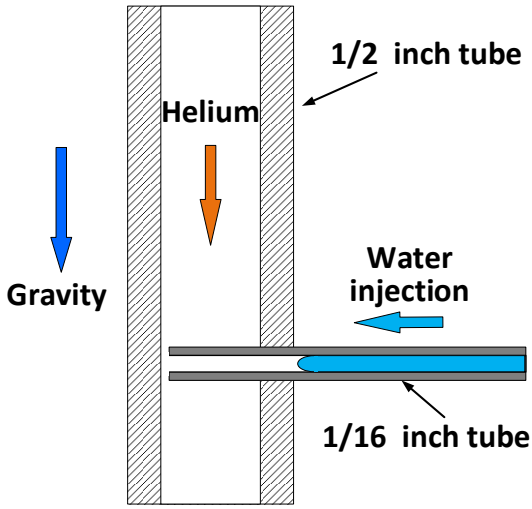

Figure 3-15 Diagram of water injection into the heating tube

In addition, it was found these accelerated oxidation sites can be avoided by introducing a high steam partial pressure for several seconds before switching back to the targeted low pressure settings. Nevertheless, the mechanism remains unclear. Although this research has not validated the above two assumptions, it points out two research topics for nuclear graphite oxidation behavior in an HTGR. It has been proposed the graphite-moisture oxidation will mainly occur at the hot plenum and active core outlet during reactor normal operations [46]. Nevertheless, if the first assumption was true, special attention should be paid to the locations where graphite directly touches metal components. If a postulated steam/water ingress accident occurs, the secondary moisture can enter the primary side as super-heated steam, water-steam mixture, or subcooled

water depending on different locations of the break. If the second assumption is confirmed later, the future analyses should cover a scenario of graphite oxidation by liquid water droplets.

3.2.3 Effects of reaction temperature on kinetic oxidation rate

It was believed the reaction temperature has a significant effect on graphite-steam oxidation rate [20], [28], [46]. Figure 3-16 and Figure 3-17 depicts the kinetic oxidation rate under different temperatures. It can be seen the oxidation rate increases almost exponentially by three orders of magnitude if the temperature is increased from 850 to 1100 °C. In addition, with a similar steam partial pressure, the oxidation rate is always slowed down by hydrogen participation. A more detailed discussion about the effect of hydrogen on the oxidation rate is provided in Section 3.2.5.

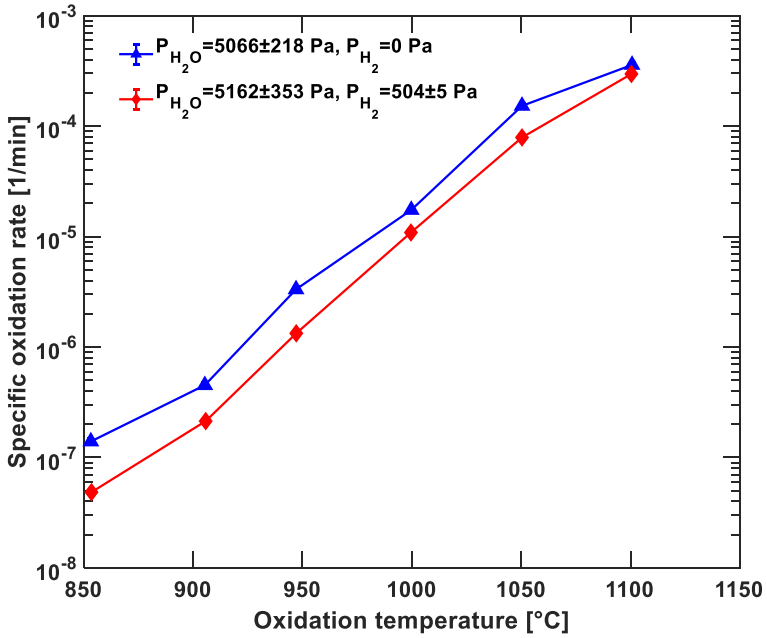

Figure 3-16 Specific oxidation rate under different temperature with steam pressure of 5 kPa

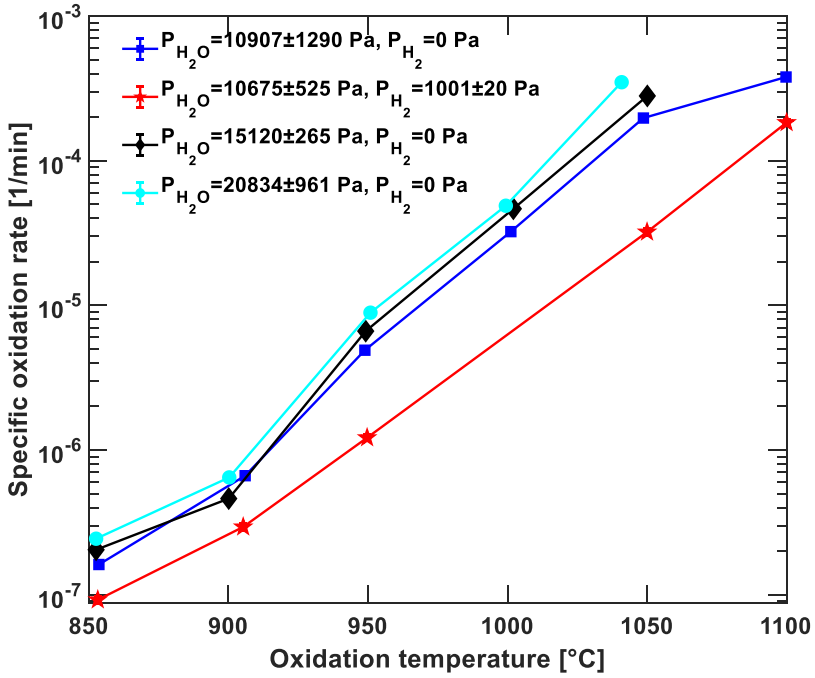

Figure 3-17 Specific oxidation rate under different temperature with steam pressure of 10k, 15k, and 20k Pa

3.2.4 Effects of steam partial pressure on kinetic oxidation rate

Figure 3-18 to Figure 3-20 shows the effect of steam partial pressure on the specific oxidation rate. In general, the specific oxidation rate increases with higher steam partial pressure. Although with limited data points, a clear trend is observed in these comparisons except for the case T=949 °C and P_{H_2}=503±8 Pa: the slop of the oxidation rate gradually decreases with increasing steam partial pressure, which means the steam partial pressure has a more prominent effect on increasing the oxidation rate when its pressure is low but its effect starts to fade away at higher values.

This phenomenon can be easily understood by considering the reaction mechanism at atomic scale. The measured oxidation is a summation of effective collisions between water molecules and graphite active sites. The total active sites within a graphite sample is limited by its volume and

microstructure. If the steam partial pressure is very low, the effective collisions are dominant by the availability of water molecules. In this regime, the addition of extra steam can significantly increase the reaction rate. On the contrary, if the quantity of water molecules becomes comparable with active graphite sites, the effect of steam partial pressure starts to saturate. It should be noted that each data point in Figure 3-18 to Figure 3-20 originates from separate experiment. Therefore, the experimental conditions are not exactly the same, and the trend of these lines is not smooth.

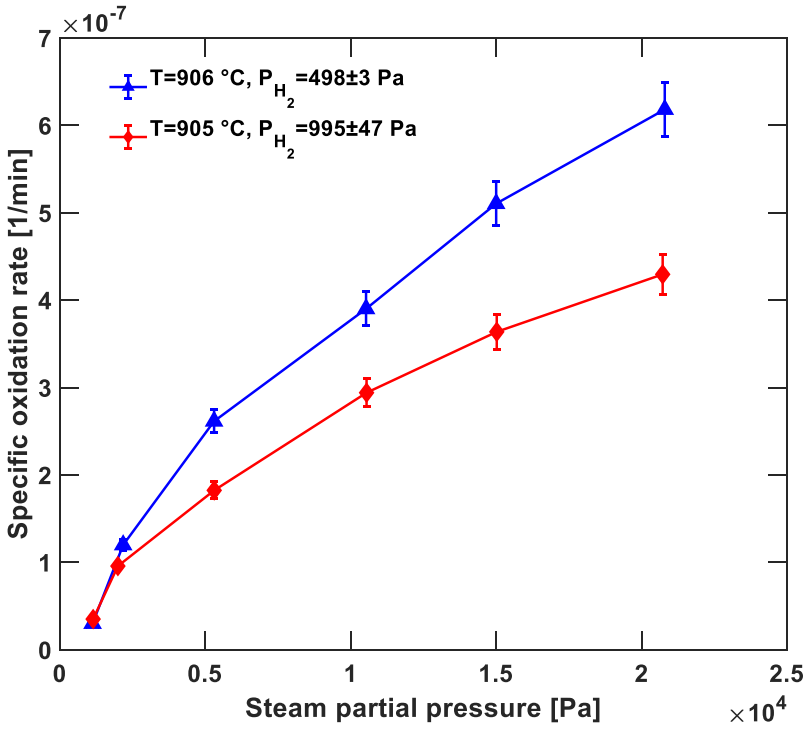

Figure 3-18 Specific oxidation rate under at 900 °C with different steam partial pressures

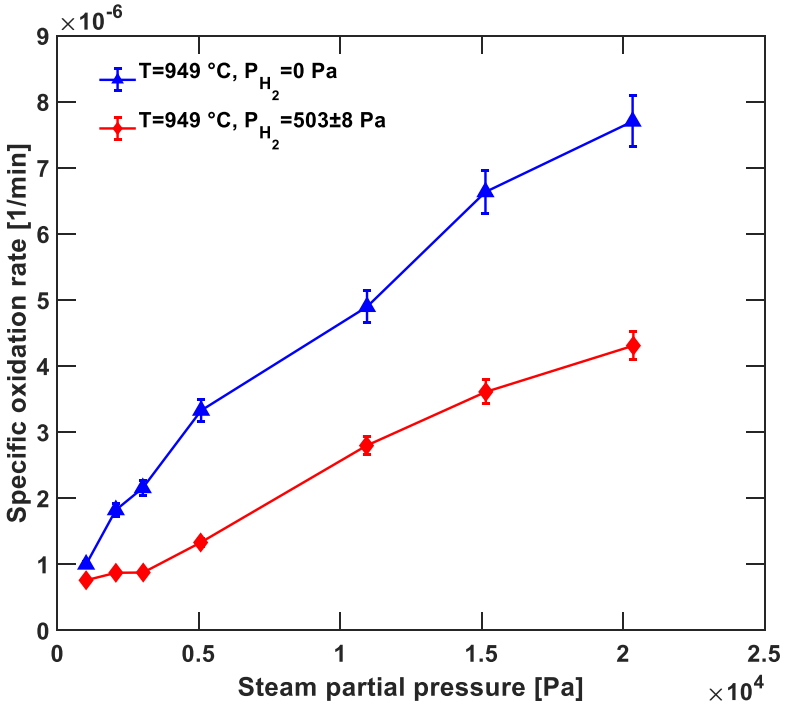

Figure 3-19 Specific oxidation rate at about 950 °C with different steam partial pressures

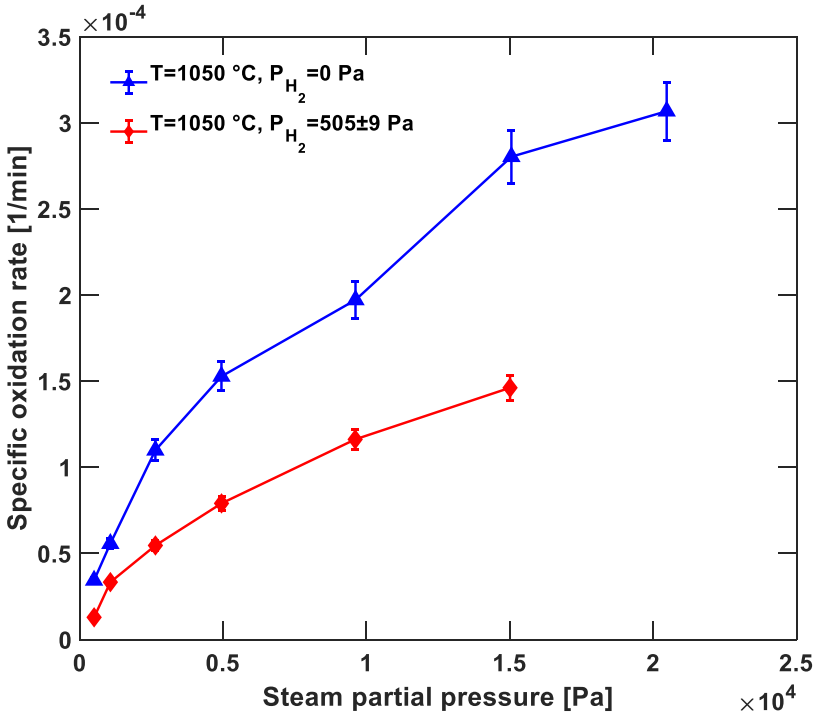

Figure 3-20 Specific oxidation rate at about 1050 °C with different steam partial pressures

3.2.5 Effects of hydrogen partial pressure on kinetic oxidation rate

The partitioning of hydrogen slows down graphite oxidation by competing with water molecules in occupying active graphite sites. However, it is unknown if this effect still exists in high steam partial pressure conditions. Figure 3-21 to Figure 3-25 depicts the specific oxidation rate under different temperature and hydrogen partial pressures. A common feature is that the oxidation rate decreases with the increase of hydrogen partial pressure, which confirms that hydrogen still suppresses graphite-steam oxidation even if with a high steam concentration, although two data points in Figure 3-22 and Figure 3-24 do not follow this trend,.

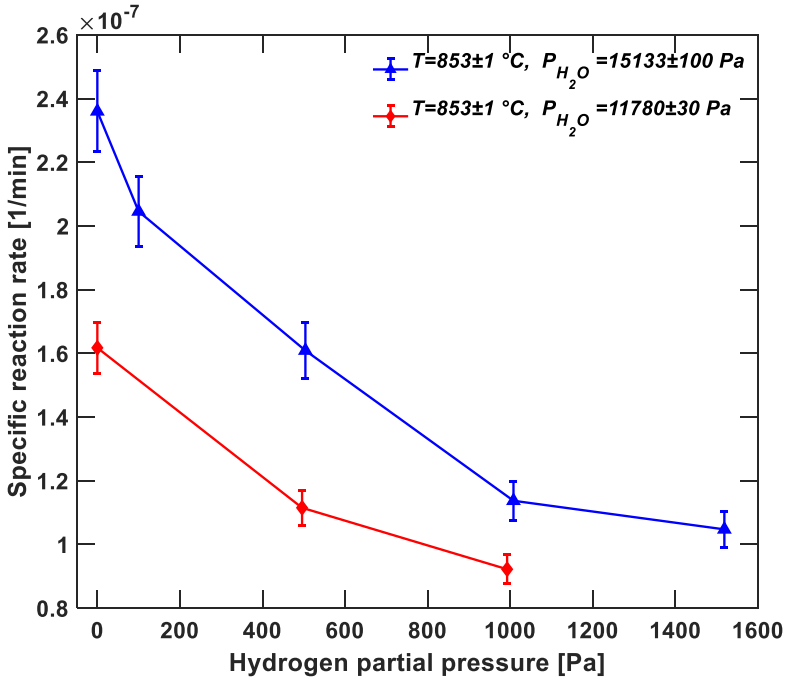

Figure 3-21 Specific oxidation rate at 853 °C with different hydrogen and steam partial pressures

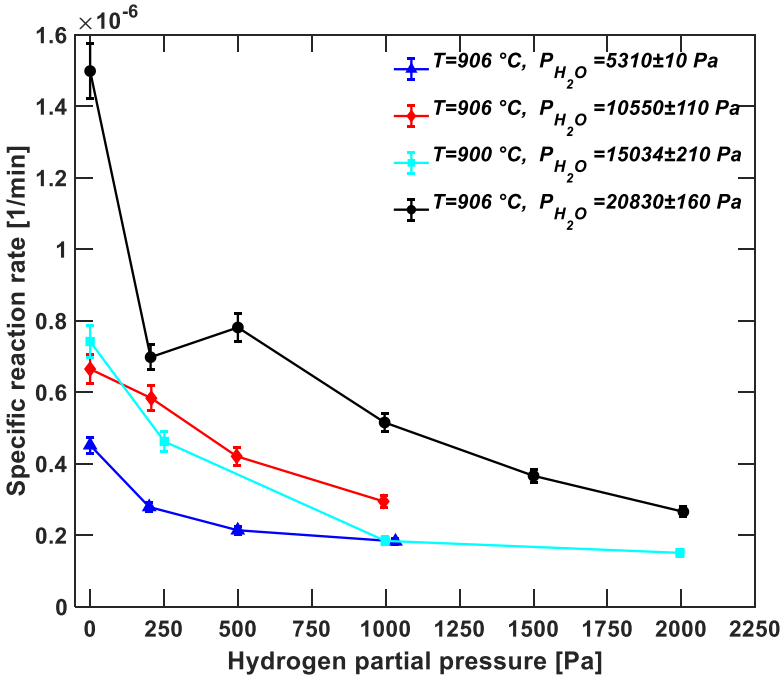

Figure 3-22 Specific oxidation rate at about 900 °C with different hydrogen and steam partial pressures

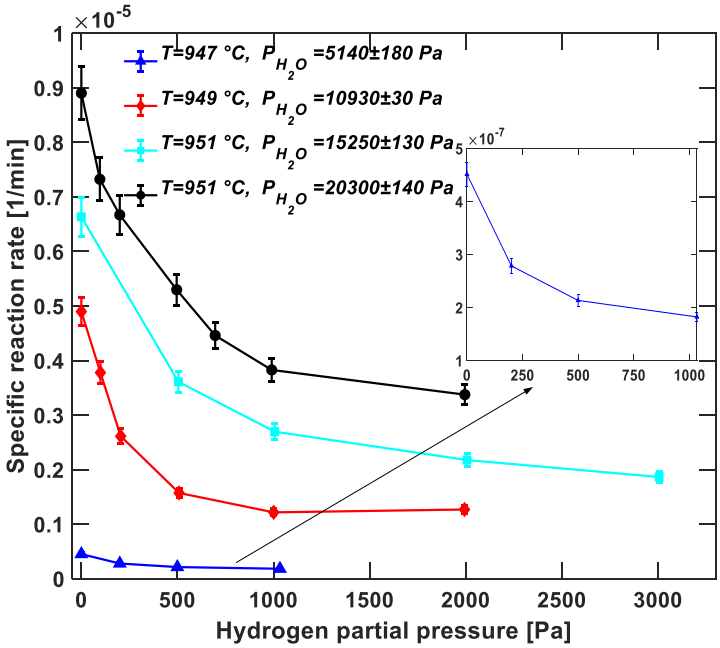

Figure 3-23 Specific oxidation rate at about 950 °C with different hydrogen and steam partial pressures

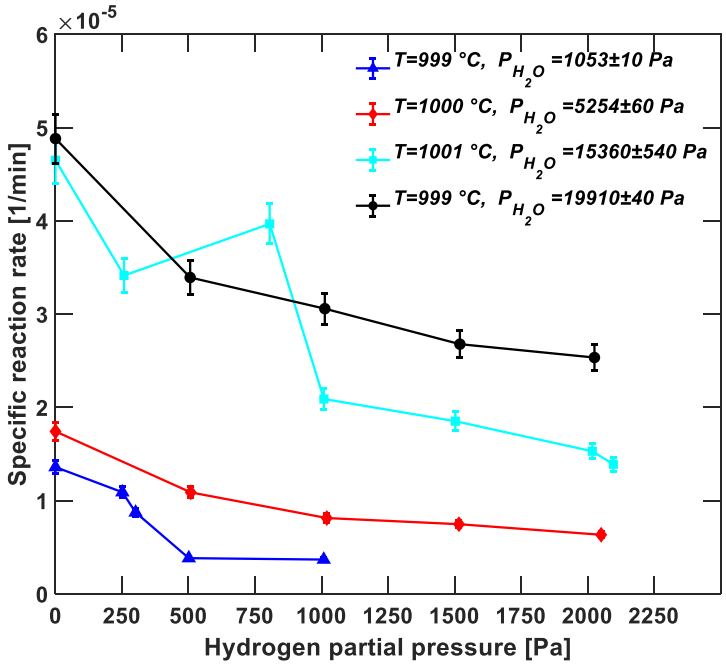

Figure 3-24 Specific oxidation rate at about 1000 °C with different hydrogen and steam partial pressure

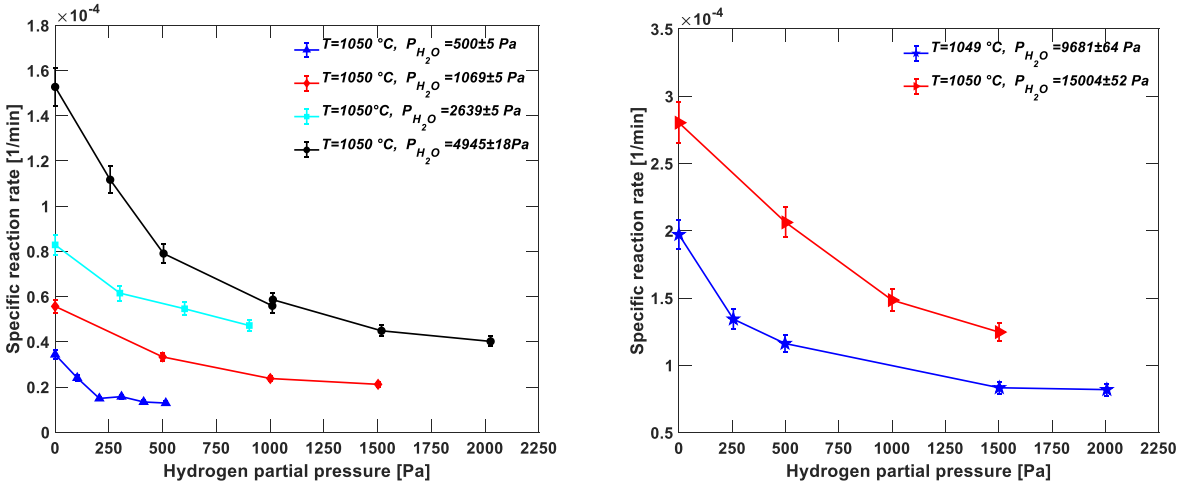

Figure 3-25 Specific oxidation rate at about 1050 °C with different hydrogen and steam partial pressures

Similar to the effect of steam partial pressures, the effect of hydrogen on slowing down graphite oxidation also tends to saturate when its concentration exceeds a certain value. The reason behind

this phenomenon is related to the ratio of graphite active sites to available hydrogen molecules, which is similar as the discussion in Section 3.2.4.

3.3 Effects of Graphite Mass Loss on Oxidation Rate

3.3.1 Theory of the effects of mass loss on graphite-steam oxidation

The chemical reaction changes the micro porous structure of graphite, which then alters the active surface area (ASA). Researchers assumed the graphite-steam reaction happens either on the grain surfaces or on the pore surfaces [29]. According to the first assumption, the ASA will be gradually decreased by chemical reaction since the grains shrink, while the second assumption leads to a contrary trend. The experiment of graphite-air oxidation using IG-110 by Fuller and Okoh (1997) supports the second model, in which the graphite oxidation rate reached a peak value at mass loss fraction of 38% [26]. In addition to the expansion of micro pores, chemical reaction also opens those isolated pores. According to the latest characterization, the density of open and isolated pores in pristine nuclear graphite IG-110 is 0.079 and 0.041 cm^3/g, respectively [48]. The isolated pores are originally inaccessible to oxidant molecules. With chemical reaction proceeds, these isolated pores will be opened and connected to the porous network, which also contributes to the increase of ASA. Figure 3-26 and Figure 3-27 show the surface condition of pristine and oxidized graphite IG-110, respectively. It can been seen the pore volume has been significantly increased by oxidation. Furthermore, the pore size is also expanded by oxidation dramatically.

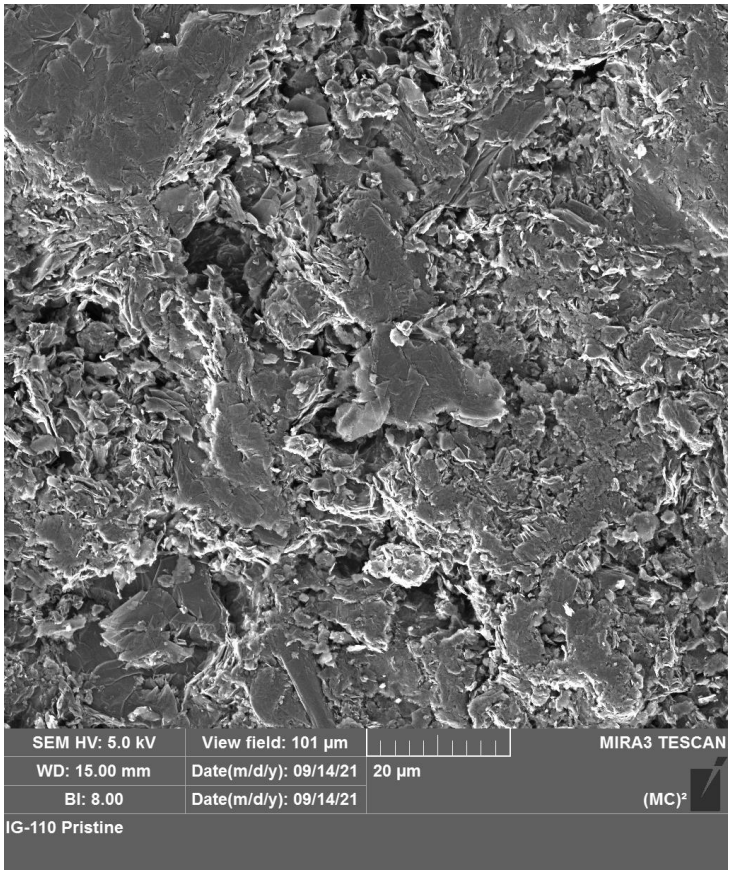

Figure 3-26 Surface of pristine graphite IG-110

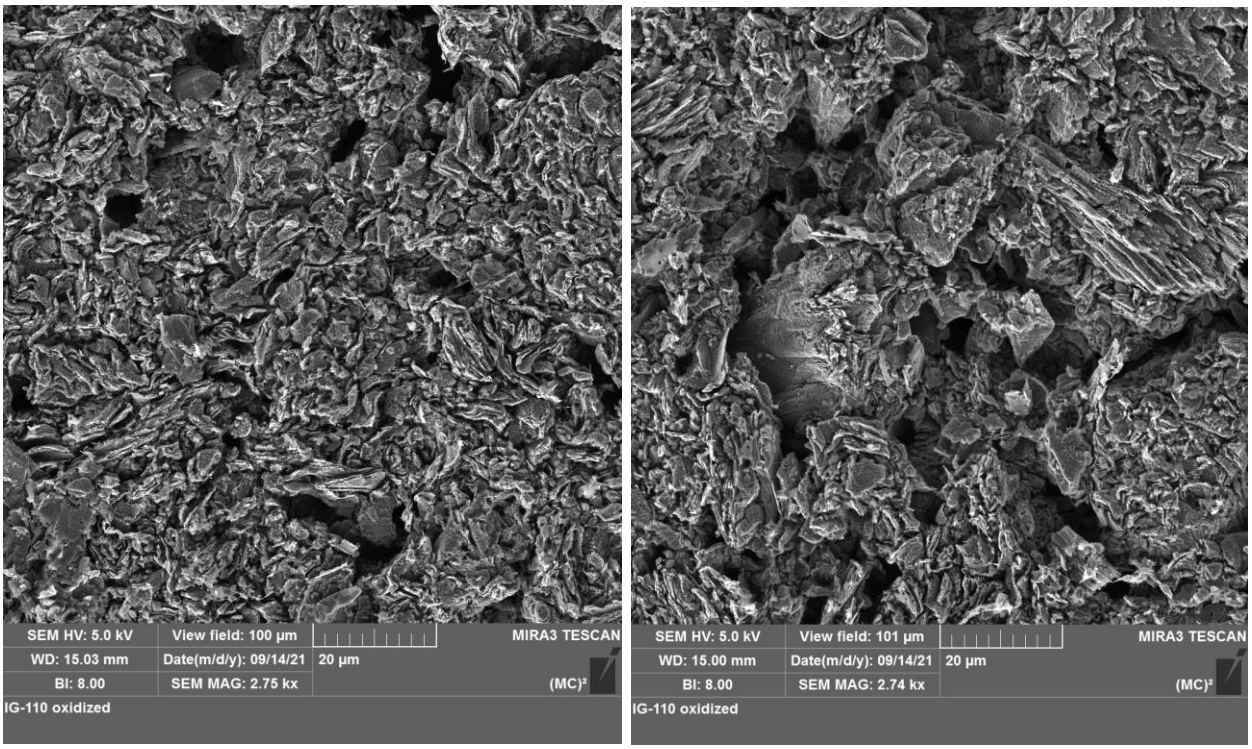

Figure 3-27 Surface of graphite IG-110 sample oxidized under condition T1002-PW16000-PH0-He10 with mass loss fraction 21.6%

When the graphite is oxidized to a certain level, the micro pores start to collapse and joint each other, which decreases ASA. The literature has related the evolution of oxidation rate with graphite mass loss fraction *X*. By assuming the micro pores in porous media consists of a series cylindrical void channels with randomly distributed radius, a semi-theoretical model was proposed to describe the reaction rate change of a heterogeneous reaction between gas and porous solids [59], [60]:

$$F_m = (1-X)\sqrt{1-\psi \ln(1-X)}\,, \tag{3-9}$$

where ψ is a graphite structural parameter defined as:

$$\psi = \frac{4\pi(1-\varepsilon_0)\lambda_0}{\left(\rho_0 A_{\mathrm{BET},0}\right)^2} \tag{3-10}$$

with ε_0, λ_0, and ρ_0 to be the graphite porosity, total pore length per unit volume, and graphite density, at the initial condition (before any oxidation), respectively. $A_{\mathrm{BET},0}$ is the specific surface area that is a measure of physical adsorption of gas molecules on a solid surface. The value of $A_{\mathrm{BET},0}$ can be measured by Brunanuer-Emmett-Teller (BET) technique. However, it is still challenging to directly evaluate the value of ψ by characterizing the complex micro structures of a nuclear graphite, especially the value of λ_0 and $A_{\mathrm{BET},0}$. For example, two clusters of pores are identified for nuclear graphite IG-110, which concentrate on a few nanometers and a few micrometers individually [48]. The pore size spectroscopy of different grades nuclear graphite can differ significantly. For example, the pore in graphite PCEA either concentrate between 5 to 10 nanometers, or between 10 to 100 micrometers. Since the focus of this research is to investigate the graphite-steam oxidation behavior, the characterization of graphite micro structure will not be studied in detail here.

The complex micro structure of nuclear graphite leads to various ψ values in literature. For example, a ψ value of 765 [26], 268[61], and 80 [41]–[43] have been used for nuclear graphite IG-110. As a result, the value of F_{m} also differs significantly. In experiment, the mass loss fraction factor F_{m} describes the ratio of specific reaction rate at a given mass loss fraction to the reaction rate with zero mass loss. Therefore, the value of ψ can be estimated by measuring F_{m} in an experiment, and fitting it to Eq. (3-9).

3.3.2 Effects of mass loss fraction on kinetic oxidation rate

Three experiments in Section 3.1.2, namely the T1002-PW15796-PH0-He15, T1002-PW16000-PH0-He10, and T1000-PW17213-PH0-He5, were used to investigate the relation

between mass loss fraction X and the specific oxidation rate $Rate_{spe}$. The history of apparent reaction rate has been shown in Figure 3-7. Another experiment at the same temperature with a lower steam concentration, namely T1002-PW10413-PH0-He15, was conducted. To derive the mass loss fraction factor, the apparent reaction rates were converted into specific reaction rate, which is shown in Figure 3-28. Two additional tests were carried out at lower temperatures, namely T863-PW8372-PH0-He10 and T909-PW14017-PH0-He10, respectively. The specific reaction rates of these two experiments are depicted in Figure 3-29 and Figure 3-30.

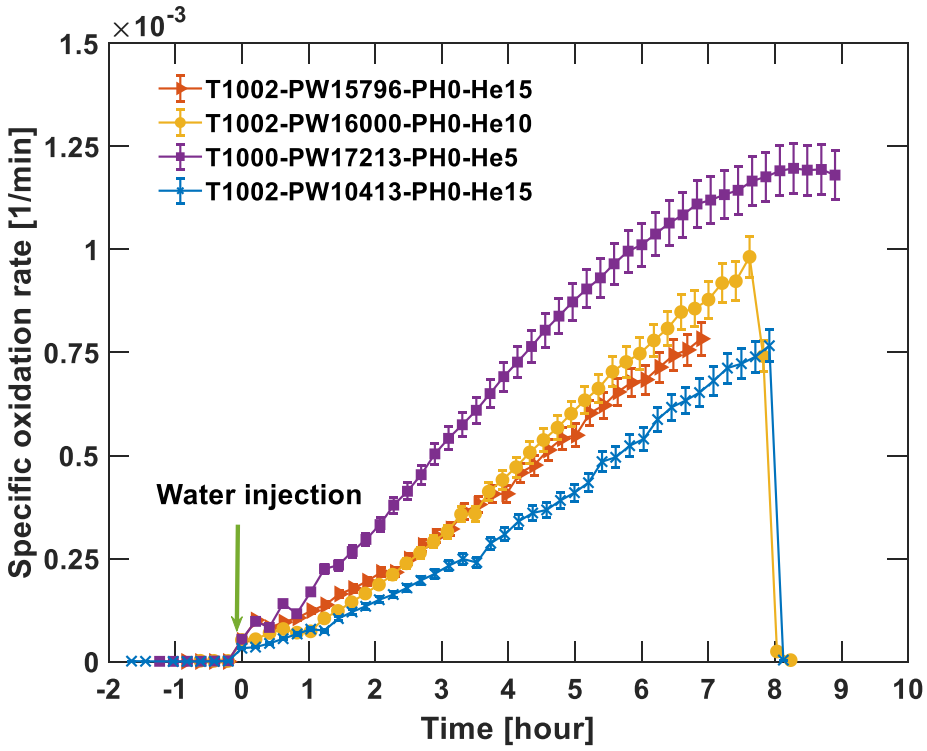

Figure 3-28 History of specific oxidation rate at reaction temperature of 1000 °C

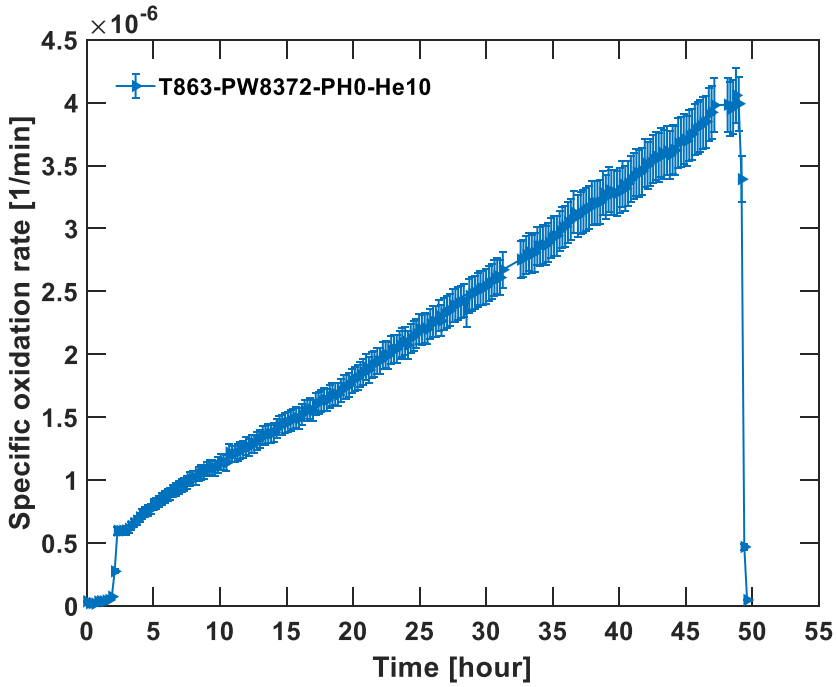

Figure 3-29 History of specific oxidation rate of test T863-PW8372-PH0-He10

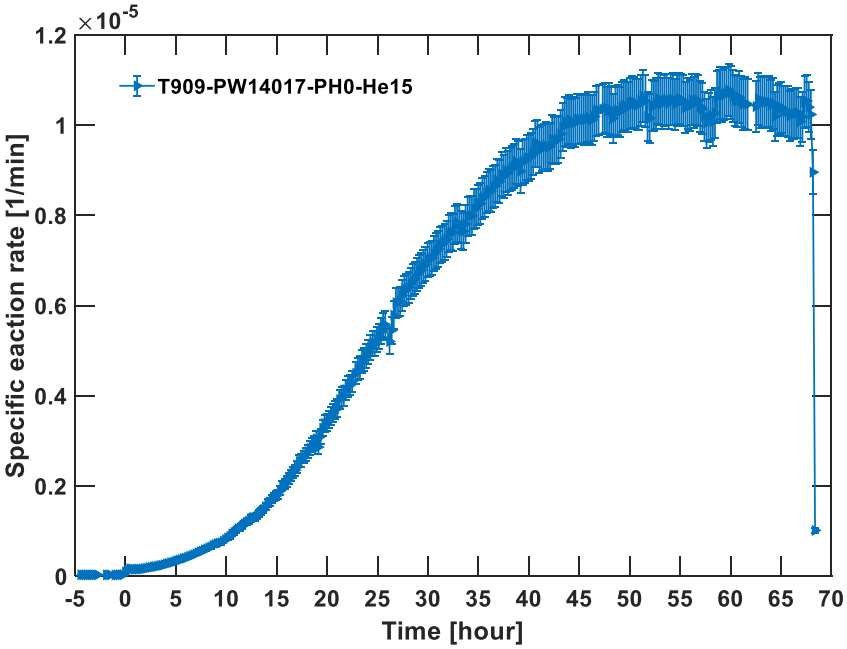

Figure 3-30 History of specific oxidation rate of test T909-PW14017-PH0-He10

Section 3.1 has confirmed the accuracy of GC measurement. Therefore, mass loss fraction at j-th measurement can be calculated by:

$$X \approx \frac{1}{2m_0}\sum_{1}^{j}\left(Rate_{\text{app}}(j-1)+Rate_{\text{app}}(j)\right)\Delta t_{j-1,j} \tag{3-11}$$

Accordingly, the specific oxidation rate can be plotted against mass loss fraction, which is depicted in to for reaction temperature of 863, 909, and 1000 °C, respectively. The solid black lines in to show the best fitting curve based on Eq. (3-9), with 95% confidence band (black dash lines). It should be noted the oxidation rate at temperature 863 °C is so slow that the mass loss fraction after 50 hours oxidation is only about 6.3×10^{-3}.

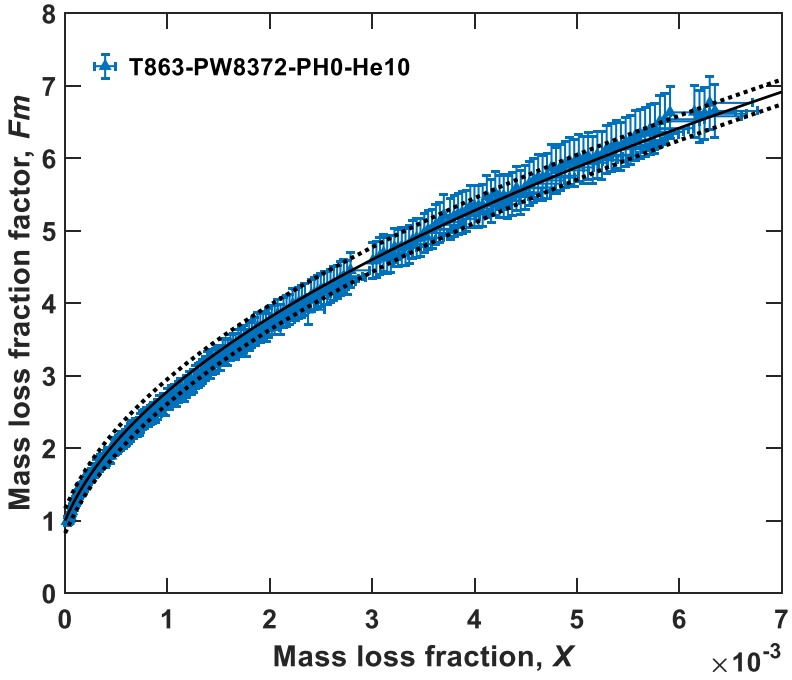

Figure 3-31 Mass loss fraction factor at reaction temperature of 863 °C

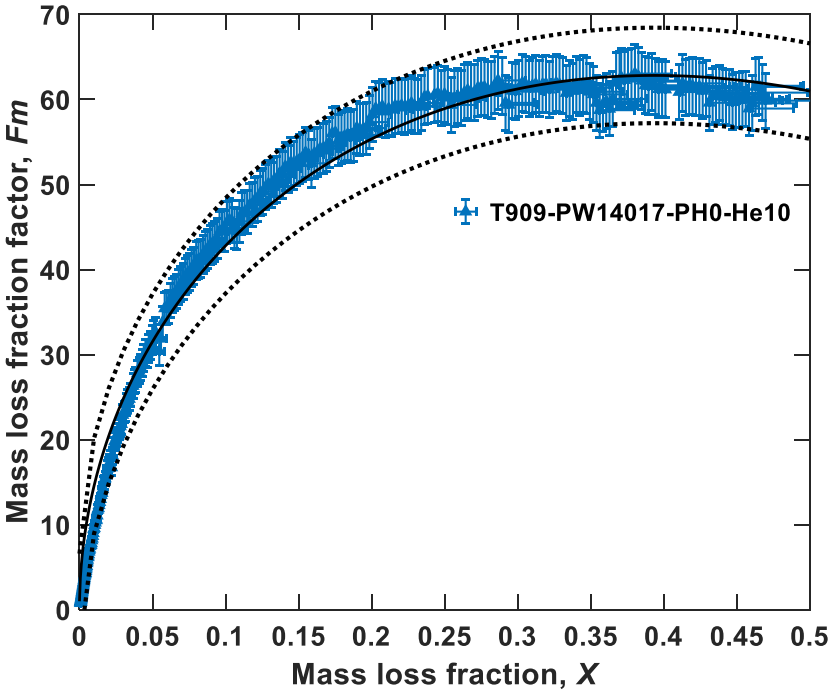

Figure 3-32 Mass loss fraction factor at reaction temperature of 909 °C

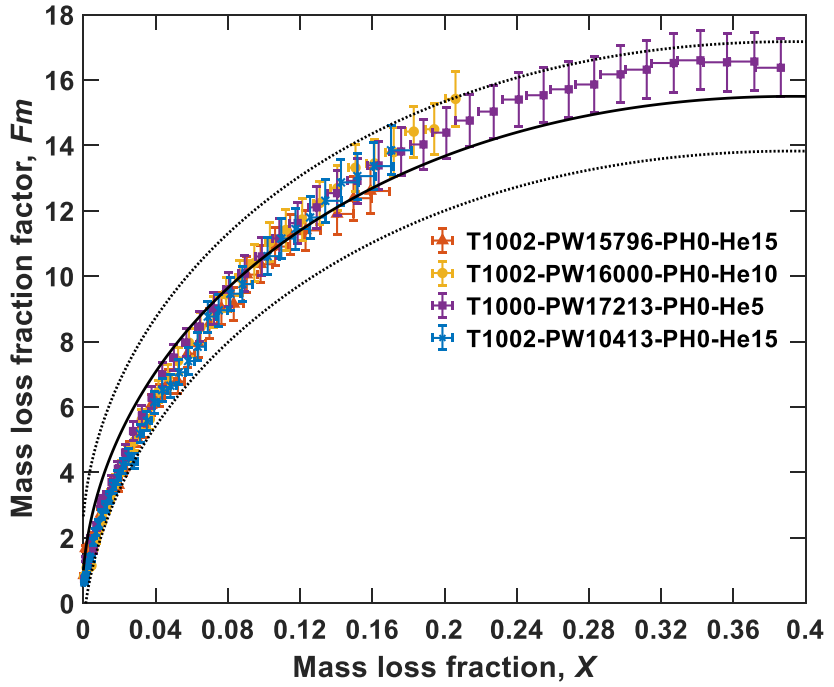

Figure 3-33 Mass loss fraction factor at reaction temperature of 1000 °C

In literature [26], the ψ value of nuclear graphite IG-110 was obtained by exposing the specimen in air at temperature of 750 °C. However, only 12 reaction rates at mass loss from 0 to 1 were used to fit Eq. (3-9). The lack of enough data points inevitably brings large uncertainties, which can be seen from . As a comparison, this research shows a more smooth history of graphite oxidation rate with mass loss fraction. On the other hand, this research supports the conclusion of graphite-air (oxygen) oxidation that the reaction rate reaches to a maximum value at mass loss about 0.3 to 0.4 [26].

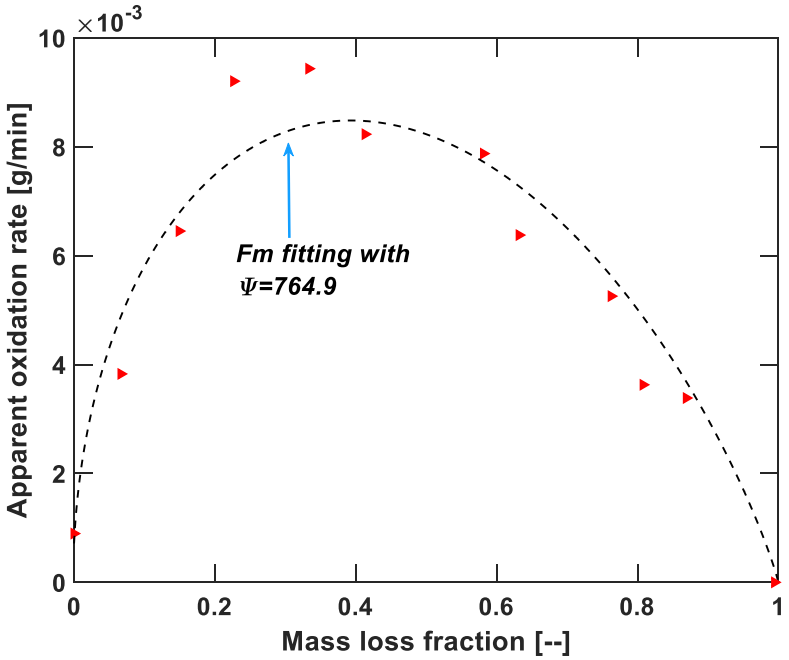

Figure 3-34 Oxidation rate of graphite-air reaction using IG-110 cylinder (D×H=8.38×18.05 mm) at temperature of 750 °C (plotted using data from literature [26])

In addition, it was found the value of ψ can be much different at different temperatures. In general, the lower reaction temperature leads to a higher ψ value. For example, the oxidation rate

at temperature of 863 °C and 1000 °C increased by 7 times at mass loss fraction of 5.1×10^{-3} and 4×10^{-2}, respectively. In order to fit the experimental data, the ψ values at temperature of 863, 909, and 1000 C are 33660, 20220 and 1304 respectively. The value of ψ obtained in this research is larger than the highest in literature, which raise a flag in nuclear reactor safety analysis: if an underestimated ψ value is used for reactor safety analysis, the actual graphite oxidation will be underestimated.

Furthermore, as shown in Figure 3-33, the specific oxidation rates with different steam concentrations overlap each other at the same reaction temperature. It is desired to perform more tests with other steam concentrations to verify this conclusion. It should be noted no hydrogen was added for experiments in this section. Therefore, the effect of hydrogen on the oxidation rate evolution is unknown.

3.4 Experiment of Integral Graphite-Steam Oxidation

3.4.1 Experimental conditions

The above experiments focus on the kinetic chemical reaction. Therefore, the graphite sample features a large surface-to-volume ratio, which is aimed to minimize the effect of gas diffusion. The objective of the experiments in this section is not only to measure the oxidation rate evolution but also to form a density distribution. Therefore, the results can be further used to validate numerical models for graphite oxidation behavior in the future. The experiments were carried out using cylindrical graphite samples with diameter of 25.4 mm and height of 50.8 mm. Using these large specimen, the effect of mass transfer can be intentionally included. A total of four experiments were conducted under different conditions, as shown in Table 3-3.

Table 3-3 Summary of integral test condition

Test No.	Test name	T [°C]	P [bar]	$\dot{V}_{He}$ [SLPM]	p_{H_2} [Pa]	p_{H_2O} [Pa]
A	T971-PW14373-PH502-He10	970.6	1.244	10	502	14,373
B	T971-PW17306-PH985-He7	970.5	1.246	7	985	17,306
C	T1001-PW15886-PH495-He10	1000.7	1.236	10	495	15,886
D	T1051-PW1896-PH109-He10	1050.7	1.243	10	109	1,896

The system pressure and temperature control of these four experiments are shown in Figure 3-35 to Figure 3-38. The pressure fluctuation in these four tests are within about 2000 Pa for most experimental time, which is only about 1.6% of system pressure. For test B, the pressure fluctuates heavily between 16 to 18 hours, which was stabilized by increasing the power of the heating tube. The fluctuation of reaction temperature is negligible, which is within 2 °C during the whole oxidation process.

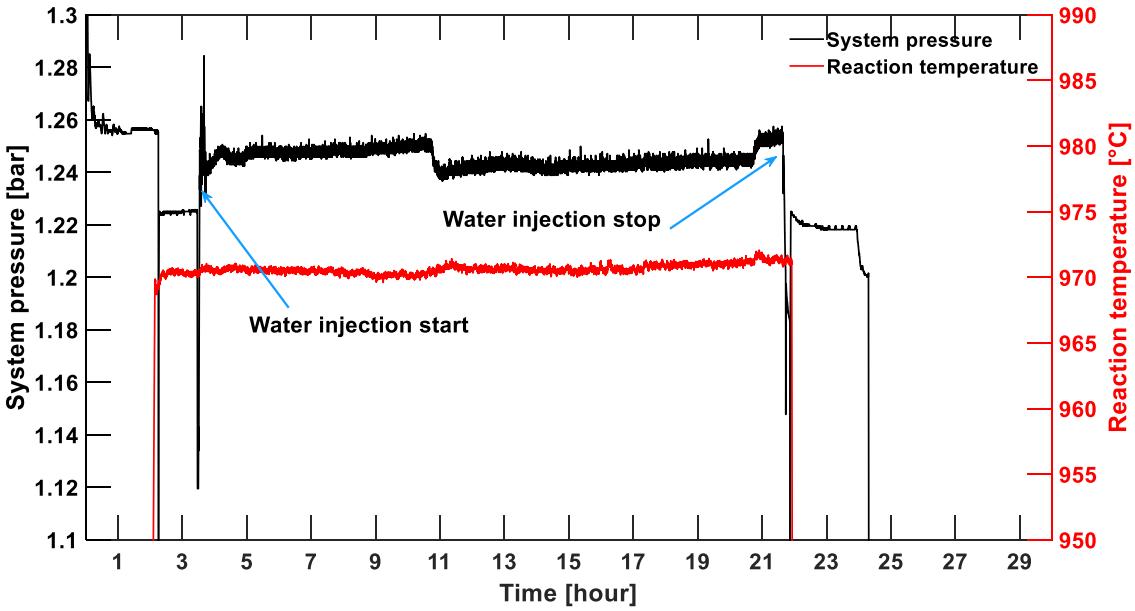

Figure 3-35 System pressure and temperature control for integral test A

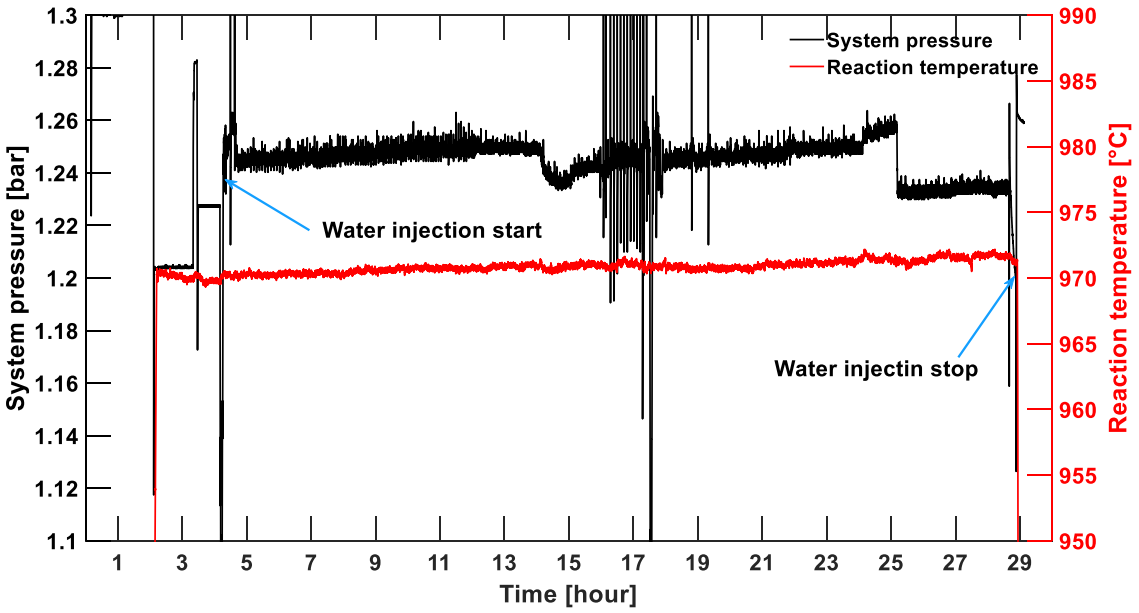

Figure 3-36 System pressure and temperature control for integral test B

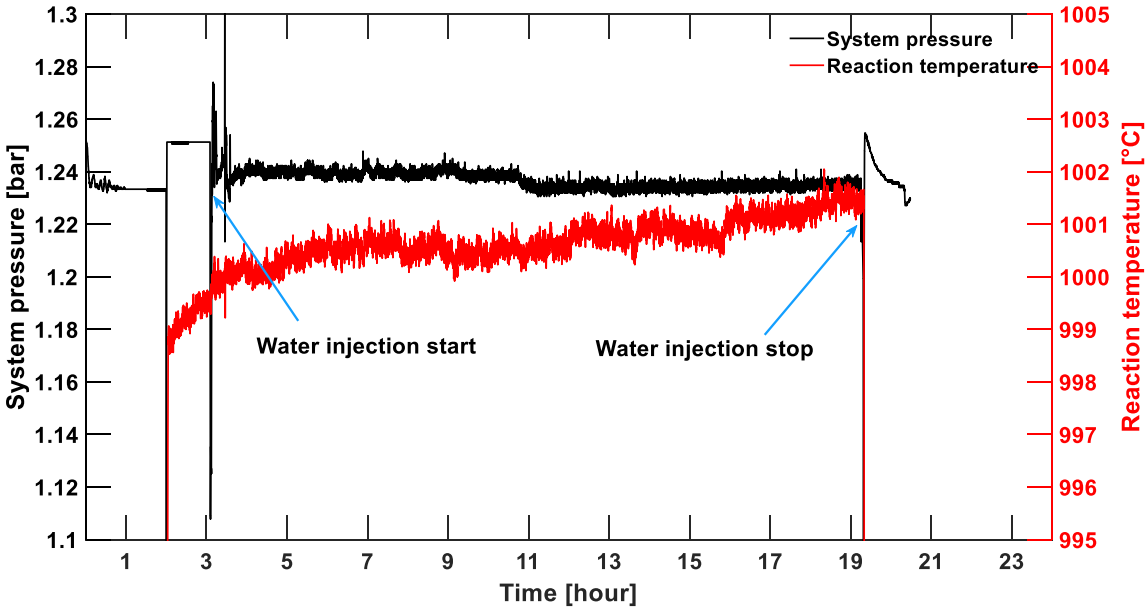

Figure 3-37 System pressure and temperature control for integral test C

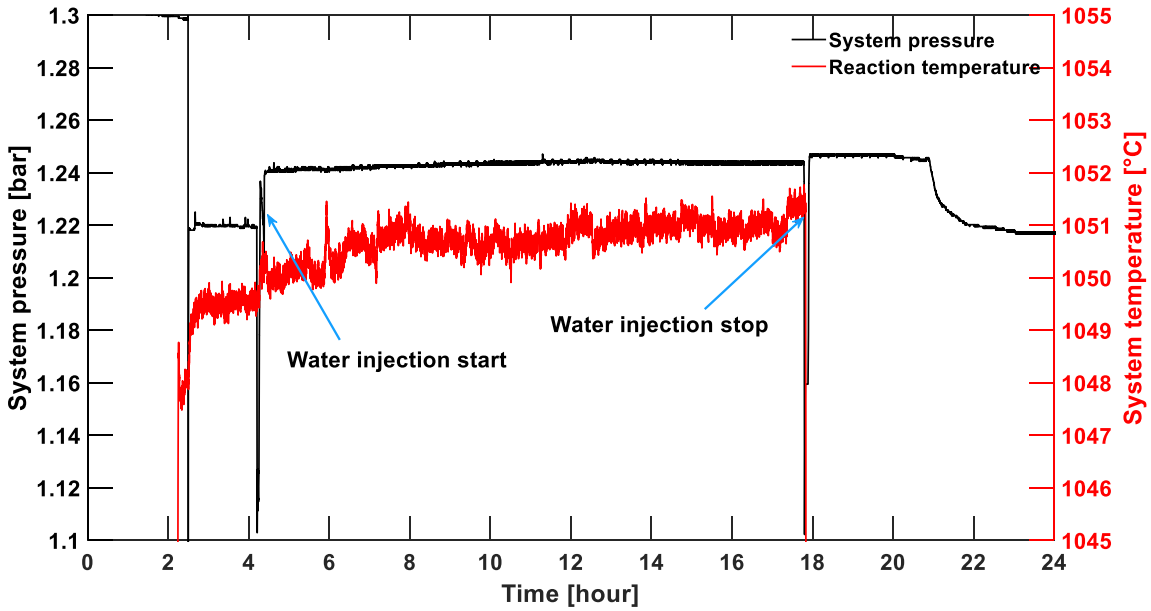

Figure 3-38 System pressure and temperature control for inegral test D

3.4.2 Measurement of apparent oxidation rate and post-oxidation density

The duration of these four experiments lasted from about 13 to 25 hours. No observable dimension changes were observed for the samples after oxidation. The dimension and mass of these four samples before and after oxidation are listed in Table 3-4. The graphite mass loss obtained by GC signal is slightly larger than the mass balance scale measurement for tests A, B, and C. For test D, the GC signal gave slightly smaller mass loss value. Nevertheless, the difference between the two measurements is small and acceptable.

Table 3-4 Mass loss of graphite sample in four integral tests

Test No.	$D \times H$ pre-oxidation [mm]	$D \times H$ post-oxidation [mm]	m_0 [±0.002 g]	Δm_{MB} [g]	Δm_{GC} [g]	Difference [--]
A	25.41×50.82	25.40×50.79	45.914	1.889	1.931	+2.2%
B	25.41×50.88	25.41×50.82	46.262	2.486	2.504	+0.72%
C	25.40×50.80	25.38×50.77	46.026	4.279	4.41	+3.1%
D	25.37×50.77	25.37×50.75	46.122	1.992	1.936	-2.8%

depicts the apparent oxidation rates. The data was shifted so the first measurement after water injection appears at time 0 for all four tests. Although the steam concentration of test B is about 20% higher than that of test A, its hydrogen concentration is about 96% higher. As a result, its apparent reaction rate is always lower. Due to the higher reaction temperature, test D shows the highest oxidation rate at the beginning. However, it is quickly surpassed by test C. An explanation is a larger volume of graphite was being oxidized simultaneously in test C. For test B, small fluctuation is observed at time between 12 to 15 hour. The fluctuation was caused by the flow instability, as shown in Figure 3-36. The pressure fluctuation can affect the measured oxidation rate via two mechanisms. First, the steam partial pressure is affected by system pressure fluctuations. Second, the change of system pressure affects the gas diffusivity, which can thereafter accelerate or decelerate the mass transfer rate.

It should be noted that local oxidization sites were found on the upper face of graphite sample in test T1051-PW1896-PH109-He10, as shown in Figure 3-40. Therefore, the measured apparent oxidation rates also include these extra reaction signals. As a consequence, the actual apparent oxidation rate, if without these local oxidation spots, should be lower than what are shown in Figure 3-39.

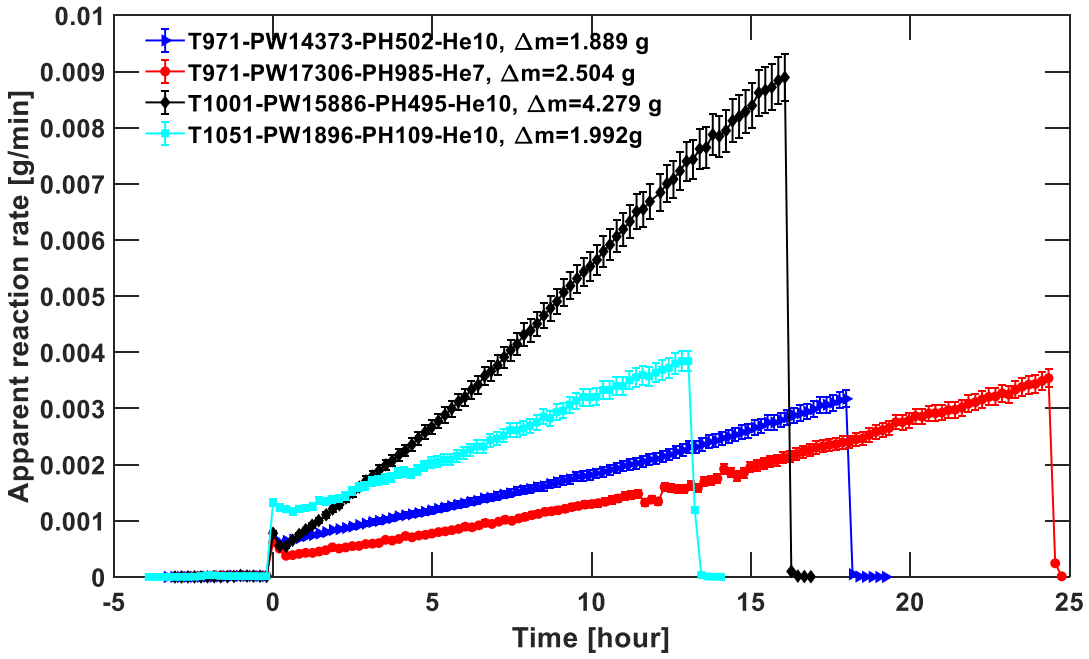

Figure 3-39 Apparent oxidation rate evolution of four integral experiments

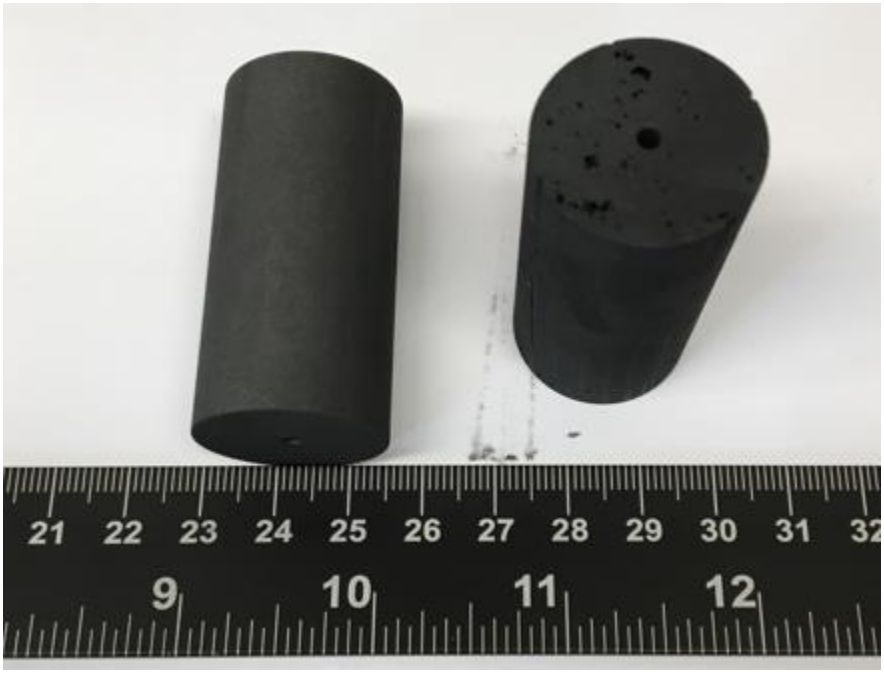

Figure 3-40 Accelerated oixdation sites on graphite sample surface for test T1051-PW1896-PH109-He10

The density profile of post-oxidation graphite cylinders was obtained by a layer-by-layer machining method using a lathe. A length section about 20 mm at the upper end of the graphite sample was reserved for the lathe chunk. A thin layer of graphite about 0.5 mm thickness and 30 mm length was peeled off each time. The dimension and remaining mass of the graphite cylinder were measured before and after each machining. In this way, both the volume and mass of each machining layer are known, which can be used to calculate the volume-averaged density. In order to prevent the sample from being overheated, cooling air was introduced to the sample. A schematic of the cutting strategy is depicted in Figure 3-41. Figure 3-42 shows an example of the graphite machining using the lathe. As a comparison, the density profile of a pristine graphite cylinder was measured first. The densities obtained by this method are a series discrete volume-averaged values. Therefore, it is important to assign them to a reasonable radial position. An area-averaged radius, defined by Eq. (3-12), is used to carry the measured density.

$$\bar{r} = \frac{\int_{r_1}^{r_2} r \cdot 2\pi r \, dr}{\int_{r_1}^{r_2} 2\pi r \, dr} = \frac{2\left(r_2^3 - r_1^3\right)}{3\left(r_2^2 - r_1^2\right)} \tag{3-12}$$

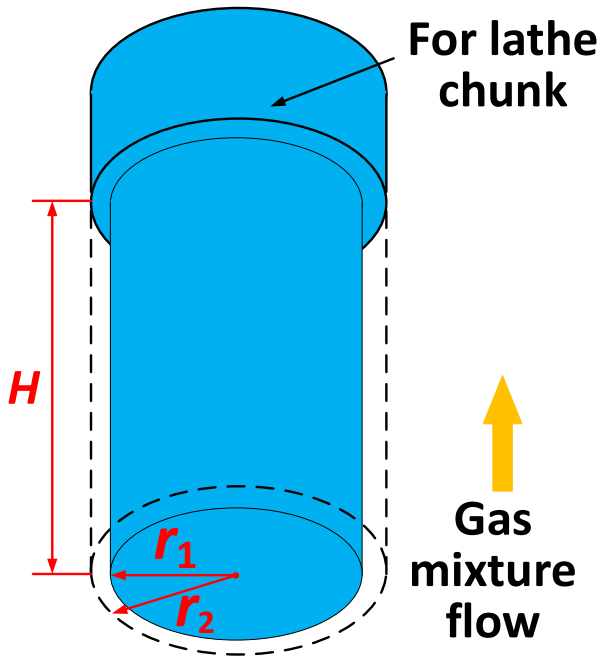

Figure 3-41 Schematic of layer-by-layer graphite maching

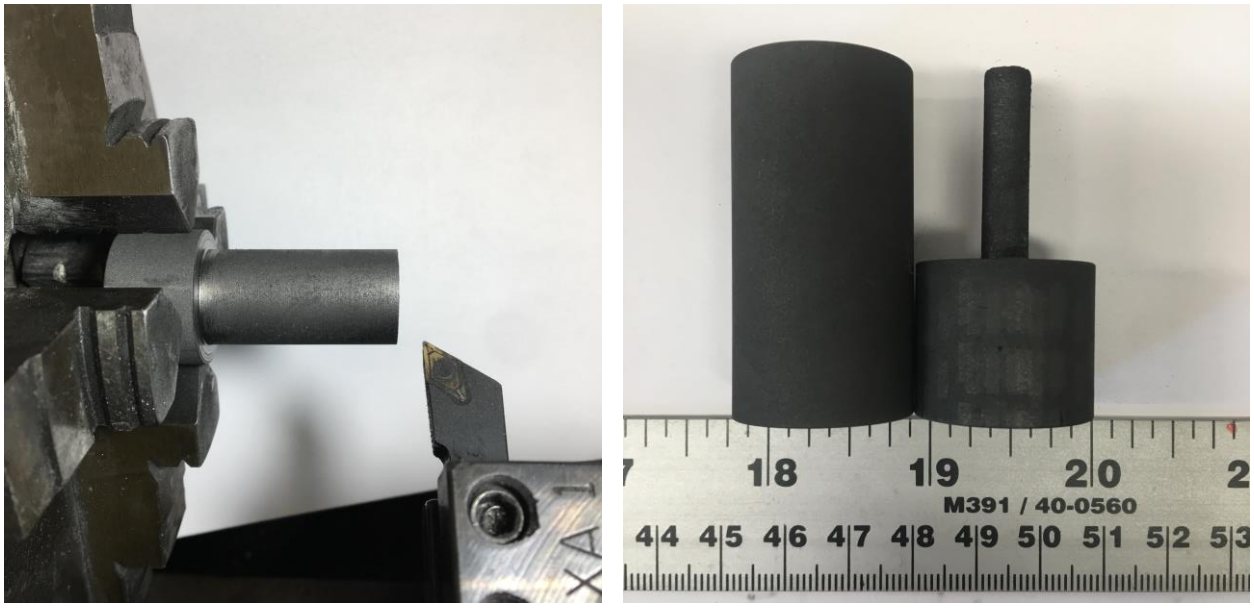

Figure 3-42 Graphite machining for density measurement

It should be noted although experiment T1051-PW1896-PH109-He10 shows some local oxidation spots on the upper face of graphite sample, the density measurement is still valuable

since those spots were not included in the machining. Figure 3-43 depicts the profile of normalized density of each graphite sample along the radial direction. The normalized density is defined as volume-averaged density at radius *r* divided by pristine density. The pristine density of each sample was calculated using its mass and volume at fresh condition by assuming the density distribution is uniform.

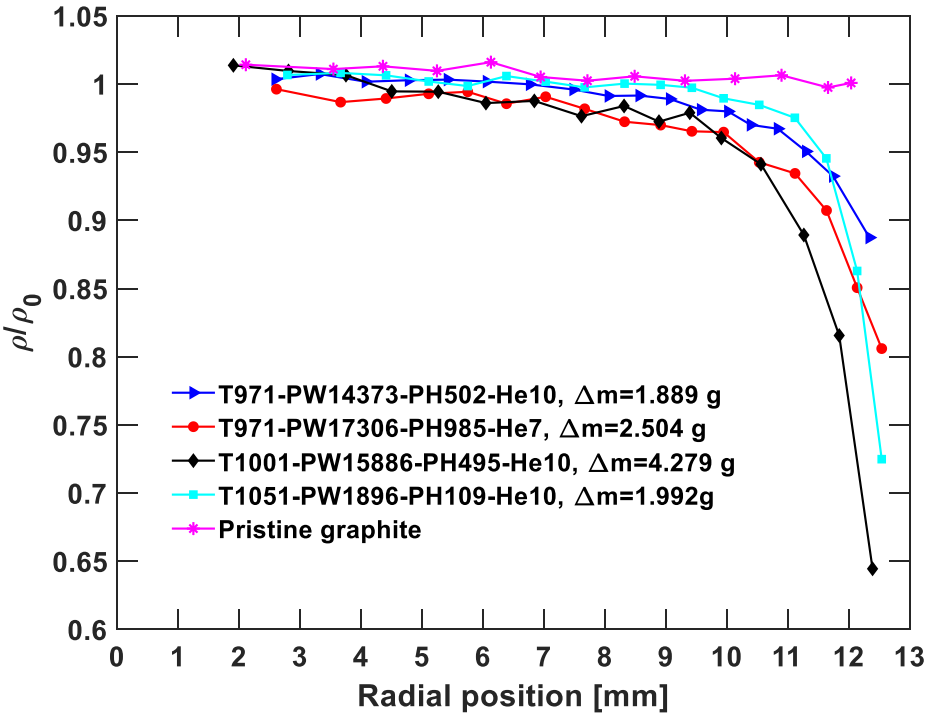

Figure 3-43 Radial density profile of cylindrical graphite specimen

The measured normalized density of the pristine graphite varies from 0.097 to 1.016. Therefore, it can be confirmed the layer-by-layer machining can reasonably measure graphite density profile. It can be seen in Figure 3-43 the central region about a few millimeters of these four samples remains almost un-oxidized. However, the density distribution near the surface is significantly different. Table 3-4 shows that test C has the largest mass loss among the four

experiments. As can be seen in Figure 3-43, its outer layer has been heavily oxidized that about 35% of graphite mass has been lost. The graphite density distribution obtained here will be used in Chapter 5 to validate the multiphysics model.

A calculation was carried out to estimate the accuracy of the above measurements. While it is challenging to analyze the reliability of each machining individually, the overall accuracy can be estimated. Figure 3-43 has shown the measured density distribution along the radial direction. A volume integration based on these curves then gives the mass of post-oxidation samples.

The density measurements were taken using step size about 0.5 mm. In the calculation, a uniform radial step size of 0.1 mm was adopted. The density at each radial position was then obtained by interpolating the values in Figure 3-43. A pristine density value was assumed for the most central region that was not machined,. Therefore, the mass of each post-oxidation cylinder can be estimated by:

$$m_{\mathrm{Int}} = \sum_{i=1}^{N} \frac{\pi}{8} \left(\rho_{i-1} + \rho_i\right)\left(r_{i-1} + r_i\right)^2 H \tag{3-13}$$

The actual mass loss in the oxidation process is obtained by comparing the weight of the sample before and after the experiment, or by integrating the GC apparent oxidation signals. Another mass loss can be estimated by deducting the value of Eq. (3-13) from the pre-oxidation mass:

$$\Delta m_{\mathrm{Int}} = m_0 - m_{\mathrm{Int}} \tag{3-14}$$

summarizes the information of graphite mass obtained by different methods. It can be seen the mass loss obtained by Eq. (3-13) is smaller than the actual value. The difference for Case D can be up to 20.3%. However, the 1.992 g mass loss obtained by mass balance scale includes those

local oxidized sites, which means the 20.3% difference is exaggerated. There are multiple reasons for the differences in . First, the random uncertainties are inevitable in the measurement. For example, the traveling length of lathe bit ("*H*" in Figure 3-41) in each machining should be maintained the same ideally. However, the measurement shows a maximum difference about 0.1mm in the actual practice. Furthermore, when anchoring the graphite sample to, and taking the graphite sample off from the lathe chunk, small amount of graphite dust is inevitably lost. In addition, the bottom surface that exhibits severer oxidation is also included in the machining, which can slightly distort the measurement.

Table 3-5 Comparison of graphite mass obtained by integration and mass balance scale

Test No.	m_0 **pre-oxidation [±0.002 g]**	m **post-oxidation [±0.002 g]**	m_{Int} **post-oxidation [g]**	Δm_{MB} **[g]**	Δm_{Int} **[g]**	**Difference [--]**
A	45.914	44.025	44.210	1.889	1.741	-7.83%
B	46.262	43.776	43.983	2.486	2.367	-4.79%
C	46.026	41.747	42.261	4.279	3.831	-10.5%
D	46.122	44.130	44.558	1.992	1.587	-20.3%

Chapter 4 Kinetic Reaction Rate Equation for Graphite-Steam Oxidation

The data obtained from Section 3.2 can be used to derive the kinetic reaction rate equations for graphite-steam oxidation. In this chapter, a multivariable optimization code was first developed on MATLAB. A theoretical analysis was performed to derive the LH reaction model using limited experimental data points. The reaction constants obtained from the theoretical analysis was then used as initial values for the multivariable optimization. In addition, a BLH reaction rate equation was also obtained using the MATLAB code. The kinetic reaction rate equations were then compared with each other. In general, the BLH equation predicts graphite-steam oxidation rate better within the experimental conditions of this work.

4.1 Theory of Multivariable Optimization

The multivariable optimization is carried out by the nonlinear least-squares solver using MATLAB [62]. The nonlinear least-square solver solves curve fitting problem of the form:

$$\min_x \left\| f(x) \right\|_2^2 = \min_x \left[f_1(x)^2 + f_2(x)^2 + \ldots + f_N(x)^2 \right] \tag{4-1}$$

where x_0 is the vector of the unknown coefficients in a given formula. The solver starts at an initial value x_0, and tries to find a combination of elements in vector x_0 so the sum of squares of the given function is minimized [63].

In the optimization process, the initial guess has a vital effect on the final values of the coefficients, and therefore on the accuracy of the kinetic model. The effect of the initial values on the fitting process can be described by a simplified demo graph, as shown in Figure 4-1. Starting at a specified initial value, the solver iterates until $\| f(x) \|_2^2$ reaches the local concave. However, the returned coefficients, i.e., the local optimization points A, B, and D, are not necessarily the best one globally. Only when the initial value falls in a certain range, defined by the two dash lines in Figure 4-1, the returned coefficients will be the global optimization.

This behavior will make the optimization process challenging if there are a large number of unknown coefficients. In addition, the value of the activation energies and the reaction frequency can vary over several magnitudes, which leads to an enormous combination of initializations. The computation time needed to run all these initializations will be unacceptable. Therefore, the objective of the optimization is to find a local combination the coefficients in LH or BLH models, which can agree the experimental data well, rather than to find the global optimized coefficients. A mean relative difference (MRD) is defined to evaluate the accuracy of the kinetic reaction rate equations:

$$\mathrm{MRD} = \frac{1}{N}\left[\sum_{1}^{N}\left(\left|\frac{Y_i - \hat{Y}_i}{\hat{Y}_i}\right|\right)\right] \tag{4-2}$$

where N is the total number of experimental data. Y and $\hat{Y}$ indicate predicted value and experimental value, respectively.

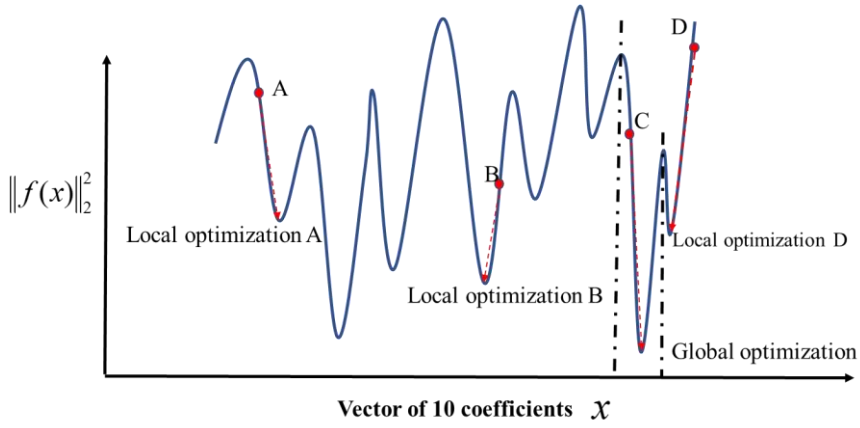

Figure 4-1 Schematic of direct absorption spectroscopy measurements

4.2 Langmuir-Hinshelwood (LH) Kinetic Reaction Rate Equation

The LH equation for graphite-steam oxidation is expressed as Eq. (4-3):

$$R_{\text{spe}} = \frac{k_1 \exp(-\frac{E_1}{RT}) p_{\text{H}_2\text{O}}}{1 + k_2 \exp(-\frac{E_2}{RT}) p_{\text{H}_2}^n + k_3 \exp(-\frac{E_3}{RT}) p_{\text{H}_2\text{O}}} \tag{4-3}$$

There are a total of seven unknown constants in the LH equation, including the reaction order for hydrogen. The values of these constants can be calculated theoretically by carefully choosing different experimental conditions. When the partial pressure of hydrogen is 0, the LH equation can be written as:

$$\frac{1}{R_{\text{spe}}} = \frac{1}{k_1} \exp(\frac{E_1}{RT}) p_{\text{H}_2\text{O}}^{-1} + \frac{k_3}{k_1} \exp\left(\frac{E_1 - E_3}{RT}\right). \tag{4-4}$$

Ideally, the reverse of specific oxidation rate is linear to the reverse of steam partial pressure at a constant reaction temperature and 0 hydrogen partial pressure. The slope of the linear line will be equal to $\frac{1}{k_1}\exp(\frac{E_1}{RT})$, and the intersection with y-axis will be equal to $\frac{k_3}{k_1}\exp\left(\frac{E_1-E_3}{RT}\right)$.

The data points of blue curves in Figure 3-19 and Figure 3-20 are rearranged to derive the LH equation theoretically, which are depicted in Figure 4-2 and Figure 4-3, respectively for reaction temperatures of 950 and 1050 °C. The slopes of the two linear fitting equations are 5.502×10^{10} and 7.939×10^{8} respectively. And the intersections with y-axis are 6.668×10^{6} and 2.515×10^{5}. Therefore, the four unknown constants, k_1, k_3, E_1, and E_3 can be rigorously obtained by solving four equations, which are 4.0989×10^{13} $Pa^{-1}s^{-1}$, 40.2084 Pa^{-1}, 570.17 kJ/mole/K, and 129.26 kJ/mole/K, respectively.

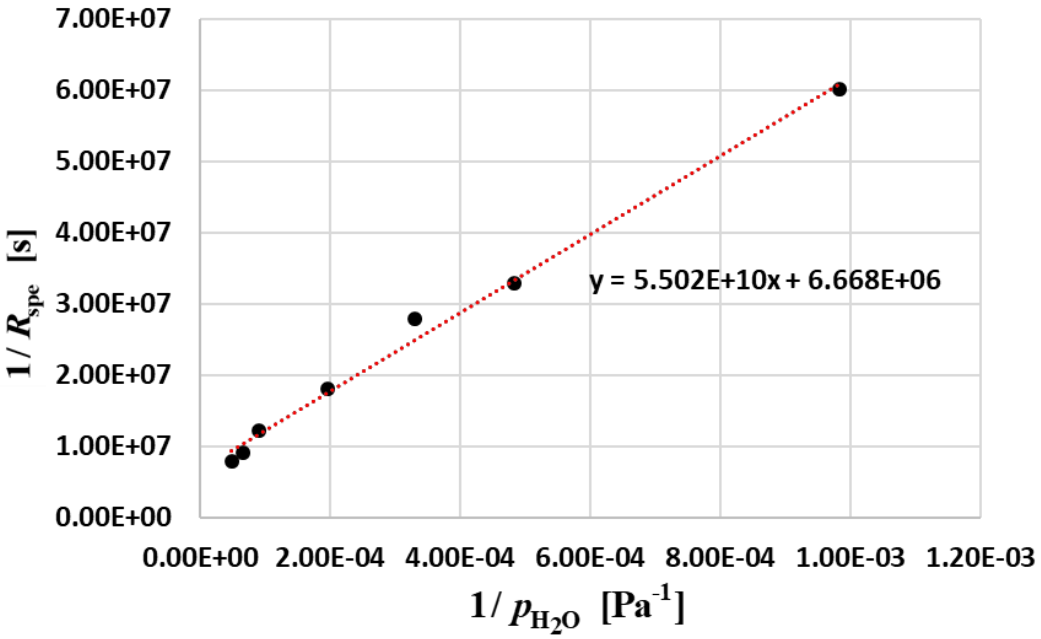

Figure 4-2 Specific oxidation rate with different steam partial pressures and zero hydrogen partial pressure at 950 °C

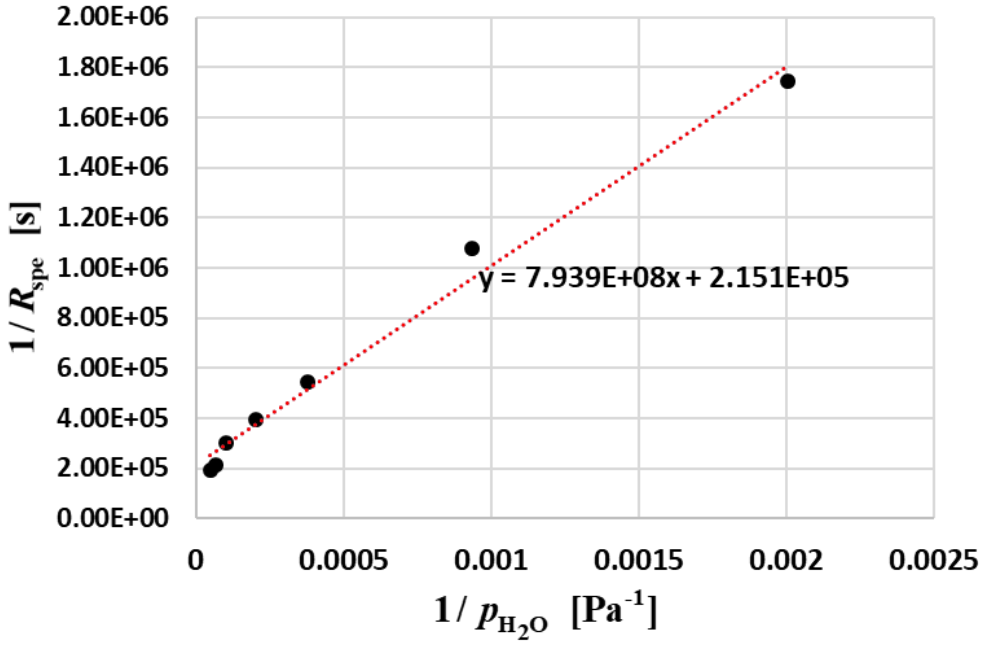

Figure 4-3 Specific oxidation rate with different steam partial pressures and zero hydrogen partial pressure at 1050°C

Next, the reaction frequency factor k_2, activation energy E_2, and hydrogen reaction order n should be determined. Eq. (4-3) can be further manipulated as:

$$\frac{1}{R_{spe}} - \frac{1}{k_1}\exp(\frac{E_1}{RT})\,p_{H_2O}^{-1} - \frac{k_3}{k_1}\exp(\frac{E_1 - E_3}{RT}) = \frac{k_2}{k_1 p_{H_2O}}\exp(\frac{E_1 - E_2}{RT})\,p_{H_2}^{n} \qquad (a)$$

$$\Downarrow$$

$$A(T) = \frac{k_2}{k_1 p_{H_2O}}\exp(\frac{E_1 - E_2}{RT})\,p_{H_2}^{n} \qquad (b) \qquad (4\text{-}5)$$

$$\Downarrow$$

$$\ln\left[A(T)\right] = \ln\left(\frac{k_2}{k_1 p_{H_2O}}\right) + \frac{E_1 - E_2}{RT} + n\ln\left(p_{H_2}\right) \qquad (c)$$

Given a specified reaction temperature and steam partial pressure, the specific oxidation rate can be plotted using Eq. (4-5c). Theoretically, a plot based on $\ln\left[A(T)\right]$ *vs.* $\ln\left(p_{H_2}\right)$ is also linear.

The slope will be the reaction order of hydrogen, and the intersection with y-axis will be equal to $\ln\left(\frac{k_2}{k_1 p_{H_2O}}\right)+\frac{E_1-E_2}{RT}$. Section 3.2.5 provides multiple plot of specific oxidation rate vs. hydrogen partial pressure under conditions of constant reaction temperature and steam partial pressure. Tentatively, two cases were used to derive the reaction constants associated with hydrogen, as shown in Figure 4-4 and Figure 4-5 with best linear fitting included. Due to the limited number of data points and possible uncertainties, the hydrogen reaction order is not consistent for the two sets of data points. The two intersections are 11.772 and 6.159, respectively. Correspondingly, the values of k_2 and E_2 can be solved to be 3.3354×10^{-14} Pa^{-n}, and -277.25 kJ/mole/K, respectively.

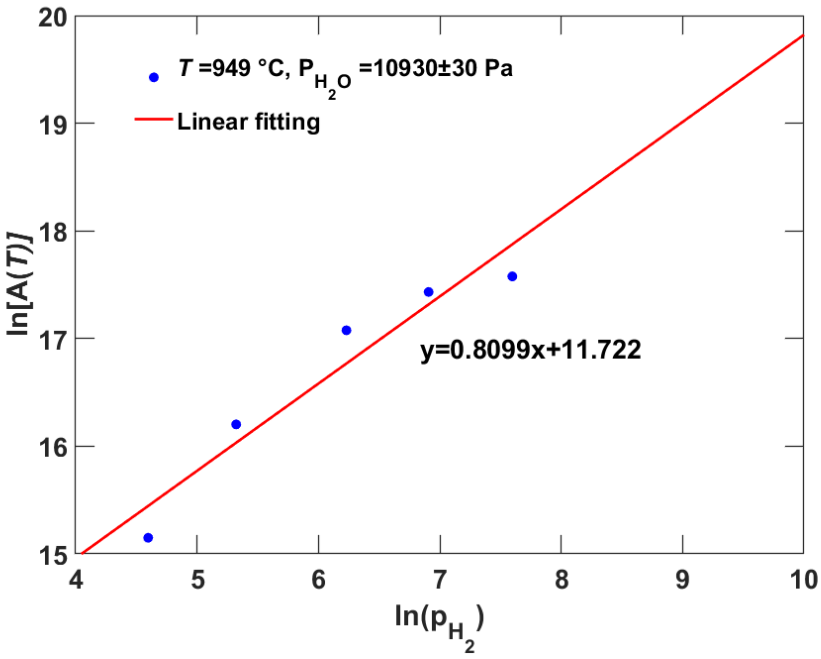

Figure 4-4 Specific oxidation rate in form of $\ln[A(T)]$ at temperature 1050°C and steam partial pressure 10 kPa

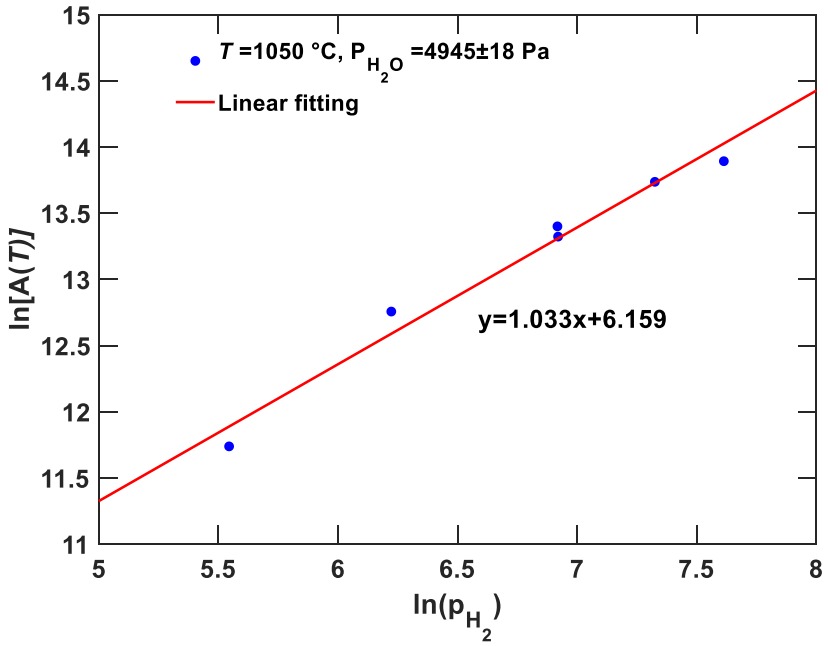

Figure 4-5 Specific oxidation rate in form of $\ln[A(T)]$ at temperature 950°C and steam partial pressure 5 kPa

The LH reaction rate equation obtained by the above theoretical analysis is listed in Table 4-1. The hydrogen reaction order is assumed to be the mean value of the two slopes in Figure 4-4 and Figure 4-5. The evaluation of this LH equation is depicted in Figure 4-6. It can be seen although the LH equation predicts comparable kinetic oxidation rates with experimental results, it tends to underestimate the low oxidation rate regime and overestimate the high oxidation rate regime. In the theoretically analyses, exponential functions were used twice, which can propagate the uncertainties of experimental data and linear fitting. Furthermore, although a total of 141 data points were obtained, only a small fraction of them were used in the derivation. Therefore, it is desired to derive the constants in LH equation by the MATLAB code using all experimental data points.

Table 4-1 Reaction constants in LH equation obtained by theoretical analysis

Reaction frequency		**Activation energy [kJ/mol/K]**	
k_1 [$Pa^{-1}s^{-1}$]	4.0989×10^{13}	E_1	570.17
k_2 [Pa^{-n}]	3.3354×10^{-14}	E_2	-277.25
k_3 [Pa^{-1}]	40.208	E_3	129.26
n [--]	0.92		

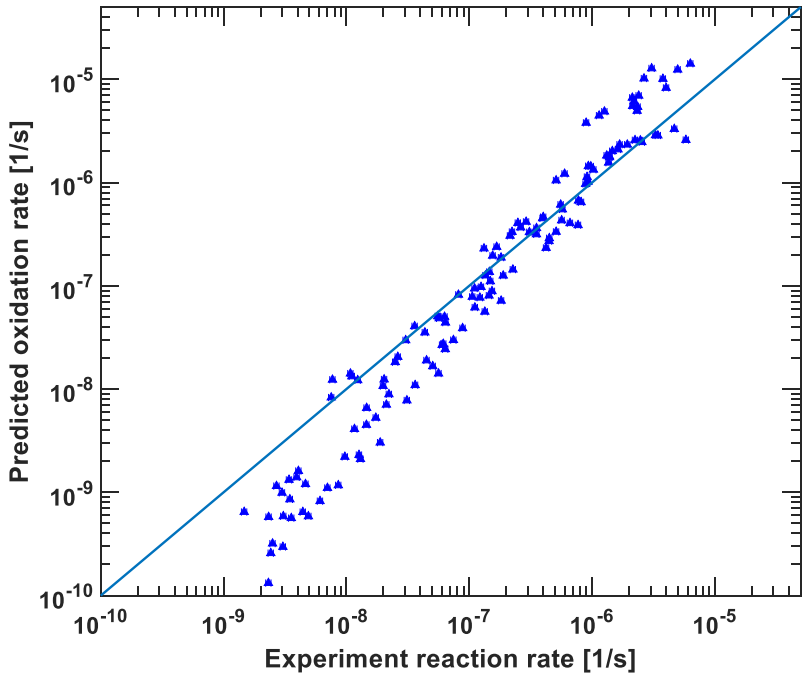

Figure 4-6 Comparison of experimental data with theoretical LH model

The values in Table 4-1 are then used as the initial guess for the multivariable optimization. The returned constants are listed in Table 4-2. In addition, Table 4-2 also provides Contescu's LH model that was obtained based on experiment at temperature 800 to 1100 C, moisture partial pressure 5 to 1000 Pa, and hydrogen partial pressure 0 to 300 Pa. The constants in the Contescu LH equation are significantly different with the optimized LH model in this work.

A comparison of the predicted oxidation rates and the experimental data is depicted in Figure 4-7. As can be seen, the optimized LH model gives better prediction than the theoretical LH model that has been shown in Figure 4-6. In addition, the optimized model has better accuracy when the oxidation rate is between 10^{-8} to 10^{-6} s^{-1}. However, large deviation is still found at the low oxidation rate regime and high oxidation regime. When the Contescu LH model was applied to the experimental conditions of this work, the predicted oxidation rates are most likely to be underestimated. The MRDs of the optimized LH model and Contescu model, evaluated using experimental data of this work, are 39.0% and 63.8%, respectively. The hydrogen reaction order of the optimized LH model is 1.83, which is higher than both the theoretical analysis and existing values in literature. Therefore, its reliability should be carefully investigated in the future. The predicted oxidation rates of the optimized LH model is shown in Figure 4-8 under various conditions. In general, the optimized LH model predicts oxidation rate qualitatively well. For example, the predicted oxidation rate increases with lifted steam partial pressure and decreased hydrogen partial pressure. In addition, it has larger slope at low steam concentration regime, which has been observed in Section 3.2.

Table 4-2 Comparison of LH models for nuclear graphite IG-110

Parameter	**This work**	**Contescu 2018** [20]
k_1 [$Pa^{-1}s^{-1}$]	3.861×10^{13}	8.3×10^{-6}
k_2 [Pa^{-n}]	1.2954	4.2×10^{-8}
k_3 [Pa^{-1}]	299.755	6.3×10^{-11}
E_1 [kJ/mol/K]	574.95	86
E_2 [kJ/mol/K]	134.75	-193
E_3 [kJ/mol/K]	148.97	-211
n [--]	1.83	0.5

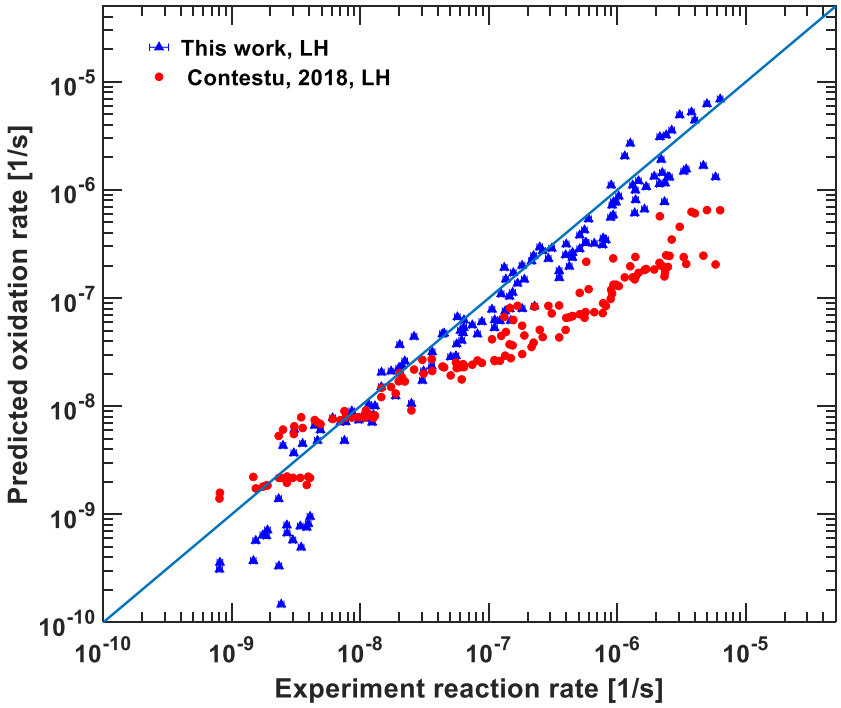

Figure 4-7 Comparison of LH models for nuclear graphite IG-110

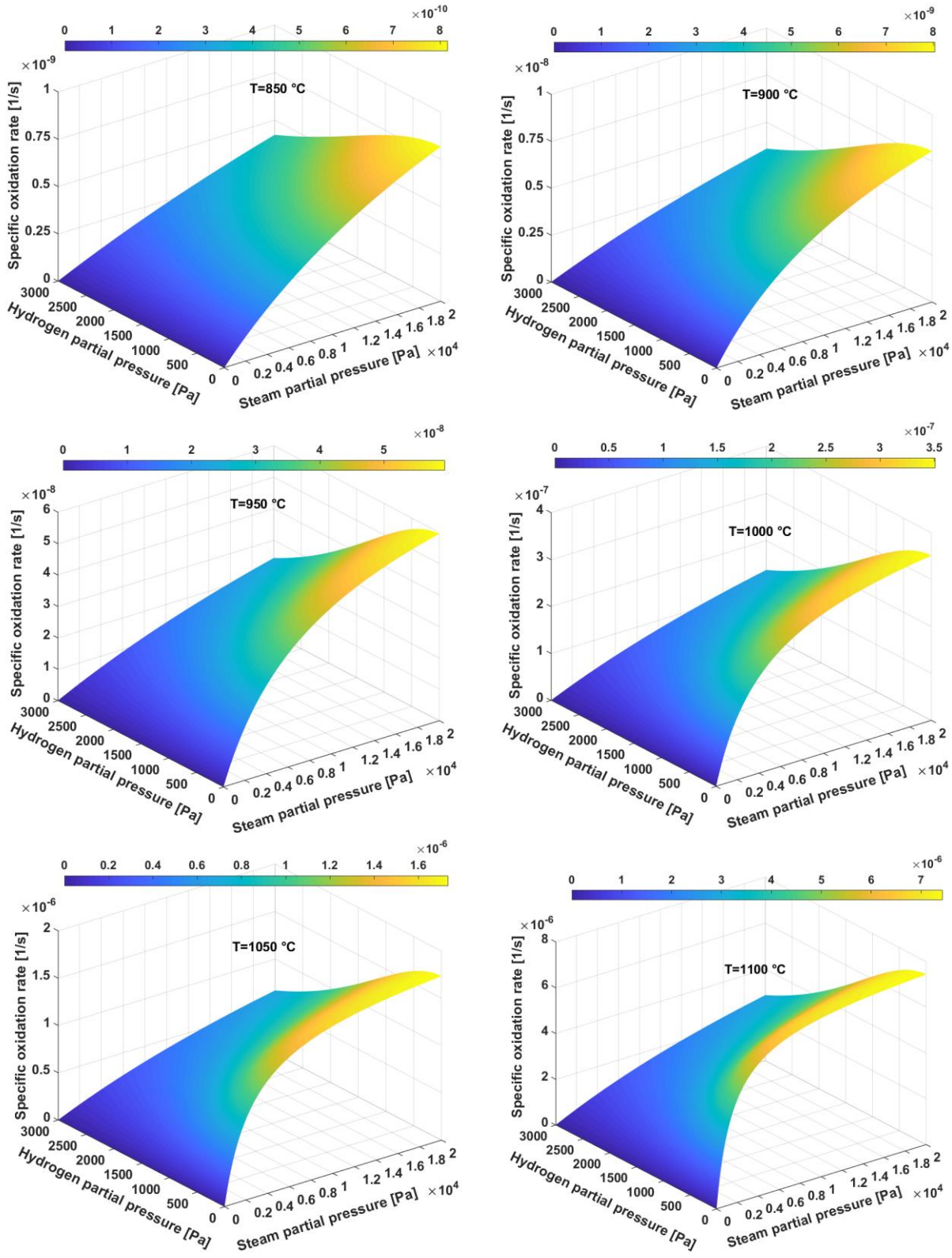

Figure 4-8 Predicted oxidation rates using the optimized LH equation under various conditions

4.3 Boltzmann-enhanced Langmuir-Hinshelwood (BLH) Reaction Rate Equation

It was found the LH model tends to underestimate the oxidation rate, especially under high temperature and high steam concentration conditions [20]. This conclusion is confirmed by the analysis in Section 4.2. Therefore, a BLH reaction rate equation was proposed to consider the broadening of active graphite sites in high temperature environment [20], in which a temperature-dependent reaction order is added to the steam term, as shown by Eq. (4-6)

$$R_{\text{spe}} = \frac{k_1 \exp(-\frac{E_1}{RT}) {p_{\text{H}_2\text{O}}}^{m(T)}}{1 + k_2 \exp(-\frac{E_2}{RT}) p_{\text{H}_2}^n + k_1 \exp(-\frac{E_3}{RT}) {p_{\text{H}_2\text{O}}}^{m(T)}} \qquad (a)$$

$$, \qquad (4.6)$$

$$m(T) = m_{\max} + \frac{m_{\min} - m_{\max}}{1 + \exp\left(\frac{T - T_0}{\theta}\right)} \qquad (b)$$

where $m_{\max}$ and $m_{\min}$ are the upper and lower limits of the range of kinetic order; T_0 is a characteristic temperature, and θ is a scaling parameter [8], [20].

While the LH reaction rate equation can be obtained by theoretical analysis, the derivation of BLH equation is more challenging due to the addition of Boltzmann equation to the steam term. As a consequence, the theoretical analysis method in Section 4.2 is no longer applicable. Therefore, the BLH equation has to be obtained by multivariable optimization. There are a total of 10 unknown coefficients in Eq. (4-6) to be optimized, excluding the reaction order of hydrogen. As discussed in Chapter 1, the energies *E* in BLH model do not reflect the activation energy because they are a joint effect of multiple elementary reactions. Therefore, the value of these energies can be either positive or negative. The coefficients *k* still represent reaction frequency,

which thereafter should be positive. The reaction order of hydrogen n has been assumed to be constant 0.75 for nuclear graphite H-451 [17], and was assumed to be 0.5 for graphite IG-110 in the BLH equation [8], [20]. In this research, n is assumed to be 0.5, 0.75, and 1.0, respectively in the optimization computation. Another optimization was run by assuming n is unknown, and limiting its value in range 0.5 to 2.0.

In order to reduce the computation time, a total only 24 data points (4 from each temperature interval with different moisture and hydrogen partial pressures) were first selected for optimization. Computations were carried out using different initializations to ensure the obtained BLH equation agrees with the 24 data. Then the rest data points were added in a few batches. The obtained coefficients in the BLH equation are listed in Table 4-3. The coefficients, except k_2, do not vary much with different assumptions for the hydrogen reaction order. If n is included in the optimization process, the optimization returns n of 0.801. The MRD associated with the four optimizations does not differ much. Considering the uncertainties in the experimental data, it is hard to determine which combination is the best since they all have very similar MRD values. On the other hand, the BLH equation obtained in this work is significantly different from the existing BLH equation which was derived using experimental data with lower vapor concentrations [8], [20].

Table 4-3 Comparison of different BLH equations

Coefficient	***n*=0.5**	***n*=0.75**	***n*=1.0**	**Unknown *n***	**Contescu (2018)**
k_1 [$Pa^{-1}s^{-1}$]	76.54	78.40	79.16	79.15	7.6×10^{-12}
E_1 [kJ/mol]	253.67	256.47	260.55	258.22	-71.0
k_2 [$Pa^{-0.5}$]	6.938×10^{-3}	1.200×10^{-3}	1.789×10^{-4}	8.232×10^{-4}	1.9×10^{-2}
E_2 [kJ/mol]	-19.32	-19.19	-20.15	-19.31	-40
k_3 [Pa^{-m}]	3.496×10^{-2}	3.496×10^{-2}	2.996×10^{-2}	3.496×10^{-2}	6.1×10^{-18}
E_3 [kJ/mol]	313.87	313.86	313.86	313.86	-374
m_{min} [--]	0.313	0.356	0.390	0.364	-0.07
m_{max} [--]	0.704	0.736	0.761	0.742	1.55
T_0 [K]	1249.9	1250.0	1250.5	1250.1	64.2
θ [K]	36.29	34.44	32.82	34.08	1327
n [--]	--	--	--	**0.801**	0.5
RMSD [%]	24.60	23.92	24.10	23.91	84.22

Figure 4-9 to Figure 4-12 show the comparison of predicted oxidation rates of the optimized BLH equations with experimental data. The predicted oxidation rates by Contescu BLH equation is also depicted in Figure 4-12. It can be seen the four optimized BLH equations of this work give very similar results. If *n* is considered as an unknown constant in the optimization, the MRD of BLH equation is 23.9%, which is the smallest. Therefore, it will be used in the following analysis.

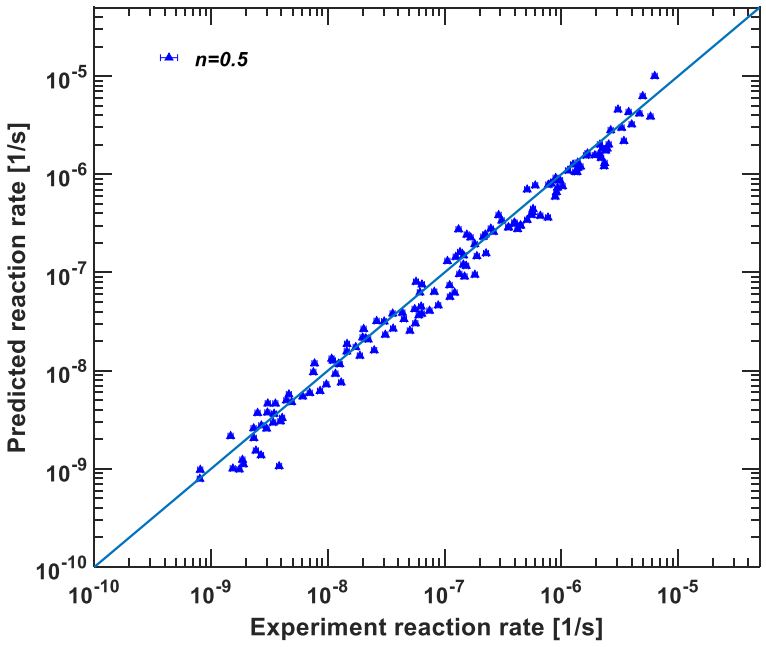

Figure 4-9 Evaluation of BLH model with pre-determined n=0.5

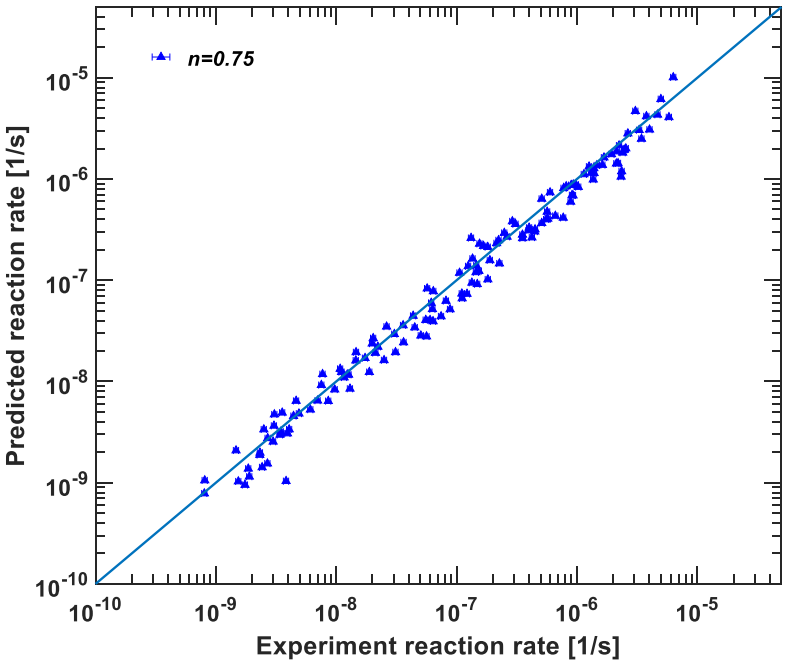

Figure 4-10 Evaluation of BLH model with pre-determined n=0.75

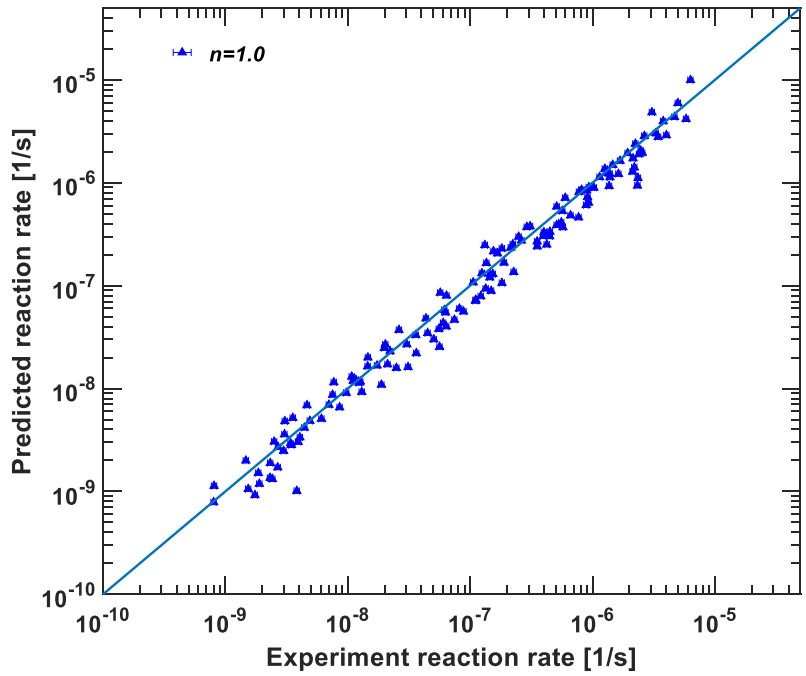

Figure 4-11 Evaluation of BLH model with pre-determined n=1.0

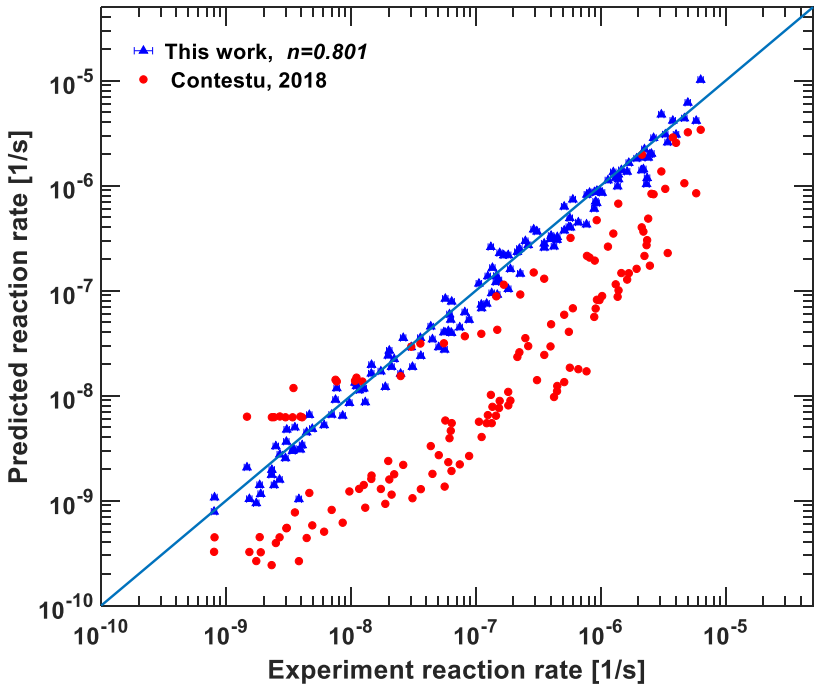

Figure 4-12 Evaluation of BLH equation with optimized n=0.801 and Contescu BLH equation

Figure 4-13 shows the predicted oxidation rates of the BLH equation at temperature 850 to 1100 °C, steam partial pressure 0 to 20 kPa, and hydrogen partial pressure 0 to 3 kPa. It can be seen this BLH model demonstrates two features that have been discussed in Section 3.2.4 and 3.2.5. First, the predicted oxidation rate always increase with steam partial pressure given a specified reaction temperature and hydrogen partial pressure. In addition, the effect of steam concentration on lifting the oxidation rate is more prominent at the beginning, and then slows down when the steam partial pressure reaches higher values. Similarly, the suppression effect of hydrogen on reaction is more obvious within a low hydrogen concentration regime. The predicted oxidation rates drop dramatically with hydrogen concentration, then tend to flatten in high hydrogen concentration regime. In conclusion, the new BLH equation of this research shows very good accuracy.

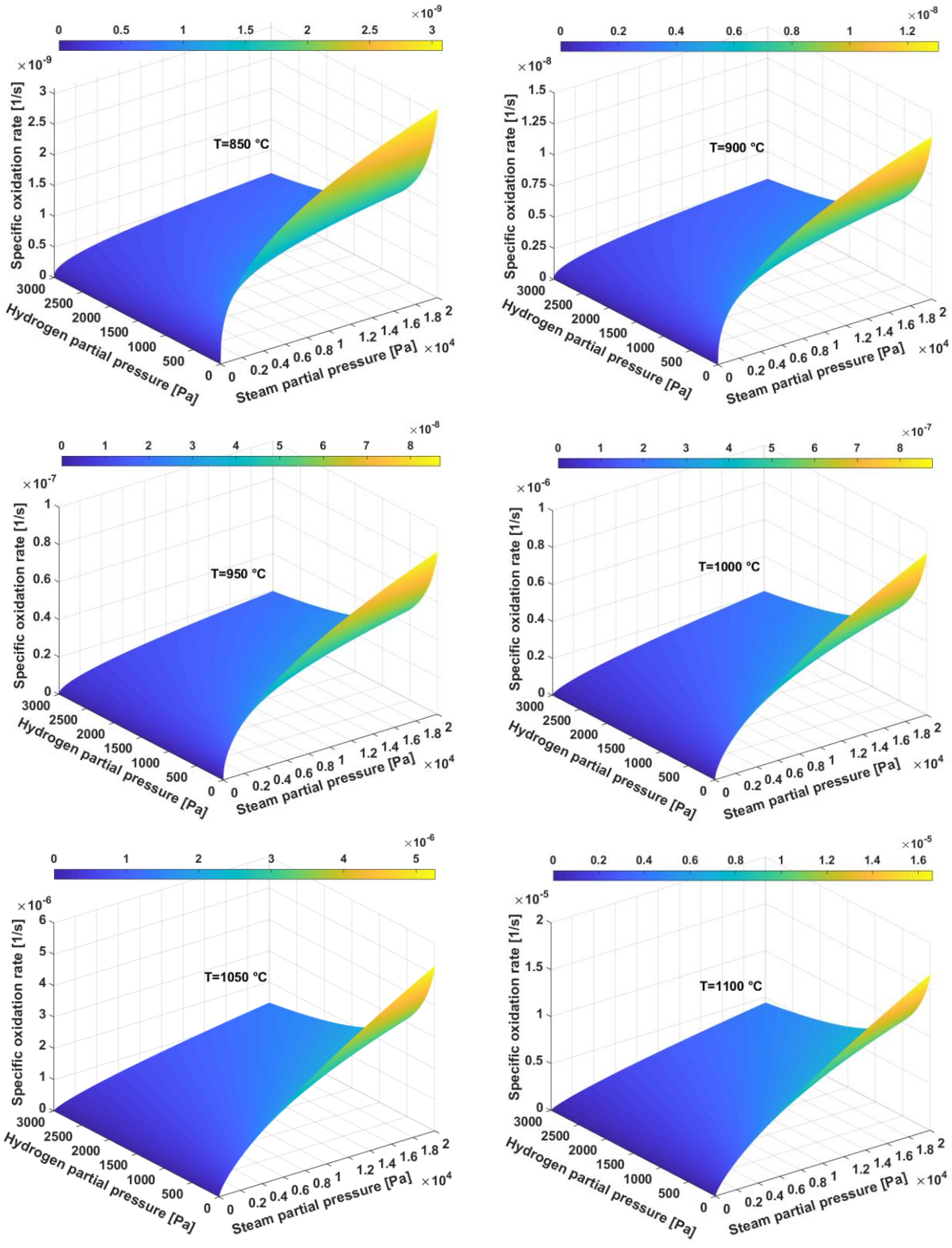

Figure 4-13 Predicted oxidation rates using optimized BLH equation

4.4 Comparison of Different Kinetic Reaction Rate Equations

Both LH and BLH kinetic reaction rate equations have been obtained in the above analyses using the experimental data. In general, the BLH equation agrees with the experimental results better than the LH equation within the experimental conditions of this work. The LH and BLH equations for graphite IG-110 were also proposed in existing literature, although under different experimental conditions. The comparison of the two equations, and existing models are cross-compared in this section.

One issue of this work and existing literature is that the steam concentration in the experiments was not extended to an extremely low level, i.e., ppm level. However, one concern of graphite-steam/moisture oxidation is the chronic corrosion during the long term reactor normal operations. If the reaction rate equations are to be used for analyses for reactor normal operations, the reader should be careful in choosing one from these equations. Figure 4-14 shows the comparison of the four reaction rate equations for graphite IG-110 at low steam concentration regime. In this figure, the hydrogen partial pressure is constant 5 Pa. It can be seen the BLH equation obtained in this work gives very similar trend as the Contescu LH equation but the absolute value is about one magnitude higher. The predicted oxidation rate by the LH equation of this work is much lower than the other three equations under low temperature, low moisture concentration condition, which means it might underestimate the oxidation rate. The Contescu BLH model, however, predicts the oxidation rate will decrease with higher temperature, which is physically unlikely. Therefore, it is suggested to use either the BLH equation obtained in this work, or the Contescu LH equation for reactor normal operation conditions.

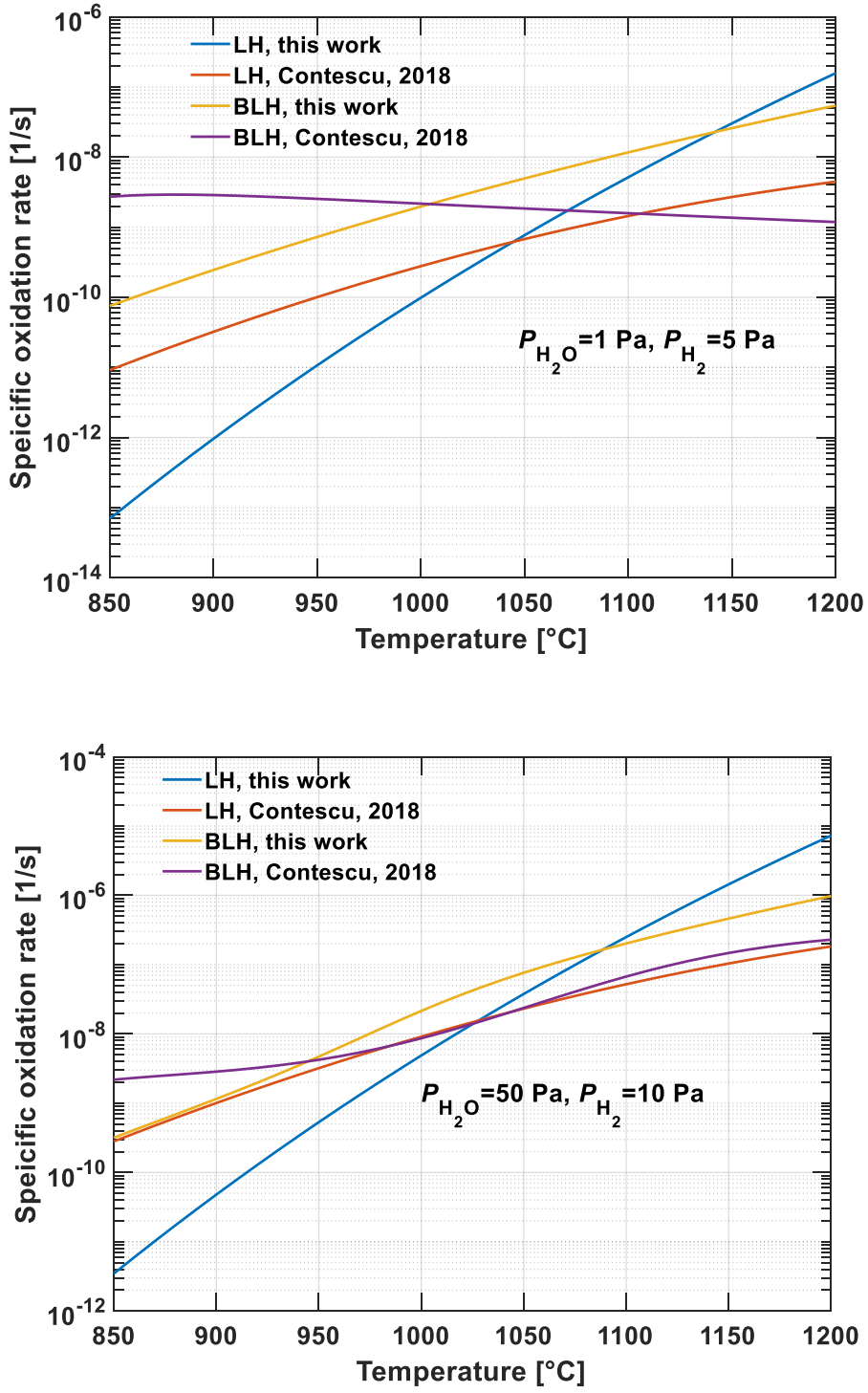

Figure 4-14 Predicted oxidation rate using different equations at low steam concentration regime

Figure 4-15 depicts the four reaction equations at a high steam/moisture concentration regime. In this figure, the hydrogen partial pressure is constant 500 Pa. It can be seen the Contscu LH equation is significantly different from the Contescu BLH equation although they were derived using the same experimental data. As a comparison, the LH and BLH equation obtained in this work agrees each other well within temperature 900 to 1100 °C. The difference of these two equations out of this temperature range is also smaller than Contescu's models, which can be regarded as an advantage. Both of the two BLH equations show an "S" shape, which is the result of adding Boltzmann reaction order to the term of steam partial pressure.

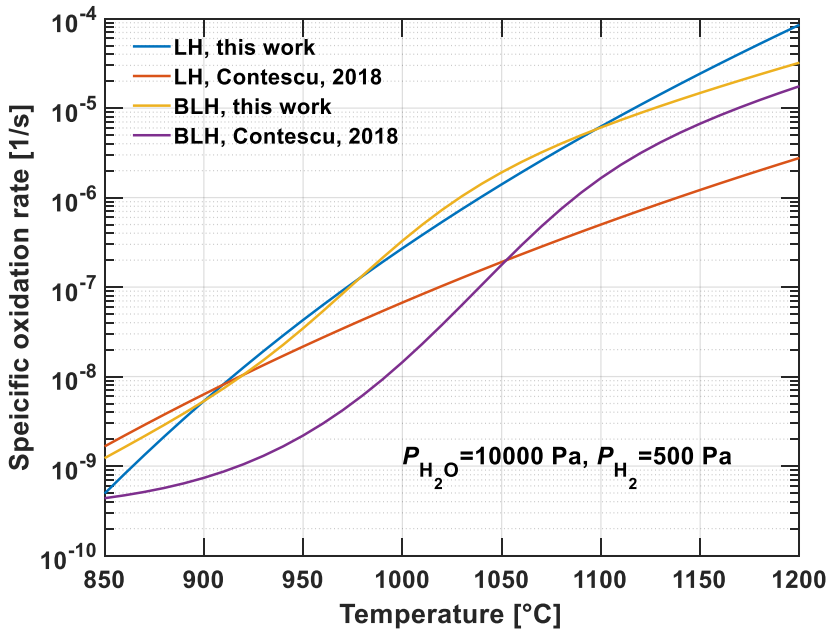

Figure 4-15 Predicting oxidation rate by different equations at high steam concentration regime

The variation of the four equations with steam partial pressure is depicted in Figure 4-16 and Figure 4-17 at constant temperature 950 and 1100 °C, respectively. It can be seen the Contescu BLH equation is the least sensitive one with increasing steam partial pressure. The predicted

oxidation rate at 10 kPa is about 6~7 times higher than that at 10 Pa, while the other three equations give much larger increase rate of oxidation rate with steam partial pressures. In addition, the four equations differ significantly at low temperature, low steam concentration regime. As shown in Figure 4-17, the predicted oxidation rate using the two LH equations tend to flatten at steam partial pressure than 1000 Pa, which is the main reason for the introduction of BLH equation. The BLH equation derived in this work is obviously different from the Contescu BLH equation. At steam partial pressure higher than 1 kPa, the Contescu BLH equation also tends to flatten although with a smaller slope than the LH equations. On the contrary, the trend of the BLH equation of this work does not change much. It should be noted that the data points in this work mainly cover steam partial pressure between 1 to 10 kPa. Therefore, the BLH equation of this work should be more reliable if steam concentration is higher than 1 kPa.

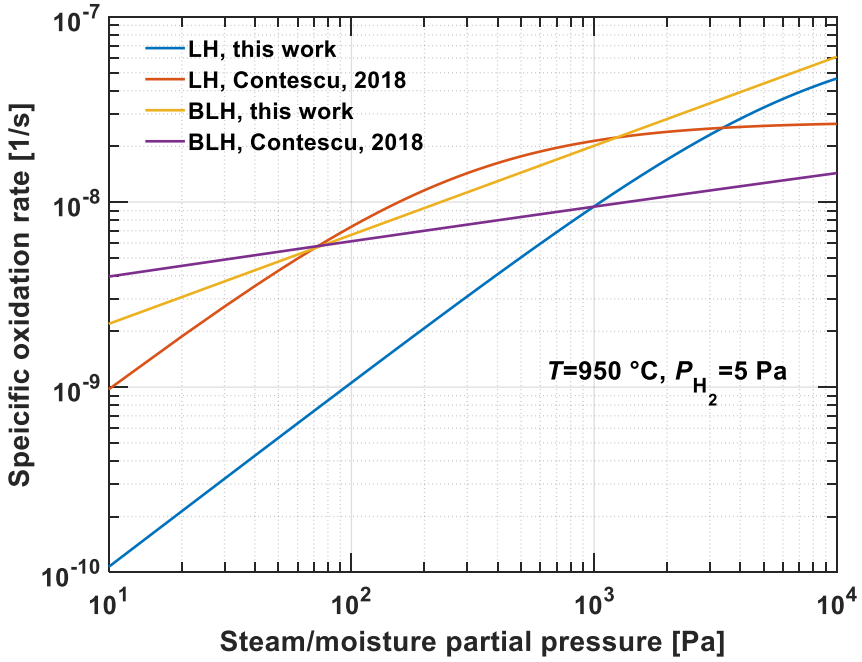

Figure 4-16 Predicted oxidation rate by different equations at fixed temperature 950 °C

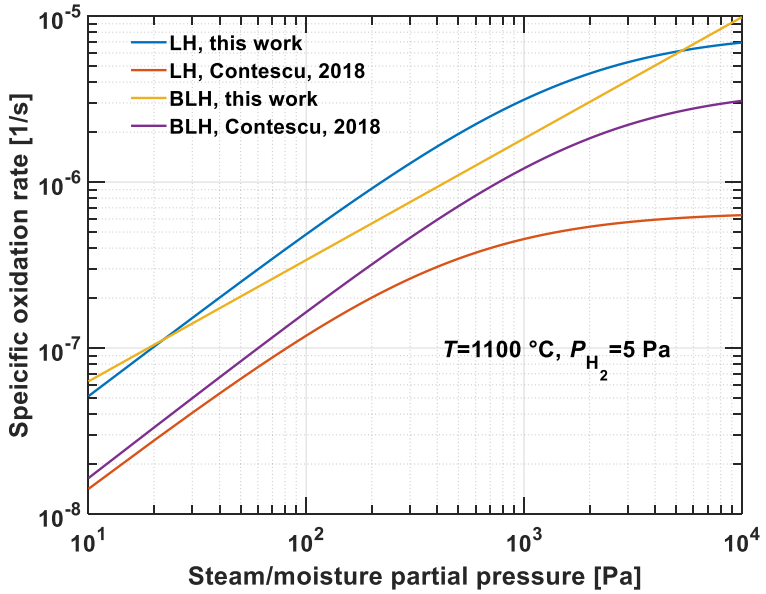

Figure 4-17 Predicted oxidation rate by different equations at fixed temperature 1100 °C

In conclusion, the four reaction equation exhibits significantly different behaviors at different conditions. However, it is suggested to use the BLH model from this work, or the Contescu LH equation for reactor normal operation conditions. For scenarios with extremely high steam concentration, the BLH model from this work is still recommended because it is derived based on steam partial pressure up to 20 kPa.

Chapter 5 Multiphysics Simulation for Graphite-Steam Oxidation

5.1 Objective of Multiphysics Simulation for Graphite-Steam Oxidation

The graphite-steam oxidation in HTGR is a complex phenomenon involving multi physical processes with the following steps:

1. Transport of water molecules in the free helium flow to the graphite surfaces;

2. Transport of water molecules in the porous graphite to the graphite active sites;

3. Water molecules react with the graphite at the active sites (C-H_2O reaction):

$$C + H_2O\uparrow \rightarrow CO\uparrow + H_2\uparrow;$$

4. Release of the reaction products (CO, and H_2); and

5. Transport of the production gases through the porous graphite back to the free helium flow.

In addition to the main heterogeneous reaction, the production gases can trigger a secondary homogenous reaction: $CO\uparrow + H_2O\uparrow \rightleftharpoons CO_2\uparrow + H_2\uparrow$, and a secondary heterogeneous reaction: $C + CO_2\uparrow \rightleftharpoons 2CO\uparrow$. At the same time as the above processes, heat transfer and graphite microstructure evolution can also affect the apparent oxidation rate. Although extensive studies

have been carried out in literature to investigate the graphite oxidation phenomena, there is a lack of effect tool to predict the graphite oxidation given a specified condition.

This chapter is aimed to develop a modeling method that can predict graphite mass loss in detail, such as the spatial distribution of graphite mass loss fraction, and the evolution of apparent oxidation rate. The multiphysics model should couple all important physical phenomena, i.e., the free flow out of graphite, porous flow in porous graphite, mass transfer in free helium flow and porous graphite domain, heat transfer, kinetic chemical reaction, as well as the evolution of micro porous structure. The numerical model will be validated against the experimental results of Section 3.4 so it can be applied to future HTGR safety analyses with better confidence.

5.2 Mathematic Models

5.2.1 Mass transfer in free helium flow channel and porous graphite media

The graphite oxidation phenomenon can be divided into three regimes, namely the kinetics controlled regime, transitional regime, and diffusion controlled regime. The kinetics controlled regime refers to oxidation at low temperature environment that the graphite oxidation is limited by chemical reaction. In this regime, the kinetic chemical reaction rate is so small that the oxidant molecules can easily diffuse into the whole volume of a graphite component. Therefore, the graphite will be oxidized more or less uniformly. On the contrary, if the reaction temperature is high enough, the kinetic chemical reaction rate will be so large that it is no longer the dominant factor in the observed oxidation rate (apparent oxidation rate). In this regime, the observed oxidation will be limited by the mass transfer rate through the boundary layer between graphite sample and free flow. In addition, the oxidant molecules will be quickly consumed once they reach the graphite sample surface, so they cannot penetrate into the inner region of graphite. As a result,

only a very thin layer of graphite will be oxidized. The transitional regime refers to the scenario that mass transfer and kinetic reaction make comparable contribution to the apparent oxidation rate, in which the graphite mass loss fraction decreases gradually from its surface into the inner region. A schematic of the three reaction regimes is shown in Figure 5-1.

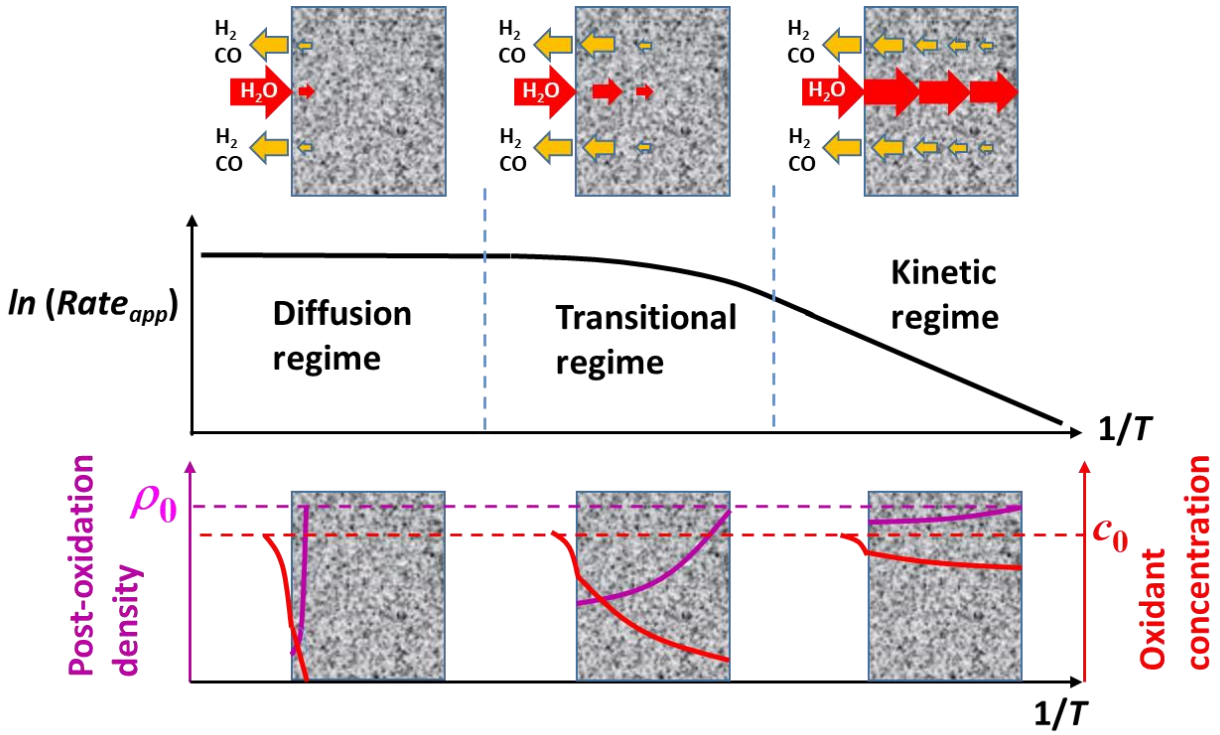

Figure 5-1 Schematic of three graphite oxidation regimes

However, it should be noted the critical temperature between two regimes is not constant. Instead, it depends not only on the kinetic reaction properties but also on the free flow conditions. For instance, the switch from diffusion regime to transitional regime will migrate to a higher temperature by increasing the free flow rate , which leads to a large Sherwood number:

$$\mathrm{Sh}=\frac{hL}{D} \tag{5-1}$$

where:

h	convective mass transfer coefficient,	m/s
L	characteristic length,	m
D	mass diffusivity	m^2/s

On the contrary, the transition tends to move to a lower temperature for small flow rate condition. During a steam ingress accident, the free helium flow in the prismatic HTGR core will gradually switch from turbulent convection to natural circulation, which will then affect the apparent oxidation behavior. In addition, the diffusion controlled regime for graphite-oxygen oxidation will appear at a lower temperature than that of graphite-steam oxidation under the same flow conditions, since the kinetic chemical reaction rate of graphite-oxygen reaction is much higher. Furthermore, the micro structure of a certain grade of graphite can also play an important role the final oxidation depth. For example, a graphite with high tortuosity, low permeability and porosity, small pores can slow down oxidant penetration. Therefore, it is critical to accurately simulate the mass transfer mechanism for graphite-steam oxidation.

Theoretically, there are three chemical reactions in graphite-steam oxidation, which are the main heterogeneous reaction (C-H_2O reaction): $C + H_2O\uparrow \rightarrow CO\uparrow + H_2\uparrow$, the secondary homogeneous reaction: $CO\uparrow + H_2O\uparrow \rightleftharpoons CO_2\uparrow + H_2\uparrow$, and the secondary heterogeneous reaction: $C + CO_2\uparrow \rightleftharpoons 2CO\uparrow$, respectively. To simplify the problem, the numerical model will only focus on the main heterogeneous C-H_2O reaction because the reaction rates of the two secondary reactions are much lower[64]. Therefore, there are a total of four gas species to be

modeled in the system. The transport of gas species *j* can be solved by the Maxwell-Stephan multicomponent gas diffusion equations:

$$\frac{\partial}{\partial t}\left(\rho\omega_j\right)+\nabla\cdot\vec{J}_j+\rho\left(\vec{u}\cdot\nabla\right)\omega_j=R_j \tag{5-2}$$

for free flow domain, and

$$\frac{\partial}{\partial t}\left(\varepsilon\rho\omega_j\right)+\nabla\cdot\vec{J}_j+\rho\left(\vec{u}\cdot\nabla\right)\omega_j=R_j \tag{5-3}$$

for porous graphite domain, respectively, where:

ρ	density of gas mixture	kg/m^3
ω	mass fraction	--
ε	graphite porosity	--
t	time	s
$\vec{J}$	mass flux	kg/m^2/s
$\vec{u}$	flow velocity	m/s
R	reaction mass source	kg/m^3/s

Since it has been assumed the only chemical reaction is the main heterogeneous C-H_2O reaction, the source term for free flow in Eq. (5-2) is thereafter always zero. The mass flux in Eq. (5-2) is calculated by:

$$\vec{J}_j=-\left(\rho\omega_j\sum_{i,i\neq j}^{4}D_{j-i}\vec{d}_i+D_j^T\frac{\nabla T}{T}\right), \tag{5-4}$$

$$\vec{d}_i = \nabla x_i + \frac{1}{p}\left[\left(x_i - w_i\right)\nabla p\right], \text{ and} \tag{5-5}$$

$$x_i = \frac{\omega_i}{M_i}\left(\sum_j \frac{w_j}{M_j}\right)^{-1}, \tag{5-6}$$

where:

ω	mass fraction	--
x	mole fraction	--
p	absolute pressure	Pa
M	mole mass	g/mol
$D_{j\text{-}i}$	binary diffusivity	m^2/s
D^T	thermal diffusion coefficient	m^2/s

The first term at RHS of Eq. (5-4) describes the molecular diffusion. The binary diffusivity is calculated by Eq. (5-7) [65]:

$$D_{j-i} = D_{i-j} = \frac{1.858\times10^{-3}T^{3/2}\left(\frac{1}{M_i}+\frac{1}{M_j}\right)^{1/2}}{p\sigma_{ji}^2\Omega_D} \tag{5-7}$$

with M and p to be the molar mass in mol/g and absolute pressure in atm, respectively. The collision diameter between two different molecular species σ_{ji} in Å is the mean value of σ_i and σ_j. The collision interval Ω_D is a function of non-dimensional temperature $\kappa T / \varepsilon_{AB}$, where $\varepsilon_{AB}/\kappa = \sqrt{\left(\varepsilon_A/\kappa\right)\times\left(\varepsilon_B/\kappa\right)}$. Figure 5-2 depicts a series of discrete $\kappa T / \varepsilon$ values and their

corresponding collision intervals, which was used as an interpolation database in the numerical model. Table 5-1 lists the Lennnar-Jones constants that were used in the diffusivity computation.

Table 5-1 Lennnar-Jones constants for diffusivity computation [65]

Gas species	He	H_2	CO	Steam
σ [Å]	2.576	2.968	3.590	2.649
ε / κ [K]	10.22	33.3	110	356

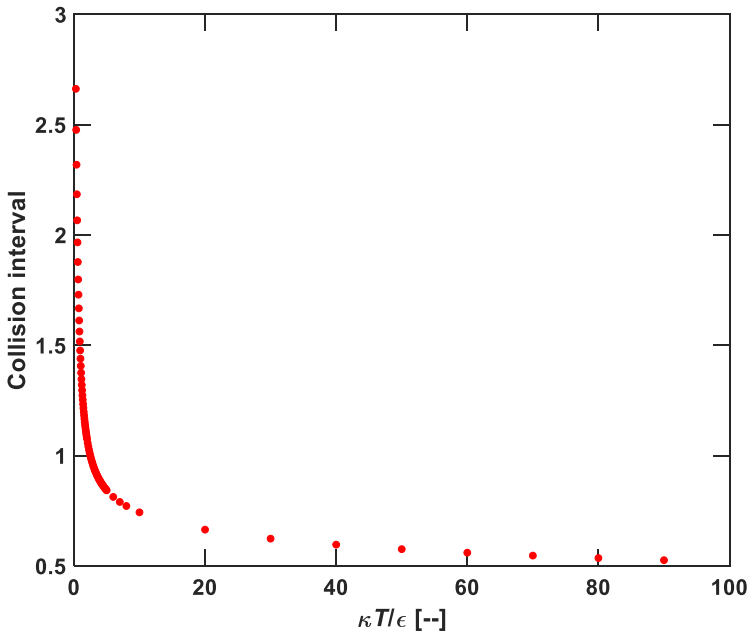

Figure 5-2 Variation of gases collision interval with non-dimensional temperature (plotted using data in literature [65])

The second term at RHS of Eq. (5-4) considers molecule diffusion that is induced by thermal diffusion. The thermal diffusion coefficient is a physical parameter having the meaning of a proportionality coefficient which establishes the dependence of the mass thermal diffusion flow of a given mixture component on the ratio of the temperature gradient to the absolute temperature. It

was believed that dominant mechanisms of mass transfer in the free flow domain is convection for bulk flow region, and molecular diffusion for laminar boundary layer. Therefore, the thermal diffusion mass transfer in Eq. (5-4) can be neglected.

The mass transfer equation for the porous graphite domain is similar to that of free flow domain, except it has to consider the porous structure, i.e., porosity, and tortuosity etc. Therefore, an effective diffusivity D_e is adopted for mass flux computation:

$$\vec{J}_j = -\left(\rho \omega_j \sum_{i,i\neq j}^{4} D_{e,j-i} \vec{d}_i + D_{e,j}^{T} \frac{\nabla T}{T} \right) \tag{5-8}$$

$$D_{e,j-i} = f\left(\varepsilon, \tau\right) D_{j-i} \tag{5-9}$$

where τ refers to the tortuosity of graphite, defined as the ratio of the length of a curve to the linear distance between its two ends . The correction function in Eq. (5-9) is usually assumed to be:

$$f\left(\varepsilon, \tau\right) = \frac{\varepsilon}{\tau} \tag{5-10}$$

The tortuosity value of a porous media can be obtained by 3-D tomography. However, it is very challenging to directly measure the tortuosity of a nuclear graphite since a small graphite volume can contain numerous pores and their diameter can vary from several nanometers to a few hundred micrometers [48]. Figure 5-3 shows a tomography image of nuclear graphite IG-110 specimen with about 0.2 mm diameter and 0.05 mm thickness. Since the resolution of this tomography is 700 nm, all micro pores less than 1.4 μm are theoretically invisible from this image. In actual practice, the tortuosity of a porous media is usually assumed as:

$$\tau = \varepsilon^{-n} \tag{5-11}$$

where the value of *n* can be unity 1 [46], [59], [66], 1/2 as the Bruggeman tortuosity model [67], or 1/3 as the Millington and Quirk tortuosity model [68]. The value of *n* has significant effect on the oxidation depth as it can lead to quite different effective diffusivity values.

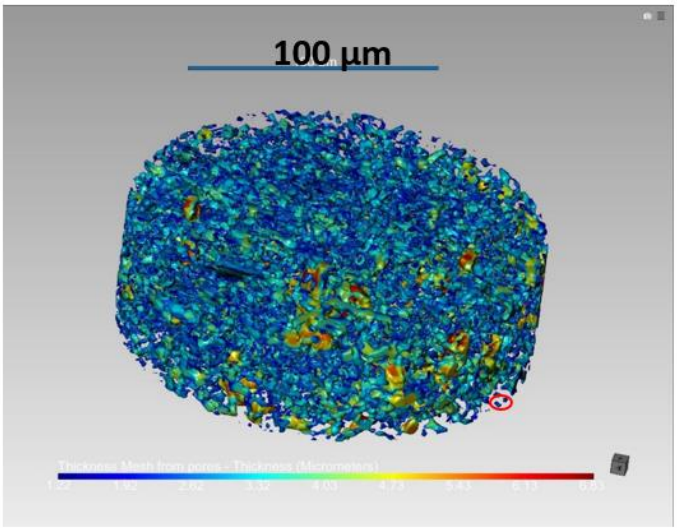

Figure 5-3 Micro porous structure of nuclear graphite IG-110 obtained by 3-D X-ray tomography with resolution of 700 nm

The mass source term in Eq. (5-3) is adopted by modifying the kinetic BLH reaction rate equation, which has been obtained in Chapter 4. It should be noted Eq. (4-6) refers to the specific oxidation rate that is in unit of 1/s. Governing equations (5-3) and (5-4) are derived using control volume methodology. Therefore, Eq. (4-6) should be multiplied by the graphite density, which then describes the consumption rate of graphite by the chemical reaction:

$$R_c = \frac{\rho_0 k_1 \exp(-\frac{E_1}{RT}) {p_{H_2O}}^{m(T)}}{1 + k_2 \exp(-\frac{E_2}{RT}) p_{H_2}^n + k_1 \exp(-\frac{E_3}{RT}) {p_{H_2O}}^{m(T)}} \quad \text{, unit in kg/m}^3\text{/s} \qquad (5\text{-}12)$$

According to the mass balance of chemical reaction $C + H_2O\uparrow \rightarrow CO\uparrow + H_2\uparrow$, the source term for steam, CO, and H_2 are:

$$R_j = \frac{\rho_0 k_1 \exp(-\frac{E_1}{RT}) {p_{H_2O}}^{m(T)}}{1 + k_2 \exp(-\frac{E_2}{RT}) p_{H_2}^n + k_1 \exp(-\frac{E_3}{RT}) {p_{H_2O}}^{m(T)}} \frac{M_j}{M_C}, \text{ unit in kg/m}^3\text{/s} \qquad (5\text{-}13)$$

where M is the molar mass. The subscript j and C indicate a gas species (steam, H_2, or CO), and carbon, respectively. Since steam is consumed by the chemical reaction, the source term for steam is always negative.

As discussed in Section 3.3, the chemical reaction alters the micro structure of graphite, which then increases the kinetic reaction rate. Therefore, a mass loss factor should be applied to the source term. In addition, impurities, up to 40 elements, inevitably existing in pristine graphite [69], [70] , although purification technique, e.g., thermal purification at temperature up to 2600 to 3000 °C, has been applied in the manufacturing process [70]. These impurities can catalyze the graphite oxidation. The oxidation rate observed in Chapter 3 already includes the effect of virgin impurities. Therefore, it is not considered here. However, the neutron fission in a nuclear reactor will produce extra impurities, which is beyond the scope of this work. In summary, the source term for Eq. (5-3) is:

$$R_j = \frac{\rho_0 F_m M_j}{M_C} \frac{k_1 \exp(-\frac{E_1}{RT}) {p_{H_2O}}^{m(T)}}{1 + k_2 \exp(-\frac{E_2}{RT}) p_{H_2}^n + k_1 \exp(-\frac{E_3}{RT}) {p_{H_2O}}^{m(T)}}, \text{ unit in kg/m}^3\text{/s} \qquad (5\text{-}14)$$

The gas diffusion can also be simulated by using the averaged gas mixture diffusion equation. When using this equation, the bulk diffusivity of component j in the gas mixture is calculated by [65]:

$$D_{j-\mathrm{m}} = \frac{1}{\frac{m_1}{D_{j-1}} + \frac{m_2}{D_{j-2}} + \cdots + \frac{m_i}{D_{j-n}}}, \tag{5-15}$$

where m_i is the molar fraction evaluated on a component *i*-free system. The effective diffusivity of component *j* in a porous graphite is calculated by considering the graphite tortuosity, gas mixture diffusivity, and Knudsen diffusivity:

$$D_{e,j} = f(\varepsilon, \tau)\frac{D_{j\text{-m}} D_{K,j}}{D_{j\text{-m}} + D_{K,j}} \tag{5-16}$$

where $D_{K,\mathrm{j}}$ is the Knudsen diffusivity:

5.2.2 Free and porous flow model

The flow velocity is needed to solve the mass transfer equations Eq. (5-2) and Eq. (5-3), which is therefore solved separately by the continuity and momentum conservation equations. To further simplify the problem, it was assumed all gas species have the same convection flow velocity. Thereafter, the flow field can be solved by single-phase flow equations rather than multi-phase flow that can be computationally expensive. The continuity and momentum equations for the free flow domain are:

$$\frac{\partial \rho}{\partial t} + \nabla \cdot (\rho \vec{u}) = 0, \text{ and} \tag{5-17}$$

$$\frac{\partial}{\partial t}(\rho\vec{u}) + \nabla\cdot(\rho\vec{u}\otimes\vec{u}) = -\nabla p + \nabla\cdot\tau + \rho\vec{g} \tag{5-18}$$

respectively, where τ and $\vec{g}$ are the stress tensor and gravitational acceleration.

The gas mixture flow in the quartz tube is laminar flow that has a Reynolds number about 50 to 200. Accordingly, the laminar flow is adopted for model validation. However, the Reynolds number of helium flow in the coolant channels of MHTGR can reach to about 50,000 during normal operations. Therefore, a turbulent model should be adopted. In this research, the turbulent flow was simulated by solving the Reynolds Averaged Naiver-Stokes (RANS) equation with k-epsilon turbulence and Algebraic y^+ model.

The micro pore structure of the graphite results in such a small velocity that the viscous term becomes dominant, which can be described by the Darcy law [71]. Therefore, the continuity and momentum equations for the porous graphite domain are:

$$\frac{\partial}{\partial t}(\varepsilon\rho) + \nabla\cdot(\rho\vec{u}) = \dot{R}, \text{ and} \tag{5-19}$$

$$\vec{u} = -\frac{\kappa}{\mu\varepsilon}\nabla p, \tag{5-20}$$

where μ and κ are gas mixture viscosity and permeability, respectively. The permeability κ can be calculated by [72]–[74]:

$$\kappa = \frac{\varepsilon r_p^2}{8\tau^2}\left(1 + \frac{\beta_s \mu}{r_p p}\sqrt{\frac{RT}{M}}\right) \tag{5-21}$$

where R, T, M, and r_p are respectively the specific ideal gas constant, temperature in Kelvin, mean molar mass of the gas mixture, and mean pore radius, where β_s is the gas-wall reflection coefficient that is assumed to be 5 [73]. In addition, the Stokes-Brinkman equation was also applied to the porous graphite domain to draw a comparison with the Darcy law. The Stokes-Brinkman equation are:

$$\frac{\rho}{\varepsilon}\frac{\partial \vec{u}}{\partial t}+\frac{\rho}{\varepsilon}\left(\vec{u}\cdot\nabla\right)\vec{u}\frac{1}{\varepsilon}+\nabla p=-\mu\kappa^{-1}\vec{u}+\nabla\cdot\mu^{*}\left(\nabla\vec{u}+\nabla\vec{u}^{T}\right), \tag{5-22}$$

which degrades to the Stokes equation when the effective viscosity μ^{*}, defined as μ/ε, is infinite. It becomes the Darcy law if μ^{*} is zero. The mean pore radius r_p is needed by Eq. (5-21), but it varies as the reaction proceeds. Therefore, it should also be modeled, which will be discussed in Section 5.2.4.

5.2.3 Heat transfer in graphite and free flow

The temperature of the free flow domain is obtained by considering convection and thermal conduction:

$$\left(\rho c_p\right)_{eff}\frac{\partial T}{\partial t}+\rho c_p\vec{u}\cdot\nabla T+\nabla\cdot\left(-k_{eff}\nabla T\right)=\dot{q}''' \tag{5-23}$$

where ρ is volume averaged density of the gas mixture, which can be calculated using ideal gas law. The symbol c_p is mass averaged specific heat at constant pressure, and k is the average thermal conductivity of gas mixture that can be obtained using Wilke formulas [58], as discussed in Section 3.2.2. When calculating the average thermal conductivity, the gas mixture is considered as a helium-steam mixture since the mole fraction of CO and H_2 is only a few hundred ppm at

maximum, which cannot make observable changes to the thermal physical properties. Since the chemical reaction is confined within the graphite volume, the source term $\dot{q}'''$ in Eq. (5-23) is zero.

The energy equation for the porous graphite domains share the same form as Eq. (5-23). The thermal physical properties are averaged using graphite and gas mixture. The enthalpy of endothermic chemical reaction $\mathrm{C}+\mathrm{H_2O}\uparrow\rightarrow\mathrm{CO}\uparrow+\mathrm{H_2}\uparrow$ is $\Delta E=-131.28$ kJ/mol. Accordingly, the energy source term should be:

$$\dot{q}'''=-131.28\frac{F_m R_{spe}\rho_0}{\mathrm{M_c}},\ \text{unit in kW/m}^3 \tag{5-24}$$

where:

R_{spe}	specific oxidation rate,	1/s
ρ_0	graphite density,	kg/m^3
$\mathrm{M_C}$	carbon mole mass,	kg/mol

5.2.4 Micro porous structure evolution

One objective of developing this numerical model is to predict the graphite density given a specified oxidation condition. The local graphite mass loss fraction at a given time can be calculated by solving the differential equation:

$$\frac{\mathrm{d}X}{\mathrm{d}t}=\frac{F_m k_1\exp(-\frac{E_1}{RT})\,p_{\mathrm{H_2O}}{}^{m(T)}}{1+k_2\exp(-\frac{E_2}{RT})\,p_{\mathrm{H_2}}^{n}+k_1\exp(-\frac{E_3}{RT})\,p_{\mathrm{H_2O}}{}^{m(T)}}, \tag{5-23}$$

with an initial condition $X(t=0)=0$.

As mentioned in Sections 5.2.1 to 2.2.3, the graphite porosity is needed by the mass transfer, flow and heat transfer equations. With mass loss fraction *X* already solved, the local porosity at a given time then can also be obtained by solving equation:

$$\varepsilon = X\left(1-\varepsilon_0\right)+\varepsilon_0 \ , \tag{5-27}$$

with an initial value ε_0. In addition, the pore diameter is needed by Eq. (5-21) to solve the porous flow. According to the mercury intrusion test, the pore diameter of graphite IG-110 can vary from several nanometers to a few hundred micrometers. A statistical analysis on the changes of pore diameter spectrum with graphite mass is too complicated to be included into the work scope of this research. Therefore, the concept of mean pore diameter is adopted in this numerical model. However, the pore diameter will be enlarged with the proceeding of chemical reaction. To quantity the gas transport in solid porous medium, the pores were assumed to be cylinders with uniform size that do not intersect with each other [75]. Later, random pore sizes are allowed with the assumption that no new pores were created in the graphite oxidation process [66], [76]. Based on these assumptions, the mean graphite pore radius at a given time can be calculated by:

$$r_p = r_{p,0}\sqrt{\frac{\varepsilon}{\varepsilon_0}} \ , \tag{5-28}$$

where subscript 0 indicates initial condition. However, Eq. (5-28) can underestimate the pore radius since the chemical reaction not only expands the pores but also opens those originally closed pores. Once two pores are connected, its diameter will increase significantly, which is not a continuous process. However, the mean pore diameter expansion can still be regarded as continuous process at a macro scale when statically large quantity of pores are involved. By the

time when this research was performed, there is not enough data in terms of the mean pore diameter as a function of mass loss fraction or graphite porosity. A correlation has been proposed in literature for nuclear graphite IG-110, which relates mean pore diameter with graphite mass fraction [77]:

$$d = 8.55\times10^{-4}X^2 - 2.5\times10^{-7}X + 10^{-8}, \tag{5-29}$$

Eq. (5-29) implies the mean pore diameter of pristine graphite is 10 nm. However, the latest characterization of IG-110 shows the mean pore diameter is 3.9 μm [48]. Due to the lack of information, an initial pore mean diameter of 3.9 μm is implemented into Eq. (5-29) in this research.

5.2.5 Thermal physical properties of different materials

A total of five chemistry materials are involved in this numerical model, namely He, H_2, CO, steam, and graphite. Their thermal physical properties are needed when solving the above governing equations. The temperature dependent thermal conductivity k, dynamic viscosity μ, and specific heat at constant pressure c_p for the four gases were obtained from National Institute of Standards and Technology (NIST) chemistry webbook database [57]. The density of the gases is calculated using ideal gas law. To solve the continuity, momentum, and energy equations, the average thermal conductivity and viscosity of the gas mixture are calculated using Wilke formulas [58], which has been introduced in Section 2.2.3. The specific heat of the gas mixture is mass-averaged.

The bulk density of graphite IG-110 was measured as 1.78 g/cm^3 in literature [48]. The thermal conductivity of graphite decreases with lifting temperature and neutron irradiation [78]. In

addition, it has been shown the thermal conductivity of post-irradiation nuclear graphite IG-110 is less sensitive to temperature, which is about 35, 27, and 22 W/m/K at 11.9, 21.8, and 24.8 dpa irradiation level, comparing with 143 W/m/K for pristine graphite IG-110 at temperature 400 K [79]. A constant thermal conductivity 35 W/m/K was assumed for irradiated graphite when simulating the normal operation of a prototypic reactor. A correlation was fitted to the data in literature [79] as thermal conductivity of pristine graphite IG-110:

$$k = -3.8515\times10^{-8}T^3 + 1.7115\times10^{-4}T^2 - 0.2851T + 233.1, \quad \text{in W/m/K} \qquad (5\text{-}30)$$

where the temperature T is in unit Kelvin. Eq. (5-30) is adopted for model validation. A comparison of this correlation with the original data is depicted in Figure 5-4. In high temperature enviroment, the specific heat of graphite are similar regardless of the graphite grades. Therefore, the equation of H-451 specific heat [5] was adopted in this research:

$$c_p = \begin{pmatrix} 0.54212 - 2.42667\times10^{-6}T - 90.2725T^{-1} - 4.34493\times10^{4}T^{-2} \\ +1.59309\times10^{7}T^{-3} - 1.43688T^{-4} \end{pmatrix} \times 4184, \text{ in J/kg/K} \qquad (5\text{-}31)$$

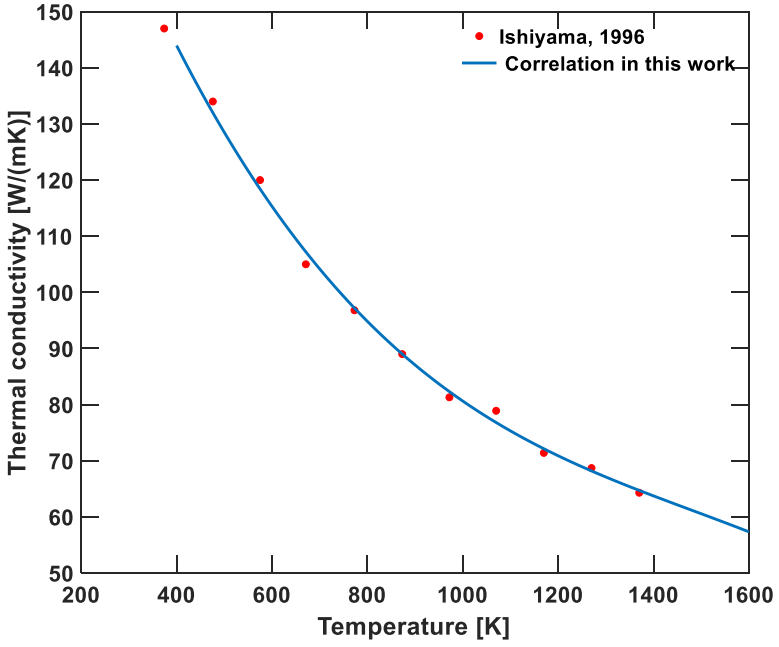

Figure 5-4 Thermal conductivity of pristine nuclear graphite IG-110

5.2.6 Mathematical coupling of governing equations

The above equations are coupled together on software COMSOL Multiphysics V5.6, using modules of Chemistry(*chem*), Transport of concentrated species (*tcs*), Laminar flow or Turbulent flow (*spf*), Heat transfer in porous media (*ht*), and Domain ODEs and DAEs (*dode*) [80]. The flow path of the numerical computation is shown in Figure 5-5. When perform two-dimensional (2-D) simulations based on experimental setup, fully coupled solver was adopted because the quantity of meshes is not too large. However, when solving the 3-D model and the full length prototypic MHTGR coolant channel, segregated solver was applied. A relative tolerance of 1e-4 was set as converge criterion.

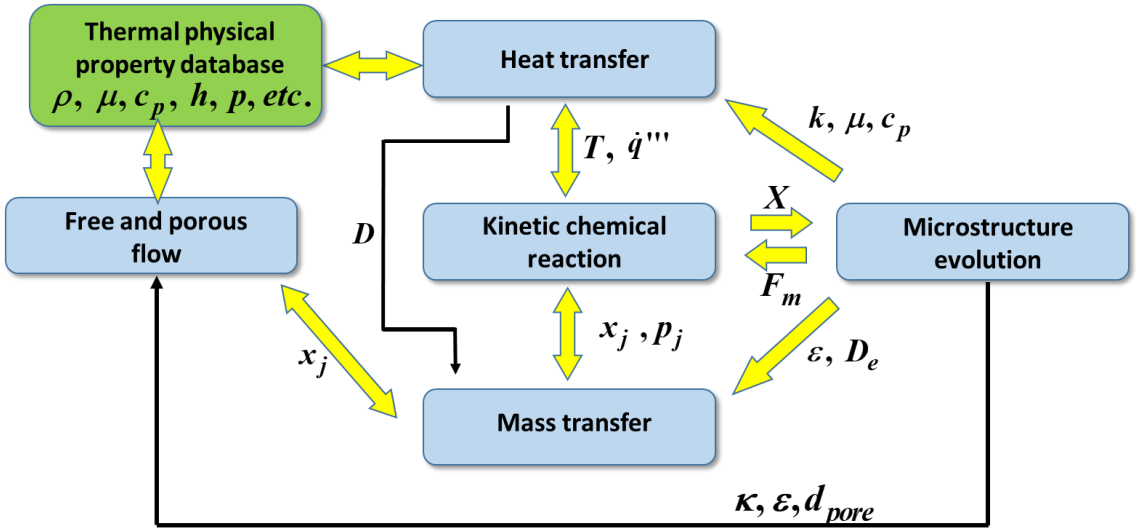

Figure 5-5 Schematic of parameter flow path in numerical simulation

5.3 Validation of Multiphysics Simulation against Experimental Data

Section 5.2 describes the mathematical modeling of graphite-steam oxidation. Its reliability should be validated before being applied to nuclear reactor safety analysis. The experimental data of Section 3.4 can be used to validate this multiphsycis model. Therefore, numerical simulations were performed according to the setup of experiment in Section 3.4.

5.3.1 Numerical model for experimental setup

In Section 3.4, cylindrical graphite samples were oxidized in gas mixture that consists of helium, steam and hydrogen. The 3-D structure of the experimental setup can be simplified into a 2-D axil symmetric domain, as shown in Figure 5-6. The reaction temperature in the experiment is controlled by two PID modules. The CFD simulation in Section 2.2.3 indicates the temperature in the upper region of the quartz tube is uniform, which was then confirmed by the measured temperature using the three thermal couples. Therefore, the inlet gas temperature and the side wall

temperature were set constant in the simulation, which is the same as the oxidation temperature. The inlet flow velocity and mole fraction of each species were also specified corresponding to the experimental setup. A pressure outlet about 1.24 bar (abs) was used as outlet boundary condition. Table 5-2 summaries the boundary conditions for the simulation.

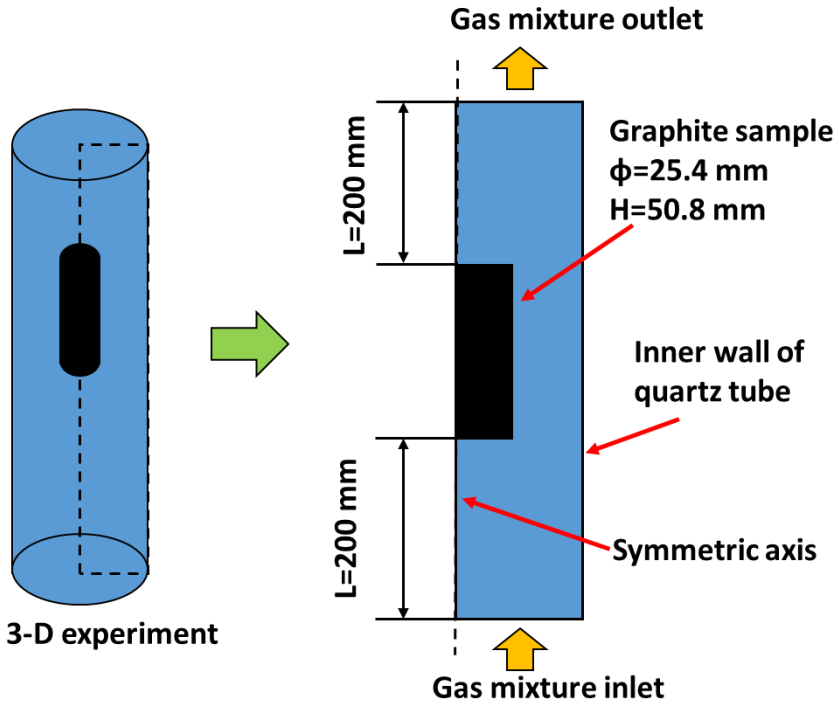

Figure 5-6 Simulation domain according to experimental setup

Table 5-2 Boundary conditions of numerical simulation

Test name	T **[°C]**	u_{in} **[m/s]**	p_{out} **[bar (abs)]**	x_{He} **--**	x_{H_2} **--**	x_{H_2O} **--**
T971-PW14373-PH502-He10	970.6	0.143	1.244	0.880	0.00404	0.116
T971-PW17306-PH985-He7	970.5	0.103	1.246	0.853	0.00794	0.139
T1001-PW15886-PH495-He10	1000.7	0.149	1.236	0.868	0.00399	0.128
T1051-PW1896-PH109-He10	1050.7	0.137	1.243	0.984	0.000881	0.0153

*: x indicates mole fraction

The mesh generation for the graphite and free flow is depicted in Figure 5-7. It should be noted the scale in Figure 5-7 is in meters. The meshes were refined near the interface between graphite and free flow to capture the large gradient of simulated parameters, e.g., the graphite density and steam concentrations.

It was found in the previous experiment that ψ in the mass loss fraction factor decreases with reaction temperature. Three ψ values have been obtained, which are 33660, 20220, and 1304, respectively for reaction temperature 863, 909, and 1002 °C, respectively. The ψ value for the first three cases in Table 5-2 were obtained by a second order interpolation based on the above three values. However, the interpolation will leads to a negative ψ value at temperature 1050 °C, which is physically incorrect. Therefore, ψ=1304 was adopted for the fourth simulation.

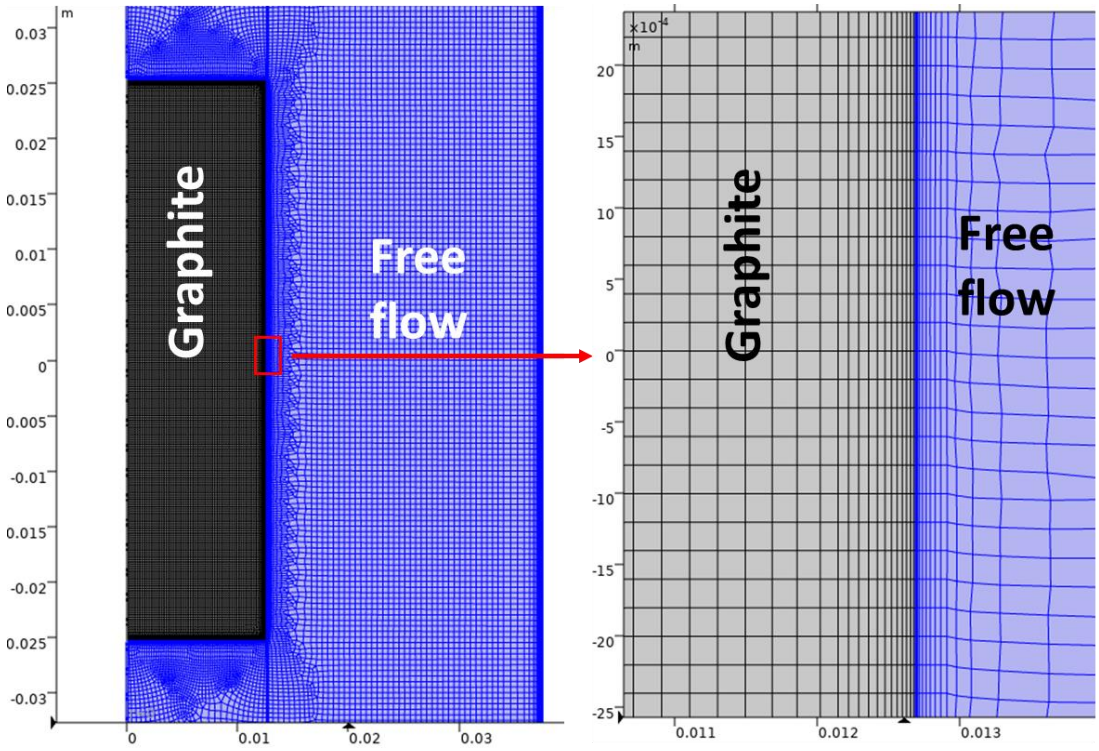

Figure 5-7 Mesh generation for graphite specimen and free flow domain

5.3.2 Comparison of simulation results with experimental data

As mentioned in Section 5.2.1, the tortuosity will have significant effect on the oxidation depth, which then leads to different density profile and apparent oxidation rate. However, there is a lack of data in literature about the tortuosity of nuclear grade graphite. Therefore, a parametric study was first performed to compare the different tortuosity models. Different values of *n* in Eq. (5-11) were tested and compared with experiment T971-PW14373-PH502-He10.

The objective here is to find a reasonable tortuosity model for graphite IG-110. The comparison of apparent oxidation rates between experimental data and simulation results is depicted in . It can be seen the simulation based on Brillington and Quick tortuosity model $f(\varepsilon,\tau)=\varepsilon/\tau$ with

$\tau = \varepsilon^{-1/3}$, and Bruggeman tortuosity model $f(\varepsilon,\tau) = \varepsilon / \tau$ with $\tau = \varepsilon^{-1/2}$ can obviously overestimate the apparent oxidation rate. The reason is these two models underestimate the tortuosity for graphite IG-110, which then leads to an overestimated effective diffusivity. Therefore, the water molecule can penetrate into a deeper region in the simulation than the actual scenario. In reality, these two models are usually applied to porous media with coarse grains. For example, the Millington and Quirk model was used for liquid and gases flow in soil [81], and the Bruggeman model was used for electrolyte flow in battery [82]. In those applications, the porous media is less compacted and the pores thereafter are relatively more straightforward than that of nuclear graphite IG-110.

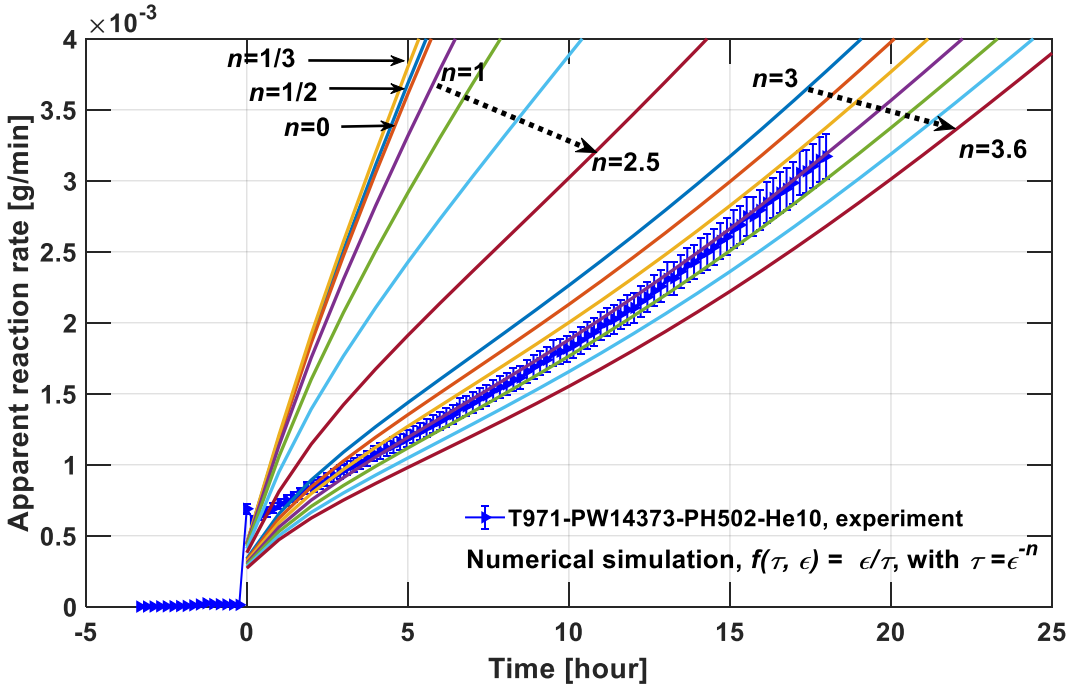

Figure 5-8 Comparison of simulated apparent oxidation rate and experimental measurement for test T971-PW14373-PH502-He10

As shown in Figure 5-8, the *n* value has to be increased to about 3.1 to 3.6 so the simulation results can agree with experimental data. However, the simulated apparent oxidation rate within the first hour is obviously lower than the measured value. There are two possible reasons for the difference. First, the pristine graphite sample can contain dust that are more active. Once steam is introduced, these graphite dust will quickly react with steam, which contributes extra apparent oxidation signal in the measurement. In addition, the BLH reaction equation has an MRD value about 24% that can affect the simulation accuracy.

It can also be imagined that a smaller tortuosity will lead to a more uniform distribution of post-oxidation density in the simulation. Figure 5-9 shows the simulated normalized density after 18 hours oxidation based on different tortuosity models. It should be noted the legend scale of the upper three cases is different from the lower ones. When using the Millington and Quirk tortuosity model, the normalized density in the central region and the outer surface of the sample is about 0.9 and 0.88 after 18 hours oxidation, respectively. As a comparison, the simulation case with $\tau = \varepsilon^{-3.6}$ indicates a major fraction of the inner volume of the sample still remains un-oxidized after 18 hours.

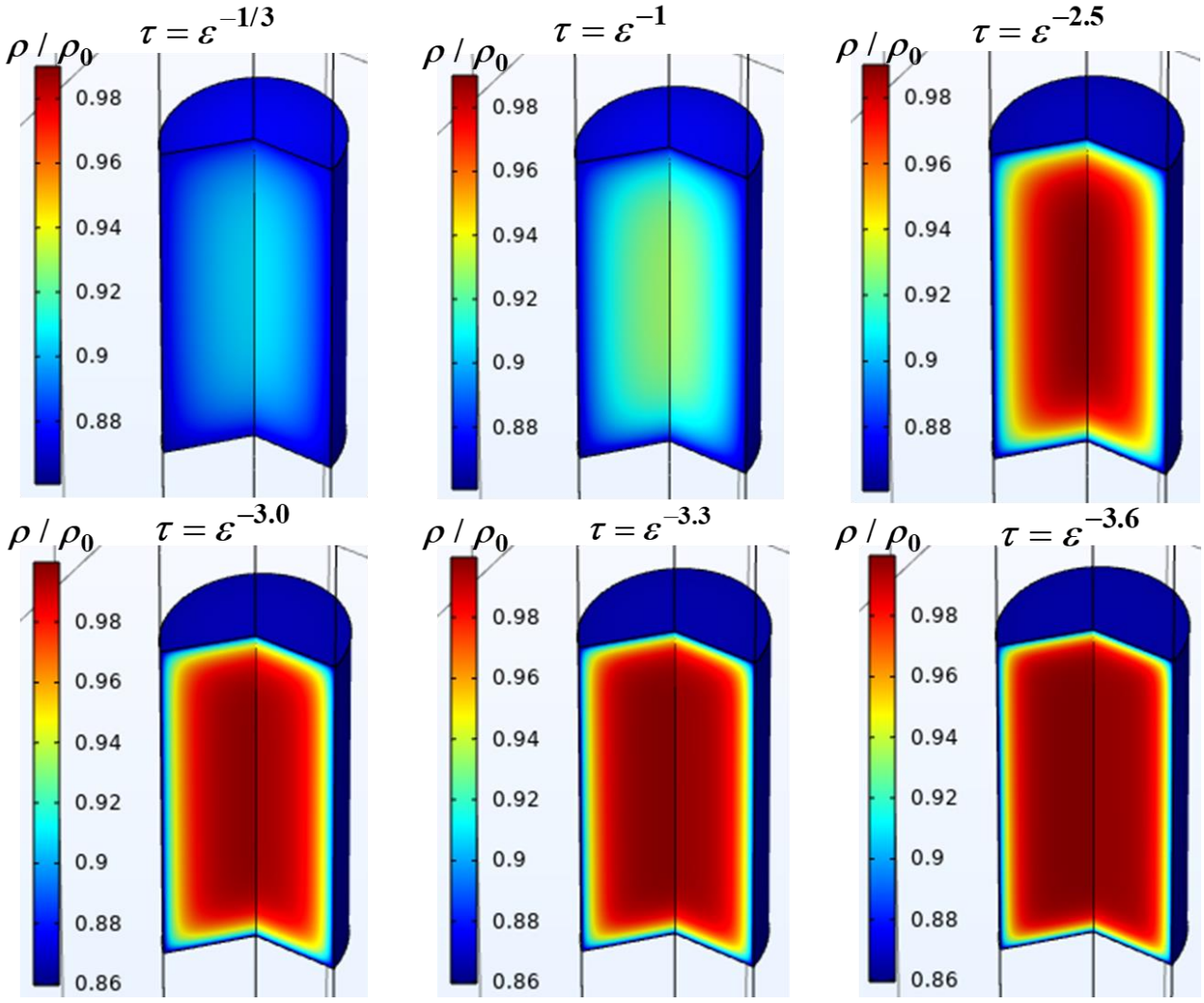

Figure 5-9 Simulated graphite density using different tortuosity models for test T971-PW14373-PH502-He10 at 18 hours

The above analysis implies a tortuosity model $\tau = \varepsilon^{-n}$ with n to be 3.2 to 3.4 might be a reasonable model to simulate the graphite-steam oxidation for IG-110. However, the agreement on apparent oxidation rate alone does not guarantee the whole oxidation process has been correctly simulated. In order to draw a conclusion, the density of the graphite sample should be used as a second criterion to evaluate the numerical model. Since the density of the graphite sample in the

experiment is not *in-situ* measured, only the post-oxidation density was compared, which is depicted in Figure 5-10. The simulations with n =3.2, 3.3, and 3.4 is demonstrated since they have the best agreement in terms of apparent oxidation rate history. In addition, another three cases with n =1/3, 2.5, and 3.6 are also displayed as a comparison. It can be seen the graphite density profile for case n = 1/3 is fairly uniform. When increase the value of n, the slope near the graphite surface becomes larger and larger. When n is within 3.2 to 3.4, the simulated density shows excellent agreement with experimental results.

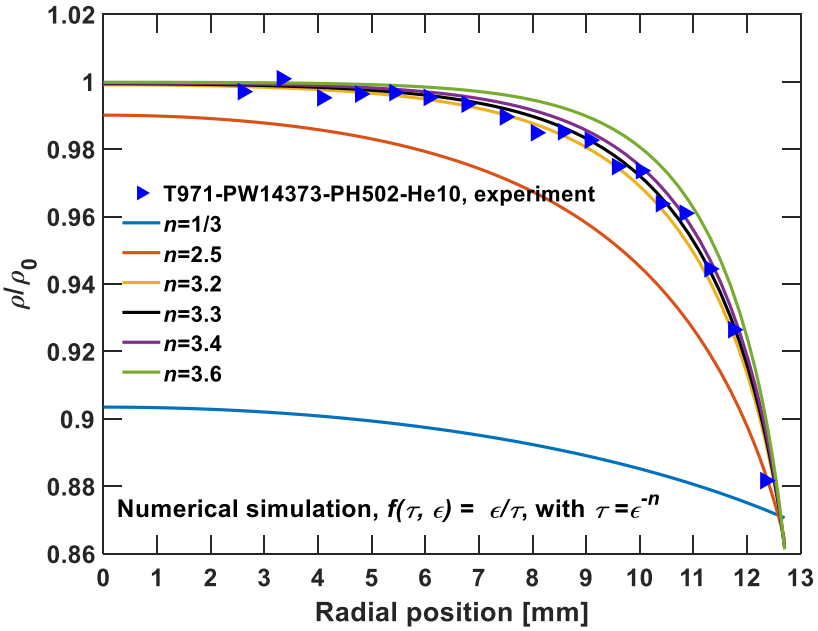

Figure 5-10 Comparison of simulated density and experimental measurement for test T971-PW14373-PH502-He10

Figure 5-11 shows the simulated evolution of graphite density (with n=3.3) for test T971-PW14373-PH502-He10. It can be seen the oxidation first occurs within a thin layer near the sample surface and migrates into the inner region gradually. The development of graphite density at the

middle height of the graphite sample is depicted in Figure 5-12 with 1 hr interval. Although the graphite density at the sample surface decreases quickly with time, the inner region within radius less than 4 mm still remains un-oxidized after 25 hours.

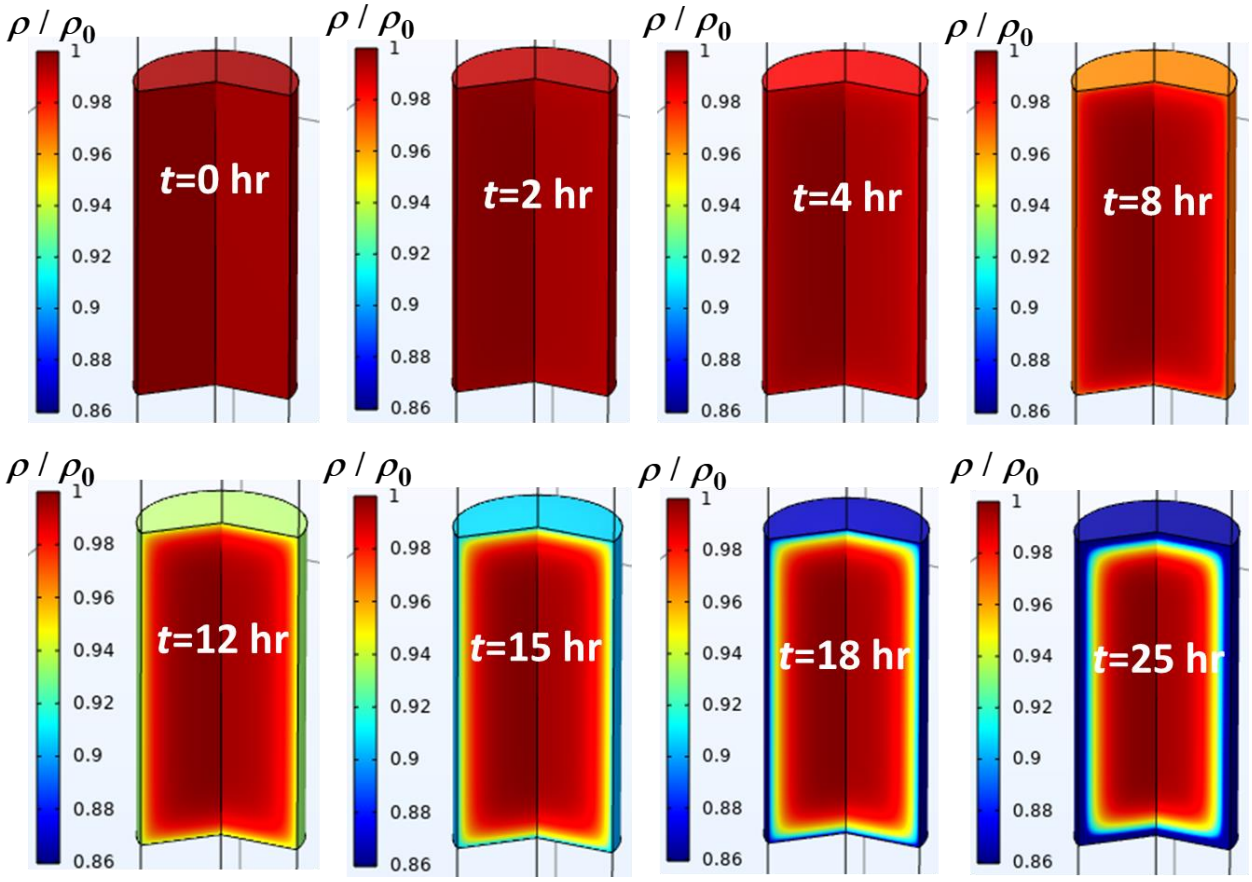

Figure 5-11 Simulated graphite density evolution for test T971-PW14373-PH502-He10

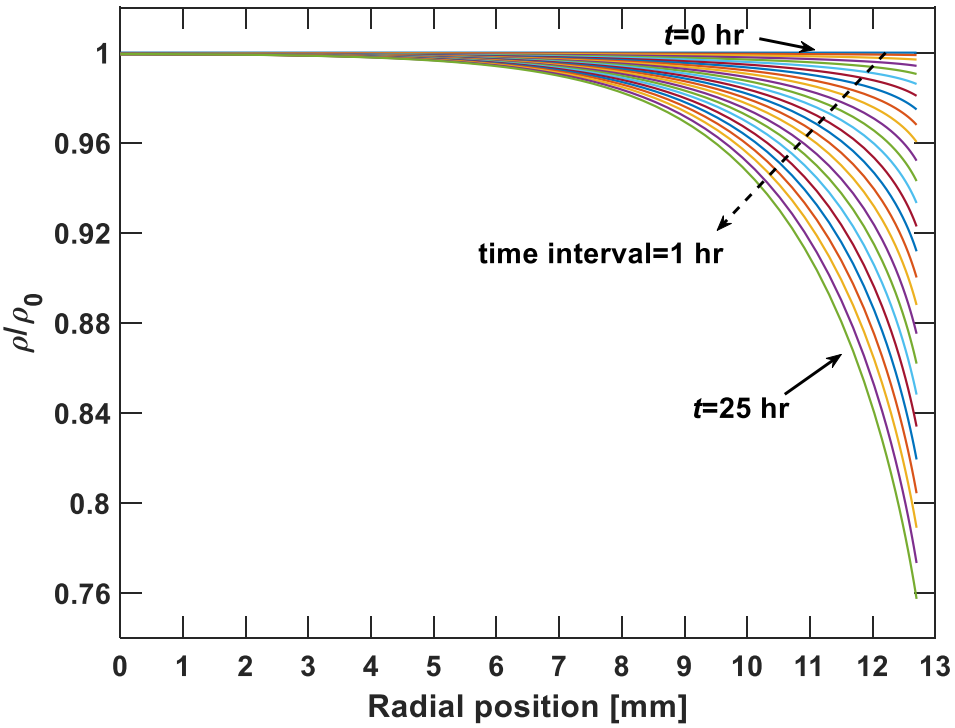

Figure 5-12 Simulated graphite density evolution at sample middle height for test T971-PW14373-PH502-He10

Figure 5-13 and Figure 5-14 depict the distribution of steam and hydrogen partial pressures. When *n*=3.3, the steam partial pressure drops from about 14.3 kPa at the graphite surface to below 1 kPa within 5 mm into the sample. As a comparison, the steam partial pressure at sample central line can be as high as 10.8 kPa if *n*=1/3 is adopted. In addition, hydrogen partial pressure also shows significant difference with different *n* values. The higher tortuosity (case *n*=3.3) will lead to a smaller effective diffusivity for all gas species. Therefore, the production gas hydrogen will be accumulated in the graphite sample, which forms a partial pressure up to about 7.5 kPa. The small steam parital pressure and large hydrogen partial pressure together prevents the inner region

of graphite from being oxidized. In terms of graphite-moisture oxidation, a high value of graphite tortuosity thereafter is desired to promote reactor safety.

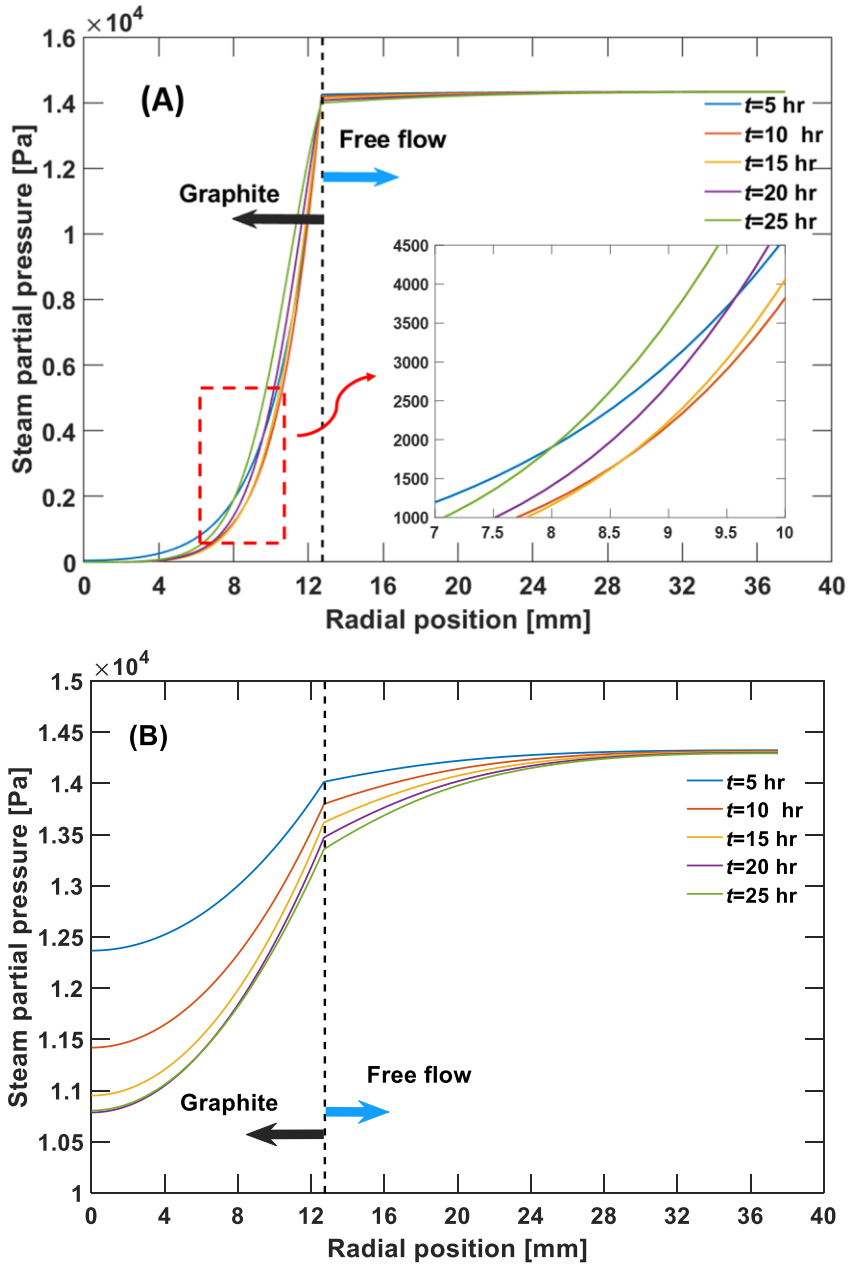

Figure 5-13 Simulated steam partial pressure in porous graphite and free flow domain for test T971-PW14373-PH502-He10: (A) $\tau=\varepsilon^{-3.3}$, and (B) $\tau=\varepsilon^{-1/3}$

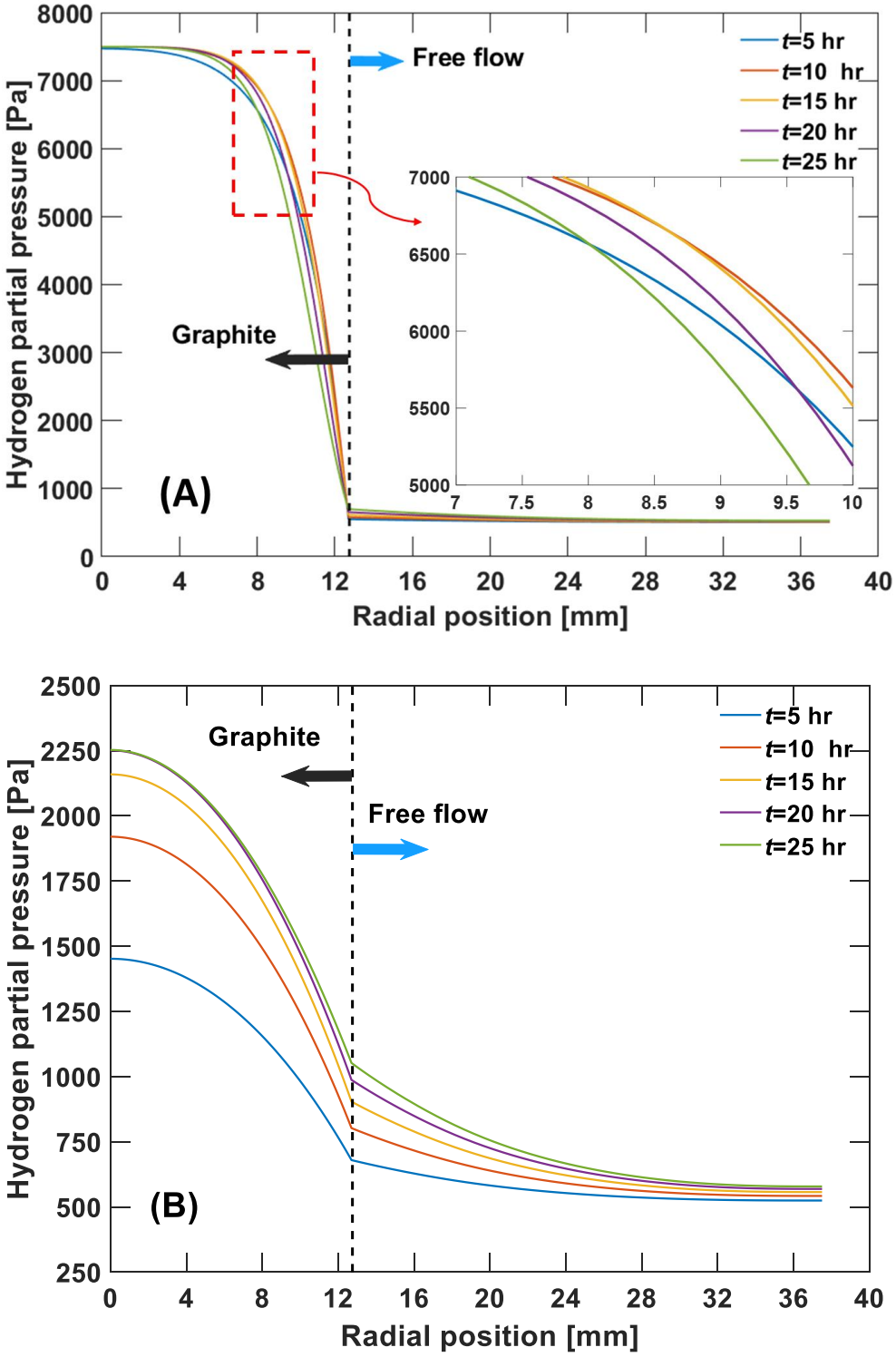

Figure 5-14 Simulated hydrogen partial pressure in graphite and free flow for test T971-PW14373-PH502-He10: (A) $\tau=\varepsilon^{-3.3}$, and (B) $\tau=\varepsilon^{-1/3}$

When looking into the zoom-in region in Figure 5-13(A) and Figure 5-14(B), it can be found the partial pressure of steam and hydrogen at a given depth can go up and down with time, which is induced by the increase of kinetic chemical reaction rate and effective diffusivity. Once the oxidation is initiated, the kinetic reaction rate starts to increase due to the effect of mass loss fraction factor F_m, which tends to block steam from penetrating. On the other hand, the micro pores are simultaneously expanded, which increases porosity and thus the effective diffusivity. These two contrary effects can overwhelm each other with time.

The concentration of gas species in the free flow region can also differ according to different circumstances in the graphite sample. For instance, if the tortuosity of graphite is very small, the chemical reaction will form a considerable mass source. Accordingly, the gradient of gas species concentration in the free flow boundary layer will be increased. In summary, the comparison with test T971-PW14373-PH502-He10 has shown the multiphysics model can simulate the graphite-steam oxidation processes well.

The rest of this section compares the simulations with experiments for the other three cases. The above analysis indicates the value of n in the tortuosity model should be about 3.2 to 3.6. Therefore, a parametric study was carried out by varying the value of n in range 3.1 to 3.6. Figure 5-15 and Figure 5-16 shows the apparent oxidation rate and radial density profile for test T971-PW17306-PH985-He7. The simulated apparent oxidation rate is slightly higher than experimental results, especially for the first several hours, but the difference is still acceptable. In addition, the predicted density distribution after 24.5 hours oxidation agrees with the experiment well.

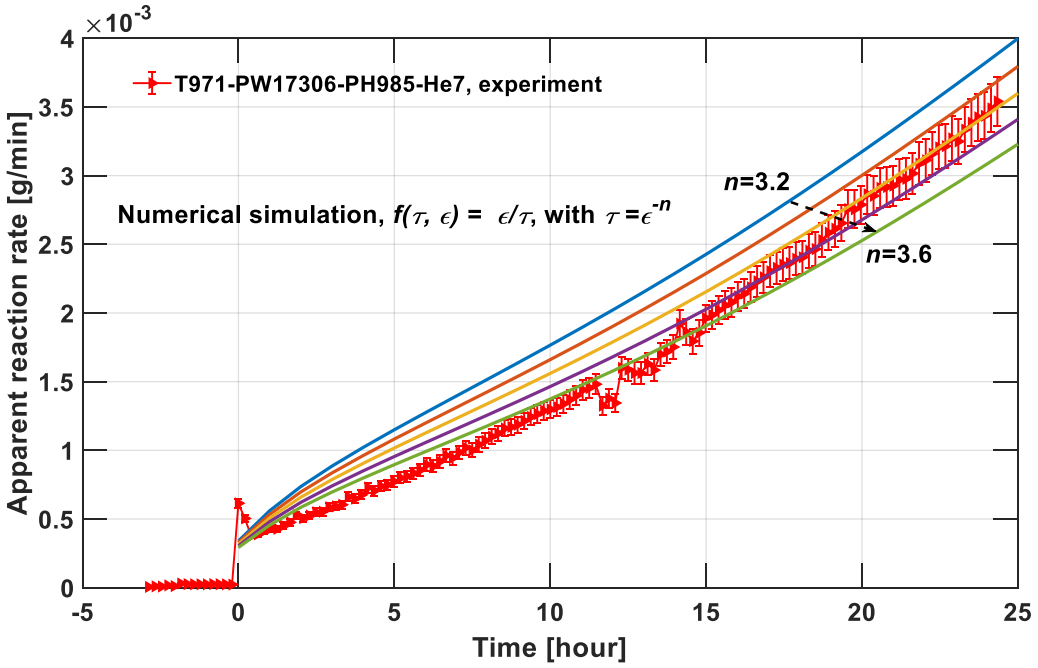

Figure 5-15 Comparison of simulated apparent oxidation rate and experimental measurement for test T971-PW17306-PH985-He7

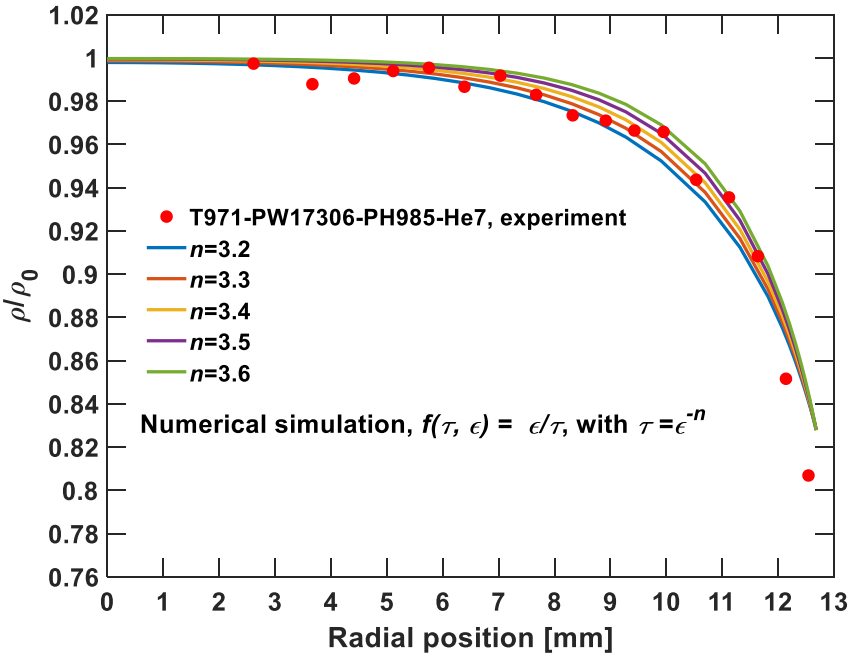

Figure 5-16 Comparison of simulated density and experimental measurement for test T971-PW17306-PH985-He7

The comparison of simulation with experiment T1001-PW15886-PH495-He10 is depicted in Figure 5-17 and Figure 5-18, respectively in terms of apparent oxidation rate and density. Similarly to the above two cases, the predicted apparent oxidation rate at the beginning is slightly higher. If the value of *n* is set as 3.3, the predicted oxidation rate will be close to the experimental data. This test has the largest mass loss among the four experiments. According to the density measurement, most oxidation still occurs within a thin layer from the graphite sample surface into the inner volume. According to the density measurement, the mass loss fraction at graphite surface reached to about 0.35 after 16.3 hours. Figure 5-18 indicates the multiphysics model still matches the experimental data well at such high oxidation level.

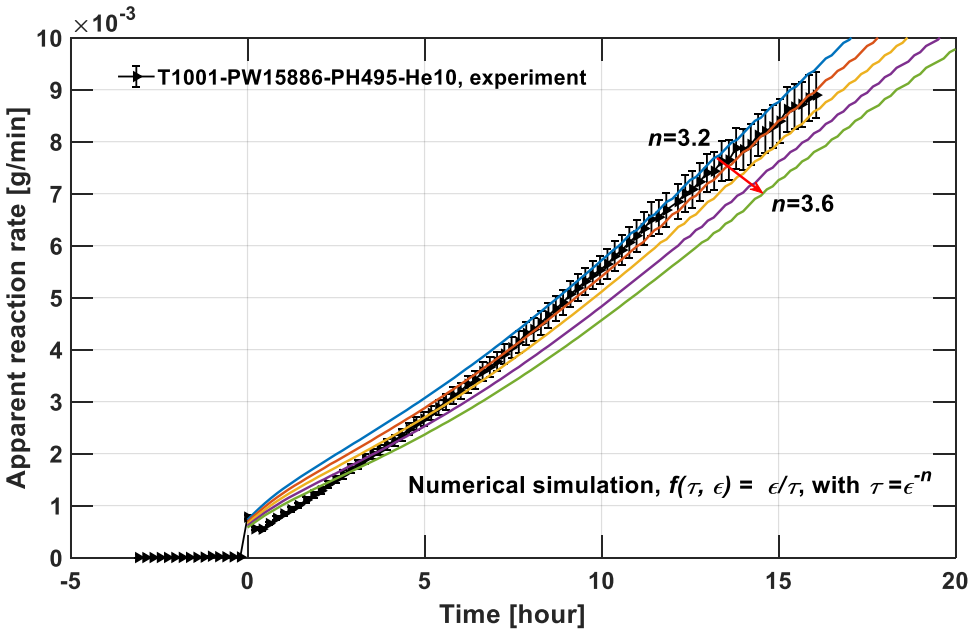

Figure 5-17 Comparison of simulated apparent oxidation rate and experimental measurement for test T1001-PW15886-PH495-He10

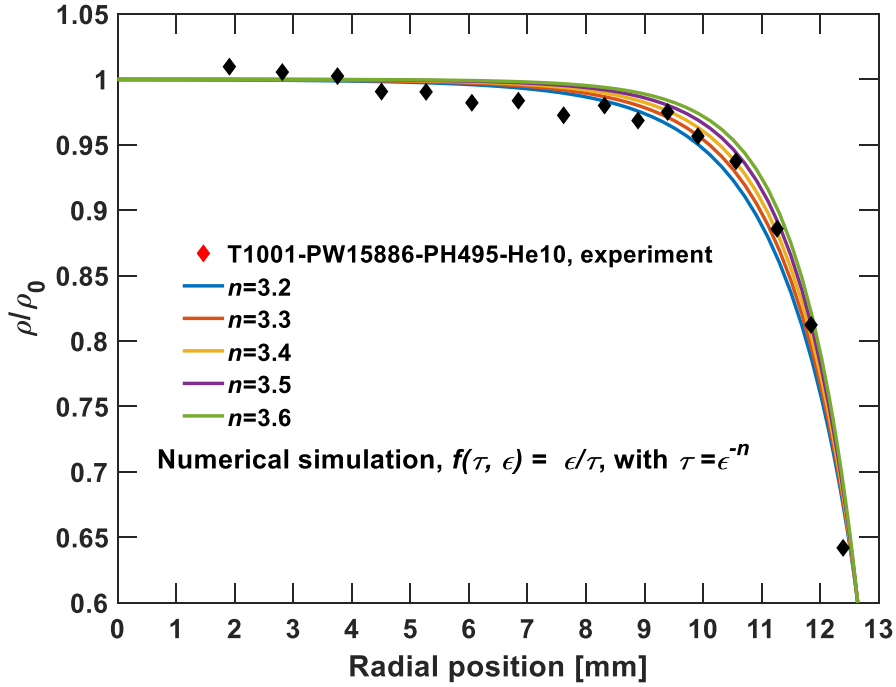

Figure 5-18 Comparison of simulated density and experimental measurement for test T1001-PW15886-PH495-He10

The validation against test T1051-PW1896-PH109-He10 is shown in Figure 5-19 and Figure 5-20. It can be seen the simulated apparent oxidation rate is smaller than the experimental measurement. As discussed in Section 3.4, a few local oxidation spots in this experiment, which contribute extra reaction signals. Although the apparent oxidation rate of this test cannot be used to evaluate the numerical simulation, the density distribution still provides valuable insights. Figure 5-20 depicts the comparison of simulated graphite density and experimental data. It can be seen the density decreases sharply within a thin layer about 1.5 mm near the surface region. The numerical model maintains accurate prediction even under this harsh condition.

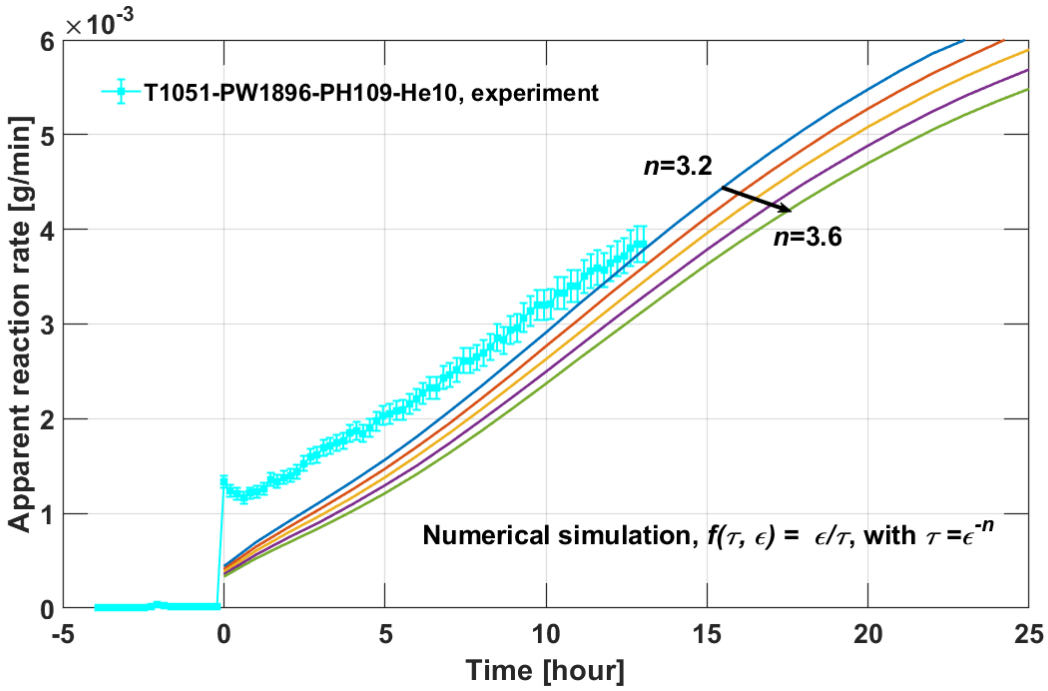

Figure 5-19 Comparison of simulated apparent oxidation rate and experimental measurement for test T1051-PW1896-PH109-He10

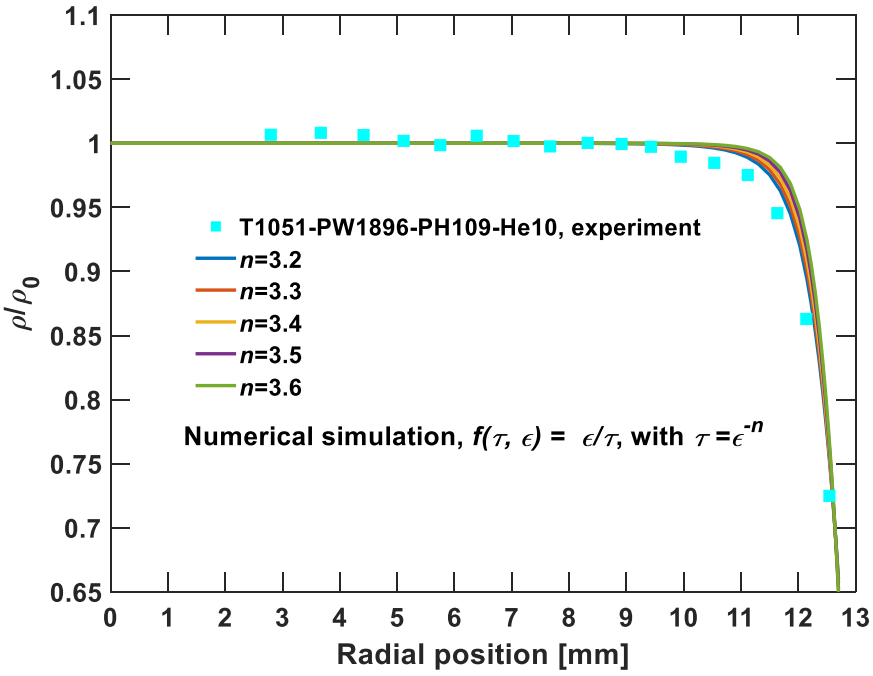

Figure 5-20 Comparison of simulated density and experimental measurement for test T1051-PW1896-PH109-He10

5.4 Summary of Multiphysics Simulation

A multiphysics model has been developed through the above efforts. The model couples flow and heat transfer for both free flow and porous graphite domain. The BLH reaction rate equation, which was derived from experimental data, is adopted as the mass source term for the gas diffusion equations. The effect of micro porous structure evolution on the oxidation behavior is also considered in the modeling. The multiphysics model has been validated against experimental data. It was found the tortuosity model has significant effect on the effective diffusivity, and therefore on the overall accuracy of the simulation results. A tortuosity model was proposed by comparing the simulation results with experimental data, which shows good suitability for all four test conditions in this work. The comparison indicate the multiphysics model has reasonably captured all important physical processes, including chemical reaction, mass transfer, and micro pore evolution.

At the same time, it should be noted the mass transfer module is not founded on dedicated experimental data. There are assumptions and models that have not been validated. Experimental investigation on the effective diffusivity is highly recommended as future works. In addition, characterization on graphite micro structures is desired to provide more accurate description about the pore sizes and tortuosity etc., especially their evolution with mass loss.

Another limit of the multiphysics model lies in its capacity to simulate high mass loss scenarios. depicts the evolution of density for test T1051-PW1896-PH109-He10 within 25 hours. According to the simulation, the normalized density at the sample surface after 25 hours oxidation will be only about 0.3. The nuclear graphite consists of fillers and binders. Once the binders are

significantly corroded, they can no longer hold the fillers together. As a result, the graphite will lose most of its mechanical strength. After that, the fillers and binders will peel off from the sample. shows an experiment with mass loss about 0.43. The sample easily broke into small pieces. However, the graphite failure is not considered in the multiphysics modeling.

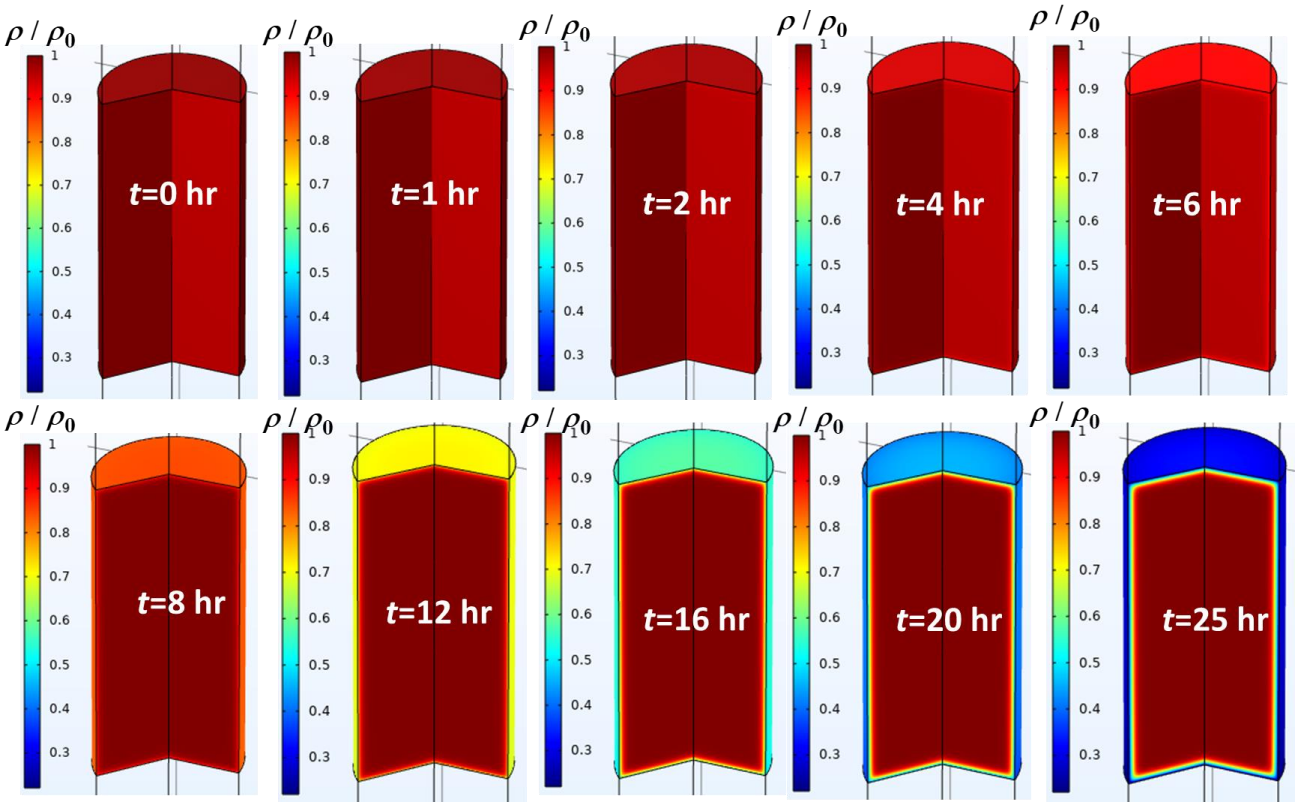

Figure 5-21 Simulated graphite density evolution for test T1051-PW1896-PH109-He10 within 25 hours oxidation

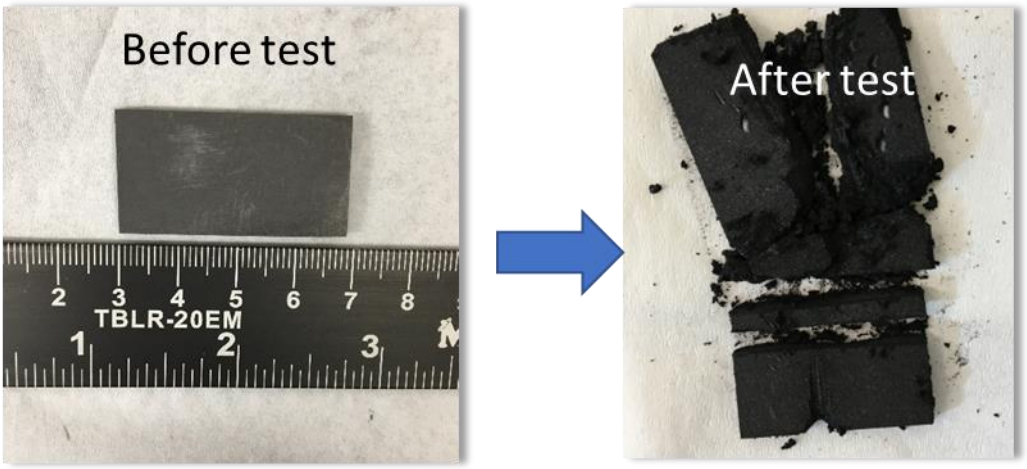

Figure 5-22 Sample broken at mass loss fraction of 0.43

Chapter 6 Numerical Simulation of Graphite-Moisture Oxidation for Prototypic HTGR

Before the experimental works, the multiphysics simulation had been carried out for HTGR based on literature review [32], [46], [83]. The multiphysics model was later improved and validated against experiments, which has been described in Chapter 5. Therefore, the simulations were performed again based on the latest progress. Some methodologies of the previous simulation are inherited by the updated simulation. For example, the simplification of prototypic 3-D coolant channel into a 2-D axially symmetric model, the benchmark of turbulence and porous flow models, and the boundary conditions are still valid, which will be introduced in Sections 6.1 to 6.3. The results of previous numerical simulation were then described in Section 6.4. The updated simulation results based on the validated model is summarized in Section 6.5.

6.1 Geometry Simplification and Mesh Independence Study

The objective of this study is to simulate the graphite-steam/moisture oxidation for a prototypic HTGR under normal operation conditions. The MHTGR design by General Atomic (GA) was chosen as the reference reactor design in this Chapter. The active core region of MHTGR consists of 66 hexagonal fuel columns. Each column has 10 fuel blocks stacked vertically, in which coolant and fuel channels are drilled [84]. The total height of the active core region is 7.93 m. The cross-sectional structure of one standard fuel block is shown in Figure 6-1(a) and one coolant unit cell is shown in Figure 6-1(b).

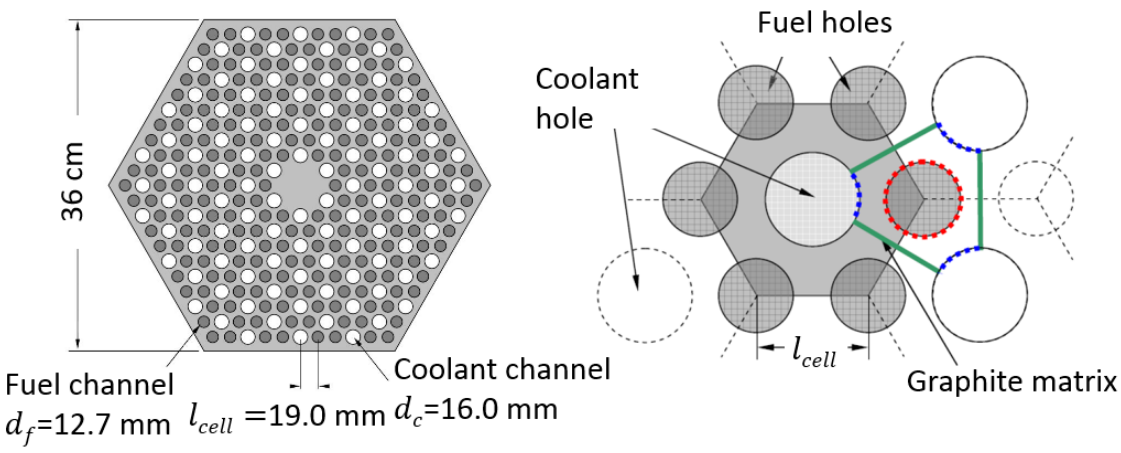

(a) (b)

Figure 6-1 Cross-sectional view of an MHTGR fuel block: (a) one standard fuel block and (b) one coolant channel-eccentric unit cell [85]

Simulation of a three-dimensional (3-D) coolant unit cell requires significant calculation resources. Therefore, it is necessary to simplify the 3-D structure into a two-dimensional (2-D) geometry without sacrificing significant simulation accuracy. The coolant unit cell was first simplified into a hollow cylinder, as shown in Figure 6-2(a), by maintaining the coolant channel diameter and solid-to-fluid volume ratio unchanged from the prototypic MHTGR design. The geometry was then further simplified into a 2-D axially symmetric simulation domain, as shown in Figure 6-2(b). The input heat flux in the 2-D model was 15.51% lower than the prototypic 3-D structure since the heating surface area in the simplified simulation domain was increased. In this way, the prototypic heating power is maintained. It should be noted the symmetric axil is located in the center of the coolant channel for all simulations in this chapter.

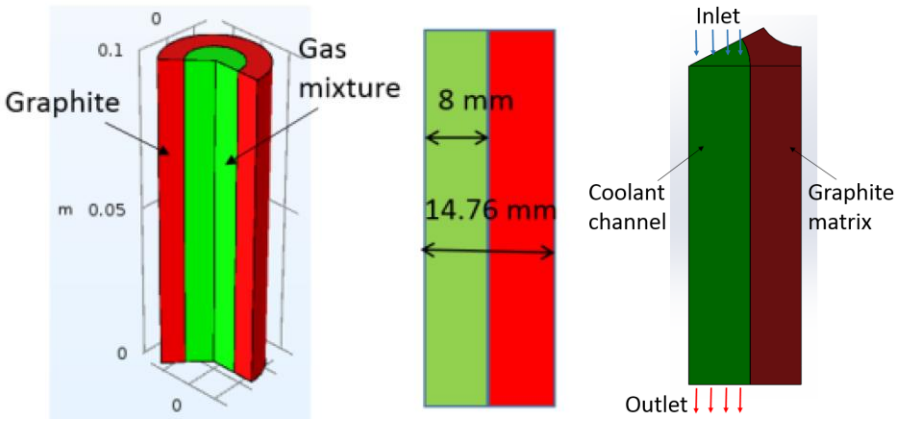

(a) (b) (c)

Figure 6-2 Structure of the simplified simulation domains: (a) 3-D hollow cylinder; (b) 2-D calculation domain; and (c) 3-D calculation domain

A mesh independence study was performed as the first step of the simulation. The study was carried out using the 2-D model with inlet gas mixture velocity of 25 m/s and temperatures of 823, 1,023, and 1,173 K. The height of the simulation domain was 100 mm and the outlet pressure was set as 6.4 MPa. Three mesh sizes were tested, as shown in Table 6-1. The moisture concentration distribution was used as a criterion to evaluate the effect of the mesh size. The simulations did not show observable differences when the gas mixture inlet temperature was 823 or 1,023 K. Only negligible differences were observed when the gas inlet temperature was 1,173 K. Theoretically, a finer mesh is needed to capture the steeper moisture concentration gradients caused by high reaction temperatures. As shown in Figure 6-3, the largest values of the moisture partial pressure difference between the results using the medium and coarse meshes, and the fine and medium meshes are no larger than 9×10^{-3} and 5×10^{-3} Pa, respectively. Therefore, the coarse mesh should already satisfy the numerical accuracy requirements. However, the fine mesh was adopted to accommodate the possible higher temperature conditions in the following analysis.

Table 6-1. Parameters for three different mesh sizes

Mesh Category	Maximum size [mm]	Minimum size [mm]	Average quality	Minimum quality	Total mesh quantity
Coarse (C)	0.4	0.03	0.994	0.808	16,750
Medium (M)	0.3	0.02	0.993	0.787	26,720
Fine (F)	0.2	0.015	0.996	0.805	52,000

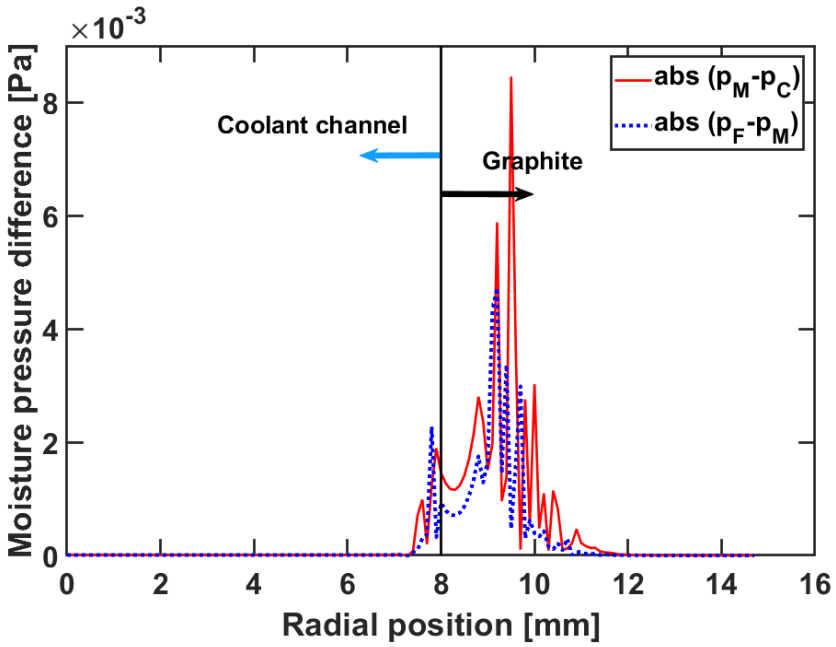

Figure 6-3 Difference of the moisture partial pressure obtained from simulations with three mesh sizes at gas mixture inlet temperature of 1,173 K.

This 2-D model was then verified by comparing with a 3-D 1/12 coolant channel unit cell, as shown in Figure 6-2(a). This 3-D to 2-D simplification does not change the vertical structure feature so only a 100 mm length section was simulated to accelerate the computation. The inlet gas mixture velocity is 25 m/s with the moisture and hydrogen partial pressures to be 14.7 and 50 Pa, respectively. A constant pressure of 6.4 MPa was set on the outlet. The top and bottom

boundaries of the graphite domain are set as no-flux and isothermal. Heat flux values of 81,797 and 95,000 W/m^2 were added to the right-hand-side boundary of Figure 6-2(b) and the curved surface in Figure 6-2(c), respectively. Three different inlet temperatures, i.e. 823, 1,023, and 1,173 K, were used in the simulations which are supposed to cover the graphite temperature for MHTGR normal operations. Structural parameters and kinetic constants derived for nuclear graphite IG-110 in literature [20] were adopted in this comparison.

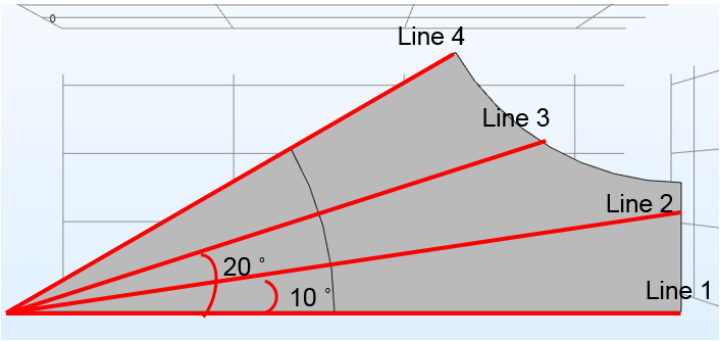

Figure 6-4 Four lines to extract 3-D simulation results

The simulation results using the 3-D model were analyzed by extracting the simulation data along the radial directions/lines at the four azimuthal angles as shown in Figure 6-4, at the half height (50 mm) of the simulation domain. Comparisons of the 3-D and 2-D results are depicted in Figure 6-5 to Figure 6-7, for the three simulated temperatures, respectively. It can be seen the 2-D model leads to slightly steeper moisture gradients in the graphite domain near the fluid-to-graphite interface, and the graphite temperature of the 2-D simulation is always 1 to 2 K lower than that in the 3-D simulation results. A relatively lower temperature in the 2-D model is expected since the total heating power was maintained the same in both models but the total heat transfer area was increased in the 2-D simulation, which means the 2-D model has shorter thermal conduction depth.

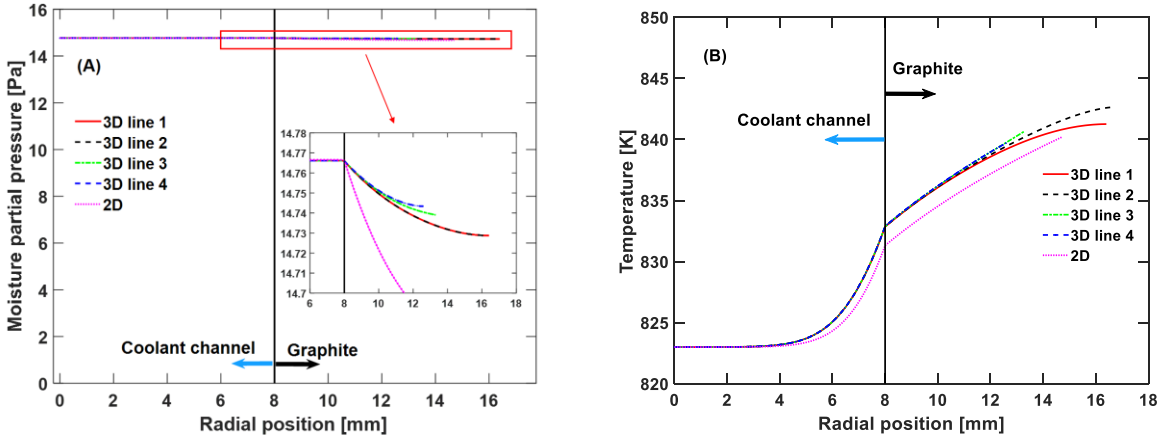

Figure 6-5 Comparison of the 3-D sand 2-D simulations for reaction temperature of 823 K: (A) moisture partial pressures and (B) gas and graphite temperature distribution along the radial direction

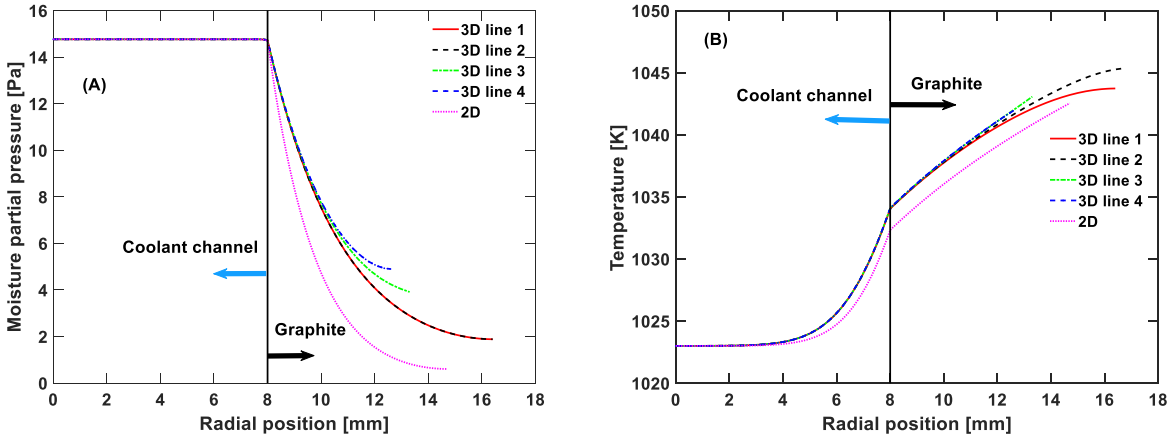

Figure 6-6 Comparison of 3-D and 2-D simulations for reaction temperature of 1,023 K: (A) moisture partial pressures and (B) gas and graphite temperature distribution along the radial direction

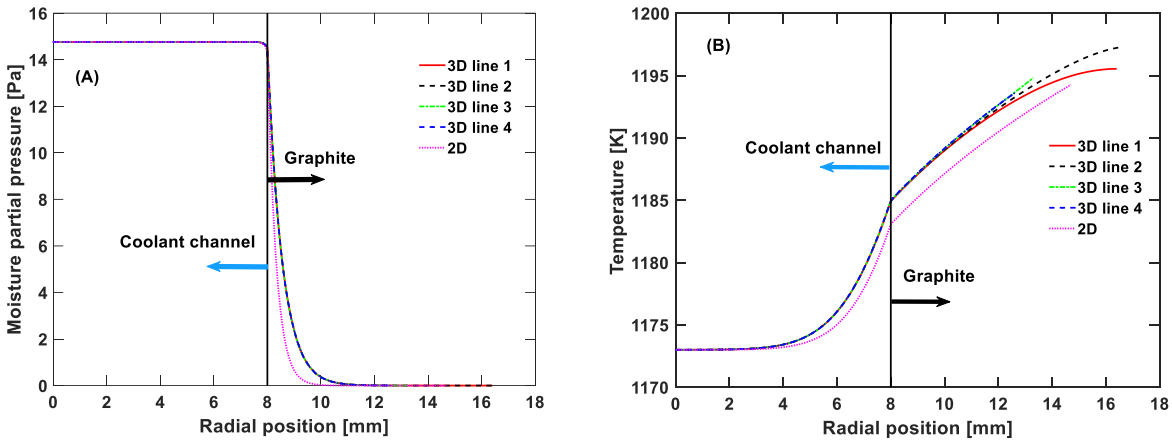

Figure 6-7 Comparison of 3-D and 2-D simulations for reaction temperature of 1,173 K: (A) moisture partial pressures and (B) gas and graphite temperature distribution along the radial direction

In general, the higher graphite temperature should lead to a steeper moisture distribution in the graphite domain due to the larger graphite-moisture reaction rate. The 3-D simulation shows higher graphite temperature than the 2-D simulation. However, the gradient of moisture concentration in graphite domain is larger for the 3-D simulation than the 2-D simulation. This phenomenon indicates that the geometry simplification could bring some distortions to the simulation results, especially to the mass transfer module. The differences might root from the change of associated boundary conditions. In the 2-D model, the no-flux condition was applied to the right boundary of Figure 6-2(b), and the curved surface in Figure 6-2(c) has the no-flux condition for the 3-D model. But the areas of these two no-flux surfaces are different.

In reality, the graphite matrix would show very different chemical reaction properties from the graphite blocks due to its different microstructures and higher impurity level. Therefore, a no-flux boundary condition is not exactly true. However, due to the lack of information for the moisture-graphite matrix reaction, a compromise with the no-flux condition was made for the current study.

It should be noted, however, that the differences in the moisture distribution between the 2-D and 3-D models are relatively small for the reaction temperature of 823 and 1173 K. At low reaction temperature, the reaction rate is far below that corresponding to the maximum mass transfer capacity, so the moisture can easily penetrate through the whole graphite width. Therefore, the moisture profiles in the graphite would be fairly uniform for both of the models, as shown in Figure 6-5(a). On the contrary, if the graphite temperature is sufficiently high, leading to a large reaction rate (diffusion controlled regime), the moisture profiles will be mainly determined by the mass transfer rate. In this case, only a thin layer near the fluid-to-graphite interface is affected by the geometry simplification. Nevertheless, if the reaction temperatures lie in the transitional regime, the moisture profiles become more sensitive to both the graphite temperature and the mass transfer rate. As a result, the difference of the moisture profiles between the simplified 2-D model and the 3-D model becomes more evident.

In general, this 3-D to 2-D model simplification is acceptable considering the significant reduction of computation time. For example, the computation time for the 3-D model using 16 Xeon CPUs is about 120 hours while the 2-D model only takes about 50 minutes. Therefore, the analyses in the following were performed based on the 2-D model.

6.2 Comparison of Different Flow Models

In the simulations presented above, the gas mixture flow was simulated by a combination of the k-ε turbulence model and Darcy law for the free flow and porous graphite domains, respectively. The model was compared with another three flow models in this section, as shown in Table 6-2. It should be noted that the inlet gas flow velocity for Cases A, B, and C leads to a turbulent flow in the coolant channel while Case D results in a laminar flow.

Table 6-2 Combination of free and porous flow models

Case number	Inlet velocity [m/s]	Re at T = 1,000 K	Free flow domain	Graphite domain
A	25	2.62×10^4	$k-\varepsilon$	Darcy law
B	25	2.62×10^4	Algebraic y^+	Darcy law
C	25	2.62×10^4	Algebraic y^+	Stokes-Brinkman
D	0.1	105	Laminar	Stokes-Brinkman

The simulation results are shown in Figure 6-8 to Figure 6-10 for the moisture partial pressure distribution along the radial direction at the half height of the simulation domain. The differences in the moisture concentrations in the graphite domain are generally negligible for the four cases, especially for Cases A, B, and C. Therefore, it can be concluded that the Darcy law and Stokes-Brinkman equation result in similar simulation results for the porous graphite domain, and the k-ε and Algebraic y^+ turbulent model generate similar results for the free flow region.

The moisture concentration profiles for Case D show obvious gradients near the free flow boundary. This phenomenon is due to the small gas momentum diffusivity in laminar flow, which requires a larger moisture gradient to transport the water molecules to the graphite domain for chemical reaction. This explanation can be verified by comparing the results of Case D in Figure 6-8 to Figure 6-10, which shows the magnitude of the moisture gradients near the graphite-fluid interface in the free flow region increase as the temperature increases.

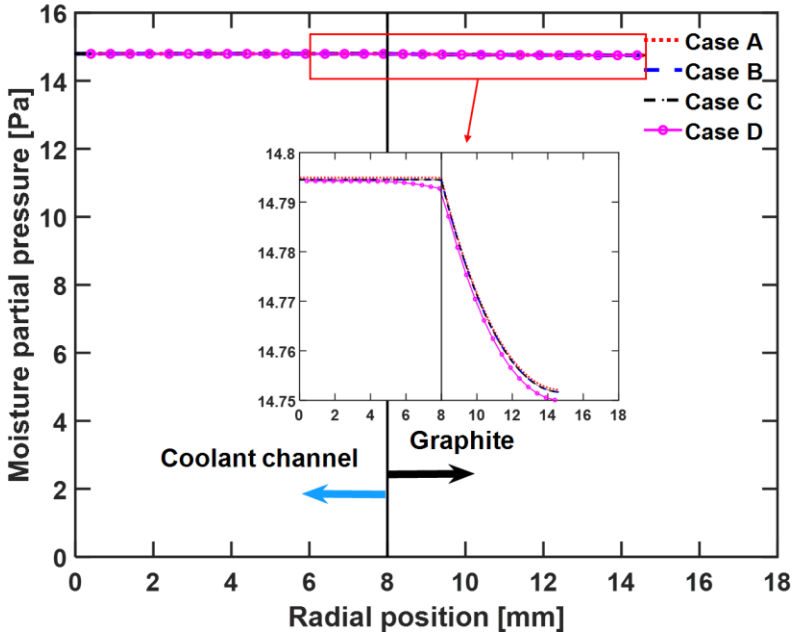

Figure 6-8 Computed moisture profiles from different flow models in the kinetics controlled regime at the gas inlet temperature of 823 K

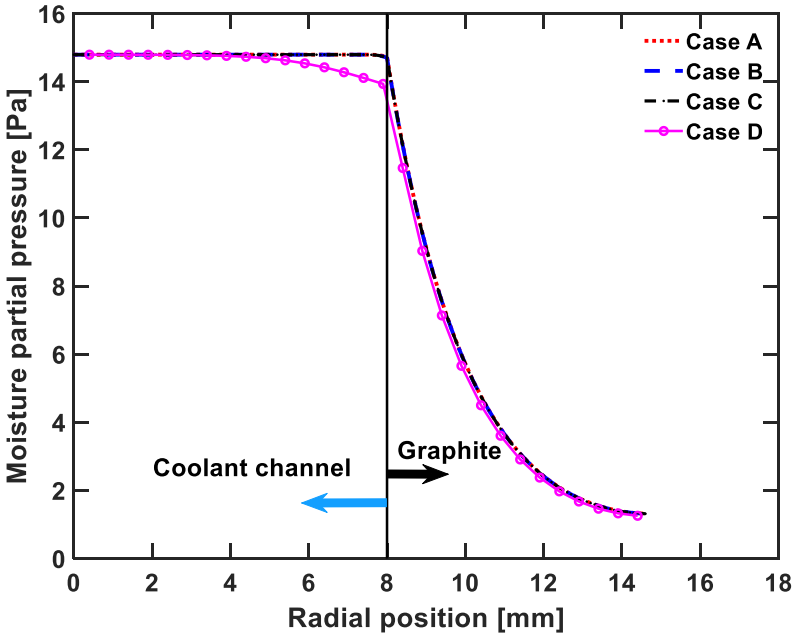

Figure 6-9 Computed moisture profiles from different flow models in the transitional regime at the gas inlet temperature of 1,023 K

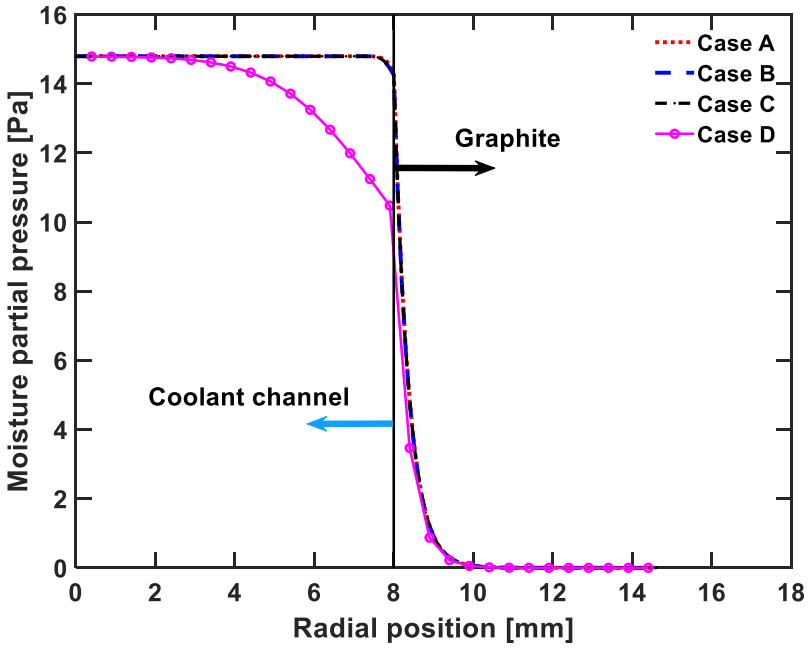

Figure 6-10 Computed moisture profiles from different flow models in the diffusion controlled regime at the gas inlet temperature of 1,173 K

6.3 Boundary Conditions

The boundary conditions for MHTGR normal operation simulation is described in this section. The effect of neutron irradiation on graphite oxidation is not included. It was believed the neutron irradiation closes the micro pores [86], which slows down the oxidation process. On the other hand, the neutron irradiation can also create new active sites. The actual effects of neutron irradiation on graphite oxidation behavior remains to be studied in the future.

The multiphysics model was first applied to investigate the chronic graphite-moisture oxidation for four grades of nuclear graphite, namely IG-110, 2114, PCEA, and NBG-17, under MHTGR normal operation conditions. The simulation for graphite-moisture oxidation for H-451 can be found in literature [32], which will not be described in detail since graphite H-451 is no

longer in commercial production. A summary of the properties of the four grades nuclear graphite is listed in Table 6-3. Due to the lack of detailed characterization of the graphite micro porous structure, some information used in this study was estimated based on a literature survey of similar grades of nuclear graphite.

Table 6-3 Summary of graphite properties

Graphite Grade	IG-110 [77], [87], [88]	2114 [87]	PCEA [87]	NBG-17 [87], [89]
Country of manufacturer	Japan	USA	USA	German
Manufacturer	Toyo Tanso	Merson	Graftech	SGL Carbon
Coke type	Petroleum	Pitch	Petroleum	Pitch
Manufacturing method	Mold	Mold	Extrude	Mold
Average grain size (μm)	40	15	800	800
Mean pore radius (μm)	1.8	1.8*	2.05*	2.05*
Structural parameter (ψ)	268	268*	80*	80*
Initial graphite density (g/cm^3)	1.75	2.01	1.84	1.89
Initial graphite porosity (%)	21.6	10	18.3	14

* Estimated values based on the literature survey

A schematic of the simulation domain is shown in Figure 6-11. The inlet gas velocity was set 16.7 m/s with a constant outlet pressure of 6.4 MPa. The inlet moisture and hydrogen partial pressures were set at 1.2 and 10 Pa, respectively. The axial power distribution of the three fuel rings in MHTGR core has been investigated using the system analysis code RELAP5-3D [90], and their results are depicted in Figure 6-12. Two methods can be adopted to apply the prototypic power distribution to the simulation domain. First, the fission power at each vertical location can be obtained by interpolating the data points in Figure 6-12. Second, polynomial correlations have

been obtained in literature [91] for the three power distributions, which can be directly used by COMSOL. To make the simulation results conservative, the maximum power distribution (Ring 1 in Figure 6-12) was applied in this study. The simulations were run for a full service period of 36 months.

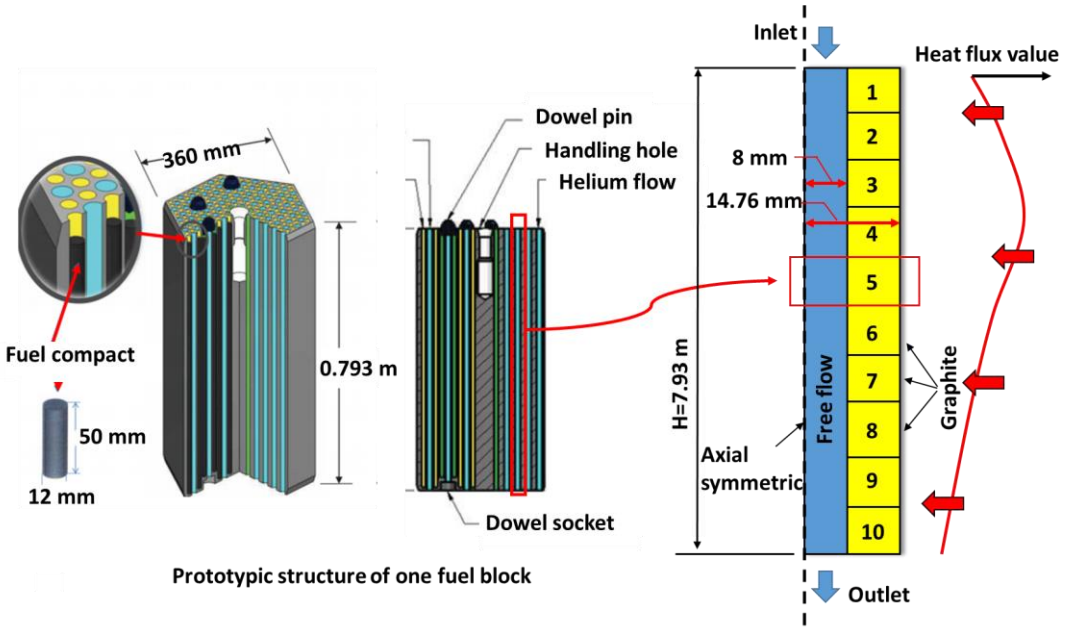

Figure 6-11 Schematic of the 2-D simulation domain for one coolant channel

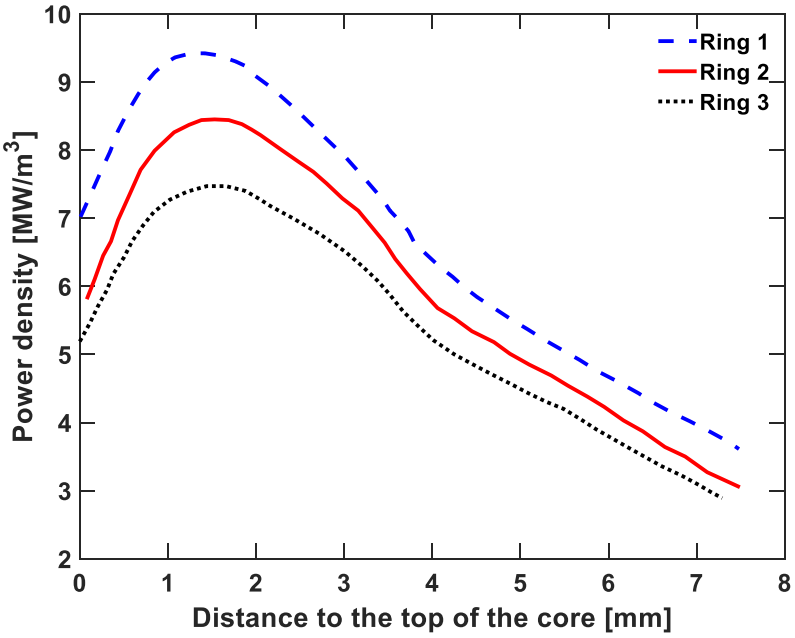

Figure 6-12 MHTGR fission power distribution (modified from literature [90])

6.4 Results Analysis and Discussion

The simulation results based on literature review for the four grades of graphite is discussed in this section. The volume-averaged and maximum graphite mass loss fraction at the end of the 36-month operation are shown in Table 6-4 for the four nuclear grades of graphite. Figure 6-13 shows the mass loss distributions in the graphite at the end of the 36-month operation period. It should be noted the x-axial scale is in millimeter and the y-axil scale is in meter. It can be seen that the graphite mass loss mainly occurs at the bottom one third or one quarter of the core region due to the higher graphite temperatures near the core outlet.

The graphite mass losses differ significantly for the four nuclear grades of graphite. For example, the maximum mass loss fraction for PCEA reaches 0.814 while it is only about 0.07 for

IG-110. The difference mainly results from the kinetic reaction rate equations of different grades of graphite. Figure 6-14 shows a comparison of Contescu LH reaction rate equations for the four nuclear grades of graphite at moisture and hydrogen partial pressure of 1.2 and 10 Pa, respectively. As can be seen, the predictions for graphite IG-110 is orders of magnitude smaller than those of the other three grades of graphite, leading to the smallest mass loss values in Table 6-4 and Figure 6-13. In this simulation, the maximum graphite temperature reaches about 1,277 K at the active core outlet. Correspondingly, PCEA is the most active one and therefore has the maximum mass loss fraction value 0.814.

Table 6-4 Average and maximum graphite mass loss values after 36-months operation

Blok No.	**IG-110**		**2114**		**PCEA**		**NBG-17**	
	Avg.	**Max.**	**Avg.**	**Max.**	**Avg.**	**Max.**	**Avg.**	**Max.**
1	3.2×10^{-15}	2.9×10^{-14}	2.3×10^{-10}	1.7×10^{-9}	7.6×10^{-11}	5.5×10^{-10}	6.6×10^{-12}	5.5×10^{-12}
2	2.4×10^{-12}	1.9×10^{-11}	5.0×10^{-8}	3.1×10^{-7}	1.4×10^{-8}	7.9×10^{-8}	2.6×10^{-12}	1.8×10^{-12}
3	6.2×10^{-10}	3.9×10^{-9}	4.5×10^{-6}	2.2×10^{-5}	9.1×10^{-7}	4.1×10^{-6}	3.7×10^{-8}	2.0×10^{-7}
4	5.3×10^{-8}	2.5×10^{-7}	1.5×10^{-4}	4.8×10^{-4}	2.4×10^{-5}	8.0×10^{-5}	2.0×10^{-6}	8.0×10^{-6}
5	1.7×10^{-6}	7.9×10^{-6}	9.1×10^{-4}	6.6×10^{-3}	2.5×10^{-4}	6.9×10^{-4}	4.0×10^{-5}	1.2×10^{-4}
6	2.4×10^{-5}	6.9×10^{-5}	2.8×10^{-3}	5.6×10^{-2}	1.1×10^{-3}	4.6×10^{-3}	3.3×10^{-4}	1.0×10^{-3}
7	2.0×10^{-4}	4.6×10^{-4}	7.4×10^{-3}	0.22	2.8×10^{-3}	2.6×10^{-2}	1.2×10^{-3}	7.1×10^{-3}
8	9.7×10^{-4}	2.9×10^{-3}	1.5×10^{-2}	0.46	6.8×10^{-3}	0.13	3.1×10^{-3}	4.3×10^{-2}
9	2.8×10^{-3}	1.6×10^{-2}	2.4×10^{-2}	0.64	1.8×10^{-2}	0.47	8.3×10^{-3}	0.21
10	6.4×10^{-3}	7.1×10^{-2}	3.1×10^{-2}	0.75	3.7×10^{-2}	0.81	2.1×10^{-2}	0.58

As shown Figure 6-13, graphite 2114 shows more uniform oxidation along the vertical direction than the other three graphite. This is also attributed to the activities of the four grades of graphite. It can be seen from Figure 6-14 that 2114 graphite shows high and more uniform activities at temperatures higher than 1,100 K.

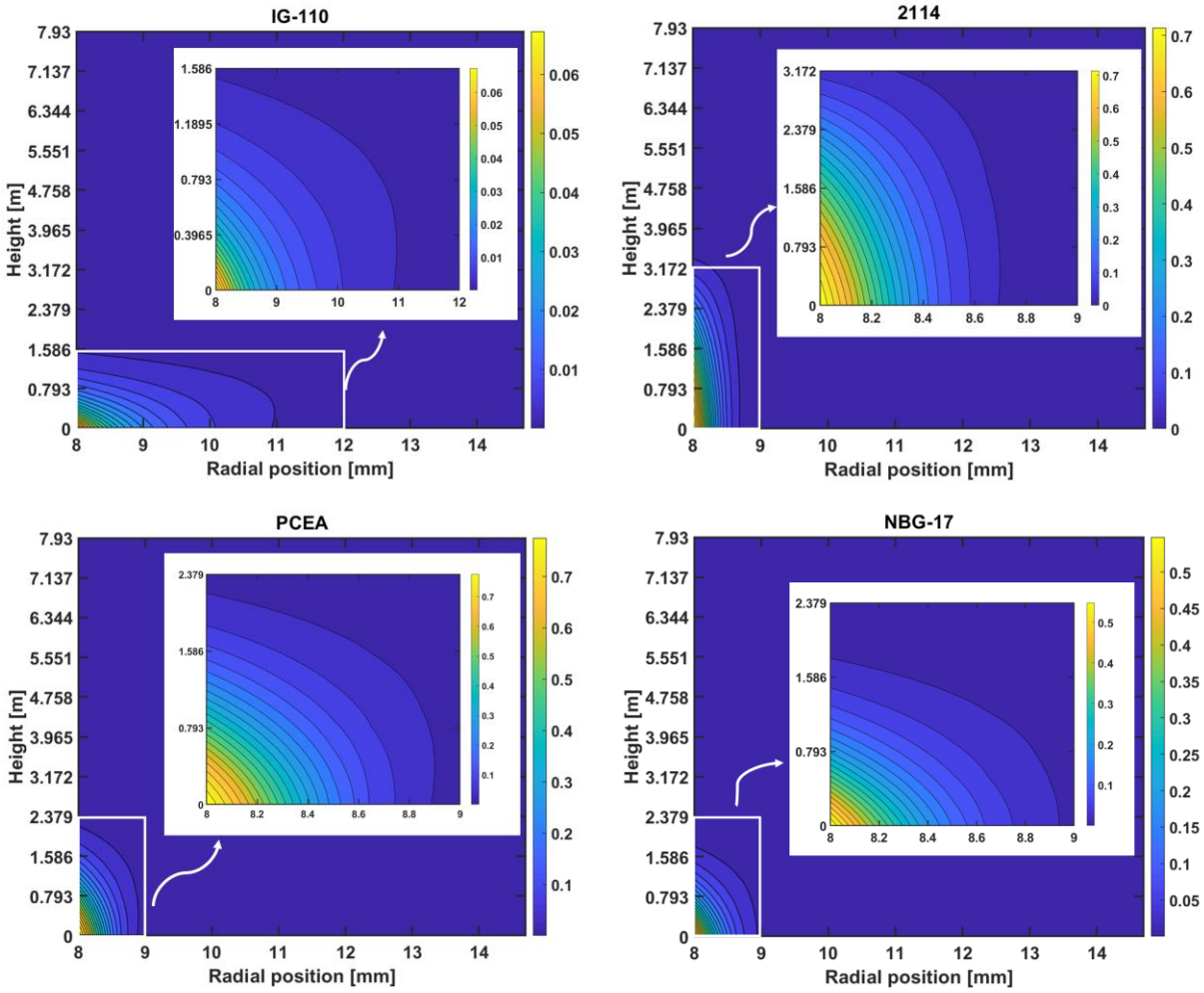

Figure 6-13 Graphite mass loss distributions in the four nuclear grades of graphite at the end of the 36-month operation period (height zero stands for the bottom of the active core)

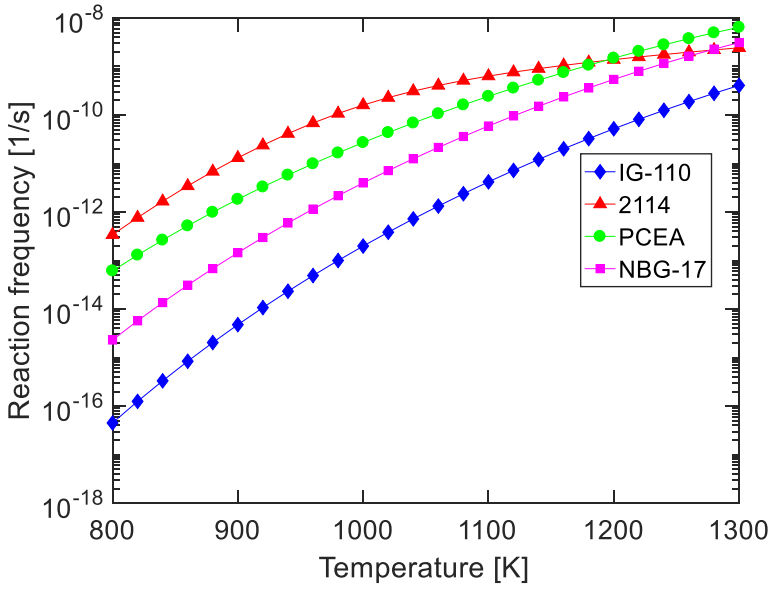

Figure 6-14 Predicted kinetic reaction rate by the Contescu LH model at $p_{H_2O} = 1.2$ and $p_{H_2} = 10$ Pa of various temperatures

The mass loss distributions were then extracted from the analysis at five depths, measured from the fluid-graphite interface into the graphite, 0.01, 0.5, 1.0, 1.5, and 2.0 mm to compare the performance of the four grades of graphite. The graphite mass losses at the five depths are shown in Figure 6-15 to Figure 6-19.

As it goes into a deeper region of the graphite, the maximum mass loss values along the vertical direction no longer appear at the core bottom. Instead, the peak of mass loss along the vertical direction gradually migrate to an upper region but their values decrease, as shown in Figure 6-15 to Figure 6-19. This phenomenon is due to the combined effect of the chemical reaction and mass transfer: if the reaction temperature is sufficiently high, the reaction becomes diffusion controlled that most water molecules would have been consumed before they penetrate into a deeper region in the graphite. Therefore, the chemical reaction can only happen within a thin layer of the graphite.

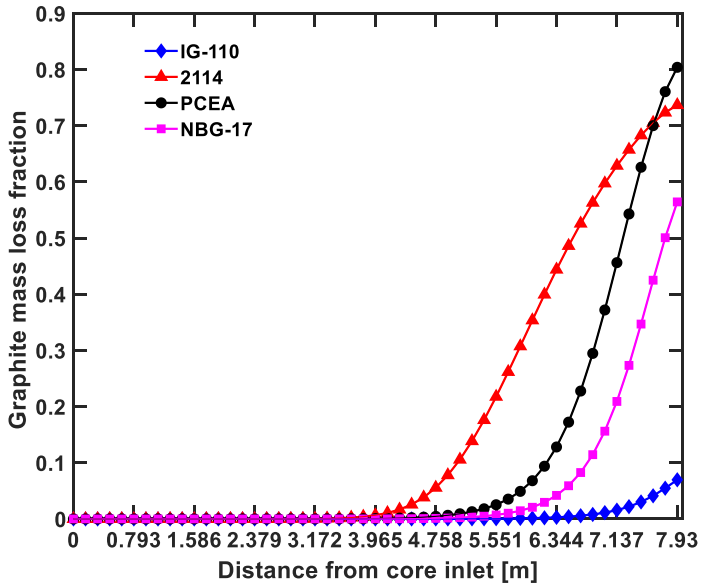

Figure 6-15 Graphite mass loss values at the depth of 0.01 mm into the graphite at the end of the 36-month operation period with $p_{H_2O} = 1.2$ and $p_{H_2} = 10$ Pa

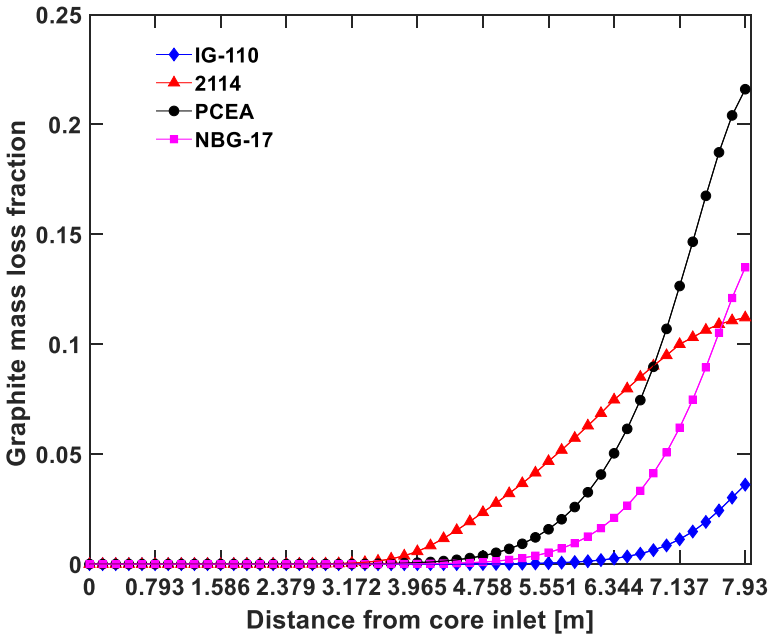

Figure 6-16 Graphite mass loss values at the depth of 0.5 mm into the graphite at the end of the 36-month operation period with $p_{H_2O} = 1.2$ and $p_{H_2} = 10$ Pa

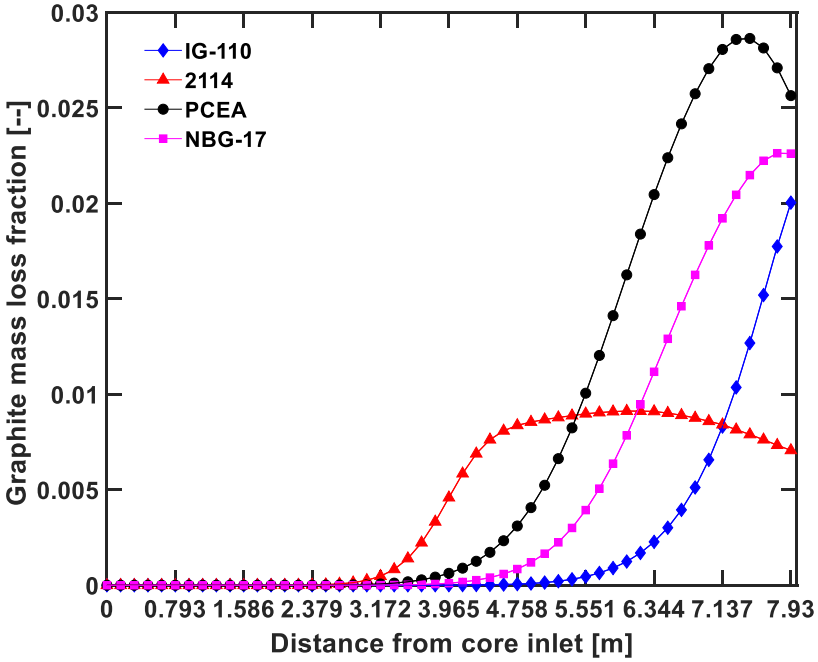

Figure 6-17 Graphite mass loss values at the depth of 1 mm into the graphite at the end of the 36-month operation period with $p_{H_2O} = 1.2$ and $p_{H_2} = 10$ Pa

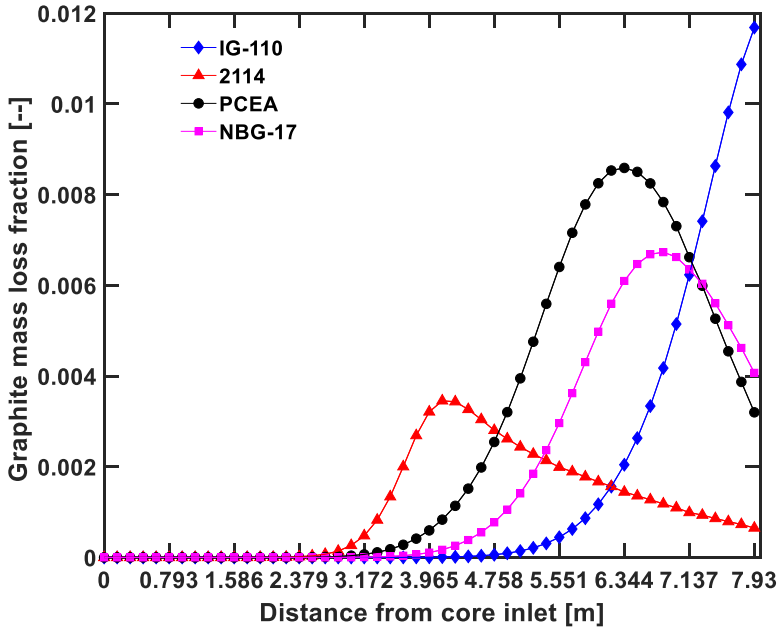

Figure 6-18 Graphite mass loss values at the depth of 1.5 mm into the graphite at the end of the 36-month operation period with $p_{H_2O} = 1.2$ and $p_{H_2} = 10$ Pa

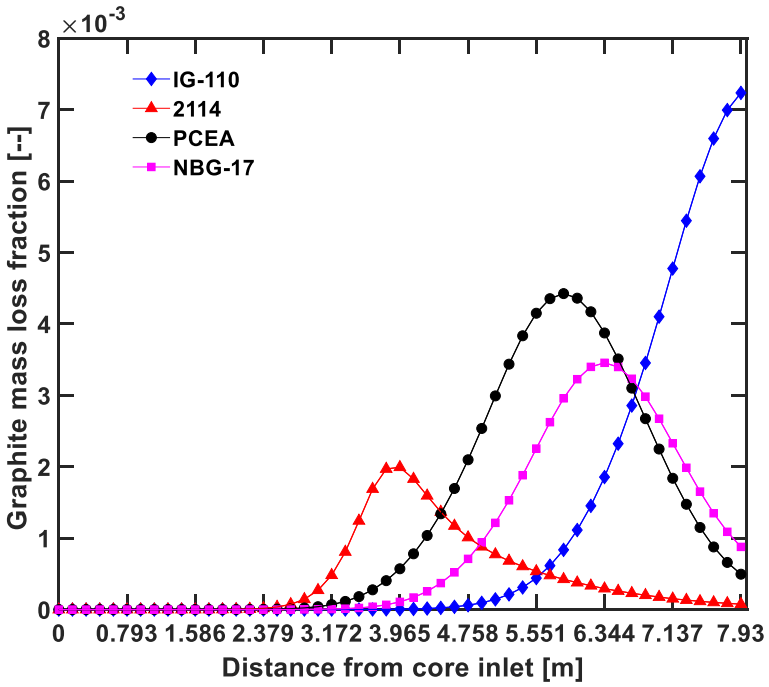

Figure 6-19 Graphite mass loss values at the depth of 2.0 mm into the graphite at the end of the 36-month operation period with $p_{H_2O} = 1.2$ and $p_{H_2} = 10$ Pa

6.5 Simulation based on Validated Multiphysics Model

The above simulation was performed using parameters in existing literature. However, the experimental works in this research proposed more accurate models for nuclear graphite IG-110, such as tortuosity, and kinetic oxidation rate equation. Therefore, the numerical simulation was updated correspondingly. In addition, it was found the computation speed of this multiphysics model is not fast enough mainly due to the large number of governing equations, thermal property correlations, and diffusivity calculations etc., which can impede its application. Therefore, a simplification is proposed to accelerate the computation, which is verified by comparing its results with the full validated model.

6.5.1 Boundary conditions

The above simulation indicates the chronic graphite-moisture oxidation during reactor normal operation mainly occurs at the bottom two fuel blocks for IG-110 due to the higher graphite temperature, as shown in Figure 6-13. Therefore, the simulation in this section will only focus on the bottom two fuel blocks (fuel block 9 and 10 in Figure 6-11). Accordingly, the inlet temperature of gas mixture should be adjusted. Figure 6-20 depicts the helium temperature in the coolant channel. At the inlet of fuel block 9, the gas temperature is 875.1 °C. The inlet velocity should be increased to 30.0 m/s accordingly so the nominal mass flow rate is maintained. The heat flux into the graphite domain is still based on the values in Figure 6-12. The simulations were run for a full service period of 36-months.

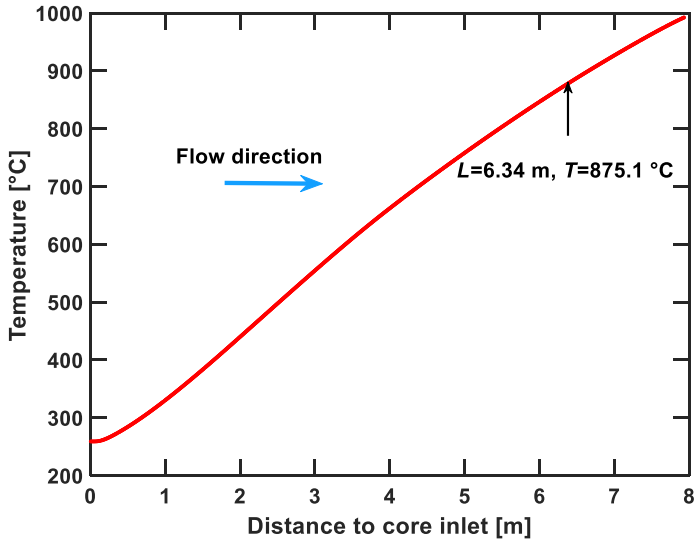

Figure 6-20 Gas mixture temperature in coolant channel under MHTGR normal operation condition

A total of four cases were simulated in this chapter, namely Cases B to E. The previous simulation for graphite IG-110 is referred as Case A in this section for comparison. The differences

of these five simulations are summarized in Table 6-5. Case E is the fully validated model as described in Chapter 5. Case B assumes tortuosity to be $\tau=\varepsilon^{-1}$. Case C uses the averaged mixture equation to solve the gas species transport. Case D is a simplified version of the validated model. In this simulation, the steady-state flow and heat transfer were first solved, which provides a constant flow and temperature field for mass transfer, kinetic chemical reaction, and micro structure evolution. In another word, the flow and temperature field will not be updated with time. Therefore, the computation time can be reduced.

Table 6-5 Models and parameters for reactor normal operation simulation

Model/Parameter	**Case A**	**Case B**	**Case C**	**Case D**	**Case E**
Gas diffusion equation	A-M[1]	M-S[2]	A-M	M-S	
Kinetic oxidation model	Contescu LH	BLH from this work			
Tortuosity model	$\tau=\varepsilon^{-1}$		$\tau=\varepsilon^{-3.3}$		
Time dependent physical field	all			tcs, chem, dode, dl[3]	all
ψ in factor F_m	265	Temperature dependent			
Mean pore diameter [μm]	3.6	3.9			
p_{H_2O} [Pa]	1.2				
p_{H_2} [Pa]	10				

1: Averaged mixture

2: Maxwell-Stephan diffusion equation

3: tsc: transport of concentrated species; chem: chemical reaction engineering; dode: domain ODEs and DAEs; dl: Darcy flow in porous media

6.5.2 Discussion on simulation results

The main simulation results are listed in . The distribution of graphite mass loss and moisture partial pressure are depicted in Figure 6-21 for height of 1.586, 0.793, and 0 m, which refers to the outlet of fuel block 10, outlet of fuel block 9, and inlet of fuel block 9, respectively.

Table 6-6 Simulation results of graphite-moisture oxidation for MHTGR after 36-months operation using validated model

Model/Parameter	**Case A**	**Case B**	**Case C**	**Case D**	**Case E**
Moisture penetration depth at *z*=1.586 m [mm]	--	1.65	1.34	1.34	1.34
Moisture penetration depth at *z*=0.786 m [mm]	--	1.27	0.41	0.41	0.41
Moisture penetration depth at *z*=0 m [mm]	--	1.12	0.38	0.38	0.41
Maximum mass loss fraction [--]	0.071	0.78	0.83	0.85	0.85
Computation time [hr]	--	31	32	17	31

It can be seen the difference between Cases, C, D, and E are negligible, which indicates the averaged gas mixture diffusion equations give similar results as the Maxwell-Stephan gas diffusion equations. However, Case D uses obviously smaller computation time than Cases C and E. Therefore, it is reasonable to solve steady-state free flow and heat transfer equations first and use them as input for the other physical processes for normal operation analysis. The simplification is valid because the oxidation rate is small. As a result, the gas production rate of H_2 and CO is not large enough to affect the gas mixture properties. The oxidation consumes carbon, which increases graphite porosity and therefore decreases the effective thermal conductivity of porous graphite domain. However, this is also a slow process. Furthermore, it can be seen the graphite mass loss mainly appears within a layer less than 0.5 mm thickness. Therefore, the thermal conductivity of the graphite domain cannot be changed obviously. However, this simplification is not suitable for

a fast transient scenario in which the flow velocity or temperature can change quickly, for example the steam ingress accident.

The simulation results of Case B are obviously different with Cases C, D, and E due to the smaller tortuosity value adopted. In this simulation, the moisture can penetrate the graphite into a deeper region. On the other hand, the maximum mass loss fraction at the graphite surface after 36-months operation is relatively smaller because the moisture partial pressure is lower at the graphite surface.

A terminology “moisture penetration depth” is listed in , which is defined in this research as the distance from sample surface into its inner region where the moisture partial pressure drops by 99%. Under this definition, the moisture can penetrate the whole graphite volume for Case A. However, it does not mean the graphite will be heavily oxidized. The maximum graphite mass loss in Case A is only about 7.01% at the end 36-months service time. As a comparison, the moisture penetration depth is only about 1.3 and 0.4 mm at height 1.586 and 0 m based on the validated model. Based on the validated model, the maximum graphite mass loss is predicted to be about 85% after 36-months operation. The big difference mainly results from the different reaction rate equations. The kinetic oxidation rate predicted by the BLH equation proposed in this work is about one magnitude higher than the Contescu LH equation. The higher kinetic oxidation rate tends to decrease the oxidation depth. In addition, the updated tortuosity model also decreases moisture penetration depth.

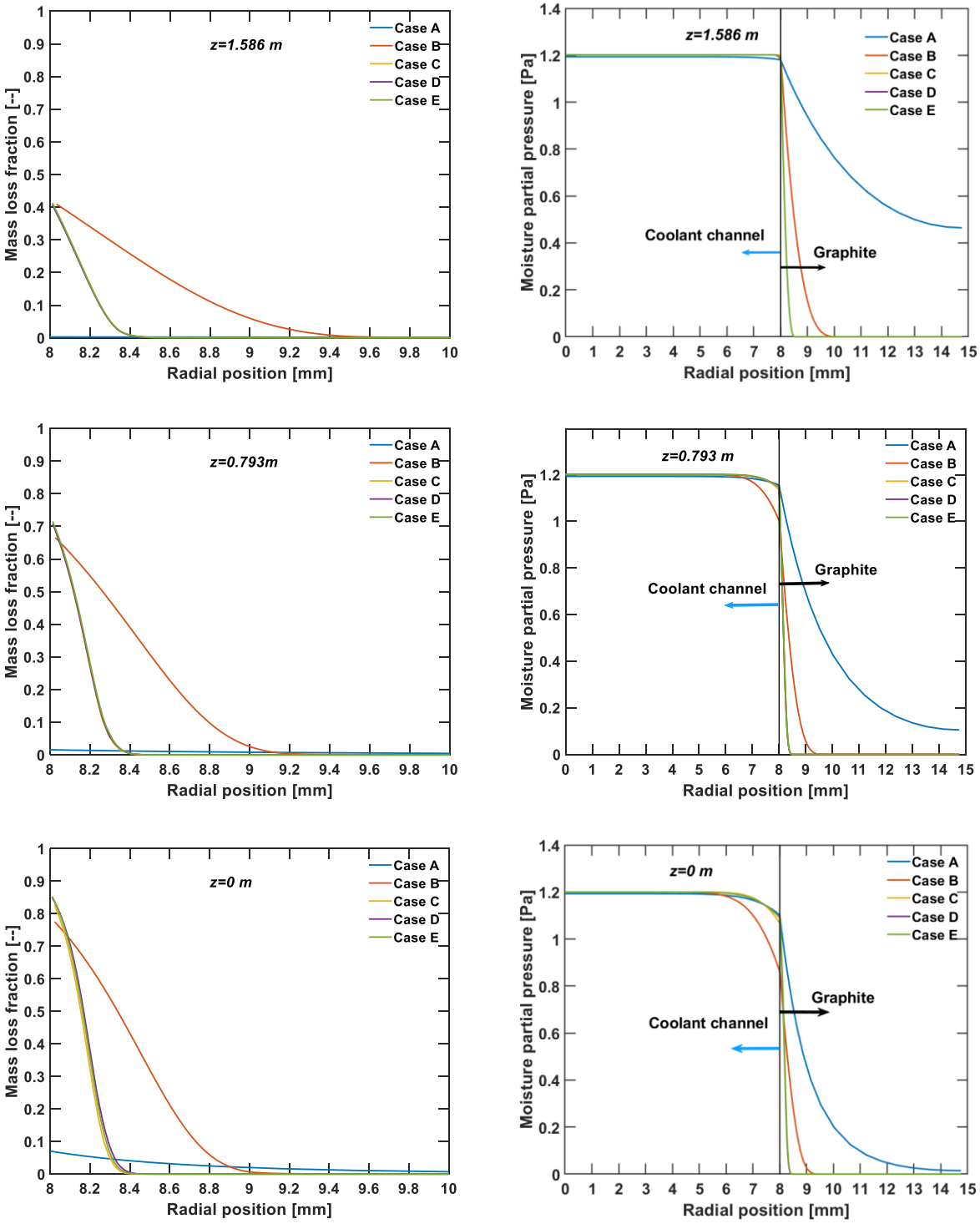

Figure 6-21 Simulated graphite mass loss and moisture concentration at end of 36-month operation

6.6 Conclusion of Graphite-Moisture Oxidation for Prototypic HTGR

The multiphysics model has been successfully applied to the graphite-moisture oxidation under MHTGR normal operation conditions. To reduce the simulation time, the 3-D coolant unit cell was simplified into a 2-D simulation domain, which maintains good accuracy. The long-term performance of four nuclear grades of graphite (IG-110, 2114, PCEA, and NBG-17) under MHTGR normal operation conditions was investigated based on literature review. A tortuosity model $\tau=\varepsilon^{-1}$ was first adopted, and the Contescu LH reaction rate equations were used as the source term for mass transfer equations. Based on the above assumptions, the simulation indicates graphite PCEA will exhibit the largest mass loss up to 81.4% on the surface due to its largest activity at temperature higher 1200 K. Graphite IG-110 has the minimum mass loss among the four grades of graphite. At the end of the 36-month operation, the oxidation mainly occurs at the bottom two or three blocks (Blocks 8 to 10 counting from the top of the core) due to their higher temperatures. In addition, the graphite mass loss quickly drops to below 1% within about1.5 to 2 mm into the graphite volume, leaving most graphite materials almost un-oxidized.

The simulation was then updated using the fully validated model. In this simulation, the BLH equation proposed by this work was used at the source term. In addition, the tortuosity model was updated. The validated model shows that during reactor normal operation, the moisture cannot trigger significant graphite corrosion. At the bottom of active core, the moisture penetration is less than 0.5 mm. Although the maximum mass loss at graphite surface can reach to about 85% at the end of 36-months operation, the oxidation is well confined within a thin layer of 0.5 mm. The majority of graphite will not be oxidized, as shown in Figure 6-22.

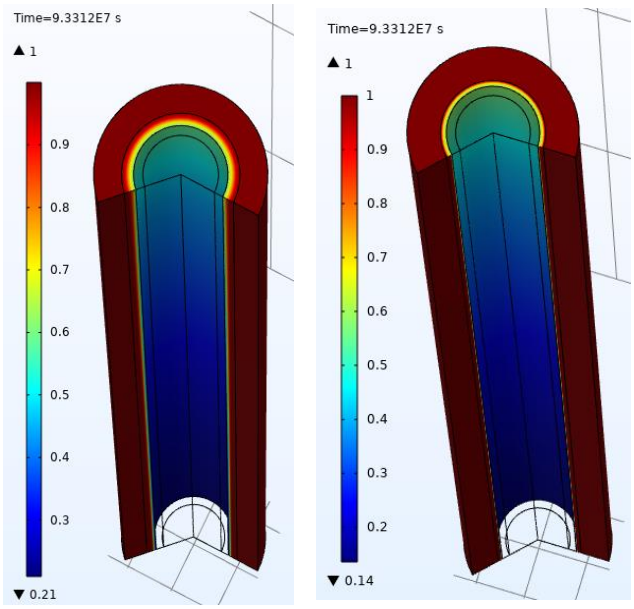

Figure 6-22 Simulated graphite density at end of 36-month operation for case B and E

The graphite mass loss distributions are critical to nuclear reactor safety analysis. A volume-uniform but smaller mass loss could jeopardize the graphite integrity much severer than a much larger but surface-concentrated oxidation. In general, the local graphite mechanical strength, such as the Yong's module, and compressive and bending strength, reduces exponentially as a function of mass loss. Through this simulation exercise, the spatial distributions of the graphite mass loss at the end of 36-monts operation can be predicted. Depending on different assumptions, the maximum mass loss can differ significantly. However, the oxidation can only occur within a thin layer of graphite into its surface. In the prototypic MHTGR design, the minimum distance from fuel compacts to the coolant channel is 4.65 mm, which means that 3.15 mm graphite still remains almost un-oxidized at the bottom region of the core based on the previous simulation. If the validated model is used, 4.15 mm graphite remains un-oxidized.

Considering the impurity control during reaction operations, the oxidation caused by moisture-graphite reaction should be less severe than the simulation results in this study. Therefore, it can be concluded that the chronic moisture-graphite oxidation alone cannot obviously reduce the graphite mechanical strength and jeopardize its integrity provided that the impurity level in the primary side be rigorously monitored and controlled.

The simulations also provide two important insights for the future investigations. First, the kinetic models of the moisture-graphite oxidation should be validated at low moisture partial pressures that are comparable to those during HTGR normal operations. Neither the Contescu LH equation nor the BLH equation proposed in this work is rigidly validated against experimental data at extreme low moisture concentrations. When the two equations are extended into moisture concentration at ppm level, they show significant difference.

In addition, the graphite mechanical strength degradation as a function of the mass loss should be included in future simulations. One assumption used in the model is that the graphite binders/fillers do not peel off, which does not hold at high graphite mass loss values. If the graphite binders/fillers peel-off occurs, the previous conclusion that only 0.5 mm of graphite will be oxidized will not be valid any more. Therefore, dedicated investigation is desired in the future to study the graphite failure at different mass loss fractions.

Chapter 7 Conclusions and Future Works

7.1 Summary of Major Conclusions

Both experimental and numerical investigation have been successfully carried out through this research. The major conclusion and breakthrough can be summarized as following:

(a). Verification of new experimental methodology: The graphite-steam oxidation was carefully investigated in this research using nuclear grade graphite IG-110. To fulfill the knowledge gap of graphite-steam oxidation within high steam concentration regimes, a test facility was designed and constructed. A high-resolution GC was applied to monitor the graphite oxidation rate online. The experimental methodology is verified by comparing the mass loss obtained from GC signals with the measurement of mass balance scale.

(b). Kinetic graphite-steam oxidation experiments: Using the test facility, the graphite-steam oxidation was experimentally investigated at temperature 850-1100 °C, steam partial pressure 0.5 to 20 kPa, and hydrogen partial pressure 0 to 3 kPa. The kinetic oxidation rate of graphite-steam oxidation was measured using thin graphite samples that favor a large surface-to-volume ratio. A total of 141 qualified data points were collected, while 37 data points were rejected due to accelerated oxidation sites.

In addition, the effect of hydrogen on inhibiting graphite-steam oxidation was clearly observed. The inhibiting effect of hydrogen is more prominent when its concentration is low, e.g., less than 500 Pa. Its effect tends to saturate after about 1500 Pa. The similar trend was also found for steam

concentrations. Under low steam concentration condition, the oxidation rate can be increased significantly if extra steam is introduced. The phenomena can be explained by the ratio of available active sites to the quantity of hydrogen or water molecules. When the quantity of hydrogen or water molecules is similar to or overwhelming over the number of active graphite sites, their effects on inhibiting/increasing oxidation rate will start to fade away.

(c). Kinetic oxidation rate equation: The oxidation rates were used to derive the LH and BLH reaction equations. A multivariable optimization code is programmed on MATLAB to narrow down the reaction constants. It was found the optimized BLH equation is more accurate in predicting the kinetic oxidation rate under the experiment conditions of this work. The MRD of the BLH equation is about 24% although the maximum difference between predicted oxidation rate with certain measurement can be as high as 55%. The different LH and BLH equations are compared. It is suggested to use either Contescu LH or the BLH equation of this work for low steam concentration regime. For conditions with steam concentration higher than 1 kPa, the BLH equation of this work is recommended.

(d). Effect of mass loss on kinetic oxidation rate: the effect of mass loss fraction on kinetic oxidation rate was investigated at three reaction temperatures. It was found the oxidation rate increases much faster with mass loss fraction under relatively lower temperatures. More experiments covering a wider temperature range with a smaller temperature interval are needed in the future to establish a solid model for this phenomenon in the future.

(e). Development of multiphyics model for graphite-steam oxidation: A multiphysics model is developed which couples flow and heat transfer in free flow and porous media. The transport of gas species, chemical reaction, and micro structure evolution of graphite were also included. To

validate the multiphysics model, four integral graphite-steam oxidation tests were carried out. In these tests, cylindrical graphite samples were used to intentionally include the effects of mass transfer. The apparent oxidation rates and post-oxidation density distribution were chosen as criterion to validate the multiphysics model. The comparison shows the numerical model satisfies both criterions well, which means the numerical model has correctly simulatedly all important physical processes.

(f). Numerical simulation of graphite-moisture oxidation for prototypic HTGR: The multiphysics model was applied to MHTGR normal operation conditions. Parameters and models in existing literature were first adopted. The performance of another three grades of nuclear graphite, namely NBG-17, 2114, and PCEA, were also investigated. Then, the simulation was updated for graphite IG-110 using the validated multiphysics model.

According to the simulation results, the graphite-moisture oxidation mainly occurs at the bottom two to three fuel blocks due to their higher temperatures. Although the maximum graphite mass loss can reach to a fairly high value, e.g., 85% for graphite IG-110, the oxidation is well confined within a layer of thickness 0.5 mm. Therefore, it can be concluded that the chronic moisture-graphite oxidation alone cannot obviously reduce the graphite mechanical strength and threaten its integrity providing the impurity level in the primary side will be rigorously monitored and controlled.

7.2 Future Works

While this research made significant progress and breakthrough in understanding the graphite-steam oxidation, it simultaneously points out some phenomena that should be investigated in the future, which are summarized as follows:

(a). Recommendations for HTGR design and safety analyses: the graphite oxidation rate can jump dramatically under some specific conditions that either involves metal catalyzers, or water droplet reaction with graphite. Therefore, it is desired to avoid direct contact between nuclear graphite and metal components in HTGR design. In addition, when performing steam ingress accident analysis for an HTGR, one scenario that should be considered is the impinging of liquid water droplet onto graphite surface.

(b). Effects of system pressure on graphite-steam oxidation: Although the steam partial pressure in the experiments of this work is comparable to a prototypic steam ingress accident scenario, the system pressure is much lower than the nominal pressure (~7 MPa) of an HTGR. Therefore, the possible effects of system pressure on graphite oxidation remain unknown. According to the theory of gas diffusion, the higher pressure leads to a smaller diffusivity, which slows down the mass transfer rate, which can prevent water molecules from penetrating into a deeper region. A detailed investigation is desired in the future.

(c). Experiments of graphite-moisture oxidation at ppm level: The kinetic oxidation model developed in this research is valid for temperature 850 to 1100 °C, steam partial pressure 0.5 to20 kPa, and hydrogen partial pressure 0 to 2 kPa. However, the steam partial pressures are too high for reactor normal operations. Therefore, it is desired to extend the experiments into a lower steam concentration regime, e.g., at ppm level, so the LH or BLH equations can be used with better confidence.

(d). Experimental works to strengthen the modeling foundation: It has to be noted some assumptions behind the multiphysics model have not been fully validated. As mentioned earlier, the tortuosity has significant influence on the effective diffusivity. To improve the accuracy of the

multiphysics mode, micro structure characterizations are needed. One of the key aspects is to investigate how the mean pore diameter and tortuosity will change with graphite mass loss. At the same time, the effective diffusivity should be directly measured using graphite at different mass loss fractions. In this way, the mass transfer in porous graphite can be validated separately.

(e) Numerical simulation of graphite oxidation in a steam ingress accident: The short term graphite-steam oxidation phenomena during a water/steam ingress accident has not been simulated due to the limited computational resources available to the author. The simulation of a fast transient steam/water ingress accident can be expensive because the time step has to be reduced to sub-seconds. Therefore, it is suggested to obtain the flow and temperature history using a system-level code first, which can be used as boundary conditions (such as the history of graphite temperature, flow velocity and steam concentration in the coolant channels, etc.) for the multiphysics model. In this way, the unknown parameters as well as mathematical equations can be reduced, so as the computation time.

Bibliography

[1] G. Alonso, R. Ramirez, E. Del Valle, and R. Castillo, "Process heat cogeneration using a high temperature reactor," *Nucl. Eng. Des.*, vol. 280, pp. 137–143, Dec. 2014.

[2] C. Fang, R. Morris, and F. Li, "Safety features of high temperature gas cooled reactor," *Sci. Technol. Nucl. Install.*, vol. 2017, 2017.

[3] General Atomics, "Next Generation Nuclear Plant (NGNP) prismatic HTGR conceptual design project final technical report," 2011.

[4] Z. Zhang *et al.*, "Current status and technical description of Chinese 2 × 250 MWth HTR-PM demonstration plant," *Nucl. Eng. Des.*, vol. 239, no. 7, pp. 1212–1219, Jul. 2009.

[5] Nuclear Energy Agency, "Benchmark of the Modular High-Temperature Gas-Cooled Reactor 350 MW core design: Volumes I and II," Feb. 2018.

[6] F. Chen and Z. Han, "Steady-state thermal fluids analysis for the HTR-PM equilibrium core," *Int. J. Adv. Nucl. React. Des. Technol.*, vol. 3, pp. 11–17, Jan. 2021.

[7] L. Lommers, F. Shahrokhi, J. Mayer III, and F. Southworth, "AREVA modular steam cycle-high temperature gas-cooled reactor development progress," in *Proceedings of the HTR*, 2014.

[8] C. I. Contescu and R. W. Mee, "Status of chronic oxidation studies of graphite," 2016.

[9] R. D. Burnette and N. L. Baldwin, "Primary coolant chemistry of the peach bottom and Fort ST. Vrain high-temperature gas-cooled reactors," 1980.

[10] Y. Wang, Y. Zheng, F. Li, and L. Shi, "Analysis on blow-down transient in water ingress accident of high temperature gas-cooled reactor," *Nucl. Eng. Des.*, vol. 271, pp. 404–410, May 2014.

[11] Y. Zheng, L. Shi, and Y. Wang, "Water-ingress analysis for the 200 MWe pebble-bed modular high temperature gas-cooled reactor," *Nucl. Eng. Des.*, vol. 240, no. 10, pp. 3095–3107, Oct. 2010.

[12] C. Wang, S. Shi, D. J. Arcilesi, X. Sun, R. N. Christensen, and P. Sabharwall, "Scaling analysis and test facility design for steam ingress accident in MHTGR ," in *NUTHOS-11*, 2016.

[13] S. Sato, K. Hirakawa, A. Kurumada, S. Kimura, and E. Yasuda, “Degradation of fracture mechanics properties of reactor graphite due to burn-off,” *Nucl. Eng. Des.*, vol. 118, no. 2, pp. 227–241, Mar. 1990.

[14] A. C. Matthews, J. J. Kane, W. D. Swank, and W. E. Windes, “Nuclear graphite strength degradation under varying oxidizing conditions,” *Nucl. Eng. Des.*, vol. 379, Aug. 2021.

[15] X. Zhou *et al.*, “Oxidation behavior of matrix graphite and its effect on compressive strength,” *Sci. Technol. Nucl. Install.*, vol. 2017, 2017.

[16] G. B. Engle, “Assessment of graphite H-451 graphite for replaceable fuel and reflector elements in HTGR,” 1977.

[17] C. Velasquez, G. Hightower, and R. Burnette, “Oxidation of H-451 graphite by steam. Part I. Reaction kinetics,” 1978.

[18] R. Bratton and T. Burchell, “NGNP graphite testing and qualification specimen selection strategy,” Idaho Falls, Idaho, USA, May 2005.

[19] E. A. Gulbransen, K. F. Andrew, and F. A. Brassart, “The oxidation of graphite at temperatures of 600° to 1500°C and at pressures of 2 to 76 Torr of oxygen,” *J. Electrochem. Soc.*, vol. 110, no. 6, pp. 476–483, Jun. 1963.

[20] C. I. Contescu *et al.*, “Beyond the classical kinetic model for chronic graphite oxidation by moisture in high temperature gas-cooled reactors,” *Carbon N. Y.*, vol. 127, pp. 158–169, Feb. 2018.

[21] F. J. Long and K. W. Sykes, “The mechanism of the steam-carbon reaction,” *Proc. R. Soc. London. Ser. A. Math. Phys. Sci.*, vol. 193, no. 1034, pp. 377–399, Jul. 1948.

[22] R. C. Giberson and J. P. Walker, “Reaction of nuclear graphite with water vapor part I. Effect of hydrogen and water vapor partial pressures,” *Carbon N. Y.*, vol. 3, no. 4, pp. 521–525, Feb. 1966.

[23] J. Gadsby, C. N. Hinshelwood, and K. W. Sykes, “The kinetics of the reactions of the steam-carbon system,” *Proc. R. Soc. London. Ser. A. Math. Phys. Sci.*, vol. 187, no. 1009, pp. 129–151, Oct. 1946.

[24] P. L. Walker, F. Rusinko, and L. G. Austin, “Gas reactions of carbon,” *Adv. Catal.*, vol. 11, no. C, pp. 133–221, Jan. 1959.

[25] J. J. Lee, T. K. Ghosh, and S. K. Loyalka, “Comparison of NBG-18, NBG-17, IG-110 and IG-11 oxidation kinetics in air,” *J. Nucl. Mater.*, vol. 500, pp. 64–71, Mar. 2018.

[26] E. L. Fuller and J. M. Okoh, “Kinetics and mechanisms of the reaction of air with nuclear grade graphites: IG-110,” *J. Nucl. Mater.*, vol. 240, no. 3, pp. 241–250, Feb. 1997.

[27] P. Wang, C. I. Contescu, S. Yu, and T. D. Burchell, “Pore structure development in

oxidized IG-110 nuclear graphite," *J. Nucl. Mater.*, vol. 430, no. 1–3, pp. 229–238, Nov. 2012.

[28] X. Luo, X. Yu, S. Yu, and J.-C. Robin, "Analysis of graphite gasification by water vapor at different conversions," *Nucl. Eng. Des.*, vol. 273, pp. 68–74, Jul. 2014.

[29] X. Luo, J.-C. Robin, and S. Yu, "Theoretical analysis of mass transfer and reaction in a porous medium applied to the gasification of graphite by water vapor," *Nucl. Eng. Des.*, vol. 236, no. 9, pp. 938–947, May 2006.

[30] X. Luo, J.-C. Robin, and S. Yu, "Effect of temperature on graphite oxidation behavior," *Nucl. Eng. Des.*, vol. 227, no. 3, pp. 273–280, Feb. 2004.

[31] X. Yu and S. Yu, "Analysis of fuel element matrix graphite corrosion in HTR-PM for normal operating conditions," *Nucl. Eng. Des.*, vol. 240, no. 4, pp. 738–743, Apr. 2010.

[32] C. Wang, X. Sun, R. N. Christensen, and S. Shi, "Numerical simulation of chronic moisture graphite oxidation for MHTGR," *Trans. Am. Nucearl Soc.*, vol. 118, pp. 723–726, 2018.

[33] C. I. Contescu, R. W. Mee, P. Wang, A. V. Romanova, and T. D. Burchell, "Oxidation of PCEA nuclear graphite by low water concentrations in helium," *J. Nucl. Mater.*, vol. 453, no. 1–3, pp. 225–232, Oct. 2014.

[34] C. I. Contescu, Y. Lee, and R. W. Mee, "Oxidation kinetics by water vapor of nuclear graphite grade 2114," Oak Ridge, TN (United States), Nov. 2018.

[35] Y. J. Cho and K. Lu, "Water vapor oxidation behaviors of nuclear graphite IG-110 for a postulated accident scenario in high temperature gas-cooled reactors," *Carbon N. Y.*, vol. 164, pp. 251–260, Aug. 2020.

[36] E. S. Kim, C. H. Oh, and H. C. No, "Experimental study and model development on the moisture effect for nuclear graphite oxidation," vol. 164, no. 2, pp. 278–285, 2017.

[37] Y. M. Ferng and C. W. Chi, "CFD investigating the air ingress accident for a HTGR simulation of graphite corrosion oxidation," *Nucl. Eng. Des.*, vol. 248, pp. 55–65, Jul. 2012.

[38] Y. M. Ferng and C. T. Chen, "CFD investigating thermal-hydraulic characteristics and hydrogen generation from graphite–water reaction after SG tube rupture in HTR-10 reactor," *Appl. Therm. Eng.*, vol. 31, no. 14–15, pp. 2430–2438, Oct. 2011.

[39] R. P. Wichner, T. D. Burchell, and C. I. Contescu, "Penetration depth and transient oxidation of graphite by oxygen and water vapor," *J. Nucl. Mater.*, vol. 393, no. 3, pp. 518–521, Sep. 2009.

[40] C. Contescu, "Validation of Wichner predictive model for chronic oxidation by moisture of nuclear graphite," Oak Ridge, TN, USA, 2019.

[41] M. S. El-Genk and J. M. P. Tournier, “Validation of gasification model for NBG-18 nuclear graphite,” *Nucl. Eng. Des.*, vol. 250, pp. 142–155, Sep. 2012.

[42] M. S. El-Genk, J. M. P. Tournier, and C. I. Contescu, “Chemical kinetics parameters and model validation for the gasification of PCEA nuclear graphite,” *J. Nucl. Mater.*, vol. 444, no. 1–3, pp. 112–128, Jan. 2014.

[43] M. S. El-Genk and J. M. P. Tournier, “Comparison of oxidation model predictions with gasification data of IG-110, IG-430 and NBG-25 nuclear graphite,” *J. Nucl. Mater.*, vol. 420, no. 1–3, pp. 141–158, Jan. 2012.

[44] Y. Liu, C. Wang, Y. Qian, and X. Sun, “Uncertainty analysis of PIV measurements in bubbly flows considering sampling and bubble effects with ray optics modeling,” *Nucl. Eng. Des.*, vol. 364, p. 110677, Aug. 2020.

[45] X. Yu, L. Brissonneau, C. Bourdeloie, and S. Yu, “The modeling of graphite oxidation behavior for HTGR fuel coolant channels under normal operating conditions,” *Nucl. Eng. Des.*, vol. 238, no. 9, pp. 2230–2238, Sep. 2008.

[46] C. Wang, X. Sun, and R. N. Christensen, “Multiphysics simulation of moisture-graphite oxidation in MHTGR,” *Ann. Nucl. Energy*, vol. 131, pp. 483–495, Sep. 2019.

[47] K. L. Jones, G. M. Laudone, and G. P. Matthews, “A multi-technique experimental and modelling study of the porous structure of IG-110 and IG-430 nuclear graphite,” *Carbon N. Y.*, vol. 128, pp. 1–11, Mar. 2018.

[48] N. C. Gallego, C. I. Contescu, and J. R. Keiser, “Progress report on graphite-salt intrusion studies,” Oak Ridge, TN (United States), 2020.

[49] A. Rabbani, M. Babaei, and F. Javadpour, “A triple pore network model (T-PNM) for gas flow simulation in fractured, micro-porous and meso-porous media,” *Transp. Porous Media 2020 1323*, vol. 132, no. 3, pp. 707–740, Mar. 2020.

[50] Q. Xiong, T. G. Baychev, and A. P. Jivkov, “Review of pore network modelling of porous media: Experimental characterisations, network constructions and applications to reactive transport,” *J. Contam. Hydrol.*, vol. 192, pp. 101–117, Sep. 2016.

[51] N. Gholizade, A. A. Amooey, and S. R. Nabavi, “Simulation of multicomponent diffusion in porous media using pore-network model,” *J. Porous Media*, vol. 23, no. 8, pp. 741–750, 2020.

[52] Department of Energy, “Preliminary safety information document for the standard MHTGR,” Oct. 1986.

[53] ASTM-7542, “Standard test method for air oxidation of carbon and graphite in the kinetic regime,” 2015.

[54] K. Otto, L. Bartosiewicz, and M. Shelef, “Catalytic steam gasification of graphite: Effects

of calcium, strontium, and barium with and without sulfur," *Carbon N. Y.*, vol. 17, no. 4, pp. 351–357, Jan. 1979.

[55] R. Yan, Y. Dong, Y. Zhou, X. Sun, and Z. Li, "Investigation of oxidation behaviors of nuclear graphite being developed and IG-110 based on gas analysis," vol. 54, no. 11, pp. 1168–1177, Nov. 2017.

[56] KTA, "Reactor core design for high-temperature gas-cooled reactors part 1: calculation of the material properties of helium," 1978.

[57] "NIST Chemistry WebBook." [Online]. Available: https://webbook.nist.gov/chemistry/. [Accessed: 05-Aug-2021].

[58] C. R. Wilke, "A viscosity equation for gas mixtures," *J. Chem. Phys.*, vol. 18, no. 4, p. 519, Dec. 1950.

[59] S. K. Bhatia and D. D. Perlmutter, "A random pore model for fluid-solid reactions: I. Isothermal, kinetic control," *AIChE J.*, vol. 26, no. 3, pp. 379–386, May 1980.

[60] S. K. Bhatia and D. D. Perlmutter, "A random pore model for fluid-solid reactions: II. Diffusion and transport effects," *AIChE J.*, vol. 27, no. 2, pp. 247–254, Mar. 1981.

[61] W. Xu, L. Shi, Y. H. Zheng, and P. Liu, "Research on oxidation model of nuclear grade graphite IG-110," *At. Energy Sci. Technol.*, vol. 49, pp. 475–480, May 2015.

[62] "Solve nonlinear least-squares (nonlinear data-fitting) problems - MATLAB lsqnonlin." .

[63] N. Chen, Q. Peng, Z. Jiao, I. van Rooyen, W. F. Skerjanc, and F. Gao, "Analytical bond-order potential for silver, palladium, ruthenium and iodine bulk diffusion in silicon carbide," *J. Phys. Condens. Matter*, vol. 32, no. 8, p. 085702, Nov. 2019.

[64] M. M. Stempniewicz, "Correlation for steam–graphite reaction," *Nucl. Eng. Des.*, vol. 280, pp. 285–293, Dec. 2014.

[65] J. R. Welty, G. L. Rorrer, and D. G. Foster, *Fundamentals of momentum, heat, and mass transfer*, 7th ed. Hoboken, NJ, USA: Wiley&Sons Inc., 2019.

[66] S. K. Bhatia and D. D. Perlmutter, "A random pore model for fluid-solid reactions: II. Diffusion and transport effects," *AIChE J.*, vol. 27, no. 2, pp. 247–254, Mar. 1981.

[67] B. Tjaden, S. J. Cooper, D. J. Brett, D. Kramer, and P. R. Shearing, "On the origin and application of the Bruggeman correlation for analysing transport phenomena in electrochemical systems," *Curr. Opin. Chem. Eng.*, vol. 12, pp. 44–51, May 2016.

[68] H. Chou, L. Wu, L. Zeng, and A. Chang, "Evaluation of solute diffusion tortuosity factor models for variously saturated soils," *Water Resour. Res.*, vol. 48, no. 10, Oct. 2012.

[69] A. Puzas, V. Remeikis, Ž. Ežerinskis, P. Serapinas, A. Plukis, and G. Duškesas, "Mass

spectrometric determination of impurities in reactor core graphite for radioactive waste composition modelling," *Lith. J. Phys.*, vol. 50, no. 4, pp. 445–449, Oct. 2010.

[70] K. Shen, X. Chen, W. Shen, Z. H. Huang, B. Liu, and F. Kang, "Thermal and gas purification of natural graphite for nuclear applications," *Carbon N. Y.*, vol. 173, pp. 769–781, Mar. 2021.

[71] P. C. Carman, *Flow of gases through porous media*, 1st ed. New York: Acamemic Press, 1956.

[72] M. P. Bacos, J. M. Dorvaux, O. Lavigne, and Y. Renollet, "C/C composite oxidation model: I. Morphological experimental investigations," *Carbon N. Y.*, vol. 38, no. 1, pp. 77–92, Jan. 2000.

[73] M. P. Bacos, J. L. Cochon, J. M. Dorvaux, and O. Lavigne, "C/C composite oxidation model II. Oxidation experimental investigations," *Carbon N. Y.*, vol. 38, no. 1, pp. 93–103, Jan. 2000.

[74] M. P. Bacos, J. M. Dorvaux, O. Lavigne, and J. Talandier, "C/C composite oxidation model: III. Physical basis, limitations and applications," *Carbon N. Y.*, vol. 38, no. 1, pp. 105–117, Jan. 2000.

[75] E. E. Petersen, "Reaction of porous solids," *AIChE J.*, vol. 3, no. 4, pp. 443–448, Dec. 1957.

[76] S. K. Bhatia and D. D. Perlmutter, "A random pore model for fluid-solid reactions: I. Isothermal, kinetic control," *AIChE J.*, vol. 26, no. 3, pp. 379–386, May 1980.

[77] W. Xu, L. Shi, Y. Zheng, and P. Liu, "Research on oxidation model of nuclear grade graphite IG-110," *At. Energy Sci. Technol.*, vol. 48, pp. 475–480, 2015.

[78] A. A. Campbell and Y. Katoh, "Report on effects of irradiation on material IG-110-Prepared for Toyo Tanso Co., Ltd," Oak Ridge, TN(USA), Nov. 2017.

[79] S. Ishiyama, T. D. Burchell, J. P. Strizak, and M. Eto, "The effect of high fluence neutron irradiation on the properties of a fine-grained isotropic nuclear graphite," *J. Nucl. Mater.*, vol. 230, no. 1, pp. 1–7, May 1996.

[80] COMSOL, "Carbon deposition in heterogeneous catalysis," Burlington, MA(USA).

[81] P. Moldrup, T. Olesen, T. Komatsu, P. Schjønning, and D. E. Rolston, "Tortuosity, diffusivity, and permeability in the soil liquid and gaseous phases," *Soil Sci. Soc. Am. J.*, vol. 65, no. 3, pp. 613–623, May 2001.

[82] D.-W. Chung, M. Ebner, D. R. Ely, V. Wood, and R. E. García, "Validity of the Bruggeman relation for porous electrodes," *Model. Simul. Mater. Sci. Eng.*, vol. 21, no. 7, p. 074009, Oct. 2013.

[83] W. Chengqi and S. Xiaodong, “Multiphysics simulation of IG-110 oxidation by moisture under MHTGR normal operation conditions,” *Trans. Am. Nucl. Soc.*, vol. 119, pp. 555–558, 2018.

[84] Nuclear Agency Energy, “NEA benchmark of the Modular High-Temperature Gas-Cooled Reactor-350 MW core designvolumes I and II,” 2018.

[85] R. Stainsby *et al.*, “Investigation of local heat transfer phenomena in a prismatic modular reactor core,” May 2009.

[86] B. J. Marsden *et al.*, “Dimensional change, irradiation creep and thermal/mechanical property changes in nuclear graphite,” vol. 61, no. 3, pp. 155–182, Apr. 2016.

[87] C. I. Contescu *et al.*, “Beyond the classical kinetic model for chronic graphite oxidation by moisture in high temperature gas-cooled reactors,” *Carbon N. Y.*, vol. 140, p. 249, 2018.

[88] T. D. Burchell, “A microstructurally based fracture polygranular,” TN, 1991.

[89] M. S. El-Genk, J. M. P. Tournier, and C. I. Contescu, “Chemical kinetics parameters and model validation for the gasification of PCEA nuclear graphite,” *J. Nucl. Mater.*, vol. 444, no. 1–3, pp. 112–128, 2014.

[90] G. Strydom and A. S. Epiney, “RELAP5-3D results for phase I (exercise 2) of the OECD/NEA MHTGR-350 MW benchmark,” in *The International Congress on Advances in Nuclear Power Plants*, 2012.

[91] C. Wang, X. Sun, and P. Sabharwall, “CFD investigation of MHTGR natural circulation and decay heat removal in P-LOFC accident,” *Front. Energy Res.*, vol. 8, p. 129, Jun. 2020.

Appendix

Appendix A: MATLAB Code of Multi Variable Optimization

```
%% Multi variable optimization

function fffit
%%for graphite system;BLH for oxidation rate
clear
format long;

global OutFile                                  % iPotentialFile
%%%%%%%%%%%%%%%%%%%%%%%%%%%%%%%%%%%%%%%%%%%%%%%%%%%%%%%%%%%%%%%%%%%%%%%%%%%%%%%%

%%%%%%%%%%%%%%%%%%%%%%%%%%%%%%%%%%%%%%%%%%%%%%%%%%%%%%%%%%%%%%%%%%%%%%%%%%%%%%%%
folder = '\\engin-storage.m.storage.umich.edu\engin-
storage\nukewang\windat.V2\Desktop\Chengqi Wang
Dissertation\Graphite_Moisture_Experiment\BLH_Analysis';
OutFile = fopen('outfile','w');
fprintf (OutFile,'outfiles for BLH fitting, Graphite IG-110');
%%%%%%%%%%%%%%%%%%%%%%%%%%%%%%%%%%%%%%%%%%%%%%%%%%%%%%%%%%%%%%%%%%%%%%%%%%%%%%%%

%%%%%%%%%%%%%%%%%%%%%%%%%%%%%%%%%%%%%%%%%%%%%%%%%%%%%%%%%%%%%%%%%%%%%%%%%%%%%%%%
% fitting variable
xA1 = 79147202.233398541808;
 xA2 = 823.213283101513;
 xA3 = 34960.126835460927;
 xE1 = -258.224591196391;
 xE2 = 19.305248840939;
 xE3 = -313.863087558206;
 xmmin =  0.363660432339;
 xmmax =  0.741634281116;
 xtheta = 34.079149643011;
 xT0 = 1250.107426412911;
 xn =  1.0;


 % xn =  1.239106595529;

x0 = [xA1,xA2,xA3,xE1,xE2,xE3,xmmin, xmmax,xtheta, xT0];  % initial guess

%%%%%%%%%%%%%%%%%%%%%%%%%%%%%%%%%%%%%%%%%%%%%%%%%%%%%%%%%%%%%%%%%%%%%%%%%%%%%%%%
```

```
%%%%%%%%%%%%%%%%%%%%%%%%%%%%%%%%%%%%%%%%%%%%%%%%%%%%%%%%%%%%%%%%%%%%%%%
%call fitting function
%%%%%%%%%%%%%%%%%%%%%%%%%%%%%%%%%%%%%%%%%%%%%%%%%%%%%%%%%%%%%%%%%%%%%%%
%Method of lsqnonlin
diffmaxchange = 10000;
diffminchange = 0.001;
findifftype = 'central';    %'central'or'forward'
maxfunevals = 100000;
maxiter = 50000;
tolfun = 1e-100;
tolx = 1e-100;
lb = [   0    0    0  -Inf  -Inf  -Inf  -10   -10  -500  800   ];      %
lower boundary
ub = [ Inf  Inf  Inf   Inf   Inf   Inf   10    10   500  2500  ];      %
uppder boundary
display = 'iter-detailed';
fprintf (OutFile,'diffmaxchange=%5i\n',diffmaxchange);
fprintf (OutFile,'diffminchange=%5i\n',diffminchange);
fprintf (OutFile,'findifftype=%20s\n',findifftype);
fprintf (OutFile,'maxfunevals=%7i\n',maxfunevals);
fprintf (OutFile,'maxiter=%7i\n',maxiter);
fprintf (OutFile,'tolfun=%14.12E\n',tolfun);
fprintf (OutFile,'tolx=%14.12E\n',tolx);      %trust-region-reflective

options = optimoptions(@lsqnonlin,'Algorithm','levenberg-marquardt',...
    'TolX',tolx,'TolFun',tolfun,...
    'DiffMinChange',diffminchange,'DiffMaxChange',diffmaxchange,...
    'FinDiffType','forward','MaxIter',maxiter,...
    'Display',display,'MaxFunEvals',maxfunevals);  % define method

[xfinal, yfinal, residual, exitflag] = lsqnonlin(@BLHfitting, x0, lb, ub,
options);
% x0: initial value
% lb: lower boundary
% ub: upper boundary
%
%%%%%%%%%%%%%%%%%%%%%%%%%%%%%%%%%%%%%%%%%%%%%%%%%%%%%%%%%%%%%%%%%%%%%%%

% output
fprintf(OutFile,'xfinal\n');
fprintf(OutFile,'%15.12f %15.12f %15.12f %15.12f \n',xfinal(1),xfinal(2),....
    xfinal(3),xfinal(4),xfinal(5));
fprintf(OutFile,'%15.12f %15.12f %15.12f %15.12f %15.12f %15.12f
\n',xfinal(6),...
    xfinal(7),xfinal(8),xfinal(9),xfinal(10));
fprintf(OutFile,'yfinal=%20.18f\n',yfinal);
fprintf(OutFile,'exitflag=%2i\n',exitflag);

%%%%%%%%%%%%%%%%%%%%%%%%%%%%%%%%%%%%%%%%%%%%%%%%%%%%%%%%%%%%%%%%%%%%%%%
fclose (OutFile);
fprintf('---------------------- the end ----------------------');

xlswrite ('BLH_coefficient.xlsx', xfinal );
end

%%%%%%%%%%%%%%%%%%%%%%%%%%%%%%%%%%%%%%%%%%%%%%%%%%%%%%%%%%%%%%%%%%%%%%%
```

```
%calculation function
function F = BLHfitting(x)
%%%%%%%%%%%% function y=calculation(x)

global OutFile                              %iPotentialFile
my_data = xlsread('IG110_Data_IV.xlsx');
my_data_sub = my_data(1:142,:);
[M, N] = size (my_data_sub);
Temp = my_data(1:142,8);
PH2O = my_data(1:142,22);
PH2 = my_data(1:142,23);

%%%%%%%%%%%%%%%%%%%%%%%%%%%%%%%%%%%%%%%%%%%%%%%%%%%%%%%%%%%%%%%%%%%%%%%%%%%%%%%

%%%%%%%%%%%%%%%%%%%%%%%%%%%%%%%%%%%%%%%%%%%%%%%%%%%%%%%%%%%%%%%%%%%%%%%%%%%%%%%
fprintf(OutFile,'xA1 = %15.12f; \n ', x(1) );
fprintf(OutFile,'xA2 = %15.12f; \n ', x(2) );
fprintf(OutFile,'xA3 = %15.12f; \n ', x(3) );
fprintf(OutFile,'xE1 = %15.12f; \n ', x(4) );
fprintf(OutFile,'xE2 = %15.12f; \n ', x(5) );
fprintf(OutFile,'xE3 = %15.12f; \n ', x(6) );
fprintf(OutFile,'xmmin = %15.12f; \n ', x(7) );
fprintf(OutFile,'xmmax = %15.12f; \n ', x(8) );
fprintf(OutFile,'xtheta = %15.12f; \n ', x(9) );
fprintf(OutFile,'xT0 = %15.12f; \n ', x(10) );
% fprintf(OutFile,'xn = %15.12f; \n ', x(11) );

xA1   = x(1);
xA2   = x(2);
xA3   = x(3);
xE1   = x(4);
xE2   = x(5);
xE3   = x(6);
xmmin = x(7);
xmmax  = x(8);
xtheta = x(9);
xT0 = x(10);
% xn    = x(11);

for i=1:1:M
    mT(i) = xmmax + (xmmin-xmmax)/(1+exp((Temp(i)-xT0)/xtheta));

    A11(i) = (10^-6)*xA1*exp(xE1*1000/(8.314*Temp(i)));
    A22(i) = (10^-6)*xA2*exp(xE2*1000/(8.314*Temp(i)));
    A33(i) = (10^-6)*xA3*exp(xE3*1000/(8.314*Temp(i)));
    %DATAF(i)   =A1*exp(-E1/(R*Temp(i))*PH2O(i)**(mmax/(1+exp()(T0-
Temp(i))/theta))))
    DATAF(i) =
A11(i)*PH2O(i)^mT(i)/(1+A22(i)*PH2(i)^1.0+A33(i)*PH2O(i)^mT(i));
end

%%%%%%%%%%%%%%%%%%%%%%%%%%%%%%%%%%%%%%%%%%%%%%%%%%%%%%%%%%%%%%%%%%%%%%%%%%%%%%%

REF = my_data(1:142,3)';                % experimental value
DATA = DATAF;                          % predicted value
```

```
WEIGHT = ones(1,M);
WEIGHT = 100*WEIGHT;

DIFF =((DATA-REF)./REF).*WEIGHT;
F = DIFF;

for i = 1:1:M
    fprintf(OutFile,'########## ref=%15.12f     DATA=%15.12f
F=%15.12f\n',REF(i),DATA(i),F(i));
end

y=sum(DIFF.^2);
fprintf(OutFile,'######### y=%15.12f\n',y);
%F
%%%%%%%%%%%%%%%%%%%%%%%%%%%%%%%%%%%%%%%%%%%%%%%%
end
```